Alma Mater Studiorum – Università di Bologna

DOTTORATO DI RICERCA IN

Scienze della Terra

Ciclo XXVI

Settore Concorsuale di afferenza: 04/A2

Settore Scientifico disciplinare: GEO/03

TRANSFORM TECTONICS AND NON-VOLCANIC OCEANIC ISLANDS

Presentata da*: Dott.ssa Camilla Palmiotto*

Coordinatore Dottorato

Prof. Vincenzo Picotti

Relatore

Dott. Marco Ligi

Co-Relatori

Prof. Enrico Bonatti

Prof.ssa Laura Corda

Esame finale anno 2014

…a mio nonno Francesco

"…It is not of volcanic origin…

It is composed of rocks, unlike any which I have met with,

and which I cannot characterize by any name, and must therefore describe…"

[*Darwin,* February 16th, 1832]

Riassunto

Le isole oceaniche possono essere suddivise, sulla base della loro origine, in vulcaniche e tettoniche. Le isole vulcaniche si formano per eccesso di magmatismo legato ad anomalie termiche o composizionali del mantello. Le isole non-vulcaniche, o "tettoniche", sono sopratutto il risultato di grandi movimenti verticali della litosfera oceanica lungo le faglie trasformi lente ed ultralente. La causa principale di questi movimenti tettonici verticali è da attribuire ad una riorganizzazione della geometria dei limite di placca trasforme, con il passaggio da una tettonica puramente trascorrente, ad una di tipo transtensivo e/o transpressivo. In entrambi i casi si ha la formazione di un'anomalia topografica positiva del fondale marino, chiamata "rilievo trasversale". I rilievi trasversali hanno generalmente un profilo asimmetrico e sono formati da rocce di crosta oceanica inferiore e/o da rocce di mantello superiore. Quando raggiungono o superano il livello del mare essi formano un'isola oceanica di origine non vulcanica. Le isole tettoniche possono trovarsi anche all'intersezione dorsale - trasforme, costituendo il cosiddetto "alto interno". In questo caso il sollevamento della litosfera è da attribuire al movimento delle faglie di dislocamento localizzate lungo i fianchi della dorsale. Un esempio attuale di alto interno vicino al livello del mare è il seamount "Anna De Koningh", situato all'intersezione tra la dorsale oceanica sud occidentale e la faglia trasforme Dutoit (Oceano Indiano).

Rilievi batimetrici e profili di sismica a riflessione mono e multicanale hanno identificato quattro paleoisole tettoniche in Atlantico Equatoriale. La paleoisola "Vema" costituisce la sommità del rilievo trasversale dell'omonima faglia trasforme, e si trova oggi circa 450 m sotto il livello del mare. Vema è composta da una piattaforma carbonatica spessa circa 500 metri, lunga circa 50 km e larga solo 5 km. Datazioni $^{87}Sr/^{86}Sr$ sui carbonati di Vema hanno permesso di porre la formazione dell'isola a circa 10 Ma, età che corrisponde ad un cambio cinematico della placca Sud-Americana e alll'instaurazione di una tettonica di tipo transtensivo che ha causato la flessurazione della litosfera oceanica e la formazione del rilievo trasversale. Tuttavia, il ritrovamento del foraminifero *"Miogypsina"* all'interno di alcuni campioni dragati in prossimità della non-conformity basamento

– piattaforma carbonatica, campioni che non è stato possibile datare, testimonia una precedente emersione dell'isola durante il Miocene inferiore, quando l'isola si trovava al lato interno dell'intersezione dorsale - trasforme. Altre tre paleoisole tettoniche, "Romanche A, B and C", costituiscono le sommità del rilievo trasversale orientale della megatrasforme Romanche, e si trovano attualmente circa 1000 metri sotto il livello del mare. Profili di sismica a riflessione multicanale mostrano un riflettore orizzontale ad alta impedenza acustica alla profondità di circa 1200 metri. Sopra questo riflettore, per ogni isola, si individua un'unità sismica stratificata, potente circa 250-300 metri. Anche queste tre isole, come quella di Vema, sono costituite da carbonati di acque basse datati con $^{87}Sr/^{86}Sr$ al Miocene superiore, tra 11 e 6 Ma. In Oceano Indiano Sud-Occidentale, lungo la faglia trasforme Atlantis II, si trova un'altra isola annegata ("Atlantis Bank"), oggi circa -700 m sotto il livello del mare. L'isola non presenta una piattaforma carbonatica, ma era al livello del mare quando si trovava all'intersezione dorsale – trasforme.

L'unico esempio attuale d'isola tettonica è l'Arcipelago di San Pietro e Paolo (Atlantico Equatoriale), lungo l'omonima faglia trasforme. L'Arcipelago costituisce la sommità di un massiccio peridotitico che si allunga in direzione della faglia trasforme attiva ed è soggetto attualmente a transpressione. Datazioni di markers del livello del mare con il ^{14}C hanno permesso di stimare un tasso di sollevamento di circa 1,5 mm/a per gli ultimi 6000 anni.

Durante il dottorato, uno studio multidisciplinare ha portato allo sviluppo di un modello di origine ed evoluzione delle isole tettoniche. A differenza di quelle vulcaniche, caratterizzate da una rapida crescita e dalla successiva subsidenza termica che porta all'annegamento, le isole tettoniche possono avere uno o più episodi di emersione legati agli effetti della tettonica verticale e del raffreddamento litosferico lungo le grandi zone di frattura oceanica.

Abstract

Oceanic islands can be divided, according to their origin, in volcanic and tectonic. Volcanic islands are due to excess volcanism caused by mantle melting anomalies. Non-volcanic islands, or "tectonic", are mainly formed due to vertical tectonic motions of blocks of oceanic lithosphere along transverse ridges flanking transform faults at slow and ultraslow mid-ocean ridges. Vertical tectonic motions are due to a reorganization of the geometry of the transform plate boundary, with the transition from a transcurrent tectonics to a transtensive and / or transpressive tectonics. The formation of a positive topographic anomaly called "transverse ridge", often strongly asymmetric, may result from the establishment of either a transpressive and transtensive regime. Transverse ridges are formed by uplifted lower oceanic crust and/or upper mantle rocks. When they are at sea level, they form an oceanic non-volcanic island. Tectonic islands can be located also at the ridge – transform intersection, being the “inner corner high”. In this case the uplift is due by the movement of the long-lived detachment faults located along the flanks of the mid-ocean ridges. A modern example of inner corner high near the sea level is the “Anna De Koningh” seamount, located at the intersection between the Southwest Indian Ridge and the Dutoit transform fault (Indian Ocean).

Bathymetry data and multichannel seismic reflection profiles have identified four tectonic sunken islands in the equatorial Atlantic. The "Vema" sunken island is at the summit of the transverse ridge adjacent to the Vema transform fault; it is now about 450 m below sea level. It is capped by a carbonate platform about 500 m-thick, 50 km-long and only 5 km-wide. Samples of Vema’s carbonates dated by $^{87}Sr/^{86}Sr$ indicate that the formation of the island occurred about 10 Ma. The same age corresponds to a kinematic change of the ridge – transform geometry and the establishment of transtensive tectonics, with flexure of the oceanic lithosphere and uplift of the Vema transverse ridge. However, the discovery of "*Miogypsina*" in samples dredged at the non-conformity boundary between the basement and the carbonate platform suggest a stage of emergence of the island during Early Miocene, when the island was an inner corner high at the ridge – transform intersection. Three tectonic sunken islands, "Romanche A, B and C", are on the

summit of the eastern transverse ridge flanking the Romanche megatrasform; they are now about 1,000 m below sea level. Multichannel seismic reflection profiles show a strong horizontal reflector at a depth of about 1200 m. Above this reflectors we observed stratified seismic units about 250-300 m-thick representing carbonate platforms consisting of shallow-water carbonates dated by $^{87}Sr/^{86}Sr$, between 11 and 6 Ma. Another sunken tectonic island, the “Atlantis Bank," today about 700 m below sea level, is located in the South-Western Indian Ridge, along the Atlantis II transform fault. This island does not have a carbonate platform but it was at sea level when it was located at the ridge-transform intersection.

The only modern example of oceanic tectonics island is the Saint Peter - Paul Archipelago (equatorial Atlantic), located along the active zone of the St. Paul transform fault. This archipelago is the top of a peridotitic massif that extends in the direction of the active transform fault and it is now a left overstep undergoing transpression. Markers of sea level dated by ^{14}C estimate a rate of uplift of the St. Paul Massif of about 1.5 mm/a for the last 6000 years.

During my PhD, a multidisciplinary study led to a model to explain the origin and evolution of oceanic tectonic islands: oceanic volcanic islands are characterized by rapid growth and subsequent thermal subsidence and drowning; in contrast, oceanic tectonic islands may have one or more stages of emersion related to vertical tectonic events along the large oceanic fracture zones.

Index

Chapter 3. Development of different modes of detachment faulting, 16.5° N at the Mid-Atlantic Ridge

Chapter 4. Oceanic Megatransforms: A New Type of Plate Boundary

Chapter 5. Non-volcanic tectonic islands in ancient and modern oceans

Thesis Outline

My PhD thesis consists of seven chapters and a final conclusion. In the first chapter I described the geodynamic of tectonic islands in three paragraphs, with a description of the main features of mid-ocean ridges, of oceanic core complexes and of oceanic transform faults. The second chapter includes the article "Seismicity of Equatorial Mid-Atlantic Ridge and its Large Offset Trasnforms", published in the journal "*InterRidge News*" (2012) and written during cruise AT21-03 (equatorial Atlantic Ocean), aboard of the R/V Atlantis II, of Woods Hole Oceanographic Institution (WHOI). The third chapter consists of an article submitted to the journal, "*InterRidge News*" (2013). This article, "Development of different modes of detachment faulting, 16.5°N at the Mid-Atlantic Ridge", describes the vertical movements along detachment faults; it was written during cruise KN21-05 (central Atlantic Ocean), aboard the R/V Knorr, of WHOI. The fourth chapter is a portion of a future article on megatransform faults. In this chapter, I describe the geological setting of Romanche, Andrew Bain and St. Paul transform faults. This article will be submitted to the Journal "*Earth Science Review*". The fifth chapter is composed by the article "Non-volcanic tectonic islands in ancient and modern oceans". This article reports most of the results of the work that I did during my PhD and it is published in the Journal "*Geochemistry, Geophysical, Geosystems*". The chapter sixth includes an article will be submitted to the Journal "*Palaeogeography, Palaeoclimatology, Palaeoecology*", where I describe the possible causes of the presence of rhodalgal-foramol facies in equatorial carbonates of the sunken tectonic islands at the equatorial latitude. Finally, in the seventh chapter I described the only known example of non-volcanic "oceanic" islands: St. Paul Rocks (Penedos de São Pedro). Studying its biology and zoology, I observed that actually these islets do not have a carbonate platform, but there are some species of corals and green algae that live in the Caribbean Sea. The absence of a carbonate platform is probably due to the continuous uplift of the islets and to their morphology characterized by flanks with steep slope.

Chapter 1

Geodynamics of oceanic tectonic islands

Oceanic islands can be divided, according to their origin, in volcanic and tectonic. Volcanic islands are due to excess volcanism caused by mantle melting anomalies either along mid-ocean ridges, (Iceand in the Atlantic Ocean), or within oceanic plates (Society Islands in the Pacific Ocean). Volcanic islands can also be formed by volcanism caused by suprasubduction "wet" mantle melting (Tonga islands in the Pacific Ocean). Tectonic islands are formed not by excess volcanism, but are due to vertical tectonic motions of blocks of oceanic lithosphere along transverse ridges flanking slow and ultraslow transform faults.

Sunken tectonic islands have been identified with bathymetric surveys and multichannel seismic reflection profiles in the equatorial Atlantic Ocean. A "Vema" sunken island has been identified on the summit of a transverse ridge at Vema transform fault; it is now ~ 450 m below sea level. Three other sunken islands are located along the summit of a transverse ridge at the Romanche transform fault; they are now between 900 and 1100 m below sea level. The only modern example of oceanic tectonic island is the Archipelago of St. Peter and St. Paul Rocks, located along the St. Paul transform in equatorial Atlantic Ocean. It is formed by five bigger islands and many small rocks, all composed of peridotitic rocks.

Vertical motions of blocks of oceanic lithosphere take place along slow mid-ocean ridges, where we have uplift due to extensional movements along long-lived detachemtents faults. They exume lower crust and upper mantle creating positive topographic anomalies called oceanic core complexes. It is now recognized that the 50% of the extension of the oceanic crust along slow and ultraslow mid-ocean ridges is due to the action of long lived detachment faults that form oceanic core complexes. The sunken tectonic island "Atlantis Bank", located along the transverse ridge at the Atlantis II transform fault (South-West Indian Ocean), is an example of oceanic core complexes. It is a gabbroid massif exumed by a long lived detachment fault. "Atlantis Bank" was a tectonic

islands when it was an inner corner high at the ridge – transform intersection, and now it is ~ 700 m below sea level.

In the first chapter of my PhD thesis I will discuss the geodynamics of oceanic tectonic islands, describing mid-ocean ridges, the formation and the evolution of oceanic core complexes, and oceanic transform faults, including a new class of transform faults called "megatransforms".

1.1 Mid-Ocean Ridges

In the middle of twentieth century, Bruce C. Heezen and Marie Tharp (Figure 1.1a) created a famous world map of the ocean floor [Figure 1.1b; *Heezen and Tharp,* 1968]. This map was the first to show a giant submarine mountain chain running along the middle of the oceans: in the modern "Theory of Plate Tectonics", it has been called mid-ocean ridge (MOR), and it is the place where two different lithospheric plates move apart and new oceanic crust is formed.

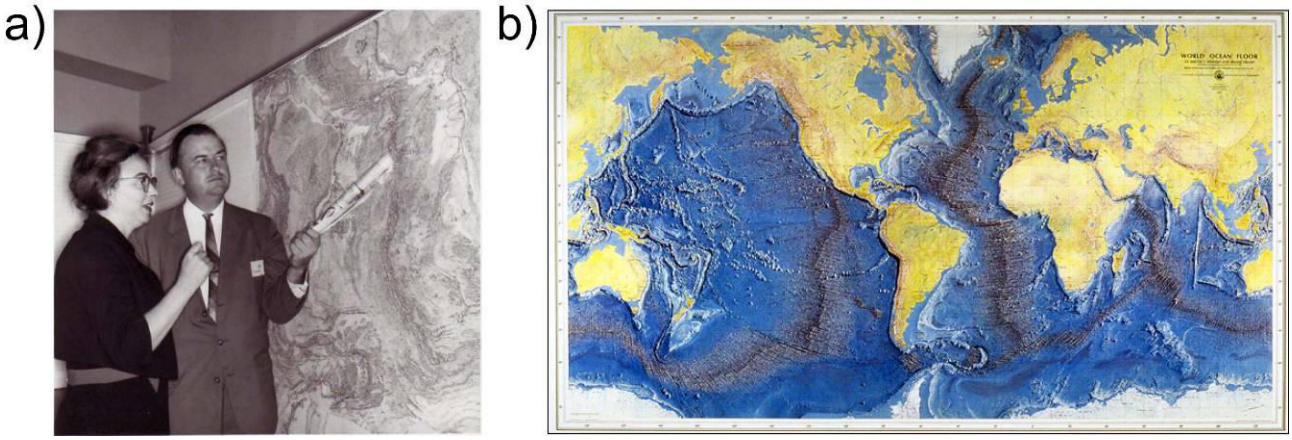

Figure 1.1 a) *Bruce C. Heezen and Marie Tharp in the 1977 [image from Wikipedia Commons];* **b)** *Heezen and Tharp's world maps of the ocean floor [Heezen and Tharp, 1968].*

The global system of mid-ocean ridges (Figure 1.2) constitutes the longest mountain chain on Earth (~ 67.000 km); it is site of intense volcanism and seismicity. It is characterized by hydrothermal circulation with temperatures exceeding 300°C, by metallogenesis with the deposition of Fe-sulfides and Fe-Mn hydroxides, hosting extraordinary biological activity (mainly bacteria), and playing an important role in the chemical exchange with sea water.

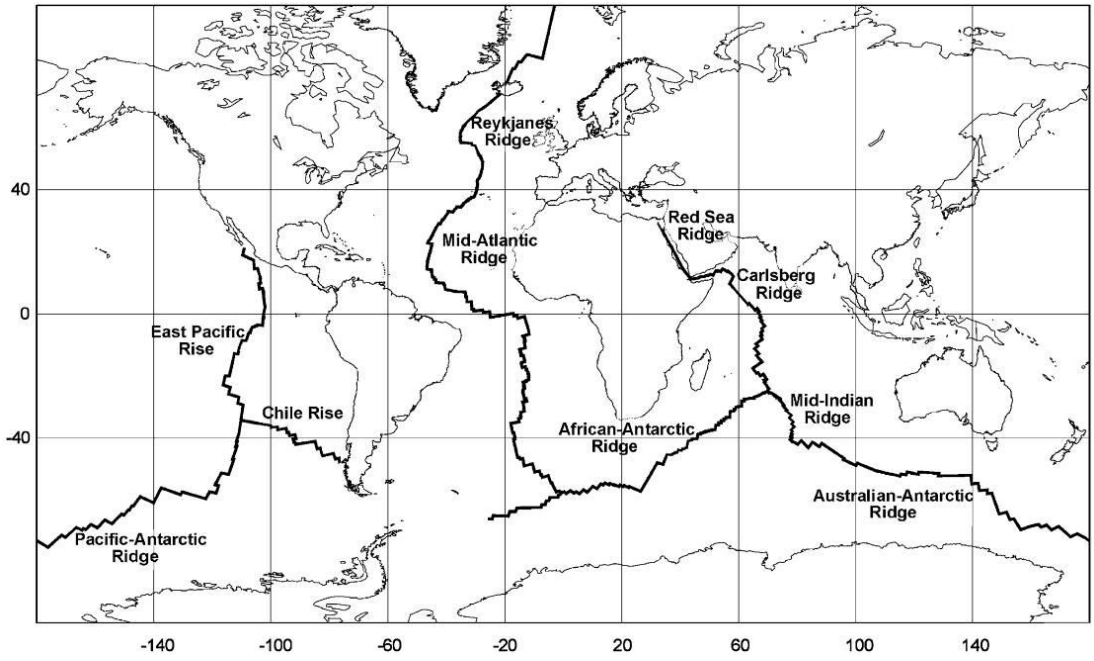

Figura 1.2 *Global system of Mid-Ocean Ridges [Rundquist and Sobolev, 2002].*

Mid-ocean ridges are characterized by a topographic relief that lies at a rather constant depth of about 2500 m below sea level respect to ocean basins (abyssal plain), that lie ~ 5000-6000 m below sea level. They present an axial valley characterized by intense volcanism and seismicity, with a neovolcanic zone where new oceanic crust is formed (Figure 1.3). Melt rises below the axial valley, from the underlying asthenosphere to subsequently solidify becoming part of lithospheric plates, creating new oceanic crust. According to *MacDonald* [1982], the velocity with which the lithospheric plates diverge from each other (spreading rate) allows to classify mid-ocean ridges in:

- fast (spreading rate between 80 and 180 mm/a, like the East Pacific Rise);
- intermediate (spreading rate between 55 and 80 mm/a, like the Juan the Fuca Ridge);
- slow (spreading rate between 22 and 55 mm/a, like the Mid-Atlantic Ridge);
- ultra-slow [*Dick et al.,* 2003], (spreading rate < 22 mm/a, like the Artic Gakkel Ridge).

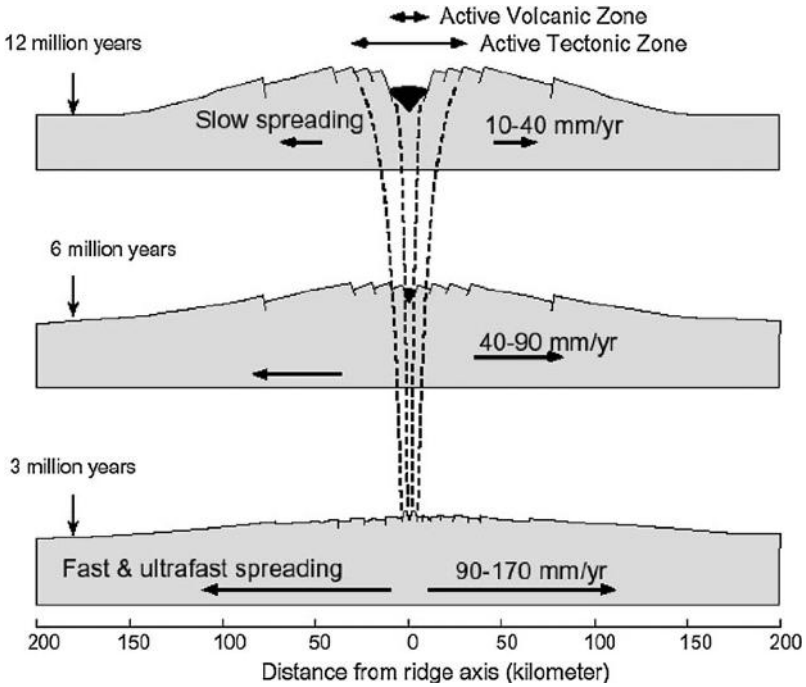

Figure 1.3 *Near-axial structural profiles across accreting ridge systems with different spreading rates showing the variable sizes of their axial rift valleys [Choukroune et al., 1984].*

1.1.1 Morphology of mid-ocean ridges

The morphology of the global system of mid-ocean ridges can be described analyzing the "spreading rate classification".

Slow MORs, like the Mid-Atlantic Ridge (MAR) in the Atlantic Ocean (Figures 1.2 and 1.4), are characterized by rugged faulted block topography, 20-30 km wide axial median valley, ~ 1-2 km deep and floored by many small volcanic edifies [*Smith and Cann,* 1993], with faults occurring along the flanks of the ridges, ~ 20-40 km from the axis, at crustal age ~ 1.5 Ma (Figure 1.4) [*Escartin and Cannat,* 1999; *Smith et al*., 2003]. *Dick et al.* [2003] recognized mid-oceanic ridges with spreading rates <12 mm/a as a distinct 'ultraslow' class. Ultra-slow MORs, like the Southwest Indian Ridge (SWIR) in the Indian Ocean, show a rugged median valley which in places exceeds 2 km deep, with a depth at the axis of over 4 km. All faults mapped at slow and ultraslow spreading centers dip toward the axis: according to many authors, these faults form during periods when no magma is available and the total slip on faults depends on the time interval between magma events. Although the flanks of slow and ultraslow MORs are cut by high-angle normal

faults, there is another type of fault that affects the morphology of slow spreading centers. They are low-angle faults, called detachment faults, that form characteristic features termed oceanic core complexes. These features have been likened to continental metamorphic core complexes, where rocks from depths of ~ 10 km are exposed at the surface. More details about the oceanic core complexes will be discussed in the second paragraph of this chapter. The axial region of fast mid-ocean ridges, like the East Pacific Rise in the Pacific Ocean (Figures 1.2), are smoother and generally lack a median valley, having instead an axial high some 1-2 km wide (Figure 1.4). Along the fast spreading centers the magmatic activity is more continuous and the faults propagation along the flanks of the ridge is minor respects slow and ultraslow MORs. Mid-ocean ridges with intermediate spreading rate, like the Juan de Fuca Ridge in the Pacific Ocean, can have either fast or slow type topography.

The morphology of the axial region along MORs depends on the thermal state and composition of the subridge upwelling mantle, linked also to spreading rate and vicinity to long offset transforms. Other factors that control the morphology of the axial region of a volcanic ridge are the tectonic strain and the magma supply; for example, much of the slow-spreading Reykjanes Ridge does not have a median valley, and in some location, the fast-spreading East Pacific Rise has a shallow axial valley. We can compare the morphology of the axial valley of the different MORs looking the Figure 1.4. This figure shows three different bathymetric profiles acquired along the East Pacific Rise (EPR), the Southeast Indian Ridge (SEIR) and the Mid-Atlantic Ridge (MAR). The morphology of the rift valley is completely different: the EPR presents a positive bathymetry and a low presence of faults along the flanks of the ridge; instead, the other two bathymetric profiles show a negative profile and intense tectonics due to high-angle faults.

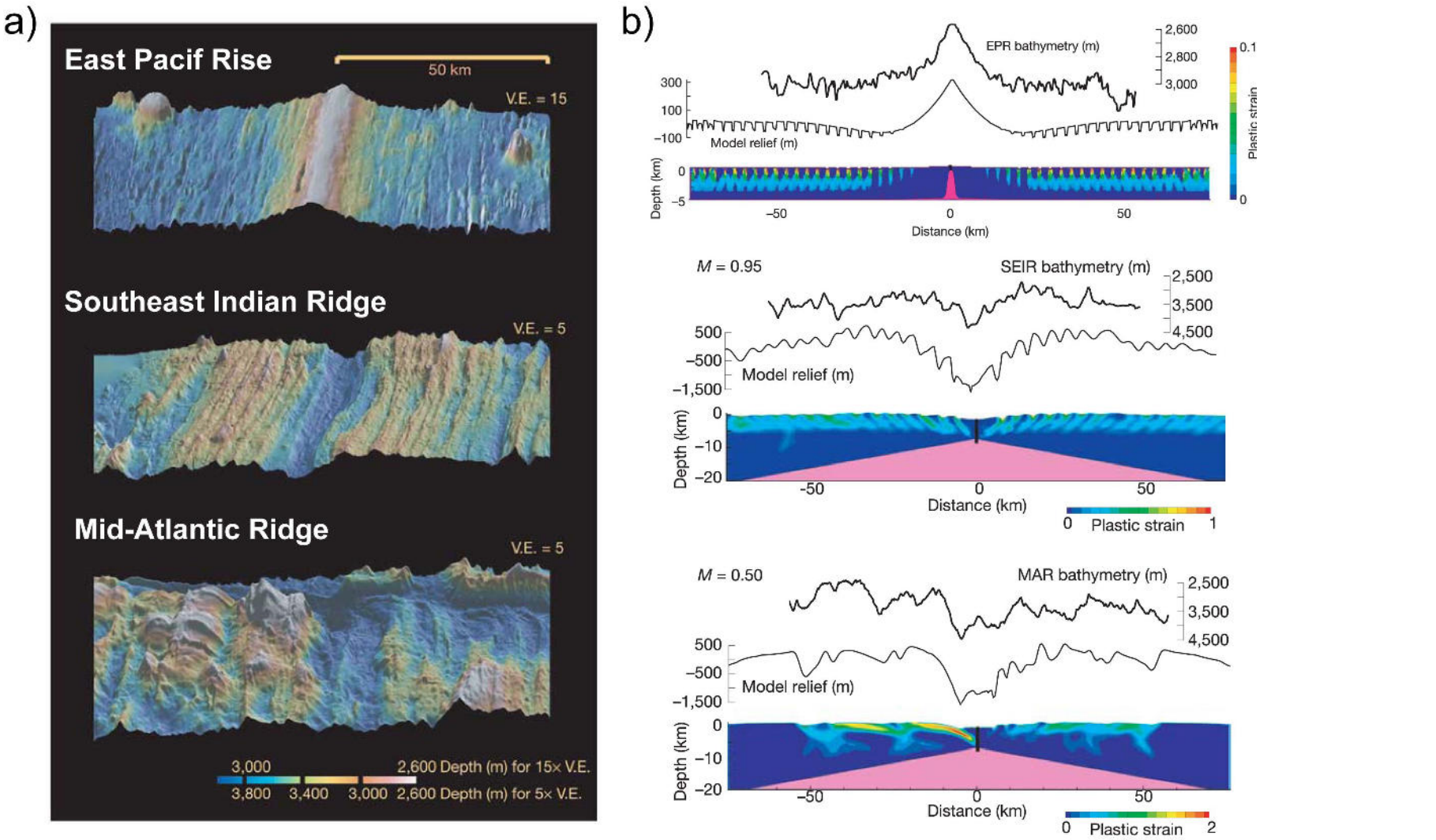

Figure 1.4 a) *Shaded relief images of bathymetry over three contrasting sections of the mid-ocean ridges. Each image shows ,40 km along the ridge axis and ,110 km across the axis [Buck et al., 2005]. V.E.= vertical exaggeration.* **b)** *Bathymetric profiles of East Pacific Rise (EPR), Southeast Indian Ridge (SEIR) and Mid-Atlantic Ridge (MAR). Results for buoyancy-dominated ridge models (EPR). Half the bending faults dip towards the axis and half away. Two results for stretching-dominated ridge models (SEIR and MAR). for different values of M, but with the same lithospheric structure [Buck et al., 2005].*

1.1.2 Oceanic crustal structure

The oceanic crustal structure has been inferred by seismic reflection and refraction methods (Figure 1.5). The oceanic crust is considerably thinner than the continental crust; it is formed by a typical lithological succession made, from top to bottom, by a layer of sedimentary material, then effusive basaltic rocks, a dyke complex and finally gabbros (Figure 1.6).

The thickness of the sediments (Layer 1) increases with the age and distance from the mid-ocean ridge system; it also depends upon sediment supply and is thus variable. The thickness varies generally from a few centimeters (or absent) in neovolcanic zones to an average of 500 meters in the ocean basins; in the valleys of oceanic fracture zone, like the Vema and the Romanche transform valleys (equatorial Atlantic), it is possible to have also ~ 1000 m of sediments. The velocity of sound in the first layer is usually slightly higher than the velocity of sound in sea water (~ 1.5 km/s), but it increases rapidly with depth as the sediments consolidate. Layer 2 is heterogeneous in both depth and age (Figure 1.6). When the velocity of sound reaches ~ 2.5 - 2.8 km/s, we are on the top of the Layer 2 [*White et al.,* 1992], formed by few hundred meters of volcanic oceanic basalt basement. The change of lithology from basalts to dikes is marked by an increase of speed of seismic P-waves (from ~ 5.8 of the basalts to ~ 6.4 km/s of the dikes). A further increase of P-wave velocity (~ 6.5-7.2 km/s) marks the transition to the deepest part of the oceanic crust, essentially formed by gabbro (Layer 3). The rapid increase of velocity in the Layer 3 is also due to the decrease in porosity resulting from secondary mineralization and filling of cracks, fissures and pores.

The layer of gabbros is more uniform of Layers 1 and 2; however, in the basal part of the gabbro's layer the seismic velocities are higher (about ~ 7.2-7.7 km/s) due probably to the presence of ultramafic serpentinized material of the upper portion of the mantle. The transition from the crust to the peridotitic mantle (Moho) is marked by a sharp increase in seismic velocity which reaches ~ 7.9-8.0 km/s in the upper part of the mantle [*White et al.,* 1992].

The average thickness of the oceanic crust is ~ 7 km, but variations occur for closer spacing of transform faults along slow and ultraslow-spreading centers, and the resultant difference in distribution of melt along slow and fast ridges.

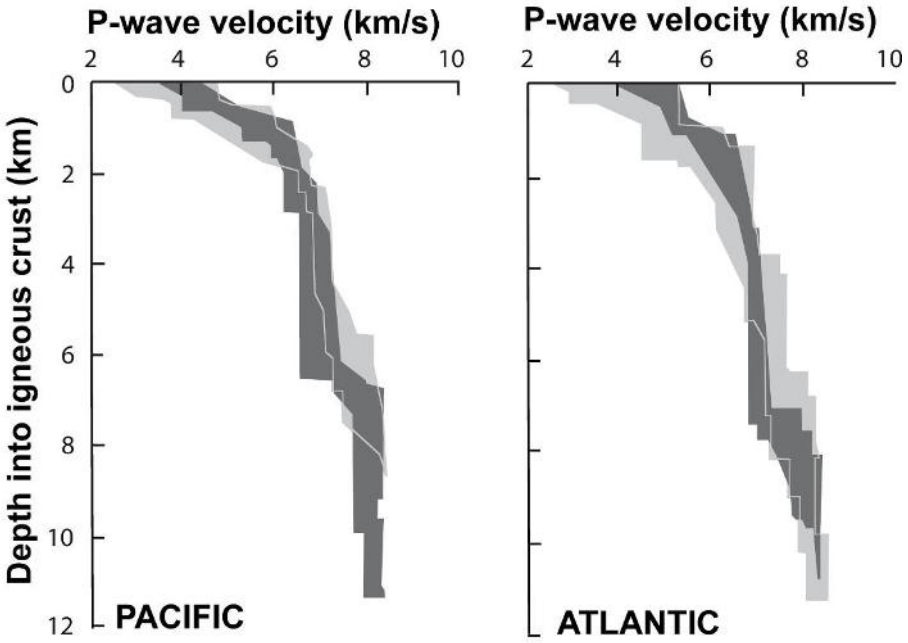

Figure 1.5 *Shaded area shows stacked velocity-depth determinations for Pacific and Atlantic oceanic crust from seismic profiles constrained by synthetic seismic modeling and with a residual depth anomaly less than 0.5 km [after White et al., 1992]. Ligth grey: young oceanic crust (Pacific, 0.2-2 Ma; Atlantic 0-7 Ma). Dark grey:mature oceanic crust (Pacific, 29-140 Ma; Atlantic, 144-170 Ma).*

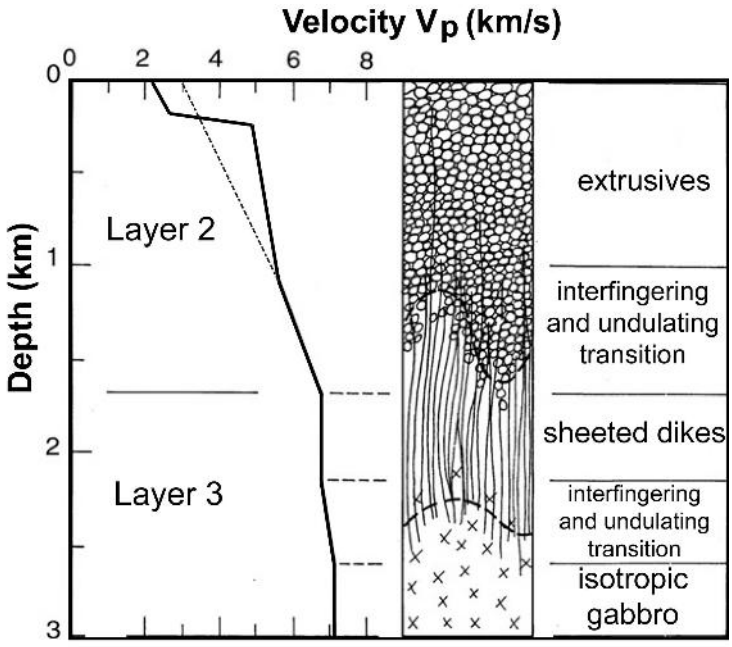

Figure 1.6 *Seismic velocity–depth model fromthe East Pacific Rise correlated with DSDP hole 504B in 6.6 Ma oceanic crust that was formed at the Costa Rica Rift with a half-spreading rate of 30–34 mm/a [modified from Bratt and Purdy, 1984; Vera and Diebold, 1994].*

1.1.3 Thermal structure of the oceanic lithosphere

New melt rises below the axial valley of mid-ocean ridges through a process of adiabatic decompression of the mantle; it then comes into contact with sea water. It cools, solidifies, acquires the magnetization of the earth's magnetic field and begins to migrate laterally and symmetrically on both sides of the ridge, following the divergent relative movement of lithospheric plates. The temperature and composition of the mantle are the main control on the melting process below MORs; they also control variations in crustal thickness and chemistry.

In the 1977, *Parsons & Sclater* found a relation between a gradual deepening of the seafloor, a decrease of the heat flow and a gradual increase of the age of the oceanic crust from the ridge axis to the abyssal plain (Figures 1.7 and 1.8). In the oceans, the surface heat flow is related to the age of seafloor: the gradual deepening of the seafloor from the axial valley is due to the progressive cooling of oceanic lithosphere with its age: h= 320 * √a, where h is the depth of the oceanic crust, 320 is a costant and "a" is the age of the oceanic crust.

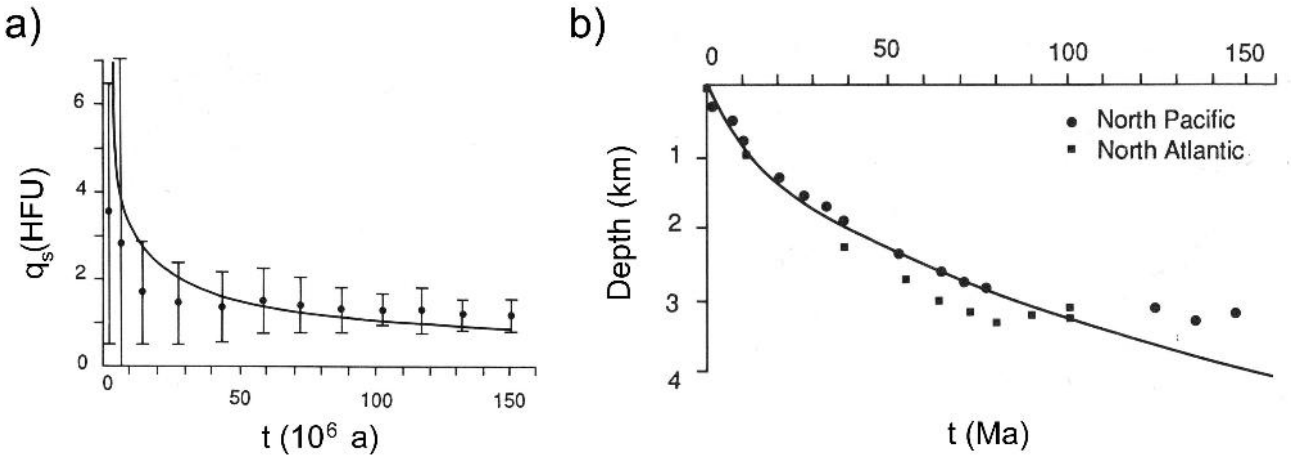

Figure 1.7 a) *Comparison of measured ocean floor heat flows (mean and standard deviation) and those predicted using the instantaneous cooling model, as a function of age [Sclater et al., 1980];* **b)** *Depth of ocean floor below the level of the ridge crest as a function of the sea floor [after Parson and Sclater, 1977]. The solid line shows the theoretical result for an instantaneous cooling model.*

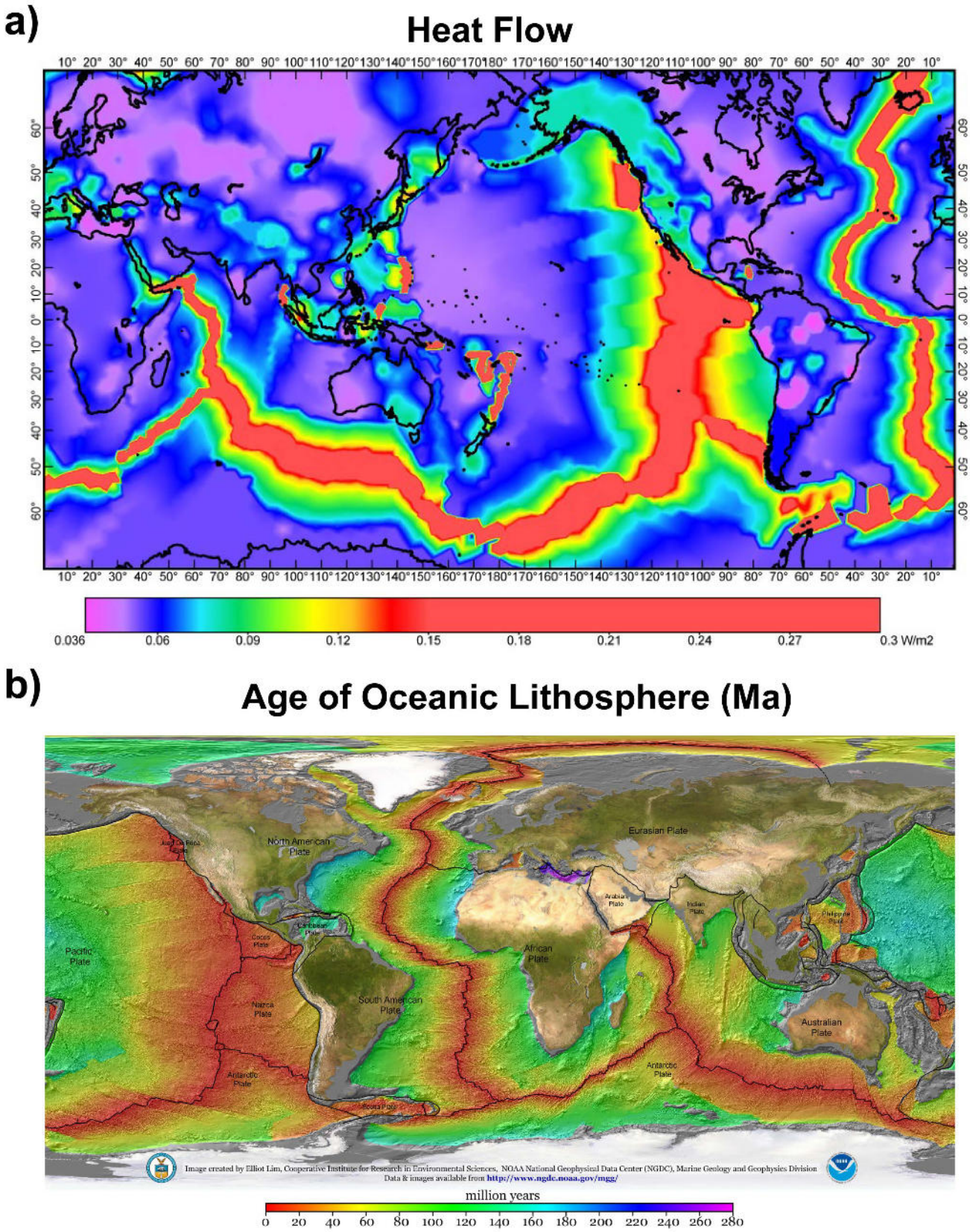

Figure 1.8 a) *Distribution of heat flows on the earth [Bird et al., 2008];* **b)** *Age of oceanic lithosphere along the oceans [Muller et al., 1997].*

In order to infer the age of the rocks along mid-ocean ridges, we study and correlate the magnetic anomalies that are the expression of the direction and magnitude of magnetic field at the earth's surface. Magnetic anomalies are attributed to thermal remaining magnetization of the basaltic oceanic crust and their value varies both in space and in time. They can be represented by an alternation of elongated continuous zones (magnetic anomalies) tens of kilometers long. These zones generally lie parallel to ocean ridges and are symmetric with respect to the ridge crest, as shown in Figure 1.9. Black or positive zones indicate the actual/normal Earth's magnetic field; white or negative zones indicate the old/reverse Earth's magnetic field. The use of magnetic anomalies to deduce the age of the ocean floor can be difficult along slow-spreading centers, where the magmatic activity is intermittent. It is easier in fast MORs, along which the anomalies occupy large areas interspersed with clear boundaries.

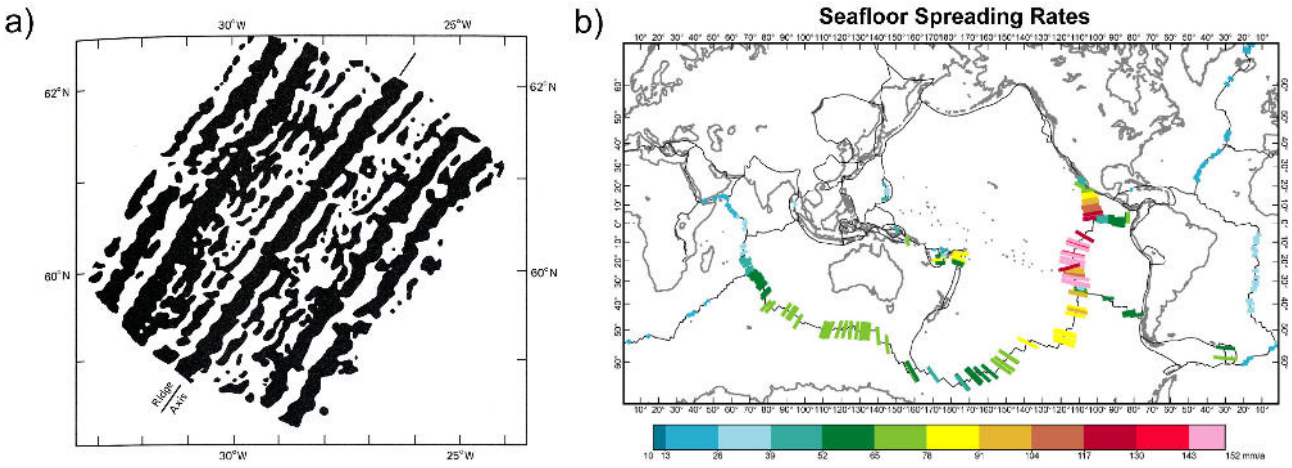

Figure 1.9 a) *Striped pattern of magnetic anomalies parallel to the Mid-Atlantic Ridge [Heirtzler et al., 1966];* **b)** *Spreading rates of mid-ocean ridges, based on identification of linear magnetic anomaly bands [Bird et al., 2008].*

1.1.4 Seismicity associated with mid-ocean ridges

Slow and ultra-slow spreading centers have a deep tectonized axial valley. Faulting on the walls of the valley creates a intense seismicity, with earthquakes hypocenters located at depths exceeding even at 8 km [*Tommey et al.,* 1985] and Magnitude < 6. Fast spreading centers, instead, are characterized by a large dome, with earthquakes hypocenters not exceeding 3 km depth. Figure

1.10 shows the distribution and kinematics of "normal-faulting" earthquakes along the global MORs system.

Multichannel seismic reflection profiles, acquired perpendicular to the axes of fast spreading centers, show a reflector (AMC – Axial Magma Chamber, Figure 1.11). A low seismic velocity zone, possibly due to partially melted material, is present below (Figure 1.11); it represents the top of a magma chamber [*Toomey et al.,* 1990]. This area of low velocity is not commonly observed below slow spreading centers, where magmatic activity is not continuous over time.

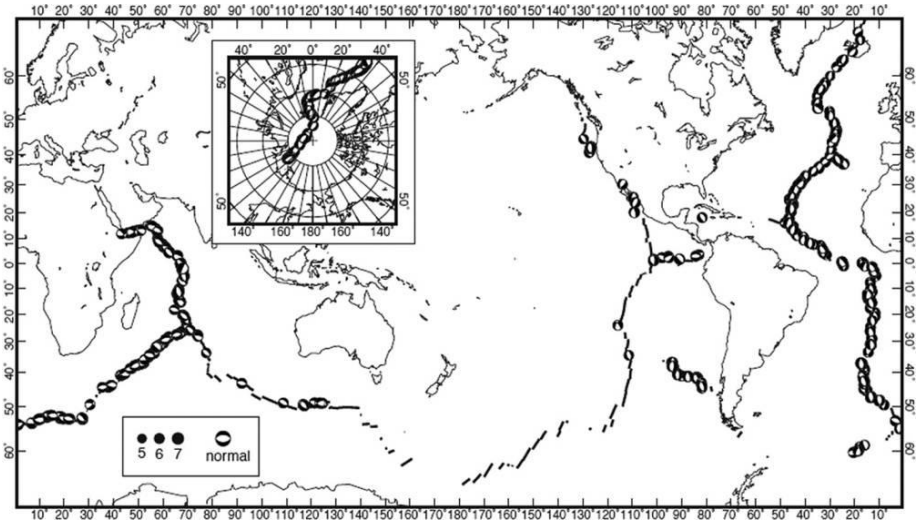

Figure 1.10 *'Spreading' normal-faulting earthquakes along divergent plate boundaries, 1977–1998. Inset, Arctic region. Solid lines, ridgeaxis [from Bird et al., 2002].*

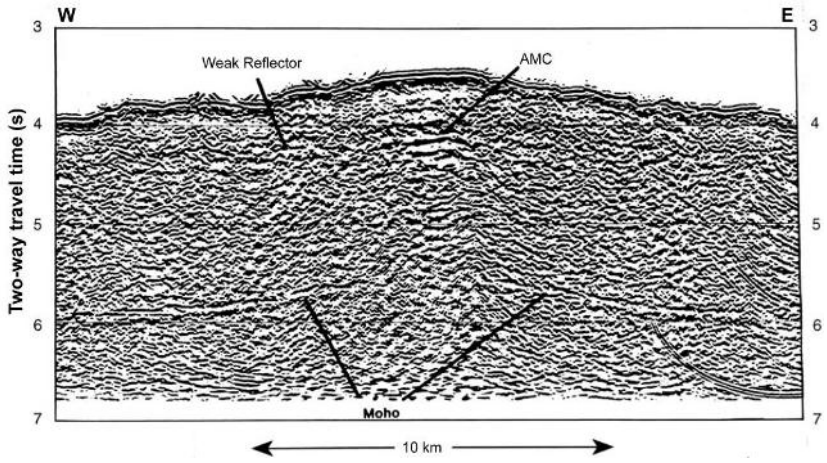

Figure 1.11 *'EastPacific Rise at 9°30'N, migrated CDP reflection profile. Seabed reflection is at 3.5–3.9 s (water depth 2.6–2.9 km). The high-amplitude signal at the ridge axis is interpreted as the reflection from the lid of an axial magma chamber (AMC). It extends weakly onto the flanks of the ridge, perhaps representing the top of a frozen chamber or the change from extrusives to dykes and gabbros. Reflections with the correct time for Moho reflections extend to within 2–3 km of the ridge axis [Detrick et al., 1987].*

1.2 Oceanic Core Complexes

It is now recognized that long-lived low-angle faults (detachement faults) are common along slow mid-ocean ridges, where the magmatic supply is intermittent over time and seismicity and vertical tectonics are intense [*Cann et al,* 1997]. Detachement faults account for 50% of the extension along slow MOR's, and they can form geological features called oceanic core complexes (Figure 1.12). Oceanic core complexes are massifs where lower crust and upper mantle rocks (gabbros and serpentinized peridotites) are exposed at the sea floor [*Smith et al.,* 2006]; in some cases, the core complexes get close to sea level, forming an oceanic tectonic island. The name for OCCs was given by analogy to metamorphic core complexes (metamorphic cores), located in core (inner) parts of orogens on continents. In essence, such complexes are represented by exposed metamorphosed deep-crustal rocks, which underwent by viscous-plastic and brittle deformation. The same situation is typical for OCCs, which are outcrops of tectonized and altered deep-seated crustal and mantle rocks in the axial parts of mid-oceanic ridges.

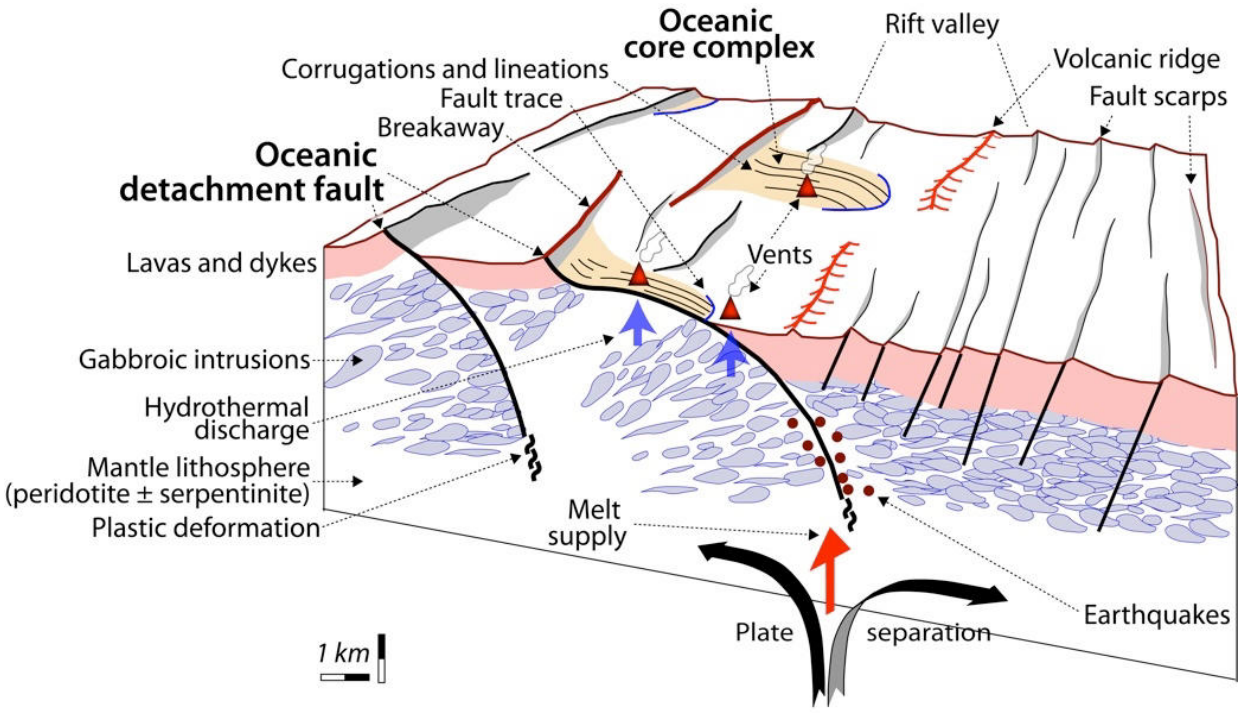

Figure 1.12 *Scheme of oceanic core complex with oceanic detachment fault [Sharkov, 2012].*

A classic example of oceanic core complex is the Atlantis Massif, located in the Atlantic Ocean (Figure 1.13). The Atlantis Massif was formed within the past 1.5–2 Ma at the intersection of the Mid-Atlantic Ridge, 30◦ N, and the Atlantis Transform Fault. The corrugated, striated central dome prominently displays morphologic and geophysical characteristics representative of an ultramafic core complex exposed via long-lived detachment faulting [*Blackman et al.,* 2002]. Geophysical data indicates that the footwall is composed predominantly of serpentinized peridotite; in contrast, the hanging wall is composed of volcanic rock [*Blackman et al.,* 2002].

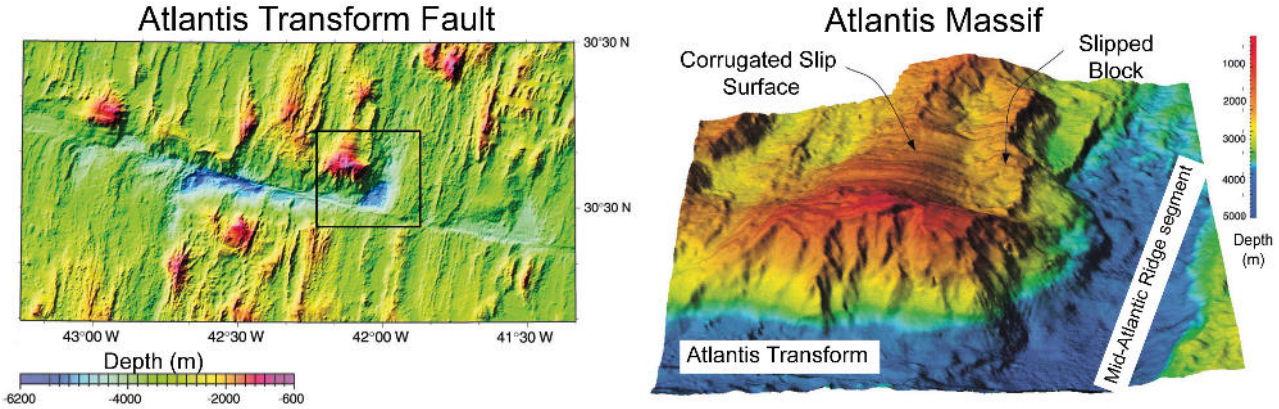

Figure 1.13 *Bathymetry of the Atlantis transform fault at 30°N on the Mid-Atlantic Ridge (Central Atlantic Ocean); black box is A 3D view of the inside corner of the Atlantis transform fault. Corrugated slip surface are shown [Cann et al., 1997].*

The typical surface corrugations can help to identify a core complex along slow-spreading centers, although their origin is still enigmatic. Corrugated slip surfaces have a wavelength of hundreds of meters, an amplitude of ten of meters, and can be seen on shaded relief maps of multibeam surveys (Figure 1.14). Evidence for active detachment faulting can be searched in the associated seismic activity at the MOR segment.

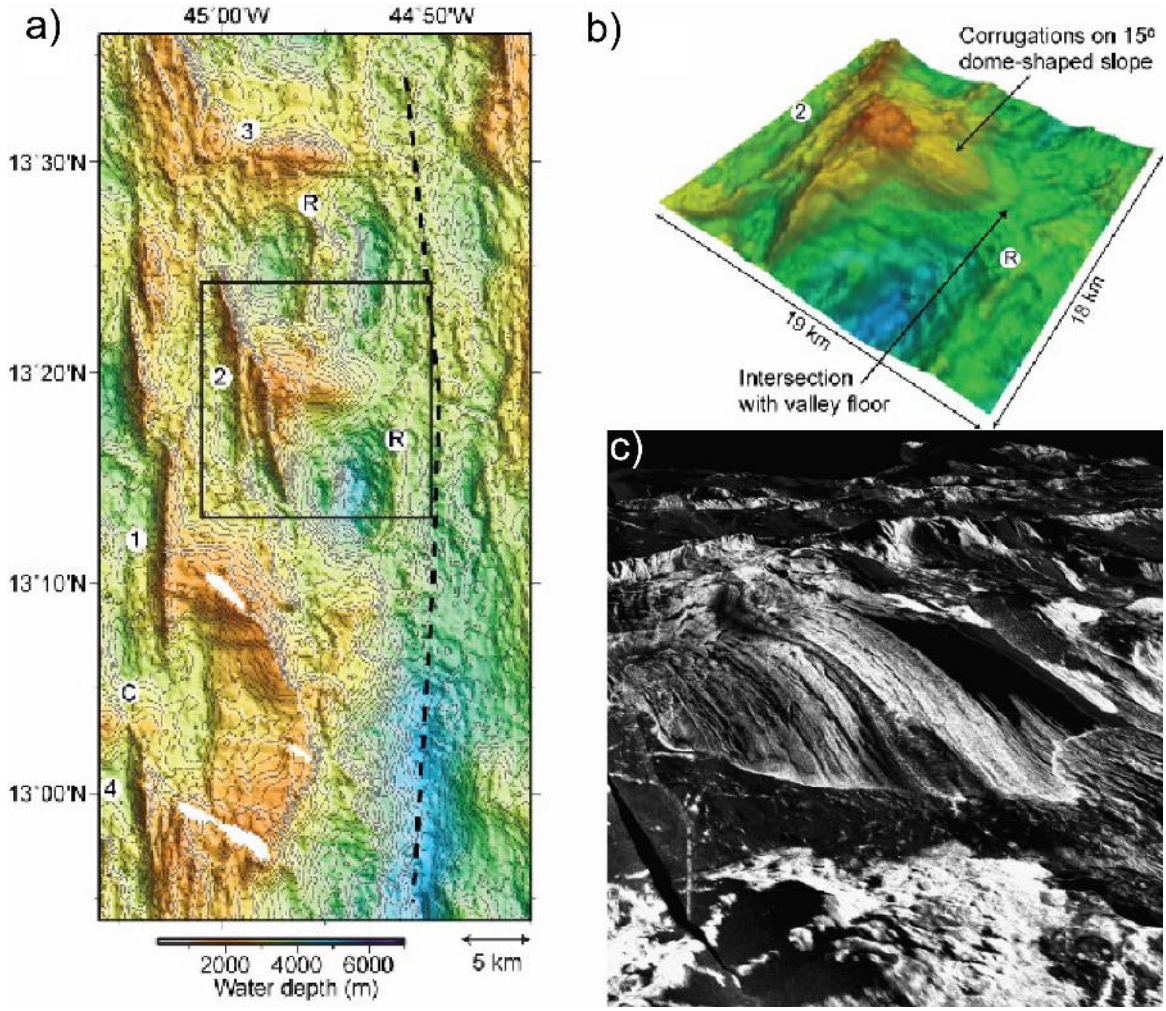

Figure 1.14. a) *Multibeam bathymetry showing detachment faults and core complexes in the 13N segment. The dashed line indicates the spreading axis [Smith et al., 2006]. The box indicates the location of the image in b and c;* **b)** *Three-dimensional perspective view of oceanic core complex '2' [Smith et al., 2006];* **c)** *Three-dimensional perspective view of oceanic core complex '2'[MacLeod et al., 2009].*

Smith et al. [2006] reconstructed the evolution of core complexes from initiation to maturity to inactivity (Figure 1.15): "…In the first stage is the subsidence of a basin within the axial valley floor, coupled with the emergence of a narrow basaltic ridge. The basin lies immediately behind the ridge, and probably forms by outward footwall rotation as a new fault initiates. The inner (eastern) side of the basin (and hence the outer side of the ridge) has the volcanic morphology of the axial valley floor, tilted at 15°-25°. As the ridge evolves, the tilt of the outer slope increases to 20°-30°. A fault scarp dipping at 15°-25° emerges on the inner side of the ridge. The next stage is the emergence of a domal corrugated fault surface that intersects the valley floor along a line convex towards the spreading axis. The corrugated surface dips at ~15° where it plunges into the valley floor. The dip of the surface gradually flattens as it emerges due to flexure of the footwall, and by

~5 km from its emergence the crest is nearly horizontal. Below the median valley floor, the detachment fault may continue at a low angle, but the early rotation of the footwall to form the basin suggests that the fault curves and steepens below the seafloor, so that the tip of the fault may lie several kilometers down. The resulting mature core complex becomes extinct when it is cut off by a normal fault".

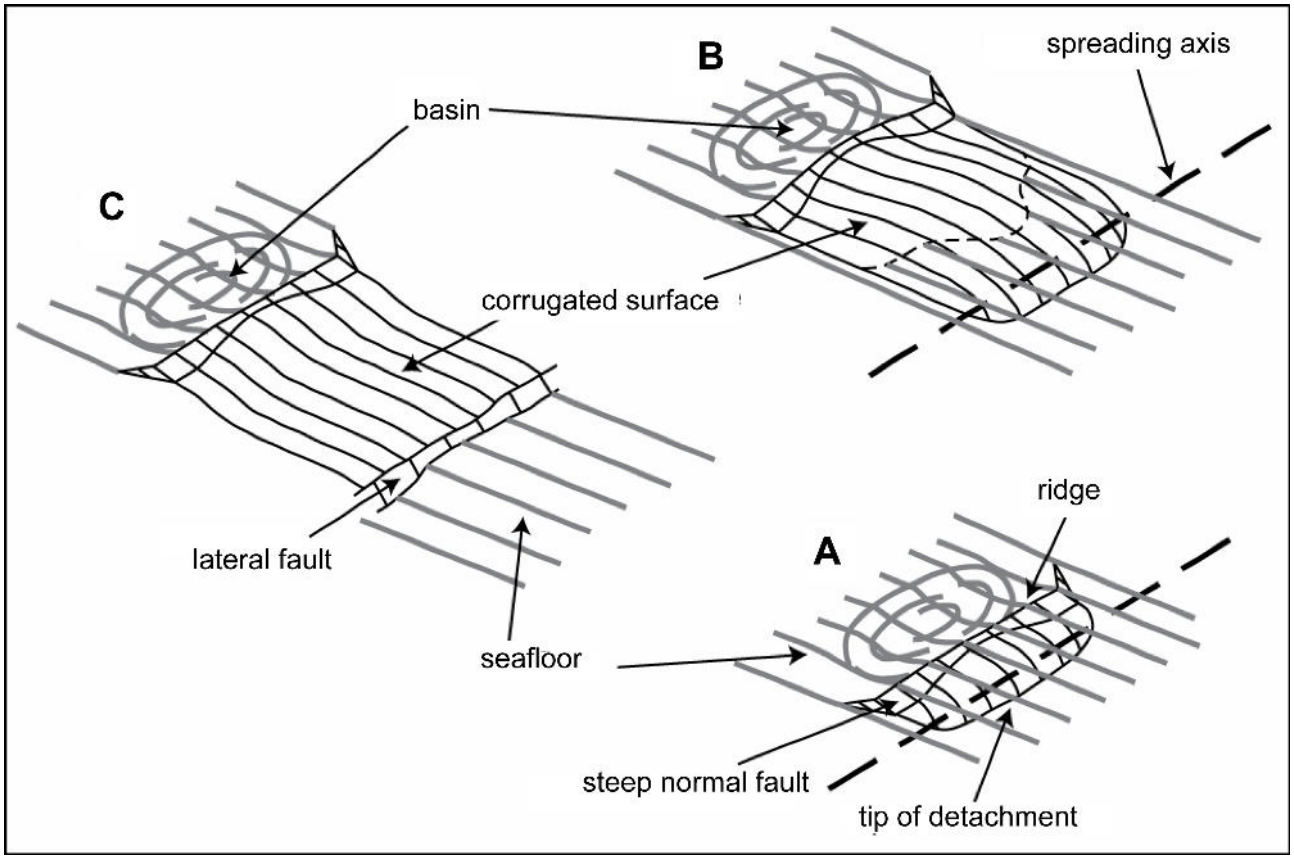

Figure 1.15 *Schematic three-dimensional oblique view of the evolution of a core complex by detachment faulting [from Smith et al., 2006]. Gray lines: seafloor (except for the detachment surface). Black lines: surface of the detachment fault and steeper normal faults, both exposed on the seafloor and below it.* **A.** *A breakaway ridge with a basin behind it. The basin is floored by volcanic sea floor, tilted up towards the breakaway ridge. The initially steep subsurface normal fault at the breakaway has already rotated to a shallower angle. A downward-curved detachment has started to form linked to the breakaway fault. Both faults are below the seafloor.* **B.** *The detachment has emerged. Dashed line: line of emergence. The fault has warped into a dome, the ridge has become arched, and little further rotation of the initial ridge has occurred.* **C.** *The detachment fault has been cut off by a later normal fault, perhaps of the breakaway of the next detachment. The dome has flattened, and the detachment fault is inactive.*

1.3 Oceanic Transform – Fracture Zones

In the 1965 Tuzo Wilson introduced the concept of the transform fault, defined them as a vertical fault plane between two lithospheric plates that slide horizontally past each other. Mid-ocean ridges systems are not continuous accretional margins; rather, they consist of a series of ridge segments offset by transform faults. The ridge segments lie nearly perpendicular to the spreading direction, whereas the transform fault lie parallel to the spreading direction, as it is shown in Figure 1.16, where the Clipperton and the Siqueiros transform faults offset the East Pacific Rise (Pacific Ocean).

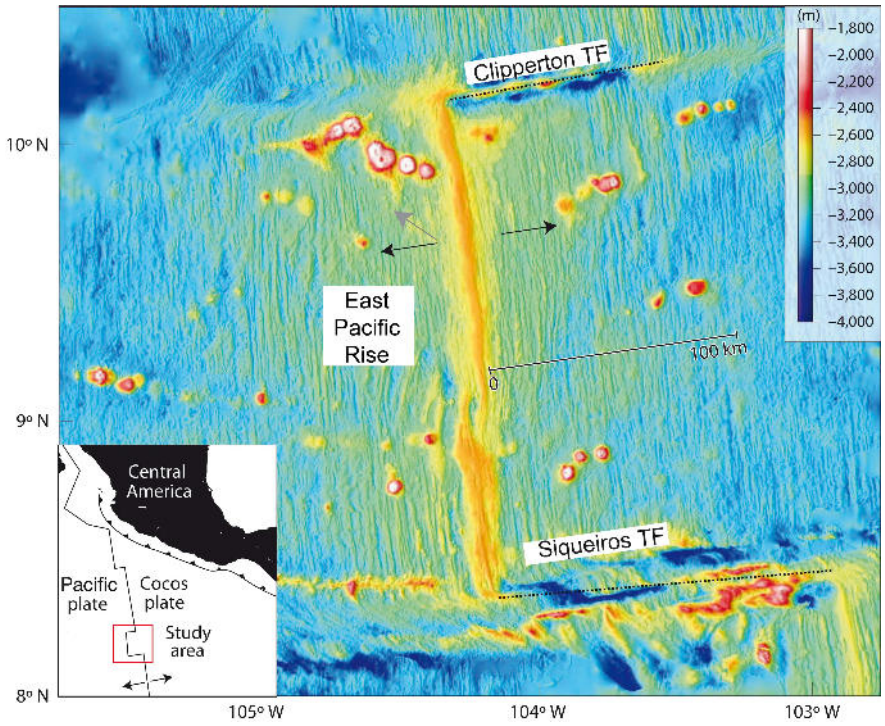

Figure 1.16 *Bathymetric map of a portion of East Pacif Rise and of its transform faults Clipperton and Siqueiros [Key et al., 2013].TF= transform fault.*

The distribution of earthquakes along the fault plane makes the difference between a transform fault and a strike-slip fault [*Sykes,* 1967]. In a transform fault that offsets a mid-ocean ridge, earthquakes are recorded only in the active zone; in a strike-slip fault seismic activity occurs instead over the entire length of the fault plane (Figure 1.17).

Oceanic transforms differ from continental transform systems because the first have a narrow deformation zone and shallower earthquakes hypocenters. The maximum depth of

earthquakes generated by oceanic transform faults corresponds roughly to the 400° C isotherm [*Rutter and Brodie,* 1987] (Figure 1.18); in constrast, the upper limit of the hypocenters of earthquakes in continental transform zones and intraplate strike-slip faults is 750° C [*Weins and Stein,* 1983].

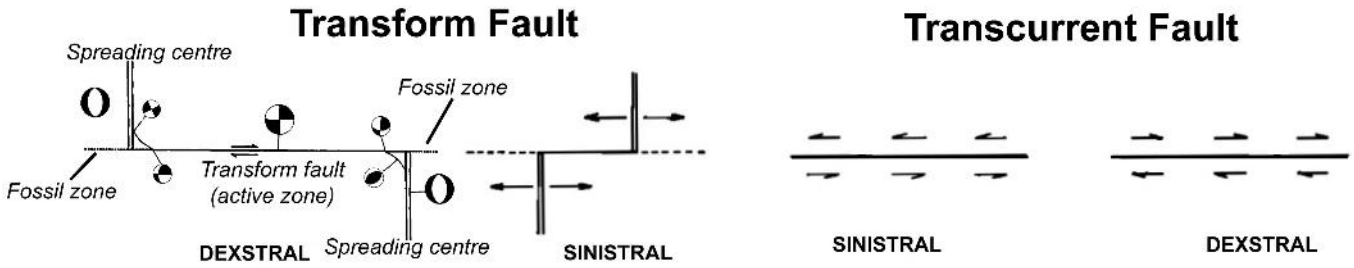

Figure 1.17 *Differences between transforms and transcurrent faults [modified from Wilson, 1965] and location of earthquakes along a transform faults [Rundquist and Sobolev, 2002].*

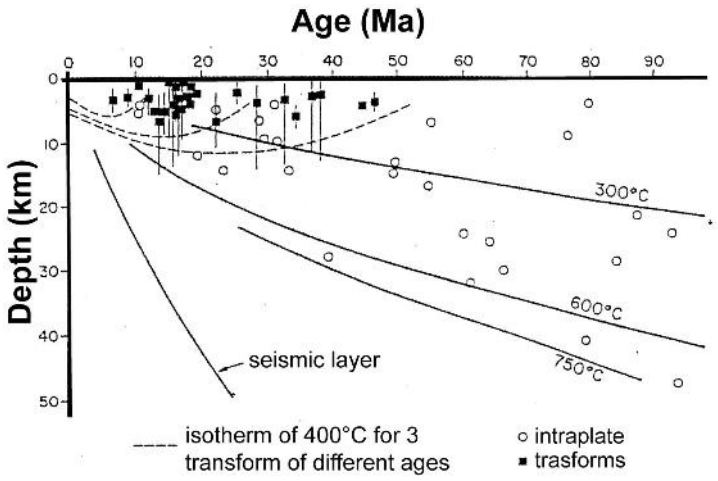

Figura 1.18 *Distribution of earthquakes along intraplate zone and transform faults [Engeln et al., 1986].*

1.3.1 Morphology

Oceanic fracture zones represent large topographic irregularities of the ocean seafloor. They are composed by a seismically active zone located between the two segments of ridge, called transform fault, and by two older seismically inactive areas called fossil zones (Figure 1.17).

The morphology of an oceanic transform [*Fox and Gallo*, 1984] fault is characterized by different structural elements (Figure 1.19). The main morphological feature is the transform valley. It is a narrow and elongated valley, flanked by a steep slope towards the valley and a more gentle

slope outwards and it continues in the fossil zones. Generally, the transform valley is filled by sediments transported by the oceanic currents, and in some cases, their thickness reaches 1 km as in the Vema and in the Romanche fracture zones (equatorial Atlantic).

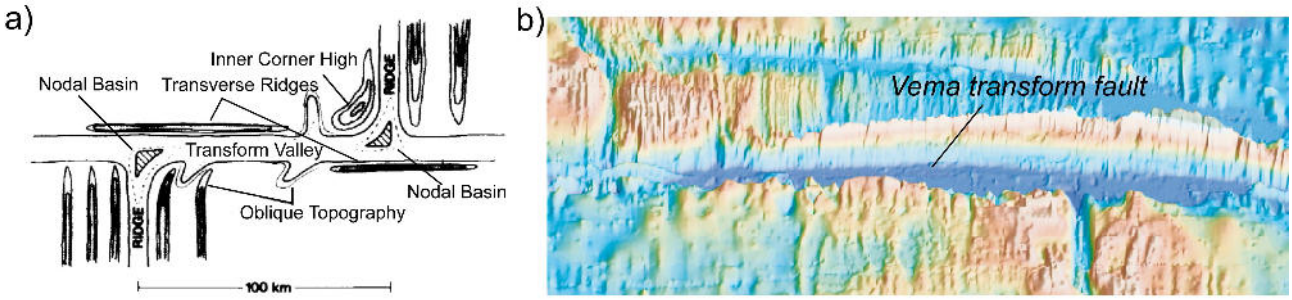

Figure 1.19 a) *Morphology of an oceanic transform fault [Fox and Gallo, 1984];* **b.** *3D bathymetric image of the Vema transform fault (central Altantic Ocean) [Cipriani et al., 2004].*

In the transform valley is located the principal transform displacement zone (PTDZ). This is an area of variable width in which lies the strike-slip fault system associated with the main transform motion. Generally it is not easy to identify the strike-slip fault in the bathymetric images, while it is possible in seismic profiles, thanks to the deformation that occurs in the sediments filling the transform valley. Multibeam bathymetry show a progressive deepening of the bottom of the valley near the ridge-transform intersection, in an area called nodal basin (Figure 1.19). The depth of the nodal basins is mainly related to the length of the offset of the transform fault [*Fox and Gallo*, 1984].

Most morphological and seismic profiles perpendicular to the direction of transform valley show a strong asymmetry. The asymmetry is generally common along the slow and ultraslow transform faults and is due to a greater development of one of the two flanks of the valley: it takes the name of transverse ridge (Figures 1.19 and 1.20). Transverse ridges are among the most important positive topographic anomalies of the ocean floor: they are one or more kilometers shallower than the adjancent “normal” crust of equivalent age and frequently they are shallower than axial spreading ridges in the same area. Geophysical and petrographical data acquired from different oceanic fracture zone suggest that transverse ridges are not the result of excess volcanism,

but rather of tectonic uplift of upper mantle and crustal blocks [*Bonatti,* 1978]. The discovery of powerful thickness of carbonates on the summit of some transverse ridges shows how, during their geological history, the tops of some of these were first above and then at sea level.

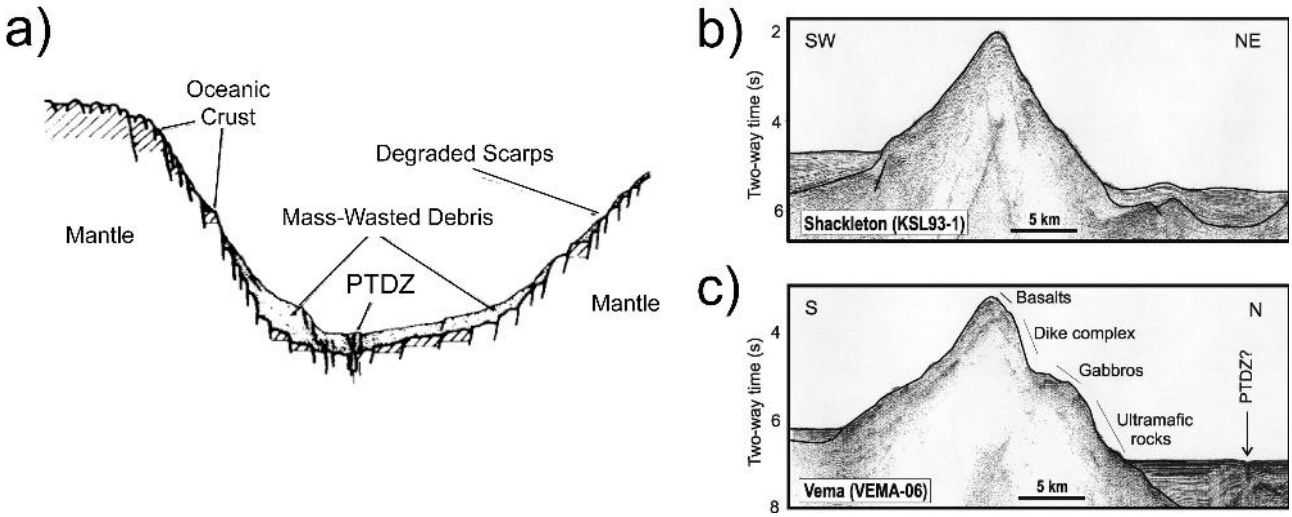

Figure 1.20 a) *Main features of an oceanic transform valley [Fox and Gallo, 1984];* **b)** *Seismic reclection profile across the Shackleton transverse ridge [Livermore et al., 2004];* **c)** *Seismic reclection profile VEMA-06 across the Vema transverse ridge [Bonatti et al., 2005].*

Some transform faults show a morphological high similar to a large seamount in the inner corner of the ridge/transform intersection. This relief is called inner corner high and it is, in many cases, the highest point along the flanks of the valley of the mid-ocean ridge (Figure 1.21) [*Severinghaus and MacDonald,* 1988]. Inner corner highs expose ultramafic and gabbroic rocks, high values of gravity anomalies and a strong seismic activity. The inner corner high is a morphological feature characteristic of slow and ultra-slow MORs. Indeed, slow transform faults with long offset make possible the contact of two lithospheres with different ages. For example, the difference of age between South American plate and the African plate in the western ridge/transform intersection of the Romanche (equatorial Atlantic), is ~ 50 Ma. The heat transfer from an hot - young lithosphere to a cold - old lithosphere cause a thermal expansion that may allow the formation of an inner corner high. In constrast, fast MORs do not present inner corner highs mainly because of a minor age difference between the plates in MOR-transform fault intersections.

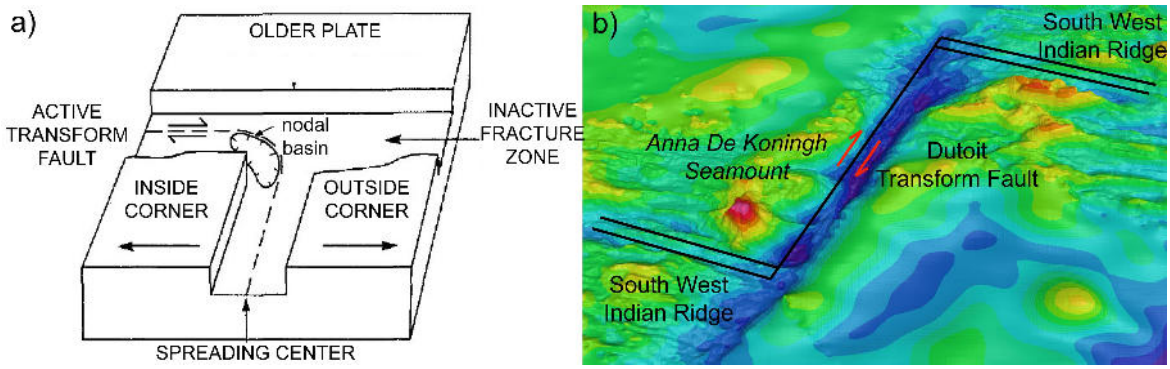

Figure 1.21 a) *Classification of a slow spreading – transform intersection region [Severinghaus and MacDonald,* 1988]; **b)** *Bathymetric image of the SWIR – Dutoit transform intersection [GEBCO_08 grid].*

1.3.2 Vertical tectonics

As previously described, the transverse ridge, when it is present, is an uplifted structure that is shallower than the surrounding displaced lithospheric plates. It is the results of large vertical uplift caused by vertical tectonics along slow and ultraslow oceanic fracture zones (Figure 1.20).

A transform fault is a plate boundary along which the relative motion of the two plates is parallel to the strike of the fault and it is geometrically described by the position of a virtual geometric point (Eulerian pole) and an angular velocity. Where their position changes over time there will be a riorganization of the geometry of the plate boundary; in particular, the segment of MORs tends to adapt rapidly to the new conditions, while the transform requires more time, especially in the case of long offsets [*Bonatti,* 1978]. A ridge-ridge transform boundary will change from a purely strike-slip regime to a "transpressional" or a "transtensional" regime [*Pockalny et al.,* 1996] (Figure 1.22 A). The formation of a topographical anomaly, often strongly asymmetric, may result from the establishment of both a transpressive or a transtensive regime. As an example, the increased presence of the Intra-transform ridges (ITRs) in fast-spreading centers could be due to the reorganization of the geometry of the plate boundaries and of the thermal structure of the lithosphere much hotter (Figure 1.24).

Although the tectonic deformation is the only accepted mechanism that can explain the total range of the uplift of the transverse ridges, several other mechanisms have been proposed:

a) *Lateral heat transfer.* According to model calculations [*Chen,* 1988; *Louden and Forsyth*, 1976], the thermal anomaly beneath the young tectonic plate at the ridge-transform intersection heats the cold and old plate across the transform causing uplift (Figure 1.22 B). This model is supported by the observation that the large uplifts in the Romanche and Vema transform faults are located close to ridge - transform intersections. Moreover, this model does not explain the vertical movements in the fracture zones beyond the region of contact with active rift segments, and the formation of transverse ridges on one side of the fault only.

b) *Viscodynamic forces.* The uplift of lithospheric and of asthenospheric material at the transverse ridge is hypothesized as due to the isostatic compensation of the deficit of mass represented by the transform valley [*Collette,* 1986]. This model is not able to explain the development of a large uplift on one side of the transform valley only (Figure 1.22 C).

c) *Thermal stress*. The thermal stress induced in the oceanic lithosphere by the thermal cooling in the course of their motion away from the spreading centers results in reduction of their linear sizes (horizontal contraction). The size reduction of a plate segment 150 km long can be as large as 300 m for a cooling of 200° C [*Collette,* 1986; *Turcotte et al.,* 1974]. During the displacement along the transform fault, marginal parts of the plate experience alternating compression and extension (Figure 1.22 D). The maximal stress is observed near axial parts of rift valleys. The near-surface part of the lithosphere is subject to compression, while the lithosphere proximal to the Moho discontinuity is subject to extension [*Turcotte et al.,* 1974]. As a result, the rising stress bends the lithosphere. The thermal stress caused by cooling and compression of the lithosphere 20 Ma old results in its bending and in uplift of the transverse ridge by 150 m [*Parmentier and Haxby,* 1986];

d) *Erosion of a lithosphere plate*. *Basile & Allemand* [2002] propose that the erosion of a lithospheric plate along the transform boundary may be an alternative mechanism to explain uplift of the walls of the transform valley and the formation of the transverse ridge (Figure 1.22 E). Moreover, this mechanism is always present in all geodynamic settings. The uplift of the lithosphere block does not exceed 35% -40% of the height difference (h) between the levels of the lithosphere plate and transform valley (Figure 1.22 E). The structure of the transform fault would provide for a certain step in topography. Since the vertical surface does not remain stable for a long time, the uplift will be subject to erosion that results in the unloading and rising due to isostatic compensation. This mechanism is not ubliquitous but can reinforce other mechanisms. The difference in height within most of the oceanic transform faults amounts to 60% (sometimes even more than 100%). This model does not explain the origin of the initial scarp across the strike of a transform (Figure 1.22 E). Furthermore, the origin of the transform valley itself is not quite clear. This phenomenon is probably related to a strip of the anomalously thin crust that formed at those ends of rift valleys where dry spreading is prevalent. Extension perpendicular to a transform fault may result in formation of a valley, while tectonic unloading may lead to the rise of fracture zone's wall. The erosion related unloading explains only an additional rise: the shallower the fault valley, the greater the contribution of tectonic unloading.

e) *Differential thermal subsidence*. The contact between two lithosphere with different ages along the fossil zone of a transform fault can generate bathymetric gradients of 2-4 km between the two edges of the fault (Figure 1.22 F). *Sandwell and Schubert* [1982] showed that even for the fracture zones, as well as for subduction zones, flexure of the lithosphere is an important process (Figure 1.22 F). Lithospheric flexure is a function of the elastic thickness, which is a function of the thermal state of the lithosphere, or of its age, and it is also function of the load's subsidence, related to the

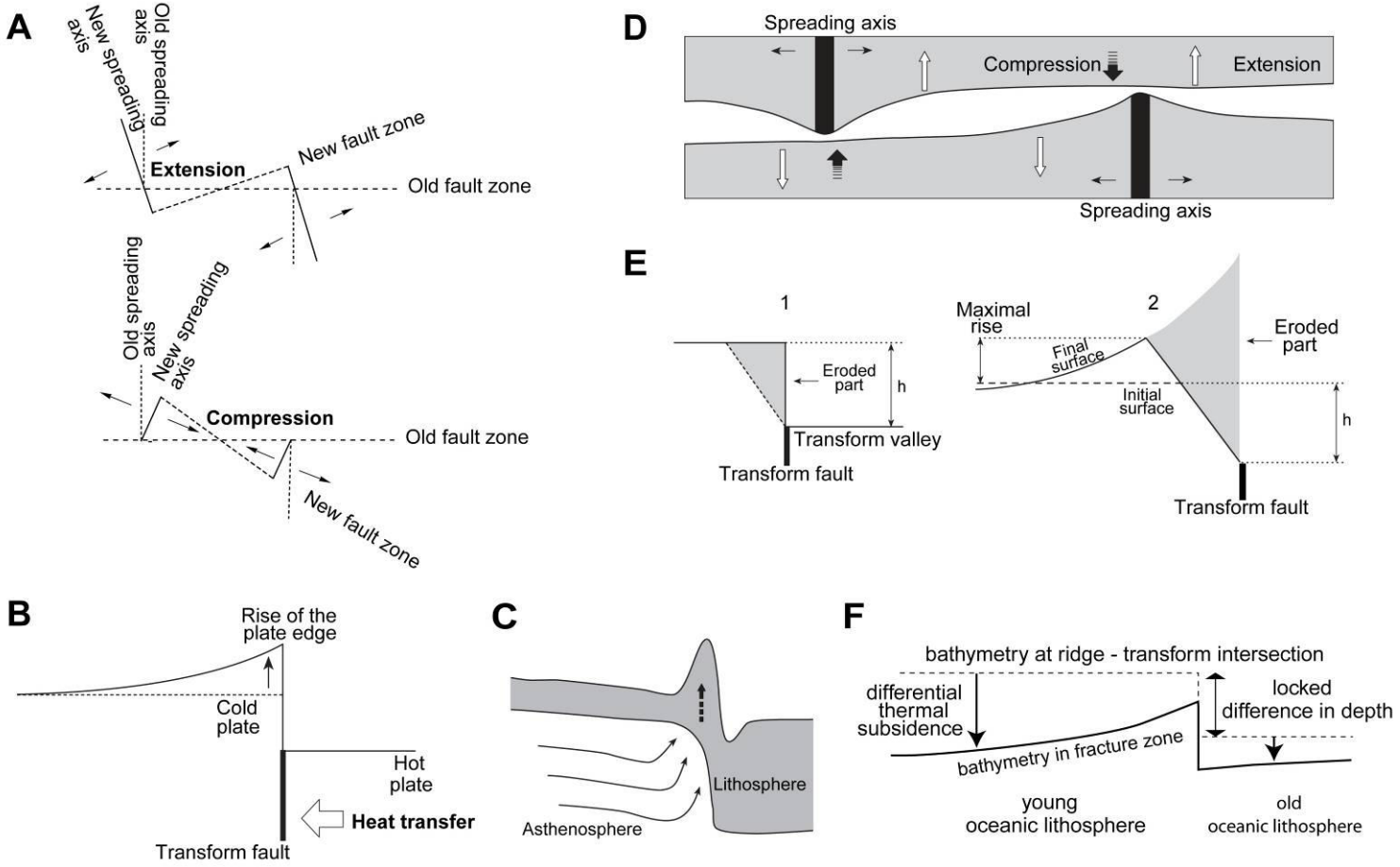

Figure 1.22 *Models of vertical movements with formation of transverse ridges [modified from Peive, 2005].* **A.** *Tectonic factors*; **B.** *The thermal effect***; C.** *Longitudinal melt flow*; **D.** *Thermal stress***; E.** *Erosion of the lithospheric plate;* **F.** *Differential thermal subsidence.*

load of crustal thickness. Therefore, the morphology of the inactive fracture zones is a direct function of the flexural deformations acquired by the lithosphere within the active area.

f) *Friction – related heating*. The movement along extended faults is accompanied by friction and release of thermal energy that can generate a temperature rise along the fault plane by 200–400°C [*Chen,* 1988]. The thermal energy resulting from the relative displacement of the northern and southern walls of the Romanche transform fault can provide an uplift of no more than 200 m in the transverse ridge. In this case, the area subjected to heating and uplifting would be about 5 km wide on both sides of the fracture zone's axis.

g) *Ultramafic diapirism*. As indicated from dredged samples, ultramafic rocks can be abundant among the rock types recovered from transverse ridges. Their serpentinization can result in a significant volume increase (up to 40%) and a decrease in density (from 3.3 to 2.6 g / cm ³), with a consequent uplift of a transverse ridge [*Komor et al.,* 1985; *Bonatti,* 1978; *Cannat,* 1996;]. Complete serpentinization of a 5-km-thick peridotite block may result in a rise of its upper boundary by 2 km. The intensity of serpentinization depends mostly on the permeability of rock to seawater and the process can be the mantle/crust interface. Fracture zones, being highly brecciated, are easily permeable to seawater. Deserpentinization accompanied by subsidence of the transverse ridge may occur during its drift across the "hot" ridge - transform intersection area. Serpentinization of ultramafic rocks begins as the temperature drops below 500° C, whereas deserpentinization may takes place as the temperature rises above 500° C. In the Romanche transform, the isotherm at 500° C may have subsided below 10 km [*Bonatti et al.,* 1994]. Near the eastern intersection with the rift valley, the thickness of the crust, which may be involved in dehydration, is 6 km. Despite the significant contribution of serpentinization to the vertical component of transverse ridge movements and considering that this process usually affects no more than 50 – 80% of the ultramafic rocks, it is difficult to explain anomalous topography with an amplitude up to 4 km without involving other mechanisms. In a recent work of *Ligi et al.* [2013], the rise of the volume of the ultramafic rocks at

the Vema transform fault (equatorial Atlantic) was estimated as relatively minimum, to confirm that this mechanism, alone, cannot explain the large anomalous topography of the transverse ridges.

1.3.3 Megatransform faults

"Megatransforms" are a class of oceanic transform boundaries which differs from a single, narrow (a few kilometers wide) strike-slip seismic zone linking two mid-ocean ridge segments [*Ligi et al.,* 2002]. Megatransoforms faults are broad complex multifault zones of deformation, similar to some continental strike-slip systems (North Anatolian transform fault). Examples are the Romanche transform, where the Mid-Atlantic Ridge is offset by a lens-shaped, about 900-km-long, 100-km-wide sliver of deformed lithosphere bound by two major transform valleys (Figure 1.23a), and the 750-km-long, 120-km-wide Andrew Bain transform on the Southwest Indian Ridge (Figure 1.23b).

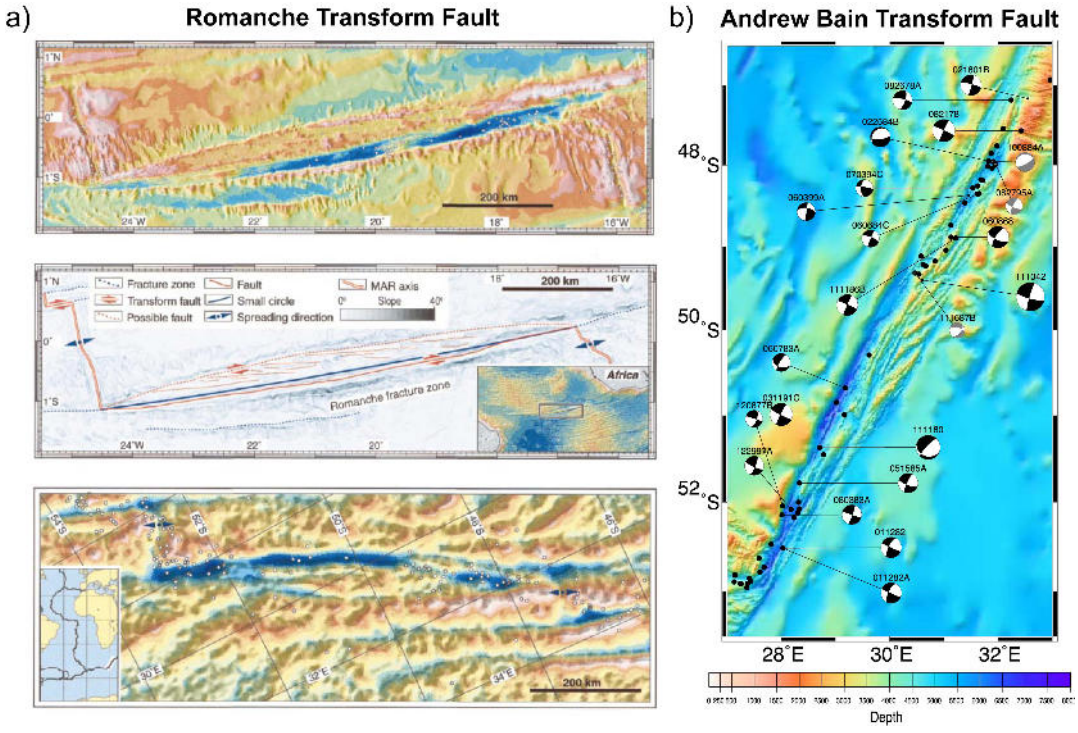

Figure 1.23 a) *The upper image is a shaded relief map from Romanche transform fault multibeam data [Ligi et al., 2002], equatorial Atlantic. Depth ranges from 7800 m (dark blue) to 1000 m (light gray). The central image is a map of maximum topographic slopes; structural sketch of area is superimposed. Spreading direction and small circle path have been computed using Africa–South America Eulerian vector of DeMets et al. [1994]. The lower image is the predicted bathymetry of equatorial area [data from Sandwell and Smith, 1997] and distribution of earthquakes in the area;* **b)** *Shaded relief map from Andrew Bain transform fault multibeam data [Sclater et al., 2005], SW Indian Ocean and distribution of focal mechanisms in the area.*

Numerical modeling predicts the development of wide multiple transform boundaries (i.e., of megatransforms) when the age offset is above a threshold value of ~ 30 Ma, i.e., in extra-long (> 500 km) slow-slip transforms [*Ligi et al.,* 2002]. Assuming an average spreading rate of about 12 cm/a, their length would exceed 12 km for a million of year: this is the reason because megratransforms are not found along fast and/or intermediate mid-ocean ridges.

1.3.4 Gravity anomalies

Crustal thickness can be estimated by combining bathymetry with gravimetry, and obtaining the Mantle Bouguer Anomaly (MBA). The MBA is obtained removing the effect of the crust, assumed 5-6 km thick, and the effects due to the water and to the thickness of sediments. It is now possible to observe deviations from the initial assumed constant crustal thickness. The MBA mainly reflects the variations of thermal structure of the mantle and the thickness / density of the crust. The gravimetric anomaly due to varation in the thermal structure can be estimated through the solution of the equation for heat transport and for heat conduction, including three-dimensional models of passive uplift of the mantle. Subtracting this component from the MBA, we obtain the Residual Mantle Bouguer Anomaly (RMBA), that allows to estimate the thickness and density variations of the oceanic crust [*Lin & Morgan,* 1992].

Some segments of slow mid-ocean ridge which are in the vicinity of the transform boundaries show thin crust due to a low grade of melting of the mantle; in constrast, fast mid-ocean ridges show a thick crust due to an high extent of subridge mantle melting (Figure 1.24). The different thicknesses of oceanic crust involve different values of residual gravimetric anomalies [*Gregg,* 2007]. Slow transform faults are characterized by values RMBA more positive than those present along segments of mid-oceanic ridge. In constrast, along fast and intermediate transform faults, values of RMBA are more negative than those present along segments of mid-oceanic ridge (Figure 1.24). The distribution of RMBA along fast and intermediate transform faults show an

excess of mass along the fault zones, which could reflect some factors such as: an increase in the porosity of the rocks, serpentinization of mantle and / or thick crust. The negative values of RMBA correspond to bathymetric high along the flanks of transform valleys, due to a thick crust.

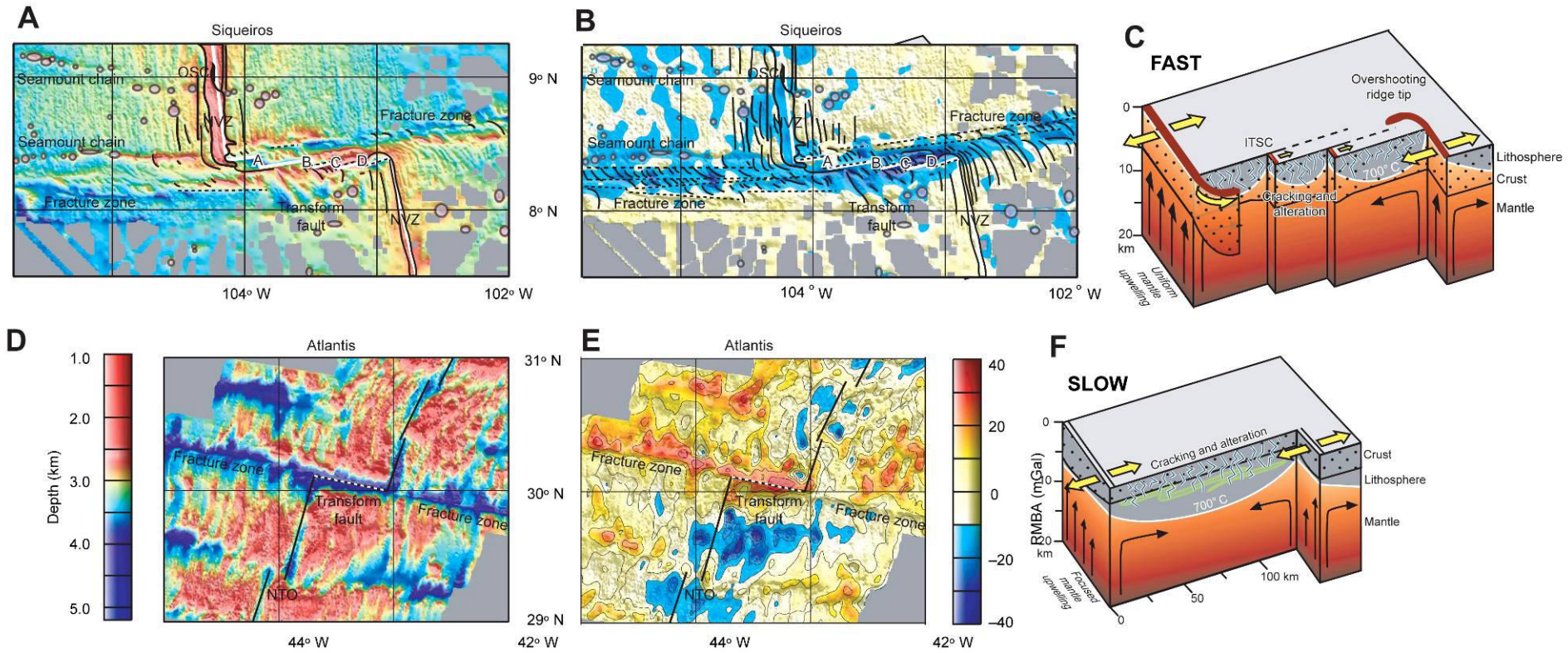

Figure 1.24 A. *Bathymetric map for the Siqueiros transform with geologic interpretation. Solid black lines indicate the seafloor fabric, circles show locations of seamounts, and dashed black lines show the locations of the fracture zones and transform fault. The solid white line indicates the location of the plate boundary used in the 3D thermal model. ITSCs are labelled A, B, C and D16. NVZ, neo-volcanic zone; OSC, overlapping spreading centre;* **B.** *Bathymetric map for the Atlantis transform. The solid black line indicates location of the plate boundary used in the 3D thermal model, and the dashed portion indicates the Atlantis transform fault;* **C.** *Slow-spreading ridges exhibit focused mantle upwelling at segment centres and crustal thinning towards segment ends and transform faults;* **D.** *Calculated RMBA map for the Siqueiros transform fault with geologic interpretation overlaid from a;* ***E.*** *Calculated RMBA map for the Atlantis transform fault;* **F.** *Fast-spreading ridges have relatively uniform mantle upwelling [Gregg et al., 2007].*

References

Basile, C., and P. Allemand (2002), Erosion and flexural uplift along transform faults, *Geophys. J. Int., 151,* 646 – 653.

Bird, P., Z. Liu, and W. K. Rucker (2008), Stresses that drive the plates from below: Definitions, computational path, model optimization, and error analysis, *J. Geophys. Res., 113,* doi: 10.1029/2007JB005460.

Bird, P., Y. Y. Kagan, and D. D. Jackson (2002), Plate tectonics and earthquake potential of spreading ridges and oceanic transform faults in Plate Boundary Zones, *Geodynamics Series. AGU, 30,* doi:10.1029/030GD12.

Blackman, D. K., J. A. Karson, D. S. Kelley, J. R. Cann, G. L. Früh-Green, J. S. Gee1, S. D. Hurst, B. E. John, J. Morgan, S. L. Nooner, D. K. Ross, T. J. Schroeder, and E. A. Williams (2002), Geology of the Atlantis Massif (Mid-Atlantic Ridge, 30◦ N): Implications for the evolution of an ultramafic oceanic core complex, *Mar. Geophys. Res., 23,* 443 – 469.

Bonatti, E. (1978), Vertical tectonism in oceanic fracture zones, *Earth Planet. Sci. Lett., 37*, 369 – 379.

Bonatti, E., D. Brunelli, W. R. Buck, A. Cipriani, P. Fabretti, V. Ferrante, L. Gasperini, and M. Ligi (2005), Flexural uplift of a lithospheric slab near the Vema transform (central Atlantic): timing and mechanisms, *Earth Planet. Sci. Lett., 240*, 642 – 655.

Bonatti, E., M. Ligi, L. Gasperini, A. Peyve, Y. Raznitsin, and Y. J. Chen (1994), Transform migration and vertical tectonism at the Romanche fracture zone, Equatorial Atlantic, *J. Geoph. Res., 99,* 21779 – 21802.

Bratt, S.R., and G. M. Purdy (1984), Structure and variability of oceanic-crust on the flanks of the East Pacific Rise between 11°N and 13°N, *J. Geophys. Res., 89,* 6111 – 6125.

Buck, W. R., L. L. Lavier, and A. N. B. Poliakov (2005), Modes of faulting at mid-ocean ridges, *Nature, 434,* 719 –723.

Cann, J. R., D. K. Blackman, D. K. Smith, E. McAllister, B. Janssen, S. Mello, E. Avgerinos, A. R. Pascoe, and E. Escartin (1997), Corrugated slip surface formed at ridge-transform intersection, *Nature, 385*, 329 – 332.

Cannat, M. (1996), How thick is the magmatic crust at slow spreading oceanic ridges?, *J. Geoph. Res., 101,* 2847 – 2857.

Chen,Y. (1988), Thermal model of oceanic transform faults, *J. Geoph. Res., 8,* 8839 – 8851.

Choukroune, P., J. Francheteau, and R. Hekinian (1984), Tectonics of the East Pacific Rise near 13°N from field observations, *Earth Planet. Sci. Lett., 68,* 115 – 127.

Cipriani, A., H. K. Brueckner, E. Bonatti, and D. Brunelli (2004), Oceanic crust generated by elusive parents: Sr and Nd isotopes in basalt-peridotite pairs from the Mid-Atlantic Ridge, *Geology, 32,* 657 – 660.

Collette, B.J. (1986), Fracture zones zones in the North Atlantic; morphology and a model, *J. Geol. Soc. of London, 143,* 5763 – 777.

DeMets, C., R.G. Gordon, D. F. Argus, and S. Stein (1994), Effect of recent revisions to the geo-magnetic reversal timescale on estimates of current plate motions, *Geophys. Res. Lett., 21,* 2191–2194.

Detrick, R.S., P. Buhl, E. Vera, J. Mutter, J. Orcutt, and J. Madsen (1987), Multichannel seismic imaging of a crustal magma chamber along the East Pacific Rise, *Nature, 326,* 35 – 41.

Dick, H. J. B., L., Lin, and H. Schouten (2003), An ultraslow-spreading class of ocean ridge, *Nature, 426,* 405 – 412.

Engeln, J. F., D. A. Weins, and S. Stein (1986), Mechanisms and depths of the Atlantic transform earthquakes, *J. Geoph. Res., 91,* 548 – 577.

Escartin, J., and M. Cannat (1999), Ultramafic exposures and the gravity signature of the lithosphere near the Fifteen-Twenty Fracture Zone (Mid-Atlantic Ridge, 14°– 16.5°N), *Earth Planet. Sci. Lett., 171,* 411 – 424.

Fox, J. P., and D. Gallo (1984), A tectonic model for Ridge - Transform – Ridge plate boundaries: implications for the structure of oceanic lithosphere, *Tectonophysics, 104,* 205 – 242.

Gregg, P. M., J. Lin, M. D. Behn, and L. G. J. Montesi (2007), Spreading rate dependence of gravity anomalies along oceanic transform faults, *Letters Nature, 448,* 183 – 188.

Heezen, B. C., and M. Tharp (1968), Atlantic Ocean Floor, Painted by Heinrich C. Berann, National Geographic Magazine, June, Special map supplement.

Heirtzler, J.R., X. Le Pichon, and J. G. Baron (1966), Magnetic anomalies over the Reykjanes Ridge, *Deep Sea Research, 13,* 427 – 433.

Key, K., S. Constable, L. Liu, and A. Pommier (2013), Electrical image of passive mantle upwelling beneath the northern East Pacific Rise, *Nature, 495,* 499 – 502.

Komor, S. C., D. Donelthon, and J. F. Casey (1985), Serpentinization of cumulate ultramafic rocks from the north arm mountain massif of the bay of wads ophiolite, *Geochimica et Cosmichimica Acta, 49,* 233 l – 2338.

Ligi, M., E. Bonatti, M. Cuffaro, and D. Brunelli (2013), Post-Mesozoic Rapid Increase of Seawater Mg/Ca due to Enhanced Mantle-Seawater Interaction, *Scientific reports, 3*, 1 – 8.

Ligi, M., E. Bonatti, L. Gasperini, and A. N. B. Poliakov (2002), Oceanic broad multifault transform plate boundaries, *Geology, 30*, 11 – 14.

Lin J., and J. P. Morgan (1992), The spreading rate dependence of three-dimensional mid-ocean ridge gravity structure, *Geophys. Res. Lett., 19,* 13 – 16.

Livermore, R., G. Eagles, P. Morris, and A. Maldonado (2004), Shackleton fracture zone: no barrie to early circumpolar ocean circulation, *Geology, 32,* 797 – 800.

Louden, K. E., and D. W. Forsyth (1976), Thermal Conduction across Fracture Zones and Gravitational Edge Effect, *J. Geophys. Res., 81,* 4869 – 4874.

Macdonald, K.C. (1982), Mid-ocean ridges: fine scale tectonic, volcanic and hydrothermal processes within the plate boundary zone, *Ann. Rev. Earth and Planet. Sci., 10,* 155 – 190.

MacLeod, C. J., R. C. Searle, B. J. Murton , J. F. Casey, C. Mallows, S. C. Unsworth, K. L. Achenbach, M. Harris (2009), Life cycle of oceanic core complexes, *Earth Planet. Sci. Lett., 287*, 333 – 344.

Muller, R. D., W. R. Roest, J. Y. Royer, L. M. Gahagan, and J. G. Sclater (1997), Digital isochrons of the world's ocean floor, J. *Geophys. Res., 102*, 3211 – 3214, doi:10.1029/96JB01781.

Parmentier, E. M., and W. F. Haxby (1986), Thermal Stresses in the Oceanic Lithosphere: Evidence from Geoid Anomalies at Fracture Zones, *J. Geophys. Res., 91*, 7193 – 7204.

Parson, B., and J. G. Sclater (1977), An analysis of the variation of ocean floor bathymetry and heat flow with age, *J. Geoph. Res*, 82, 803 – 827.

Peive, A. A. (2005), Vertical tectonic movements of the crust in transform fracture zones of the central atlantic, *Geotectonics, 40*, 25 – 36.

Pockalny, R.A., P. Gente, and R. Buck (1996), Oceanic transverse ridges: A flexural response to fracture zone-normal extension, *Geology, 24,* 71–74.

Rundquist, D. V., and P. O. Sobolev (2002), Seismicity of mid-oceanic ridges and its geodynamic implications: a review, *Earth Sci. Rev., 58,*143 – 161.

Rutter, E. H., and K. H. Brodie, (1987), On the mechanical properties of oceanic transform faults. *Annales Tectonicae, 1*, 87 – 96.

Sandwell, D.S, and G. Schubert (1982), Litospheric flexure at fracture zones, *J. Geoph. Res., 87,* 4657 – 4667.

Sandwell, D. T., and W. H. F. Smith (1997), Marine gravity anomaly from Geasat and ERS-1 satellite altimetry, *J. Geophys. Res., 102,* 10039–10054.

Sclater, J. G., N. R. Grindlay, J. A. Madsen, and C. Rommevaux-Jestin (2005), Tectonic interpretation of the Andrew Bain transform fault: Southwest Indian Ocean, *Geochem. Geophys. Geosyst., 6,* doi:10.1029/2005GC000951.

Sclater, J. G., C. Jaupart, and D. Galson (1980), The Heat Flow Through Oceanic and Continental Crust and the Heat Loss of the Earth, *Rev. Geophys. and Space Physics, 18,* 269 – 311.

Severinghaus, J. P., and K. C. MacDonald (1988), High inside corner at ridge – transform intersections, *Mar. Geophys. Res., 9,* 353 – 367.

Sharkov, E. V. (2012), Cyclic Development of Axial Parts of Slow-Spreading Ridges: Evidence from Sierra Leone Area, the Mid-Atlantic Ridge, 5-7°N, *Tectonics - Recent Advances, ISBN* 978-953-51-0675-3.

Smith, D. K., and J. R. Cann (1993), Building the crust at the Mid-Atlantic Ridge, *Nature, 365,* 707–715.

Smith D. K., J. R. Cann, and J. Escartín (2006), Widespread active detachment faulting and core complex formation near 13°N on the Mid-Atlantic Ridge, *Nature,* doi:10.1038/nature04950.

Smith D. K., J. Escartín, M. Cannat, M. Tolstoy, C. G. Fox, D. R. Bohnenstiehl, and S. Bazin (2003), Spatial and temporal distribution of seismicity along the northern Mid-Atlantic Ridge (15°–35°N), *J. Geoph. Res., 108,* 8-1 – 8-22.

Sykes, L. R. (1967), Mechanism of earthquakes and nature of faulting on the Mid-Atlantic Ridge, *J. Geoph. Res., 72,* 2131 – 2153.

Tommey, D. R., S. C., Solomon, G. M., Purdy, and M. H. Murray (1985), Microearthquakes beneath the median valley of the Mid-Atlantic Ridge near 23°N: hypocenters and focal mechanisms, *J. Geoph. Res*, *90,* 5443 – 5458.

Turcotte, D. L. (1974), Are Transform Faults Thermal Contraction Cracks?, *J. Geophys. Res. 79,* 2573–2577.

Vera, E. E., and J. B. Diebold (1994), Seismic imaging of oceanic layer 2A between 9°30'N and 10°N on the East Pacific Rise from two-ship wide-aperture profiles, *J. Geoph. Res*, *99,* 3031 – 3041.

Weins, D. A., and S. Stein (1983), Age dependence of oceanic intraplate seismicity and implications for lithospheric evolution, *J. Geoph. Res*, *88,* 6455 – 6468.

White, R.S., D. P. McKenzie, and R. K. O'Nions (1992), Oceanic crustal thickness from seismic measurements and from rare earth element inversions, *J. Geophys. Res., 97,* 19683 – 19715.

Wilson, J. Y. (1965), A new class of faults and their bearing on continental drifts, *Nature, 207*, 343 – 347.

Chapter 2

Seismicity of the Equatorial Mid-Atlantic Ridge and its Large Offset Transforms

R. Parnell-Turner, C. Palmiotto, A. Zheleznov, D. Smith, M. Fowler, D. Bonnemains, K. Bursaw, C. Holly, R. Dziak

Published in InterRidge News: International Research, 21, p.24-27, 2012

Abstract

The equatorial Mid-Atlantic Ridge is distinctive for its long-offset transforms and an inferred mantle thermal minimum south of Romanche fracture zone, resulting in overall low melt production. In addition, the North America-South America-Africa triple junction has migrated through the region. Consequentially, the equatorial Atlantic provides an ideal laboratory for testing ideas about modes of spreading, short-term earthquake predictability, and triple junction dynamics at slow-spreading ridges. The centerpiece of this project is an autonomous hydrophone array, which will obtain a two-year, continuous record of seismicity at the equatorial Mid-Atlantic Ridge. The temporal and spatial patterns in seismicity will be exploited to answer questions regarding the role of detachment faults in plate accretion, earthquake nucleation in oceanic lithosphere, and deformation associated with triple junctions. Here we present the regional multibeam bathymetric dataset, collected on the transit legs of Cruise AT21-03 in June/July 2012 (Figure 2.1), during which two hydrophones were deployed and maintenance carried out on a third instrument. We also suggest that in the future, the community could benefit from the opportunistic acquisition of valuable multibeam data through sharing information on the planned routes of upcoming cruises.

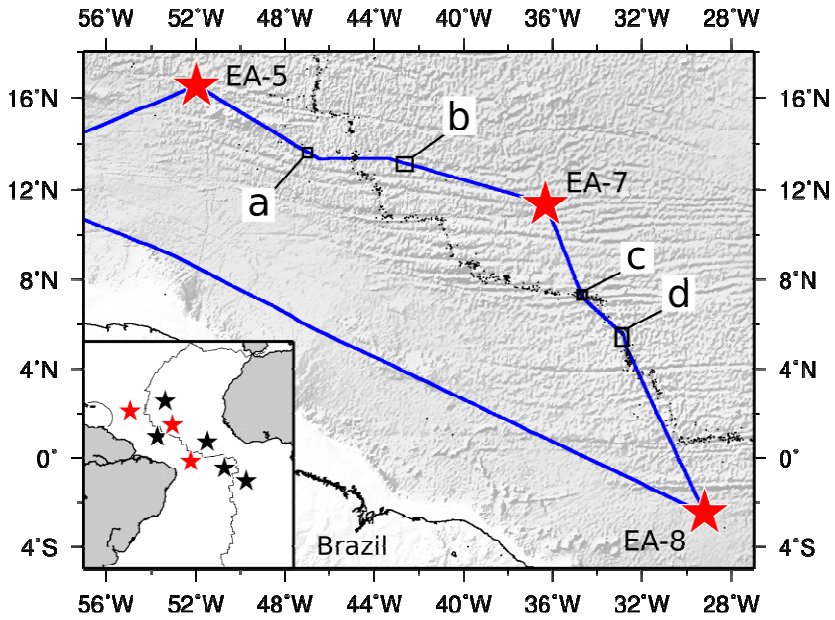

Figure 2.1 *Map showing route of Cruise AT21-03. Blue line: cruise shiptrack; red stars: hydrophone deployment locations; black stars: existing hydrophones; black dots: teleseismic earthquakes; black boxes: location of map in Figure 2.2 (boxes labelled a and b), in Figure 2.3 (box c) and in Figure 2.4 (box d).*

2.1 The hydrophone instrument and mooring

Autonomous hydrophones continuously record data, sampling at 250 Hz with a 110 Hz cut-off and a 16-bit analog/digital resolution. The hydrophone element is a single ceramic hydrophone attached to a titanium pressure case, with a pre-whitening filter to reduce the effects of ambient noise. Timing is constrained with a Q-Tech crystal oscillator clock (accurate to <1 s/yr) that is GPS synchronized before deployment and after recovery. All data are processed by logging computer, and then written to industrial hard drives rated to -20°C. A total of 164 standard alkaline D-cell battery packs provide the power required for up to 24 month deployments.

In the equatorial Atlantic, the hydrophones have been deployed about 300-500 km away from each side of the ridge axis, typically in water depths of 4000-5000 m. The instrument package is moored at a water depth of approximately 850 m, which is appropriate for surface-reflected sound propagation in the Sound Fixing and Ranging (SOFAR) channel. The hydrophone is suspended 50 m below a 37” syntactic foam flotation package, and the pressure case is attached to a seafloor anchor via ¼” Vectran and low stretch 5/16” Yalex mooring cable. The design is intended to reduce strumming noise from the cable that can be generated by local currents. After deployment, an

accurate anchor location is obtained by ranging on the acoustic release transponder. The entire mooring is recovered via an acoustic release attached to a degradable iron anchor.

Additional information on the hydrophone moorings, instruments, and data processing can be found at: http://www.pmel.noaa.gov/vents/acoustics/haru_system.html.

2.2 AT21-03 multibeam bathymetry

Transit legs between the three hydrophone deployment sites provided an excellent opportunity to map regions of the equatorial Atlantic Ocean and MAR axis previously unexplored. During the 18 day cruise, over 110,000 km^2 of multibeam bathymetry and associated acoustic backscatter data were acquired using a Kongsberg EM122 echosounder, operating at 12 kHz. The multibeam data collected during the expedition have provided new insights into crustal accretion and evolution and argue for having multibeam echosounder systems operating during all expeditions whenever possible. In future, with information on upcoming cruises and proposed ship tracks published prior to sailing, valuable multibeam data could be collected in areas of interest to the community. In the following sections we describe some of the observations made from our newly collected multibeam bathymetry.

2.3 Off-axis Oceanic Core Complexes (OCCs)

OCCs are massifs in which lower-crustal and upper-mantle rocks such as gabbros and serpentinized peridotites are exposed at the seafloor on long-lived faults known as detachment faults [*Blackman et al.,* 1998; *Tucholke et al.,* 1998; *Smith et al.,* 2008]. We now understand that detachment faults, which involve significant fault rotation and the formation of core complexes, may account for close to 50% of the extension at the northern MAR between 12° and 35°N.

Smith et al. [2006, 2008] and *MacLeod et al.* [2009] described the 13°N segment of the MAR in which a number of detachment faults extend for 75 km along the western flank of the

spreading axis, and a field of extinct core complexes extends westward away from the axis for at least 100 km. What was not known was how far off-axis extinct detachment faulting could be found, nor whether the east flank had a similar history dominated by detachment faults and core complex formation. We took advantage of our transit to collect additional multibeam data in the region in order to answer these questions.

Based on the multibeam data alone, we identified extinct OCCs on the eastern and western flanks of the MAR near 13°N (Figure 2.2). The characteristics used to identify these features included one or more of the following: a domed surface dipping gently toward the ridge axis; corrugations on the domed surfaces oriented parallel to the spreading direction [*Cann et al.,* 1997]; outward facing scarps created by the flexural rotation of an originally steep inward facing fault [*Buck*, 1988], and narrow linear ridges, which are produced at the detachment fault breakaway as the top of the fault rotates. Two extinct core complexes were identified on the western flank of the MAR about 220 km from the axis (Figures 2.1 and 2.2a). The OCC at 47.05°W has distinctive linear ridges associated with it, as well as corrugations parallel to the spreading direction. The feature at 46.85°W is backed by a characteristic outward-facing fault and looks to be the southern section of a larger feature to the north, similar to others OCCs seen closer to the axis. On the eastern flank of the axis, a series of three extinct core complexes was identified about 75 km from the axis. In addition, a similar set of OCCs was identified farther off axis, about 220 km east of the axis (Figures 2.1 and 2.2b). Although no corrugations were identified, the three features shown in Figure 2b have steep slopes of between 20° and 25° facing away from the axis and slightly domed, gently dipping surfaces facing west towards the axis.

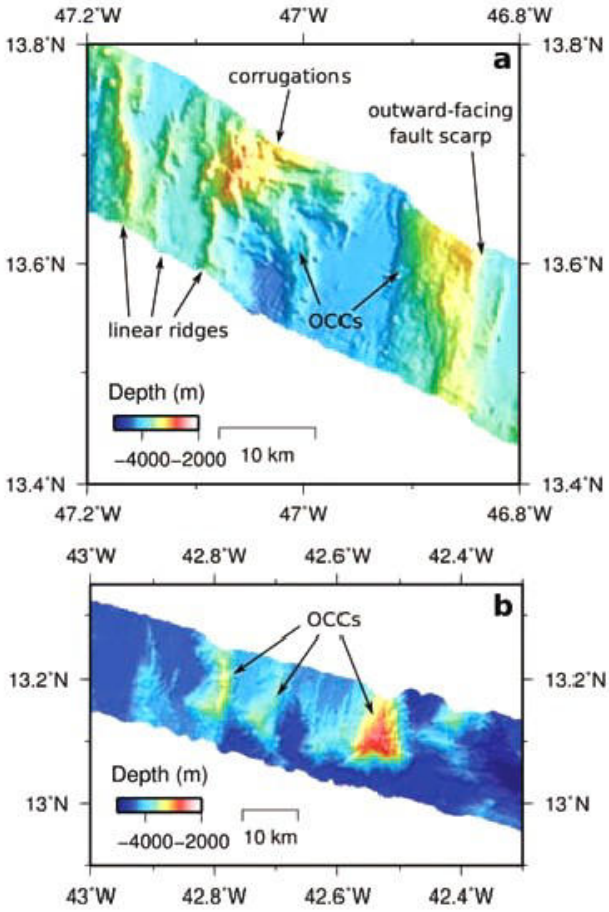

Figure 2.2 *Examples of extinct OCCs located more than 200 km off-axiS.* **a)** *OCCs on the western flank of the MAR. Note the corrugations (labelled) on the western core complex. Linear ridges marking the tops of rotated faults are also abeled;* **b)** *three extinct OCCs located in the eastern flank of MAR. These core complexes were active at 13°N segment and indicate that detachment faulting has been common on both side of the MAR in this region.*

The occurrence of OCCs east of the MAR at the 13°N region indicates that core complex formation is not limited to the western side of axis and may have been occurring on both sides of the spreading center simultaneously. The identification of core complexes as far as 220 km from the MAR on both sides of the axis suggests that detachment faulting has been occurring at this section of the MAR axis for the past ~20 Myrs.

2.4 Intra-trasform spreading center, 7°40'N

Segmented transform systems consist of several faults offset by short axial rifts referred to as intra-transform spreading centers (ITSCs) [*Menard and Atwater*, 1969; *Searle,* 1983; *Pockalny et al.,* 1997], where active seafloor spreading and crustal accretion are occurring [*Fornari et al.,* 1989; *Hekinian et al.,* 1992; *Perfit et al.,* 1996]. Intra-transform spreading centers are believed to result from plate motion changes over the last few million years that has caused extension within the transform. The spreading centers may have begun as 'leaky' transforms and later evolved into organized spreading centers with continued extension [*Pockalny et al.,* 1997].

We mapped the western portion of the spreading center which joins two transform valleys within the Doldrums FZ near 7.3°N, 34.7°W (Figure 2.3).

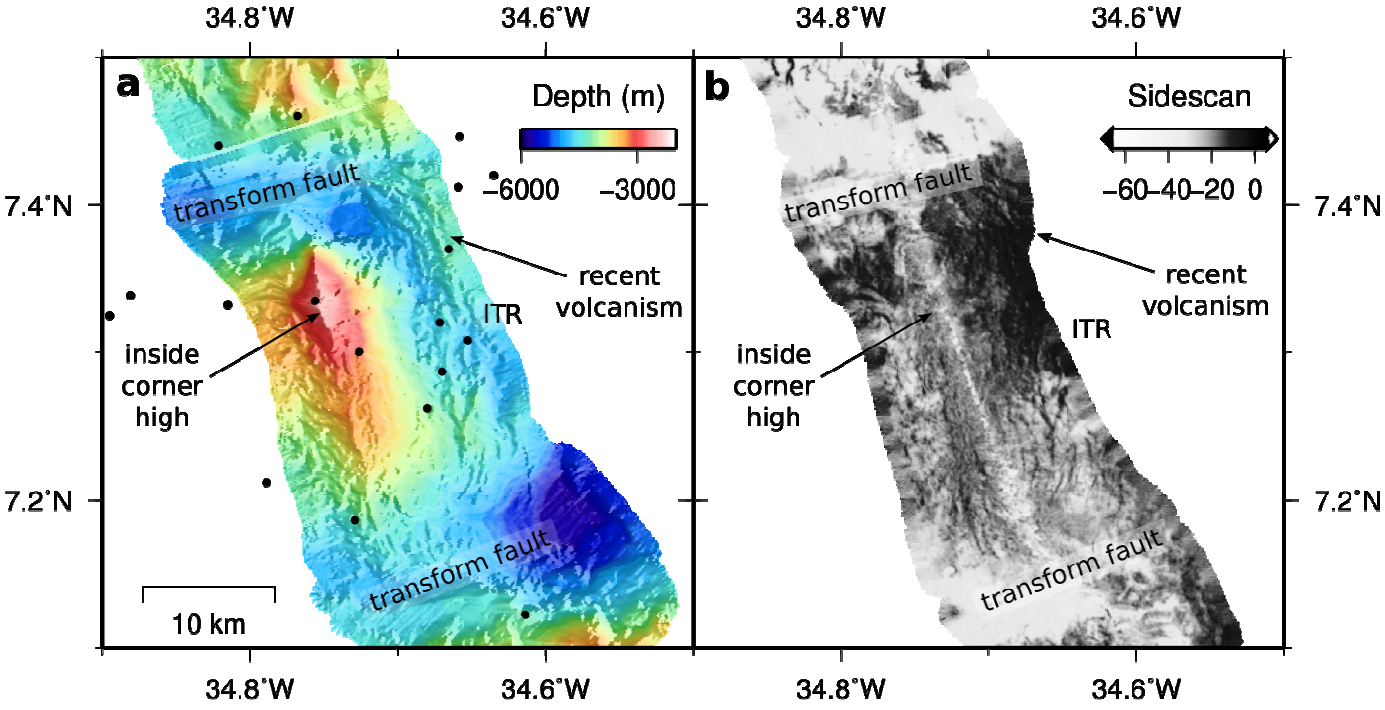

Figure 2.3 *Intra-transform ridge located at 7°N.* **a)** *Multibeam bathymetry data. Black circles: teleseismic earthquakes; ITR: Intra-Transform Ridge. An axial volcanic ridge is observed on the eastern edge of the data;* **b)** *sidescan backscatter image derived from multibeam data. The high backscatter of the axial volcanic ridge indicates that the ITR is magmatically avtive.*

The axial valley is oriented NW-SE, and is about 30 km in length. Hummocky terrain on the valley floor forms an axial volcanic ridge with high backscatter as seen in the sidescan data derived from the EM122 and suggests recent volcanic activity in this short spreading segment. The northern

intersection of the axis and transform fault contains a nodal basin about 5000 m in depth, which curves to the west. The southern nodal basin, which is only partially imaged, reaches depths of 5600 m. The western rift mountain at 7.3°N rises to a height of ~2.5 km above the axial valley floor, and has a NW-SE trending crest. Teleseismic earthquakes in this ridge segment (Figure 2.3) are mostly located off-axis although a small number of events are located in the axial valley itself. Since teleseismic earthquakes error locations are large, we will have to wait for the hydrophone-recorded seismicity to know if these earthquakes are associated with movement on the transform faults or some other process at the spreading center.

2.5 Mid-Atlantic Ridge, 5°N

Data were acquired over the ridge axis in the region of 5 °N, approximately 90 km of which is shown in Figure 2.4. High backscatter, hummocky terrain and circular features are indicative of widespread present day volcanism in the axial valley. Between 5.2 and 5.4°N, the center of the axial valley is dominated by a ~35 km-long ridge, which rises to a height of ~200 m above the valley floor. The symmetrical shape of its flanks and the hummocky texture suggest the ridge is volcanic in origin, although the sidescan data are inconclusive since the ridge is directly beneath the ship centerbeam. To the west of the axial valley, we have noted two features, ~10 km in length, which may indicate active detachment faulting. They show a curved geometry in plain view, and their smooth backscatter signature suggests they are not hummocky and thus, not volcanic in origin.

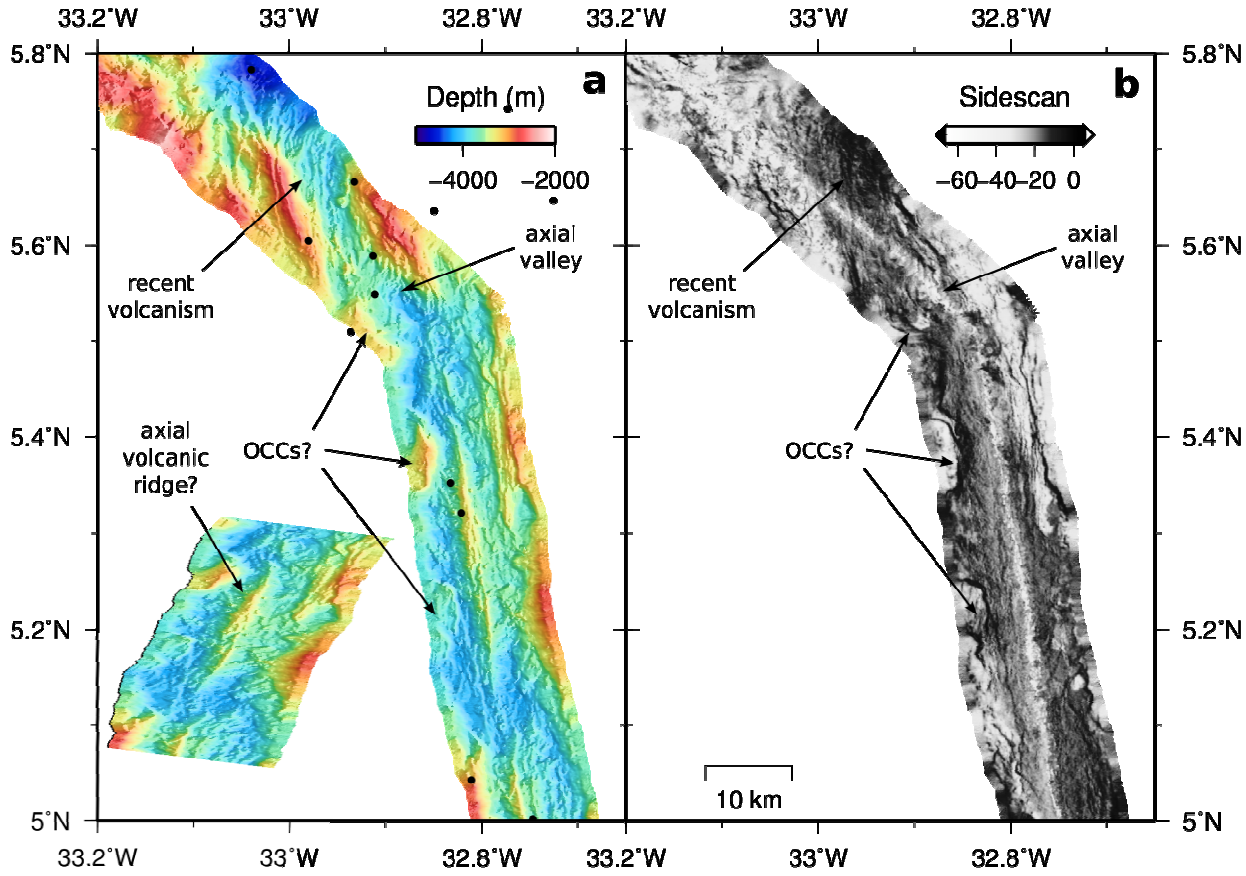

Figure 2.4 *Single ship track along the MAR near 5°N.* **a)** *Multibeam bathymetry data. Black circles: teleseismic earthquakes. An area oh high backscatter indicating recent volcanism is marked. An axial volcanic ridge is observed between 5.1°N and 5.4°N. Two features that we interpret as detachment faults are labeled on the western flank of the axis;* **b)** *Sidescan backscatter image derived from the multibeam data.*

2.6 Next steps

In the next stage of this project we will recover the hydrophone moorings in 2014 after two years of data acquisition. The data will be analyzed to identify earthquake locations, and used to interpret the seismicity at the ridge axis and fracture zones in the context of what we know about the geologic structures. The hydrophone data will be made available soon after completion of the cruise. The earthquake locations will also be made available once they are obtained.

During the recovery cruise, additional multibeam data will be collected to add to the existing bathymetry database; these will be made available through the National Geophysical Data Center (http://www.ngdc.noaa.gov/mgg/bathymetry/multibeam.html). We are now in the process of

obtaining all existing bathymetry data to generate a map of the equatorial Atlantic region as a resource for the entire community.

Acknowledgements

The hydrophone project is supported by the U.S. National Science Foundation OCE 1062238 (D. Smith, R. Dziak PIs). InterRidge Cruise Bursaries enabled CP, RPT and AZ to participate in cruise AT21-03. We gratefully acknowledge the excellent co-operation of the Captain, crew and scientists aboard R/V Atlantis during Cruise AT21-03.

References

Blackman, D. K., J. R. Cann, B. Janssen, and D. K. Smith (1998), Origin of extensional core complexes: Evidence from the Mid-Atlantic Ridge at Atlantis Fracture Zone, *J. Geophys. Res., 103*, 21315 – 21333.

Buck, W. R. (1988), Flexural rotation of normal faults, *Tectonics, 7*, 959 – 973.

Cann, J. R., D. K. Blackman, D. K. Smith, E. McAllister, B. Janssen, S. Mello, E. Avgerinos, A. R. Pascoe, and E. Escartin (1997), Corrugated slip surface formed at ridge-transform intersection, *Nature, 385*, 329 – 332.

Escartin, E., D. K. Smith, J. R. Cann, H. Schouten, C. H. Langmuir, and S. Escrig (2008), Central role of detachment faults in accretion of slow-spreading oceanic lithosphere, *Nature, 455,* 790 – 794.

Hekinian, R., D. Bideau, M. Cannat, J. Francheteau, and R. Hebert (1992), Volcanic activity and crustle-mantle exposure in the ultrafast Garrett transform fault near 13°28'S in the Pacific, *Earth Planet. Sci. Lett., 108*, 259 – 275.

MacLeod, C. J., R. C. Searle, B. J. Murton, J. F. Casey, C. Mallows, S. C. Unsworth, K. L. Achenbach, and M. Harris (2009), Life cycle of oceanic core complexes, *Earth Planet. Sci. Lett., 287*, 333 – 344.

McGuire, J. J., M. S. Boettcher, and T. H. Jordan (2005), Foreshock sequences and short-term earthquake predictability on East Pacific Rise transform faults, *Nature, 434*, 457 – 462.

Menard, H. W., and T. Atwater (1969), Origin of Fracture Zone Topography. *Nature, 222*, 1037 – 1040.

Perfit, M. R., D. J. Fornari, W. I. Ridley, P. D. Kirk, J. Casey, K. A. Kastens, J. R. Reynolds, M. Edwards, D. Desonie, R. Shuster and S. Paradis (1996), Recent volcanism in the Siqueiros transform fault: picritic basalts and implications for MORB magma genesis. *Earth Planet. Sci. Lett., 141*, 91 – 108.

Pockalny,A., P. J. Fox, D. J. Fornari, C. Macdonald, and M. R. Perfit (1997), Tectonic reconstruction of the Clipperton and Siqueiros Fracture Zones:Evidence and consequences of platemotion change forthelast 3 Myr, *J. Geophys. Res., 102,* 3167 – 3181.

Roest, W. R. and B. J. Collette (1986), The Fifteen Twenty Fracture Zone and the North American-South American plate boundary. *J. Geol. Soc., 143*, 833 – 843.

Searle, R.C. (1983), Multiple, closely spaced transformfaultsin fast-slipping fracture zones, *Geology, 11*, 607 – 610.

Smith, D.K., J. R. Cann, and J. Escartin (2006), Widespread active detachment faulting and core complex formation near 13°N on the Mid-Atlantic, *Nature, 442*, 440 – 443.

Smith, D. K., J. Escartin, H. Schouten, and J.R.Cann (2008), Fault rotation and core complex formation: Significant processes in seafloor formation at slow-spreading mid-ocean ridges(Mid-Atlantic Ridge, 13-15°N), *Geochem. Geophys. Geosys., 9*, Q03003, doi:10.1029/2007GC001699.

Tucholke, B. E., J. Lin, and M. C. Kleinrock (1998), Megamullions and mullion structure defining oceanicmetamorphic core complexes on the Mid-Atlantic Ridge, *J. Geophys. Res.,* 103, 9857 – 9866.

Chapter 3

Development of different modes of detachment faulting, 16.5° N at the Mid-Atlantic Ridge

D. K. Smith, H. Schouten, H. J. B. Dick, J. R. Cann, V. Salters, H. Marshall, F. Ji, D. Yoeger, A. Sanfilippo, R. Parnell-Turner, C. Palmiotto, A. Zheleznov, H. Bai, B. Urann, W. Junkin, S. Dick, M. Sulanowska1, P. Lemmond, S. Curry

Submitted to InterRidge News: International Research, 22, p.21-26, 2013

Abstract

During May and June of 2013, we surveyed and sampled a region of the Mid-Atlantic Ridge (MAR) centered on 16.5N. In this region detachment faulting occurs along ~120 km of the western flank of the ridge axis which exhibits varying local magmatic budgets. The study area presents excellent examples of several different modes of active detachment faulting. Regional multibeam bathymetry, gravity, and magnetic data were collected out to about 60 km (~5 Ma) on each side of the axis to understand the spreading history. Autonomous Underwater Vehicle (AUV) Sentry collected high-resolution multibeam bathymetry, side-scan, magnetic, chirp, and water column data in critical locations complemented by photographs from the WHOI Towcam. We also completed an extensive dredging program in the region. The data are being used to characterize fault terminations, assessing where detachment faults are active, how they evolve off-axis, whether they link along the axis, and their relationship to magma budget at the axis. Here we present a preliminary description of 4 modes of detachment faults that accommodate extension of the western rift valley wall.

3.1 Study Area

Figure 3.1 shows the location of the study area near 16.5° N at the MAR. A previous study identified two distinctive, parallel linear ridges (East and West Ridges, Figures 3.2 and 3.3) on the west side of the axis as the rotated tops of detachment faults (breakaways) [*Smith et al.,* 2008]. East Ridge, because it is closer to the volcanic axis, was interpreted as a newly emerging detachment fault forming a rafted block sitting on the top of the older West Ridge detachment. The corrugated massif at the south end of West Ridge was identified as a core complex. On the east side of the ridge axis at 16.63N, Krasnov, a large, extinct hydrothermal vent field (Figure 3), has been the focus of several studies [e.g., *Cherkashov et al.,* 2008].

The 16.5N region has a high rate of seismicity. There are 29 teleseismic events listed in the NEIC catalog (http://earthquake.usgs.gov/earthquakes/eqarchives/epic/). In addition, 391 hydroacoustically-recorded events were identified during four years of monitoring [*Smith et al.,* 2003] yielding an astonishing average of about one earthquake (roughly > magnitude 2.5-3.0), every three days. Based on the seismicity rate and their interpretation of the morphology, *Escartín et al.* [2008] concluded that the west flank of the 16.5N area is one of active detachment faulting.

3.2 Data

During the KN210-05 cruise, regional multibeam bathymetry, gravity, and magnetic data were collected out to ~5 Ma on each side of the axis (tracklines, Figure 3.1) to understand the spreading history. Corrugations west of North and West Ridge detachment faults (labeled on Figure 3.3) indicate that in this region detachment faulting has dominated the west flank of the ridge for at least 3 Ma.

AUV Sentry completed 14 dives and collected high-resolution multibeam bathymetry, side-scan, magnetic, chirp, and water column data in each of the survey boxes shown in Figure 3.2. Sentry seafloor photographs were obtained along short lines during two of the dives (box

immediately east of East Ridge and the westernmost box over the North detachment fault, Figure 3.2).

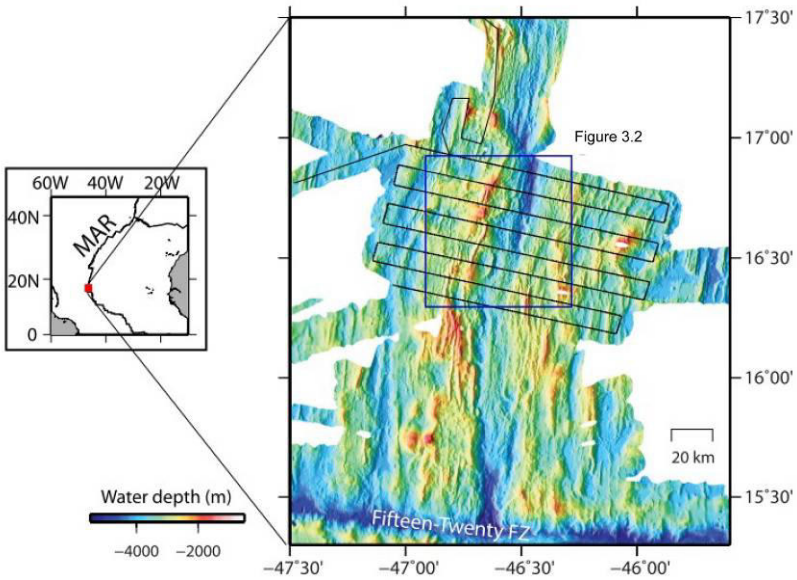

Figure 3.1. *Location of the study region near 16.5N at the MAR showing the tracklines along which we collected SeaBeam bathymetry, gravity, and magnetics data. The location of Figure 3.2 is marked.*

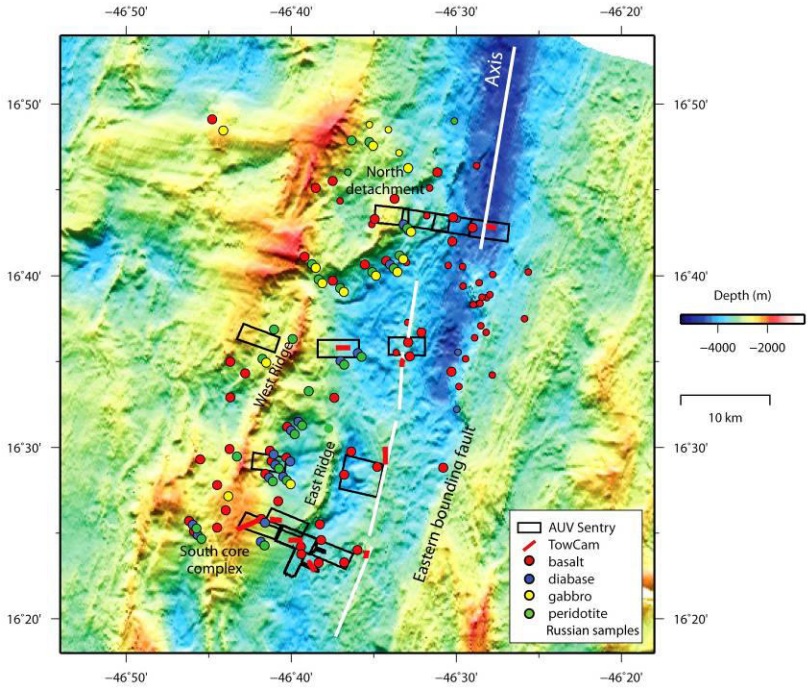

Figure 3.2 *Bathymetry map showing the locations of the AUV Sentry dives, Towcam dives, and rock samples obtained during R/V Knorr 210-05. Also included are samples locations from the Russian data archive. The Russian samples are primarily located on the eastern side of the axis and in the north.*

In addition, bottom photographs and water column data were collected in areas of interest during 9 dives of the WHOI Towcam (short red lines, Figure 3.2). Finally, an extensive dredging program was completed in the region. Rocks were obtained in 73 dredges adding to the samples previously collected by our Russian colleagues [*G. Cherkashov* personal communication, 2013]. The types of rocks collected and their locations are shown in Figure 3.2 (smaller circles indicate Russian samples). Dredges and Towcam dives were run during and between AUV Sentry surveys. The extensive suite of data collected in the 16.5N region allows us to interpret detachment faults and core complexes confidently.

3.3 Four modes of detachment faulting

The four seafloor units representing modes of active detachment faulting are outlined by white lines in Figure 3.3. Examples of the Sentry bathymetry and sidescan obtained in these areas are shown in Figure 3.4.

3.3.1 South core complex

South core complex is a classic, corrugated, domal massif. As seen on the SeaBeam data, the corrugations have wavelengths varying between 400 and 1600 m, and relief of 50-100 m. Sentry high-resolution bathymetry data show that the exposed footwall close to where it emerges from beneath the hanging wall has a dip of < 10o. The Sentry data also reveal corrugations on a smaller scale (wavelength of 100 m or so and relief of <10 m). The termination of South core complex fault is located ~8 km from the axial volcanic ridge (AVR), which is broad (~4.5 km wide) and has a relief of about 300 m. Towcam photographs at the top of the AVR (short red line, Figure 3.2) show areas of minimal sediment cover suggesting that the AVR is volcanically active. Despite several attempts, we were unable to sample the lower footwall of South core complex, which we speculate is due to it consisting of a massive smooth fault surface that exposes gabbro. Similar sampling

problems have been encountered at other oceanic core complexes exposing massive gabbro that have not been broken by mass wasting and cross-faulting.

3.3.2 East Ridge

East Ridge is a medium-offset normal fault that is active close to the spreading axis. Its termination lies ~3.5 km from the AVR, which is consistent with a new normal fault dipping at 60° that cuts the base of a 6-km thick crust at a point beneath the magmatic axis. We think that the section of older detachment (West Ridge, Figure 3.2) behind East Ridge ceased being active when extension on East Ridge detachment fault was initiated and furthermore, that the arcuate shape of East Ridge (Figure 3.3) indicates that the detachment fault has linked with South core complex and West Ridge detachment fault to form a single detachment fault along the axis. The southern end of East Ridge where it intersects the corrugated surface of South core complex is shown in Figure 3.4a. We interpret the corrugated surface behind East Ridge as the abandoned section of West Ridge detachment fault. Several dredges on the inward facing slope of East Ridge recovered pillow basalts indicating that the fault throw is insufficient as of yet to expose lower crust or dikes.

The dip of the outward-facing slope of East Ridge is ~20° and the axis-facing scarp 30°-40° yielding a normal fault with an initial dip angle of between 50-60° (obtained by summing the inward and outward dips) and indicating significant flexural fault rotation [*Buck,* 1988]. The AVR adjacent to East Ridge is approximately 3 km wide with a relief of 300 m, similar to the AVR just to the south. Towcam photographs of the AVR (short red line, Figure 3.2) indicate that this section of the AVR also is volcanically active.

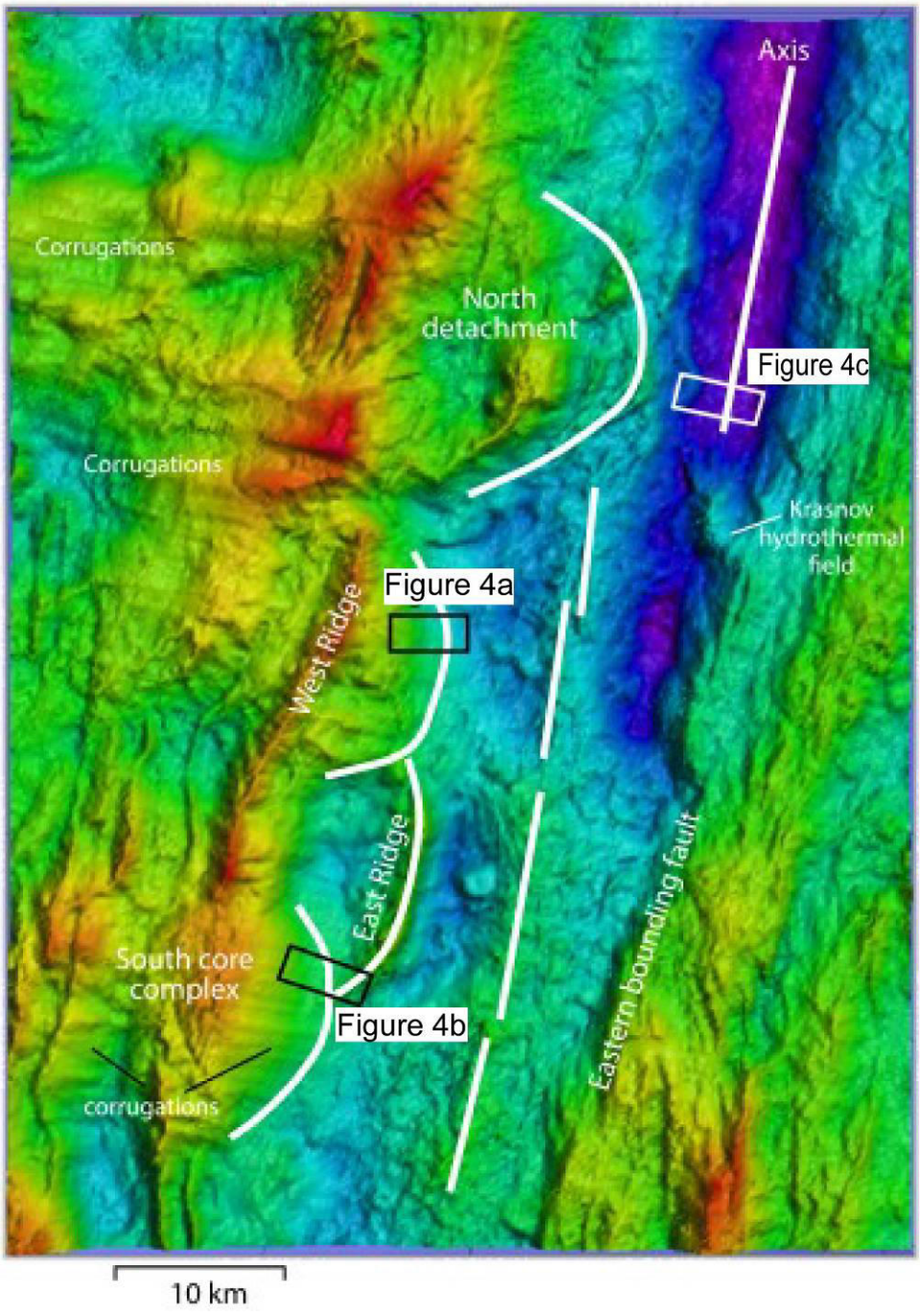

Figure 3.3 *Bathymetry map centered on 16.5N. Major features near the axis are labeled. Arcuate white lines outline the four surface units representing four contrasting modes of detachment faulting. Straight white lines indicate the spreading axis. Labeled boxes show the locations of AUV Sentry data shown in Figure 3.4.*

3.3.3 West Ridge detachment fault

West Ridge detachment fault is corrugated, but the corrugations are only observed on the Sentry high-resolution bathymetry (Figure 3.4b), not the Seabeam bathymetry. These small-scale corrugations have wavelengths of about 50 m and relief of <10 m. The exposed footwall near the ermination dips at an angle of 18°, which is steeper than observed at South core complex (<10°). The termination of West Ridge fault is about 5 km from the AVR. Numerous dredges on the inward facing slope of West Ridge detachment fault recovered peridotite, diabase and pillow basalt. The rougher terrain and ease with which it was dredged indicates that this terrain was more easily disrupted by faulting and mass wasting than the penecontemporaneous uniformly smoothly corrugated footwall of South core complex. This is consistent with a stratigraphy of massive serpentinized peridotite cut by diabase dikes overlain by scattered pillow basalts. The AVR adjacent to West Ridge fault is narrower (1.5-2 km wide) than to the south, but its relief is the same (300 m). In addition, the top of the AVR is on average a few hundred meters deeper than the AVRs in front of South core complex and East Ridge. Towcam photographs (short red line, Figure 3.2) appear similar to those obtained to the south suggesting that this AVR also is volcanically active. Volcanism may be more anemic in this section or the AVR may be currently building.

3.3.4 North detachment fault

The North detachment fault borders a deep, narrow rift axis (Figure 3.3), which suggests that this section of the ridge is magma starved. Sentry data obtained over the axis (Figure 3.4c) show that the valley floor is covered by a thin veneer of volcanic flows that have not constructed an AVR. On the west flank of the ridge, three back-tilted fault blocks whose tops are covered by hummocky flows have been carried off axis. West of these fault blocks is a massif from which we sampled gabbro and peridotite. We interpret the western flank of the axis in this region as a detachment fault

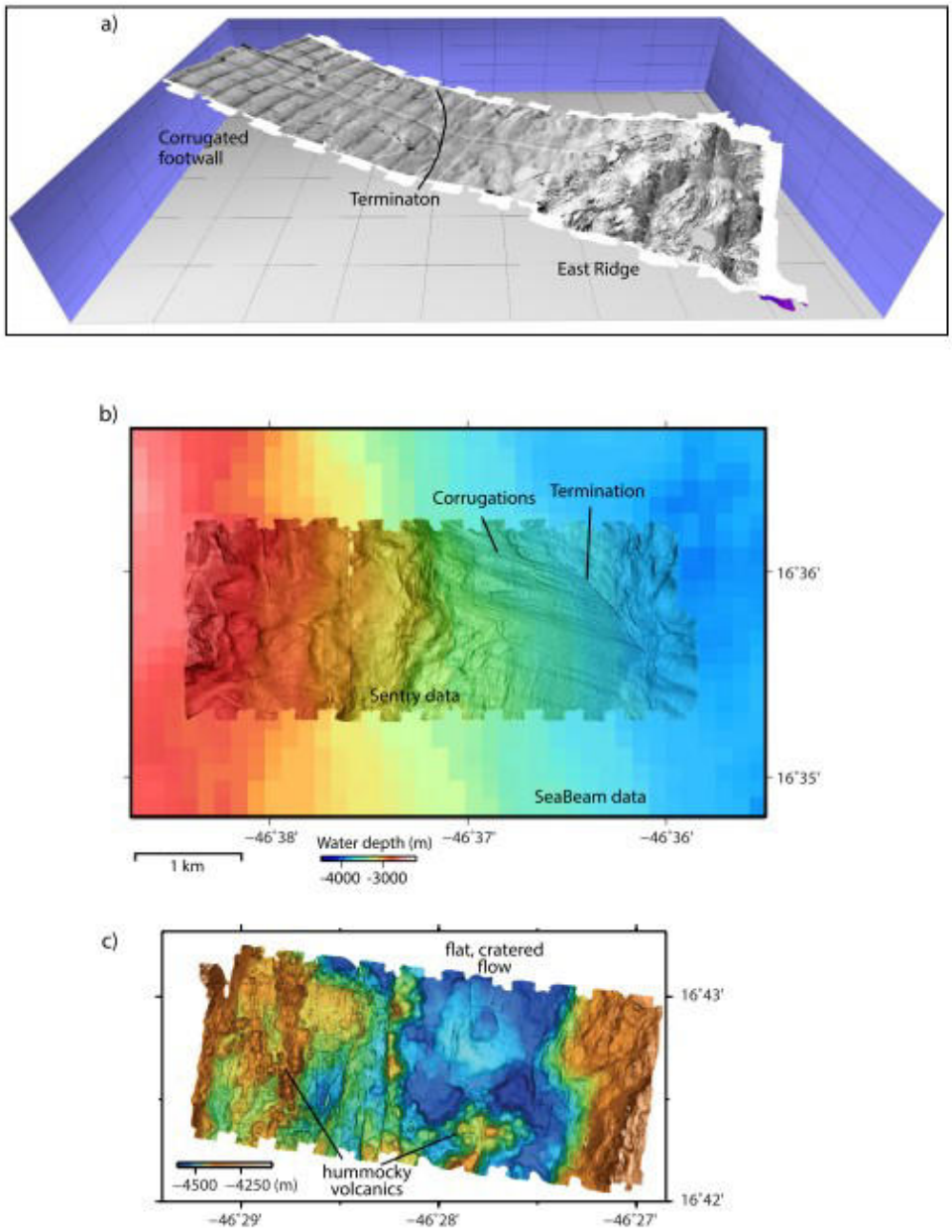

Figure 3.4 *Examples of Sentry data for the boxes shown in Figure 3.3.* **a)** *Sidescan sonar overlain on bathymetry data shows the southern section of East Ridge fault and the abandoned termination of West Ridge to its west.* **b)** *Sentry bathymetry over West Ridge detachment overlain on Sea Beam data. Note that the corrugated surface and fault termination are not seen on Sea Beam data.* **c)** *Sentry data over the ridge axis adjacent to North detachment fault. Eruptions have produced hummocks and a flat cratered lava flow but not a large axial volcanic ridge in this deep rift valley.*

that is mostly covered by short-lived rider blocks, with a basement composed of small gabbro intrusions in serpentinized peridotite overlain by scattered pillow basalts.

3.4 Discussion

Here we summarize some of the preliminary results from the KN 210-05 cruise within the context of previous studies. Numerical modeling has suggested that long-lived detachment faults form primarily in regions of reduced magma supply [*Buck et al.,* 2005; *Olive et al.,* 2010; *Tucholke et al.,* 2008], and this is supported by their common occurrence at the end of segments where it is inferred that magma supply is low [*Tucholke et al.,* 2008]. In our study region, however, these ideas do not hold up. The differing modes of detachment faulting described above (South core complex, East Ridge and West Ridge detachments) occur along sections of the ridge axis with a robust AVR (aside perhaps from a narrowing and deepening of the AVR adjacent to West Ridge). In fact, the most robust AVR appears to be adjacent to South core complex suggesting abundant volcanism and high magma supply. Also, it is interesting to note that at the magma poor section of the axis in the north, the detachment surface is covered by rider blocks. These observations are opposite to what has been previously proposed (i.e., that corrugated surfaces form in regions of low magma supply and rider blocks form toward the center of the segment where local magma budget is high [e.g., *Reston and Ranero,* 2011]. Our preliminary results suggest that variations in local magma budget may not be the only mechanism controlling the surface expression of detachment faults. Moreover, we see that active detachment faulting continues to occur at similar scales from north to south despite the widely varying magma budgets indicated by our sampling.

Acknowledgments

We would like to thank the captain and crew of the R/V Knorr for their hard work during cruise KN210-05. The over-the-side operations (Sentry, Towcam, dredging) were handled efficiently and with expertise, and allowed us to meet our demanding schedule.

References

Buck, W.R. (1988), Flexural rotation of normal faults, *Tectonics, 7 (5),* 959 – 973.

Buck, W.R., L.L. Lavier, and A.N.B. Poliakov (2005), Modes of faulting at mid-ocean ridges, *Nature, 434,* 719 – 723.

Cherkashov, G., V. Bel'tenev, V. Invanov, L. Lasareva, M. Samovarov, V. Shilov, T. Stepanova, G.P. Glasby, and V. Kuznetsov (2008), Two new hydrothermal fields at the Mid-Atlantic Ridge, *Mar. Geores. Geotech., 26,* 308 – 316.

Escartín, J., D.K. Smith, J. Cann, H. Schouten, C.H. Langmuir, and S. Escrig (2008), Central role of detachment faults in accretion of slow-spread oceanic lithosphere, *Nature, 455,* 790 – 794, doi:10.1038/nature07333.

Olive, J.-A., M.D. Behn, and B.E. Tucholke (2010), The structure of oceanic core complexes controlled by the depth distribution of magma emplacement, *Nature Geo., 3,* doi:10.1038/NGEO888.

Reston, T.J., and C.R. Ranero (2011), The 3-D geometry of detachment faulting at mid-ocean ridges, *Geochem. Geophys. Geosys., 12,* Q0AG05, doi:10.1029/2011GC003666.

Smith, D.K., J. Escartin, M. Cannat, M. Tolstoy, C.G. Fox, D. Bohnenstiehl, and S. Bazin (2003), Spatial and temporal distribution of seismicity along the northern Mid-Atlantic Ridge (15°-35°N), *J. Geophys. Res., 108,* doi: 10.1029/2002JB001964.

Smith, D.K., J. Escartin, H. Schouten, and J.R. Cann (2008), Fault rotation and core complex formation: Significant processes in seafloor formation at slow-spreading mid-ocean ridges (Mid-Atlantic Ridge, 13-25°N), *Geochem. Geophys. Geosyst., 9,* Q03003, doi:10.1029/2007GC001699.

Tucholke, B.E., M.D. Behn, W.R. Buck, and J. Lin (2008), Role of melt supply in oceanic detachment faulting and formation of megamullions, *Geology, 36,* 455 – 458, doi:10.1130/G24639A.1.

Chapter 4

Oceanic Megatransforms: A New Type of Plate Boundary

Ligi, M., Bonatti, E., Palmiotto, C., Pasini, V., et al.

In preparation for *Earth Science Review*

Abstract

The introduction by Wilson of the concept of transform fault was a key step in the development of the theory of Plate Tectonics. Transform faults offset the axis of mid-ocean ridges, and are the locus of strike-slip motion at the boundary of two plates that slide past each other. Oceanic transform boundaries are manifested by narrow (a few km) highly seismic strike-slip fault zones joining the two offset ridge segments. This is in contrast with continental transform systems, such as the St. Andrea or the N. Anatolian faults, that display broad (>100 km) and complex areas of deformation. The idea of simple, narrow oceanic transform faults has found at least two exceptions. One is the Romanche transform, that offsets the equatorial Mid-Atlantic Ridge by over 900 km, displaying a lens-shaped, >120 wide complex zone of deformation between the two ridge axes. The other is the Andrew Bain transform, that offsets the South West Indian Ridge (SWIR) by about 750 km, also shows a wide (about 100 km) lens shaped zone of deformation.

In this paper we describe the peculiar features of these transforms and we propose call them as "Megratransforms". We define them as "megatransforms". The St. Paul transform offsets (equatorial Atlantic) functioned probably as a megatransform up to about 50 Ma. Oceanic megatransforms constitute a new type of plate boundary that forms when the age offset is > 30 million years. The broad deformation zones could be considered as semistationary microplates.

4.1 Introduction

The concept of transform fault, introduced by *Tuzo Wilson* in 1965 to explain offsets of the axis of mid-ocean ridges, has played a major role in the theory of Plate Tectonics. The distribution of seismicity along mid-ocean ridges [*Sykes,* 1967] confirmed Wilson's interpretation, whereby transforms faults are the locus of strike-slip motion and act as plate boundaries where two oceanic plates slide past each other.

Subsequent work established that:

a) the length of transform offsets in mid-ocean ridges ranges from near zero to almost thousand kms;

b) the zone of strike-slip deformation in oceanic transform faults is generally only a few kms wide. The small width of strike/slip deformation zones even in long offset oceanic transforms allows identification of "small circles" that define a pole of rotation for the motion of the plates adjacent to the transform;

c) transform offsets are frequent (about one each 50 km) in slow-spreading ridges (Mid-Atlantic Ridge) but less frequent (about one each 100 km) on fast-spreading ridges (East Pacific Rise). However, it has recently been found that transform offsets are nearly absent from long stretches of ultra-slow ridges, i. e., Gakkel Ridge [*Michael et al.,* 2003];

d) transform offsets affect significantly the subseafloor thermal structure of ridge segments as they approach a transform boundary causing a "cold edge effect" [*Fox and Gallo*, 1984]. This effect may lower the extent of melting of the subridge mantle and decrease crustal thickness as the transform is approached;

e) transform offsetting slow spreading ridges are the locus of intense vertical tectonics due to transtension or transpression related to small changes in ridge/transform geometry [*Bonatti*, 1976].

The narrow strike slip deformation zone of oceanic transforms constrasts with the wide (> 100 km) and complex deformation zone typical of continental transform system, such as the St Andreas or the Anatolian Faults. However, this pattern finds some exceptions in a few long-offset oceanic transforms that display a wide (> 100 km) deformation zone similar to that continental transforms system. We have called this new type of plate boundaries "oceanic megatransforms".

We include in this class of boundaries the Romanche Transform in the equatorial Atlantic, and the Andrew Bain Transform in the SW Indian Ocean (Figure 4.1). We will also discuss some transforms systems that behaved probably as "megatransforms" at some stage in the past, but evolved then into normal transform system. The St Paul system in the equatorial Atlantic is an example (Figure 4.1).

We will describe here the main features of these two systems, review the general characteristics of "oceanic megatransforms", and discuss their origin and evolution.

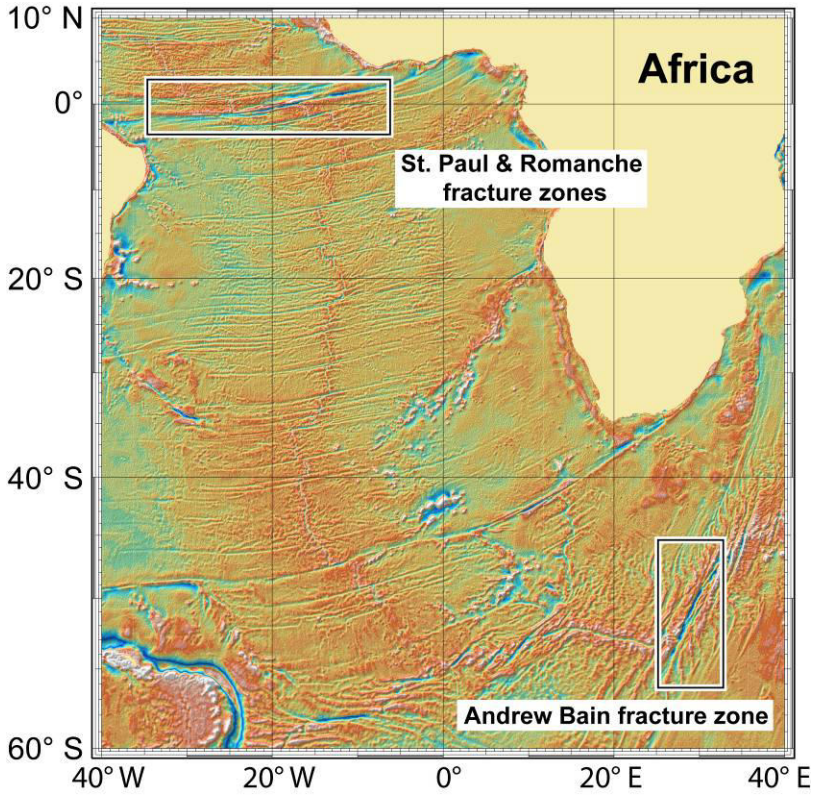

Figure 4.1 *Free air satellite imagery of the southern Atlantic and western Indian Oceans. Boxes show location of Romanche and Andrew Bain megatransforms, and of St. Paul transform system.*

4.2 Methods

Geophysical data summarized in this paper were obtained from the Romanche and St.Paul fracture zones during a number of expeditions with research ships Vema and Conrad (LDEO), Pillsbury and Gillis (University of Miami), Explora (OGS), Strakhov and Gelendzhik, operated by ISMAR–CNR, Italy.

Geophysical data from the Andrew Bain fracture zone were obtained during an expedition with the research ship Strakhov, operated by ISMAR–CNR, Italy, together with the Geological Institute of Moscow (GIN-RAS), Russia.

4.2.1 Bathymetric multibeam and seismic reflection data

Details on acquisition and processing parameters can be found in *Bonatti et al.* [1994] and *Gasperini et al.* [1997] for the Romanche surveys. Geological and geophysical data acquired at Andew Bain were merged with old data acquired by *Grindlay et al.* [1996] and *Sclater et al.* [2005].

We merged the multibeam data with the predicted bathymetry (GEBCO) to create the full bathymetry of the Romanche, St. Paul and Andrew Bain Transform faults. In order to examine the distribution of the Mantle Bouguer Anomalies we calculated the thickness of the sediments analyzing all the mono and multichannel seismic profiles available in the Romanche, St. Paul and Andrew Bain Transform faults areas.

Spatial analysis and mapping were performed using the GMT [*Wessel and Smith*, 1995] and PLOTMAP [*Ligi and Bortoluzzi*, 1989] packages.

4.2.2 Gravity Data

We calculated first the Free Air Anomaly (FAA) of the Romanche, St. Paul and Andrew Bain Transform faults. Secondly, to examine sub-seafloor density variations, we calculated the Mantle Bouguer Anomaly using the method of *Kuo and Forsyth* [1988], *Prince and Forsyth* [1988], and *Lin et al.* [1990], subtracting from FAA the predicted gravity effects of the column of seawater,

of the thickness of sediments and of a 6 km thick model crust. We assumed a density of the crustal layer of 2,700 kg/m^3, and of the underlying mantle of 3,300 kg/m^3, in accordance with values used in previous studies of the Mid-Atlantic Ridge [e.g., *Kuo and Forsyth,* 1988; *Lin et al.,* 1990; *Blackman and Forsyth,* 1991; *Morris and Detrick,* 1991; *Detrick et al.,* 1995]. We further calculated the Residual Mantle Bouguer Anomaly (RMBA) by removing theoretically calculated lithospheric cooling effects from the MBA. The thermal model was calculated using the three-dimensional passive upwelling model of *Morgan and Forsyth* [1988]. Reference asthenospheric temperature was assumed to be 1.320°C at a depth of 100 km. The half-spreading rate was set to be ~ 17,5 km/Ma for the Romanche and St. Paul transforms [*Cande et al*., 1988], and ~ 16 km/Ma for the Andrew Bain transform [*Ligi et al.,* 2002]. We also calculated a model of relative crustal thickness variation by downward continuing the RMBA to an assumed mean depth of 9 km to investigate the amplitude of crustal thickness variations that are required to explain the observed RMBA.

4.3 Results

4.3.1 Romanche Megatransform

The Romanche transform offsets the equatorial Mid-Atlantic Ridge by 900 km and it is the longest transform boundary between the African and South American plates. Its name derives from the French research vessel *Romanche*, that discovered the deepest point of the Atlantic Ocean (*Vema Deep*, -7856 m) in the active zone of the fault, excluding the Porto Rico and the Sandwich trenches. Gravity images [*Haxby,* 1987] show that the Romanche fracture zone can be traced across the equatorial Atlantic from an offset of the Gulf of Guinea continental shelf to an E-W branch of the North Brazilian Ridge on the American side. Thus the Romanche probably originated as a continent/continent transform at the time of initial rifting of the equatorial Atlantic Ocean.

The morphology of the Romanche differs from that of most oceanic fracture zones, and it is similar to the morphology of continental transform faults. Multibeam bathymetry of the Romanche revealed not a single narrow transform valley, but a lens-shaped, 900-km-long, 100-km-wide, highly deformed area joining the two Mid-Atlantic Ridge segments (Figure 4.2A). The tips of the lens-shaped deformed region correspond to the eastern and western Mid-Atlantic Ridge transform intersections. Romanche is characterized by a southern long and deep E-W trasform valley, flanking North another shallower seismic valley and South a prominent transverse ridge (Figure 4.2A). The southern valley joins the two ridge-transform intersections in the western and eastern regions and it marks the present-day principal transform boundary (Figure 4.2A). Modern seismicity suggests present-day strike-slip motion along the southern valley, and probably elsewhere within the lens-shaped deformed region [*Ligi et al.,* 2002]. The southern valley is morphologically characterized by the presence of the Principal Transform Displacement Zone (PTDZ). The width of the southern valley is about 20 km, and it is deeper than the northern fossil valley. Its depth ranges from 5000 m below sea level near the western ridge – transform intersection, to about – 7800 m in the Vema Deep. The depth is about 5500 m below sea level near the eastern ridge – transform intersection. The northern valley extends into a deformed region: it is larger than the southern valley: the mean depth is about 4000 m below sea level, and its width changes from a few km near the ridge – transform intersection to about 50 km in the central zone of the transform valley (Figure 4.2A). This valley is filled by hundreds of meters of turbidite sediments, and its morphology is characterized by several NW-SE alternateing ridges and valleys.

Different phases of reorganization of the geometry of the Romanche transform boundary created different positive and negative topographic anomalies. Two of them are significant and show the complexity of the Romanche tectonics. The first is the negative anomaly “Vema Deep” (-7856 m), located in the southern transform valley; Vema deep is the deepest point of the Romanche valley and its origin is correlated to a transtensive tectonic phase.

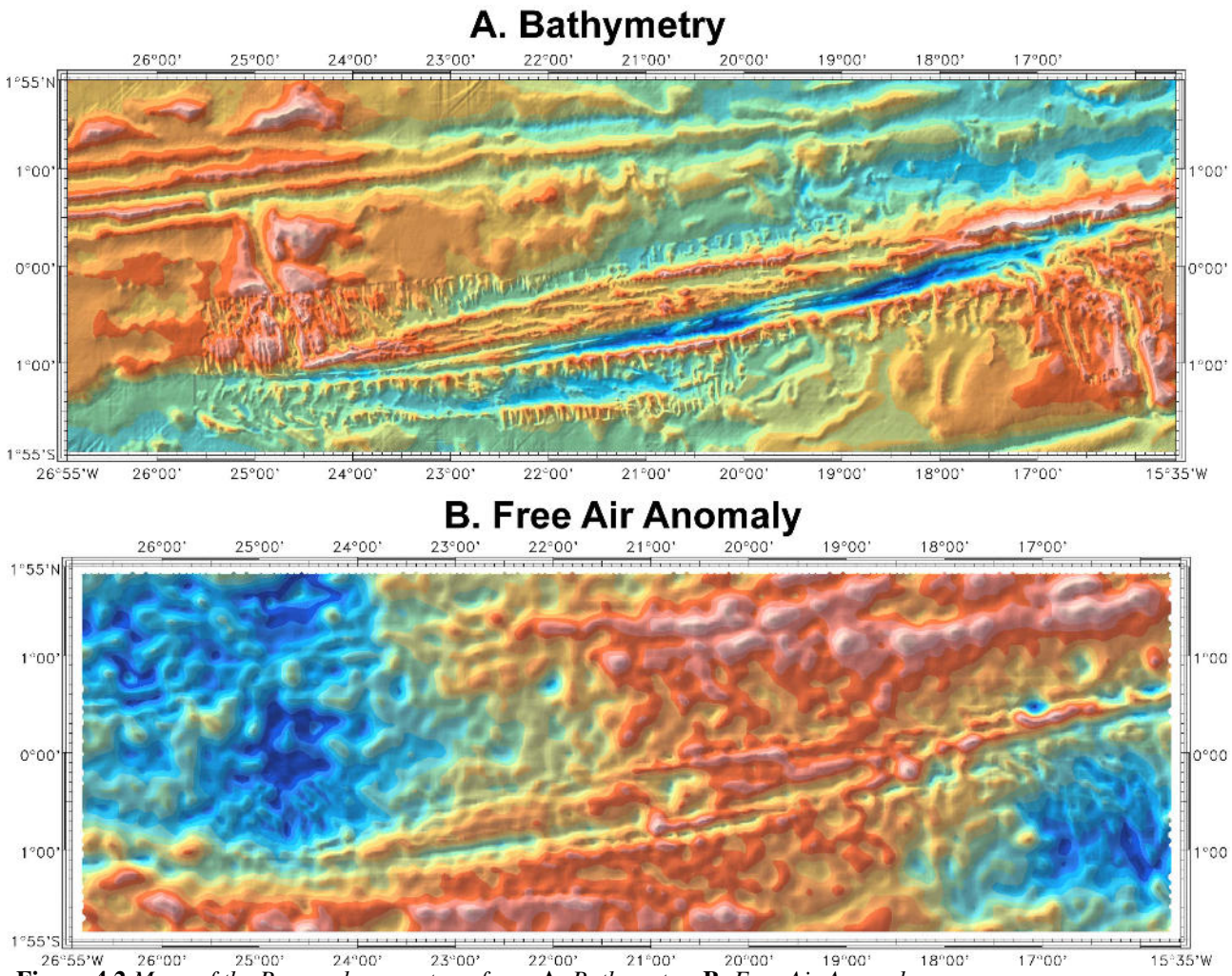

Figure 4.2 *Maps of the Romanche megatransform.* **A.** *Bathymetry;* **B.** *Free Air Anomaly.*

The second feature is the positive topographic anomaly represented by the northern transverse ridge (-875 m), located at the eastern ridge – transform intersection and along the eastern fossil zone of the Romanche. This portion of the transverse ridge flanks the northern side of the transform and rises up to 4 km above the level predicted by the thermal contraction depth-(age)$^{1/2}$ law, if we assume a constant ridge/transform geometry and an average spreading rate of 1.75 cm/yr (half rate) both north and south of the transform for the last 50 Ma. The origin of this large positive anomaly is probably related to a transtensive tectonic phase. The western and the eastern ridge – transform intersections (RTIs) are characterized by deep nodal basins (about 5000 - 5500 m of depth). The eastern RTI is not well defined morphologically, contrary to the western RTI. In these regions the new oceanic crust that rises along the segment of Mid-Atlantic Ridge is in contact with

the cold and old lithosphere of the other lithospheric plate. According to *Cande et al*. [1988], the Romanche has a slip rate of 32 mm/a; so, there is an age offset of about 55 Ma [*Bonatti et al.,* 1994]. The southern active transform valley shows the actual PTDZ, and this is the area where there were large earthquakes in the last 50 years.

Figure 4.2B shoe the map of the Free Air Anomaly (FAA) of the Romanche Transform. The FAA map show the contrast of density of the rocks in the area, and it resembles the bathymetric map.

4.3.2 Andrew Bain megatransform

The Andrew Bain Transform (ABT) is the longest of a set of close-spaced South West Indian Ridge (SWIR) transforms that includes Dutoit on the SW side; Marion and Prince Edwards on the NE side. Given the ultraslow spreading rate of the adjacent plates, the slip rate along the ABT is very small (16 mm/a); it follows that, although the ABT offset is significantly shorter than that of the Romanche megatransform, its age offset (~ 54 million years) is similar to that of the Romanche.

Previous work on the ABT has been scant [*Grindlay et al.,* 1996], in part because it is located in a remote and inhospitable region of the ocean. We carried out field work at the ABT in February/March 2006 with the research ship Akademik Strakhov of the Geology Institute of the Russian Academy of Sciences. We produced a new multibeam map that, together with *Grindlay et al*. [1996] previous data, covers the SW half of the ABT region and we expanded the magnetometric and gravimetric coverage of the area. We obtained multichannel seismic reflection profiles across the central part of the transform and sampled rocks from the SW Ridge/transform intersection and from the SW transverse ridge.

Multibeam topography (Figure 4.3A) confirms that the ABT is characterized by a broad (~ 120 km near mid point) multifault deformation zone, separating the Antarctic from the African (Nubian) plate.

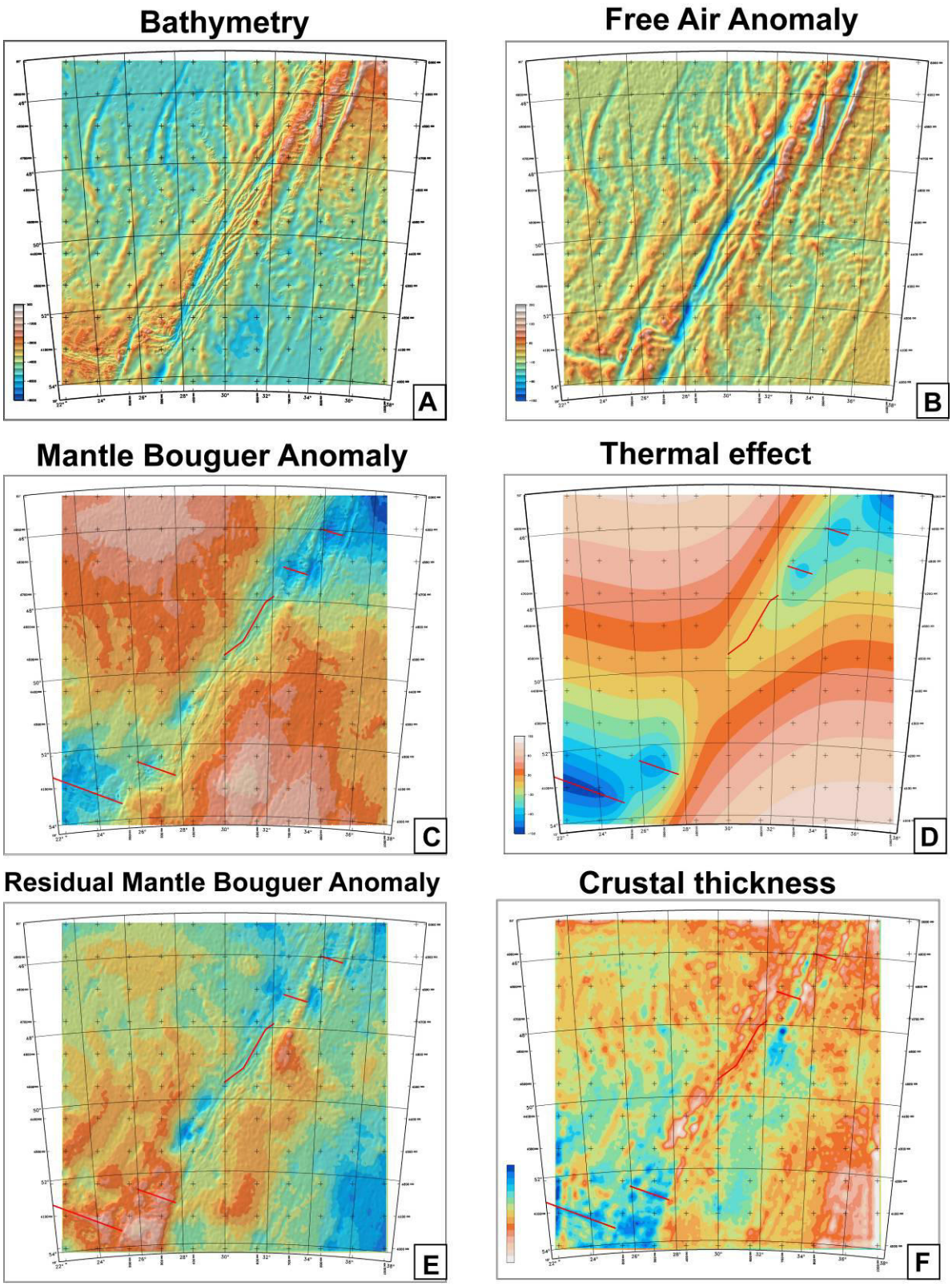

Figure 4.3 *Maps of the Andrew Bain megatransform.* **A.** *Bathimetry;* **B.** *Free Air Anomaly;* **C.** *Mantle Bouguer Anomaly;* **D.** *Thermal effect;* **E.** *Residual Mantle Bouguer Anomaly;* **F.** *Crustal Thickness.*

The transform domain consists of a 400 Km long, broad southwestern transform valley connected via a series of transform relay zones to a narrower, 150 Km long northeastern transform valley. Oblique en echelon structures characterize the central part of the transform domain. The two boundaries of the southern deformation zone converge towards the SW ridge/transform intersection, so that the deformed area in the SW half of the ABT has a half-lens shape, similar to that of the deformed area of the Romanche megatransform [*Ligi et al.,* 2002], but contrasting with the narrow strike-slip deformation zone of other known oceanic transforms.

The SWIR as it approaches the ABT from the SW is manifested by two en echelon rift valley segments. Our sampling indicates that SW rift valley is carpeted by fresh pillow basalts at a site roughly 100 Kms from the intersection with the ABT; but by mantle-derived peridotites at sites 80 kms from the intersection. This may mean that subridge production of basaltic melts wanes out already 90 Km from the intersection, leaving crust-free lithospheric mantle outcropping on the sea floor: again a situation similar to that observed where the Romanche Transform is approached from the south by the Mid Atlantic Ridge. The primary cause of the quasi-absence of basaltic crust near both the Romanche and the Andrew Bain ridge/transform intersections is probably the strong "cold edge effect" produced by the large age-offset transforms, that limits the extent of mantle melting. The actual intersection area is structurally rather diffuse; structural lineations curve towards the transform side and a clear inner-corner high is missing: a structural setting similar to that observed at the Romanche-MAR eastern intersection.

In contrast, the NE intersection where the SWIR segment approaches the ABT from the Marion transform, appears to have a more "normal" structure. The reason is probably that the "cold edge effect" is tempered by a "hotter" thermal regime due to the vicinity of the Marion hot spot. This interpretation is confirmed by the contrasting composition of mantle-derived peridotites sampled from the vicinity of the two ridge/transform intersections. The peridotites sampled close to the SW intersection have undergone a degree of melting lower than that estimated from the peridotites sampled close to the NE intersection, near the Marion hot spot.

Seismicity is exceptionally intense along the ABT. The strongest event ever recorded in the ocean basins outside subduction margins [magnitude 8.1; *Okal and Stein*, 1987] occurred within the ABT deformation zone in 1942. Recent ABT seismicity, prevalently strike slip but with also a significant extensional component, is mostly alined along the southwestern valley although activity has been detected elsewhere within the deformation zone.

We could not create a map of thickness of sediment for the ABT region, because we do not have a large number of multichannel seismic profiles. Figure 4.3B show the map of Free Air Anomaly: it reflects the density variations of the rocks and it looks similar to the bathymetric map. We obtained the map of Mantle Bouguer Anomaly (Figure 4.3C) the effect of the bathymetry and of a crustal model 5-km thick removing form the map of the Free Air Anomaly. Most negative values are located below the western side of the segments of the SW Indian Ridge, where the Bull's eye mantle anomaly is located [*Kuo and Forsyth,* 1988]; in contrast, most positive values of MBA are located along the easterm portion of the ABT. Negative values indicate a maximum melting degree below the segments of the mid-ocean ridge and evidence the regions in which magma production is higher; in contrast, positive values evidence the region characterized by a minimum malting degree and by a thicker lithosphere layer.

We removed the thermal effect of the mantle (Figure 4.3D) from the values of the Mantle Bouguer Anomaly, and we obtained the map of the Residual Mantle Bouguer Anomaly (RMBA), shown in the Figure 4.3E. The distribution of the RMBA shows that the ABT can be divided in two main regions. Eastern ABT region is characterized by low value, and it presents a thick crust; in contrast, western region is characterized by high value of RMBA, and it present thinner crust. We can deduce that magmatic supply of the ABT region changes with the geographical position: it is higher North of ABT, and lower South of ABT.

Finally, the Figure 4.3F shows the variation of the crustal thickness of the region. This map show the topography of the top of the mantle at 9 km of depth.

4.4 Origin of megatransform plate boundaries

The ratio: length of offset/maximum width of the deformation zone is lower in continental transform systems that in oceanic transforms, except for the ABT and Romanche megatransforms.

The broad, lens shaped transform deformation zones of the ABT and Romanche transforms contrast with the narrow deformation zone of most oceanic transform faults. The broad deformed areas observed at these two transforms could be considered as two semistationary "transform microplates" located between major plates moving in opposite directions: the African-S. American plates in the case of Romanche and the Antarctic-Nubian plates for A. Bain. Thus, these two megatransforms constitute a new type of plate boundary, different in many respects from the classic transform boundaries of Wilson.

We discuss now possible mechanisms by which megatransforms boundaries are generated. Romanche and A. Bain are the transforms with the longest ridge/ridge offset of the entire global ridge system. Other transforms with comparable offset lengths are the Eltanin (offset ~ 800 Km) and Pitman Fracture Zone, all intersecting the East Pacific Rise. However, none of these transforms show the anomalous, broad deformation zone observed at the Romanche and A. Bain boundaries, implying that offset length is not the main or only factor in the construction of broad megatransform boundaries. However, the age offset of the Romanche and A. Bain transforms is close to 50 Ma, due to their relatively slow slip rate: by far the largest age offset of the entire mid ocean ridge system. In contrast, Pacific long-offset transforms, although with offset length comparable to that of Romanche and Andrew Bain, have a much lower age offset (< 30 Ma) due to their fast slip rate. Large age offset, rather than offset length, might then be the key ingredient required to form broad megatransform boundaries.

The subtransform thermal/rheological lithospheric structure depends on the age offset, that determines the thickness of the brittle layer defined by the 600 °C isotherm. *Ligi et al.* [2002] proposed that the extreme thickness of the lithosphere, hence its rheology, must be a factor in

determining the unusual width and complex geometry of mega-transforms. They found that long-offset (900 km) faults produce two major symmetrical faults joining the two ridge segments, with a lens-shaped area between as observed around Romanche and Andrew Bain transform faults.

4.5 St. Paul Paleomegatransform System

How stable through time are oceanic megatransforms? Some observations obtained at the St. Paul transform (equatorial Atlantic) may provide a partial answer. The St. Paul transform offsets the equatorial Mid Atlantic Ridge by ~ 580 km; its active zone is characterized by strong seismicity and volcanism. Figure 4.4A shows the bathymetry of the St. Paul region. St. Paul transform can be divided in four right echelon branches, separated by two segment of Mid-Atlantic Ridge and three small Intra-Trasform Ridges (ITRs), called in literature, from West to East, ITRC, ITRB and ITRA [*Hekinian*, 2000]. The ITRs present a narrow and deep axial valley (~ 4500 m deep), long 20-30 km; their morphology is very similar to that of the axial valleys of the slow spreading center [*Fox and Gallo,* 1984]. We inquire as to when did these short centers of crustal accretion develop, and whether they formed within a former St Paul megatransform.

According to satellite gravimetry, the trace of the St Paul transform extends to the borders of Africa and S. America, indicating that St Paul, just as Romanche, acted as a transform boundary since the early stages of opening of the equatorial Atlantic, i.e., roughly 100 Ma. On the other hand, the traces of the second order fracture zones separating the intratransform spreading centers extend up to crust about 50 Ma (Figure 4.4A) suggesting that they became active only around the time. Reconstruction of the St. Paul transform boundary before the development of the three intratransform spreading centers shows a wide (~ 90 km) lenticular deformation zone, similar those observed at the Romanche and Andrew Bain megatransforms. Moreover, given a 580 km offset length and a spreading rate of 1.5 cm/a [*Rusby and Searle,* 1993], the age offset was roughly ~ 40 Ma. This age offset is indeed higher than the ~ 30 Ma threshold indicated by numerical models of

Ligi et al [2002], above which broad megatransfomrs are predicted. It appears, therefore, that the 580 km long 90 km wide St. Paul megatransform evolved roughly 50 Ma into four "secondary" transforms offsetting ridge segments by 285, 140, 70 and 60 km, respectively. The cause of these readjustments of geometry is change of the transcurrent tectonics in a transtensive tectonics.

We created a map of a sediment thickness (Figure 4.4B) analysing about 20 multichannel seismic reflection profiles and merging the results with two map of thickness made by the Russian Institute of Moscow. The map shows a few sediments along the segments of Mid-Atlantic Ridge and along the three ITRs; in contrast, in the active and fossil transform valleys we recorded hundreds of turbite sediments. The Figure 4.4C shows the distribution of the free air anomalies in the region. Removing the contribution of the column of sea water, of the sediments thickness and of a model crust of 5 km we obtained the map of the Mantle Bouguer Anomaly (Figure 4.4D).

Finally, the figures 4.4E and 4.4F show the thermal effect of the mantle to the gravity and the distribution of the Residual Mantle Bouguer Anomalies along the St. Paul transform region. The Mantle Bouguer Anomaly and the Residual Mantle Bouguer Anomaly show very negative values along the segments of Mid-Atlantic Ridge; moreover, the values below the northern segment of Mid-Atlantic Ridge are more negative of those below the southern segment, near the Romanche FZ. Negative values are also in all the northern zone of the St. Paul transform fault: this is interesting because generally most negative values of RMBA are located not below the transform fault, which presents generally positive values (like the Romanche FZ). Finally, the Figure 4.4G shows the variation of the crustal thickness of the region. This map show the topography of the top of the mantle at 9 km of depth.

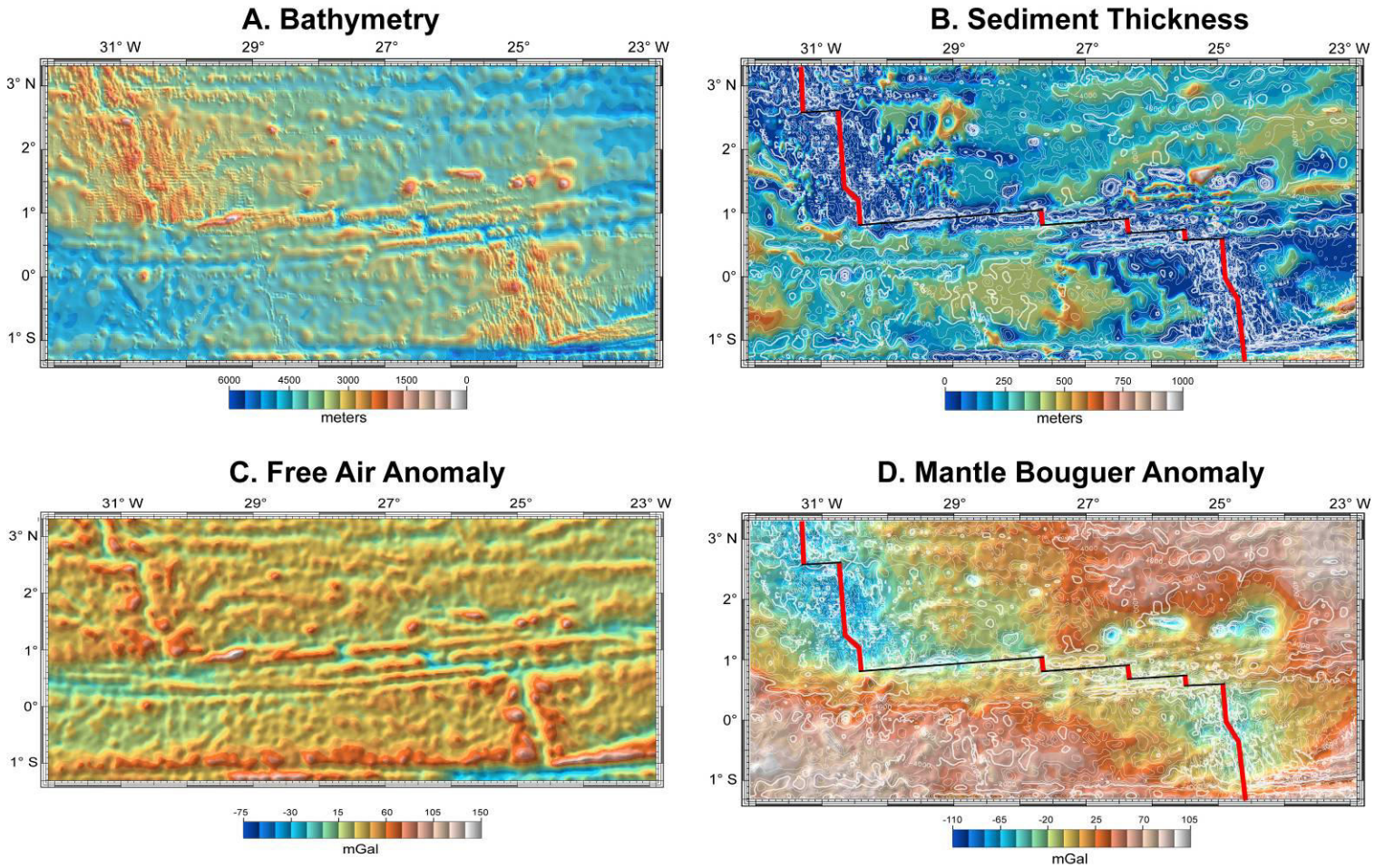

Figure 4.4 *Maps of the St. Paul transform.* **A.** *Bathymetry;* **B.** *Sediments thickness;* **C.** *Free Air Anomaly;* **D.** *Mantle Bouguer Anomaly.*

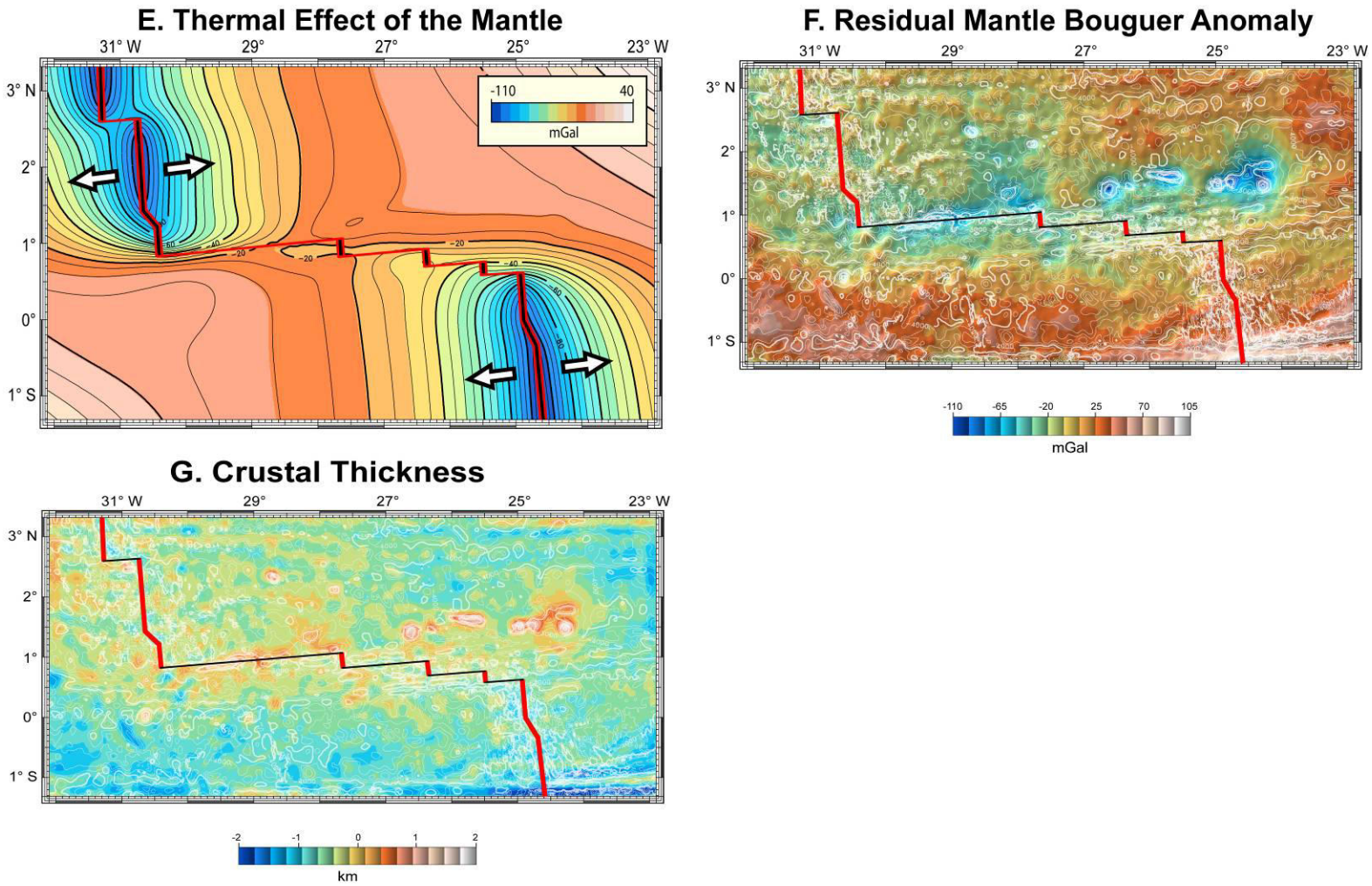

Figure 4.4 continued *Maps of the Romanche megatransform.* **E.** *Thermal effect;* **F.** *Residual Mantle Bouguer Anomaly;* **G.** *Crustal Thickness.*

The plate boundary of the St. Paul transform before the development of the three intratransform spreading centers was a broad (~ 90 km) wide lenticular deformation zone, similar to that of the Romanche and Andrew Bain megatransforms. Moreover, given a 580 km offset length and a spreading rate of 1.5 cm/a (Rusby, 1993), the age offset was ~ 40 Ma. This age offset is indeed higher than the ~ 30 Ma threshold indicated by numerical models of *Ligi et al*. [2002], above which broad megatransforms are predicted. It appears, therefore, that the 580 km long 90 km wide St. Paul megatransform evolved roughly 50 Ma into four "secondary" transform that offset ridge segments by 285, 140, 70 and 60 km, respectively. Infact, the age of formation of the three ITRs, excluding ridge's jumps and intraplate deformations, can be calculated to: ITRC, 48.5 Ma (middle Eocene), ITRB, 17 Ma (middle Miocene), ITRA, 13,5 Ma (Upper Miocene). The present structure of St. Paul Domain is the result of its evolution from a single to a multiple fracture zones, probably after reorganizations of the geometry of the plate boundary between Africa and South America. Analyzing the positions of eulerian pole of the South Atlantic in the last 60 Ma, it appears that magnetic anomaly 25 (about 58 Ma) had a progressive change in West direction.

In case of a right transform fault, like the St. Paul, a change of position in West direction will involve a transtension along the active zone and the probably formation of the three ITRs.

4.6 Conclusions

This part of my PhD thesis includes work in progress on the definition of megatransforms, a new type of plate boundary where the transform fault is characterized by a wide (~ 100 km) complex zone of strike-slip deformation. Megatransforms form in long (several hundreds km) offsets of slow and ultra-slow spreading ridges, with age offset > 30 Ma.

I briefly illustrated three examples of oceanic megatransforms, i. e., Romanche and St. Paul in equatorial Atlantic Ocean, and the Andrew Bain in the Southwest Indian Ocean.

References

Blackman, D. K., and Forsyth, D. W., 1991, Isostatic compensation of tectonic features of the Mid-Atlantic Ridge, 25°-27°20'S, *Journal of Geophysical Research, 96,* 11,741 - 11,758.

Bonatti, E. (1976), Serpentinite intrusions in the oceanic crust, *Earth Planet. Sci. Lett., 14.*

Bonatti, E. (1978), Vertical tectonism in oceanic fracture zones, *Earth Planet. Sci. Lett., 37,* 369 – 379.

Bonatti, E., M. Ligi, L. Gasperini, A. Peyve, Y. Raznitsin, and Y. J. Chen (1994), Transform migration and vertical tectonics at the Romanche fracture zone, equatorial Atlantic, *Journal of Geophysical Research, 99,* 21, 779 - 802.

Cande, S. C., J. L. LaBraque, and W. F. Haxby (1988), Plate kinematics of the South Atlantic: isochron C34 to present, *J. Geophys. Res., 93,*13479–13492.

Detrick, R. S., H. D. Needham, and V. Renard (1995), Gravity anomalies and crustal thickness variations along the Mid-Atlantic Ridge between 33°N and 40°N, *Journal of Geophysical Research*, 100, doi: 10.1029/94JB02649.

Fox, J. P., and D. Gallo (1984), A tectonic model for Ridge - Transform – Ridge plate boundaries, implications for the structure of oceanic lithosphere, *Tectonophysics, 104,* 205 – 242.

Gasperini L., E. Bonatti, D. Brunelli, G. Carrara, A. Cipriani, P. Fabretti, D. Gilod, M. Ligi, A. Peyve, S. Skolotnev, S. Susini, P. Tartarotti and N. Turko (1997), New data on the geology of the Romanche F.Z., equatorial Atlantic: PRIMAR-96 cruise report, *G. Geol., 59,* 3–18.

Grindlay, N. R., J. A. Madsen, C. Rommevaux, J. Sclater, and S. Murphy (1996), Southwest Indian Ridge 158 E–358 E: A geophysical investigation of an ultra-slow spreading mid-ocean ridge system, *InterRidge, 5,* 7–11.

Haxby, W. F. (1987), Gravity field of the World's Oceans, NOAA, Boulder, Colo.

Hekinian ,R., T. Juteau, E. Gràcia, B. Sichler, S. Sichel, G. Udintsev, R. Apprioual, and M. Ligi (2000), Submersible observations of equatorial atlantic mantle: the st. paul fracture zone region, *Marine Geophysical Researches, 21,* 529 – 560.

Kuo, B., and D. W. Forsyth (1988), Gravity Anomalies of the Ridge-Transform System in the South Atlantic Between 31 and 34.5 ~ S: Upwelling Centers and Variations in Crustal Thickness, *Mar. Geophys. Res., 10,* 205 – 232.

Ligi, M., and G. Bortoluzzi (1989), PLOTMAP: geophysical and geological applications of good standard quality cartographic software: *Comput. Geosci., 15*, 519–585.

Ligi, M., E. Bonatti, L. Gasperini, and A. N. B. Poliakov (2002), Oceanic broad multifault transform plate boundaries, *Geology, 30,* 11–14.

Lin, J., G. M. Purdy, H. Schouten, J.-C. Sempéré, C. and Zervas (1990), Evidence from gravity data for focused magmatic accretion along the Mid-Atlantic Ridge, *Nature, 344,* 627–632.

Lin J., and J. P. Morgan (1992), The spreading rate dependence of three-dimensional mid-ocean ridge gravity structure, *Geophysical Research Letters, 19,* 13 – 16.

Michael, P. J., C. H. Langmuir, H. J. B. Dick, J. E. Snow, S. L. Goldsteink, D. W. Graham, K. Lehnertk, G. Kurras, W. Jokatq, R. Mu¨he, and H. N. Edmonds (2003), Magmatic and amagmatic seafloor generation at the ultraslow-spreading Gakkel ridge, Arctic Ocean, *Nature, 423,* 956 – 961.

Morris, E., and Detrick, R.S. (1991), Three dimensional analysis of gravity anomalies in the mark area, mid-atlantic ridge 23°N, *Journal of Geophysical Research, 96,* doi: 10.1029/90JB02173.

Okal, E.A., and S. Stein (1987), The 1942 Southwest Indian Ocean Ridge earthquake: Largest ever recorded on an oceanic transform, *Geophys. Res. Letts., 14,* 147-150,

Phipps Morgan, J., and D.W Forsyth (1988), Three-dimensional flow and temperature perturbations due to a transform offset: Effects on oceanic crustal and upper mantle structure, *Journal of Geophysical Research, 93,* 2955–2966.

Prince, R. A., and Forsyth (1988), Horizontal Extent of Anomalously Thin Crust near the Vema Fracture Zone from the Three-Dimensional Analysis of Gravity Anomalies, *Geophys. Res., 93,* 8051 – 8063.

Rusby, R.I., and R.C. Searle (1993), Intraplate thrusting near the Easter microplate, *Geology, 21,* 311 – 314.

Sclater, J. G., N. R.Grindlay, J.A. Madsen, and C. Rommevaux-Jestin (2005), Tectonic interpretation of the Andrew Bain transform fault: Southwest Indian Ocean, *Geochemistry Geophysics Geosystems, 6,* doi: 10.1029/2005GC000951.

Sykes, L. R. (1967), Mechanism of earthquakes and nature of faulting on the Mid-Atlantic Ridge, *J. Geoph. Res., 72,* 2131 – 2153.

Wessel, P., and W. H. F. Smith (1995), New improved version of the Generic Mapping Tools released: *EOS, Transaction of American Geophysical Union*, *79*, 579.

Wilson, J. Y. (1965), A new class of faults and their bearing on continental drifts, *Nature, 207*, 343 – 347.

Chapter 5

Non-volcanic tectonic islands in ancient and modern oceans

C. Palmiotto, L. Corda, M. Ligi, A. Cipriani, H. J. B. Dick, E. Douville, L. Gasperini, P. Montagna, F. Thil, A. Borsetti, B. Balestra, E. Bonatti

Published in Geochemistry, Geophysics, Geosystems, 14, p.4698-4717, 2013.

Abstract

Most oceanic islands are due to excess volcanism caused by thermal and/or compositional mantle melting anomalies. We call attention here to another class of oceanic islands, due not to volcanism but to vertical motions of blocks of oceanic lithosphere related to transform tectonics. Sunken tectonic islands capped by carbonate platforms have been previously identified along the Vema and Romanche transforms in the equatorial Atlantic. We reprocessed seismic reflection lines, did new facies analyses and $^{87}Sr/^{86}Sr$ dating of carbonate samples from the carbonate platforms. A 50-km-long narrow paleo-island flanking the Vema transform, underwent subsidence, erosion and truncation at sealevel; it was then capped by a 500 m thick carbonate platform dated by $^{87}Sr/^{86}Sr$ at ~11-10 Ma. Three former islands on the crest of the Romanche transverse ridge are now at ~900 m bsl; they show horizontal truncated surfaces of oceanic crust capped by ~300 m thick carbonate platforms, with 10 to 6 Ma Sr isotopic ages. These sunken islands formed due to vertical tectonics related to transtension/transpression along long-offset slow-slip transforms. Another tectonic sunken island is Atlantis Bank, an uplifted gabbroic block along the Atlantis II transform (SW Indian Ridge) ~700 m bsl. A modern tectonic island is St Peter and St Paul Rocks, a rising slab of upper mantle located at the St Paul transform (Equatorial Atlantic). “Cold” tectonic islands contrast with “hot” volcanic islands related to mantle thermal and/or compositional anomalies along accretionary boundaries and within oceanic plates, or to supra-subduction mantle melting that gives rise to islands arcs.

5.1 Introduction

Oceanic islands, such as those scattered across the Pacific ocean, can be viewed as anomalies relative to the "depth versus square root of age" law [*Sclater et al.,* 1971], derived from cooling of oceanic plates as they move away from mid ocean ridges. Since *Wilson* [1963] and *Morgan* [1972], oceanic islands have generally been regarded as due to excess volcanism, related to mantle thermal and/or compositional anomalies. In the Pacific they are generally aligned parallel to the motion of the Pacific plate (a classic example is the Hawaiian-Emperor Chain), probably because they form as the plate transits above a quasi-stationary plume. As a volcanic island leaves the plume site, volcanism ceases, the plate cools, and the island subsides and sinks below sea level, in a mechanism hinted at already by *Darwin* [1844].

We describe here a different type of oceanic islands, i.e., non-volcanic, tectonic islands formed by vertical motions of slivers of oceanic lithosphere due to transform tectonics. We will discuss old and new data on sunken tectonic islands capped by carbonate platforms detected close to equatorial Atlantic transform faults (Figure 5.1a and [*Bonatti et al.*, 1977; 1983; 1994a; 1994b]). We reconstructed their origin, evolution and demise based on reprocessed seismic reflection profiles, and on new facies analysis as well as paleontological and Sr isotopic dating of carbonate samples. We will also describe an island formed by uplift and subsidence of a gabbroic block along the Atlantis II transform in the SW Indian Ridge (Figure 5.1b), and a present-day tectonic island, i.e., St. Peter-Paul Rocks in the equatorial Atlantic (Figure 5.1a). These observations on present-day and fossil tectonic islands will lead to a simple classification of oceanic islands based on their origin.

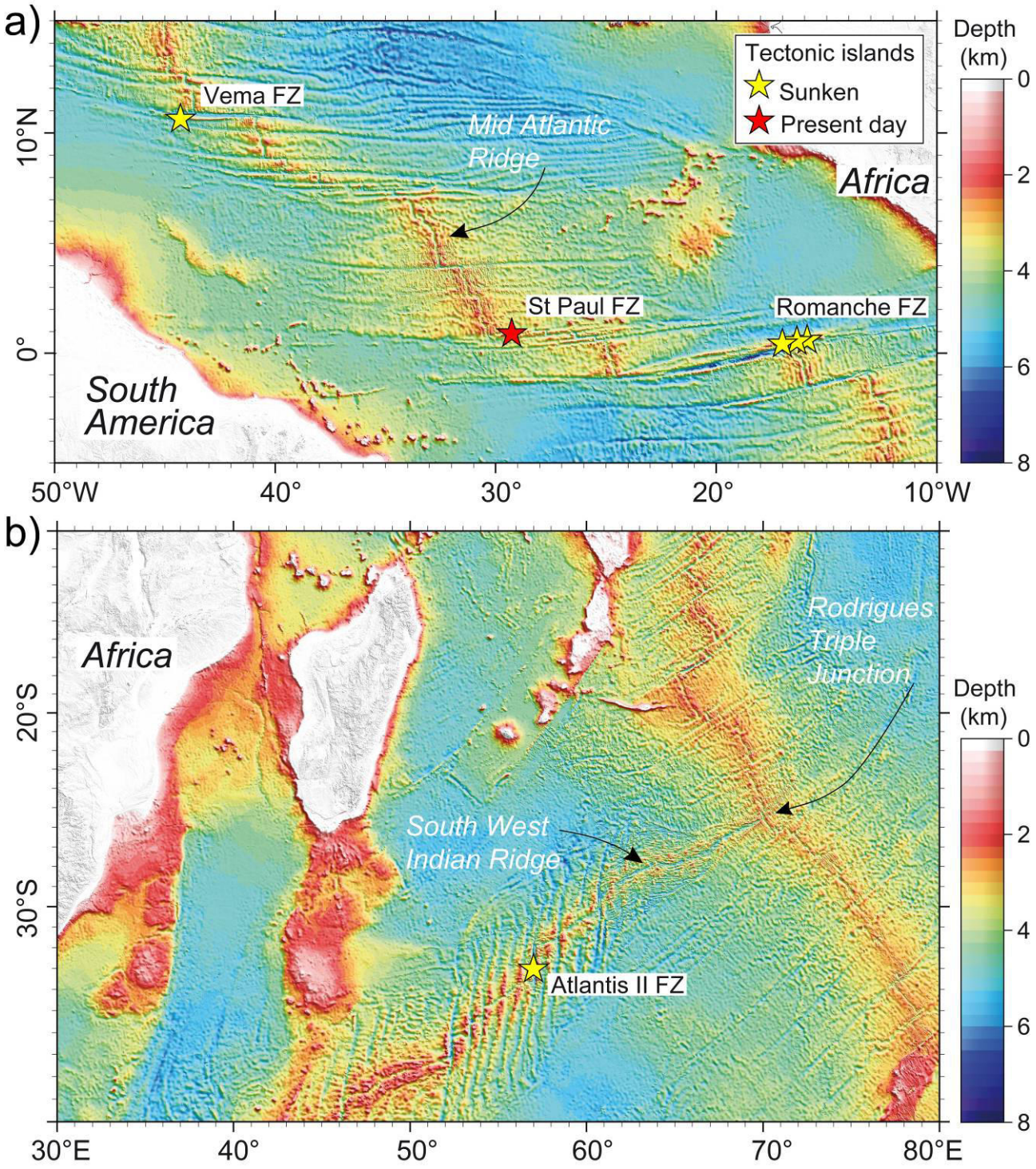

Figure 5.1 a) *Geographical and geological setting of the Vema, St. Paul and Romanche fracture zones (FZs) along the equatorial Mid Atlantic Ridge;* **b)** *geographical and geological setting of the Atlantis II transform along the South West Indian Ridge. Bathymetry data are from General Bathymetric Chart of the Oceans (GEBCO_08 grid). Stars indicate locations of tectonic islands (yellow, sunken; red, modern).*

5.2 Methods

5.2.1 Geophysics

Bathymetric and seismic reflection data summarized in this paper were obtained from the Vema and Romanche fracture zones during a number of expeditions with research ships Vema and Conrad (LDEO), Pillsbury and Gillis (University of Miami), Explora (OGS), Strakhov and Gelendzhik, operated by ISMAR–CNR, Italy. Details on acquisition and processing parameters can be found in *Fabretti et al.* [1998] and *Bonatti et al.* [2005] for the Vema surveys, and in *Bonatti et al.* [1994] and *Gasperini et al.* [1997a] for the Romanche surveys. Seismic reflection data obtained from the Vema and Romanche platforms have been reprocessed in order to carry out post stack depth migration. Post stack depth migration was achieved by a finite difference approximation to the wave equation (MIGZWE), using acoustic velocities derived from analysis of reflected/refracted arrivals by fitting P-wave amplitudes and arrival times of recorded shot gathers with those of synthetic gathers obtained by forward two-points ray-tracing [*Cerveny et al.*, 1988]. Additional sequences were applied to remove bottom surface multiples using a 2D SRME (Surface-Related Multiple Elimination) technique and adaptive filters; and to attenuate random and coherent noise, by filtering in the common shot, offset, receiver domains as well as f-k and tau-p domains.

Data for Atlantis Bank were obtained on site surveys for ODP and IODP Legs 118 and 176. These included dredging, magnetics, narrow beam echo sounding and the Canadian ROV ROPOS from the British Antarctic Survey ship James Clark Ross Cruise 31, and the British Geologic Survey diamond coring drills. The Japanese Agency for Marine-Earth Science and Technology RV Yokosuka deployed the DSRV Shinkai 6500 on two cruises (MODE98 Leg 4 and Cruise YK01-14) and RV Kaire deployed the ROV Kaiko (MODE 2000 Leg 4).

Spatial analysis and mapping were performed using the GMT [*Wessel and Smith*, 1995] and PLOTMAP [*Ligi and Bortoluzzi*, 1989] packages.

5.2.2 Facies Analysis

Facies analyses were carried out by macroscopic and binocular microscope examination of carbonate samples and by thin section studies under the petrographic microscope.

5.2.3 Strontium Isotope Analysis

Ages of the carbonates were estimated by Sr isotopes measured by thermal ionization mass spectrometry (TIMS) and Multi-Collector Inductively Coupled Plasma Mass Spectrometry (MC-ICPMS). Carbonate chips (35 to 70 mg) chosen from the interior, least altered parts of the sample, were handpicked and mechanically cleaned using a dental drill in order to remove fine-grained sediments or other visible contaminants. The sub-samples were inspected under a binocular microscope and then crushed into a powder with an agate mortar and pestle.

5.2.3.1. TIMS

The majority of the samples (28) were transferred to acid-cleaned bullets and rinsed three times with quartz-distilled water and one time with methanol in ultrasonic bath. Powders were then leached with 0.05N HCl. Bulk samples were dissolved in double distilled 3N HNO_3 and Sr was separated using standard ion exchange techniques, using Eichrom Sr-SPEC resins. Sr isotopes were measured by dynamic multi-collection on a VG 54 TIMS at Lamont-Doherty Earth Observatory. The $^{87}Sr/^{86}Sr$ ratios were normalized to a stable isotopic $^{86}Sr/^{88}Sr$ ratio of 0.1194 and corrected for machine bias to a NBS-987 value of 0.71024±0.00004 [*Terakado et al.,* 1988]. Separate analyses of NBS-987 standard gave a mean $^{87}Sr/^{86}Sr$ value of 0.710264±0.000016 (2σ, n = 25, corresponding to an external reproducibility of 22 ppm).

5.2.3.2 MC-ICP-MS

The remaining 19 samples were rinsed three times with MilliQ water in acid-cleaned bullets before leaching with 0.3% acetic acid to remove 30-40% of $CaCO_3$. This first leaching step is designed to remove ions from exchangeable or leachable sites on the mineral surfaces. The remaining material was rinsed with MilliQ water and leached again with 0.4% acetic acid to remove 30% of $CaCO_3$ for analysis, following a procedure by *Li et al*. [2011]. The supernatant solutions were evaporated and adjusted to 3N HNO_3 for ion exchange chromatography. The solutions were loaded into 300 µl columns containing 100-150 µm bead size Eichrom Sr-SPEC resin to remove matrix and isolate Sr from the interfering elements Ca, Rb, REE. The columns were pre-flushed with 1 ml 3N HNO_3 and 3 ml MilliQ-water and conditioned using 1 ml 3N HNO_3. Strontium was eluted from the columns with 2.5 ml MilliQ-water and each solution was adjusted to 0.5N HNO_3 for elemental and isotopic measurements.

Strontium isotope ratios were measured using the MC-ICPMS ThermoScientific Neptune^{Plus} at LSCE (Gif-sur-Yvette, France). Prior to the extraction of Sr for isotopic analysis a small aliquot of each sample solution was analysed for Ca, Sr, Rb and REE concentrations using a quadrupole ICP-MS (Xseries^{II} Thermo Fisher Scientific). The Ca/Sr mass ratios ranged between 40 and 1800. After chemistry, Ca/Sr mass ratios were reduced to 0.8-1.2 and Rb concentrations were systematically below the detection limit. All the solutions were then diluted to 50 ppb Sr and introduced into the Neptune using an ESI-APEX desolvating system and a 100 µl/min nebulizer. The sensitivity for 50 ppb Sr solution was 7 V on ^{88}Sr peak and the blank level (0.5N HNO_3) was 0.01 V. The samples and standards were analysed in a static multi-collection mode in a single block of 50 cycles with an integration time of 8 seconds per cycle. The instrumental mass fractionation was corrected for by using a stable isotopic $^{86}Sr/^{88}Sr$ ratio of 0.1194 and an exponential law. The efficient chromatographic purification eliminated most of the Ca (Ca/Sr ratio 0.8-1.2) and Rb. No isobaric corrections for Ca dimers and argides were required and only minor corrections for ^{87}Rb to

^{87}Sr were considered. A correction was also applied for krypton isobaric interferences. The effects of double charged REE on the Sr isotope masses were not considered due to the very low absolute REE abundances in the carbonates and the chromatographic purification. Repeated measurements of strontium isotope standard NBS-987 during the analytical session yielded a mean $^{87}Sr/^{86}Sr$ value of 0.710269±0.000014 (2σSD, n = 19, corresponding to an external reproducibility of 20 ppm). The $^{87}Sr/^{86}Sr$ ratio for all the samples was corrected for instrumental bias to an accepted value for NBS-987 of 0.71024±0.00004 [*Terakado et al.,* 1988]. All the $^{87}Sr/^{86}Sr$ ratios were converted into numerical ages using the regression curves LOWESS look-up table version 4: 08/04 [revised from *McArthur et al.,* 2001].

5.3 Results

5.3.1 Sunken Island at the Vema Transform

The Mid Atlantic Ridge is offset at 11° N by the ~320 km-long Vema transform (Figure 2a). A ~5 km deep transform valley is filled by over 1 km thick horizontally stratified turbidite deposits of probable South American derivation (DSDP Sites 216 and 353). A transverse ridge runs parallel to the transform on its southern side (Figure 2a); it consists of a sliver of flexured and uplifted oceanic lithosphere [*Bonatti et al.,* 2003, 2005]. Multichannel seismic reflection profiles along the summit of the transverse ridge imaged on its western, shallowest portion a strong horizontal reflector (Reflector B) extending along the crest for roughly 50 km (Figure 3a). This reflector is capped by a ~500 meters thick unit. The unit above Reflector B gives acoustic velocities in the range 2-3 km/sec, consistent with carbonate rocks. The seismic profile shows stratification above reflection B and a rather incoherent pattern below it (Figure 3a), suggesting that Reflector B corresponds to the interface between the limestones and the top of the oceanic crust, an interpretation confirmed by extensive sampling [*Bonatti et al.,* 1983, 1994a]. Acoustic velocities jump to ~4 km/sec immediately below Reflector B, in line with the prevalence of upper crustal

basalts. They then increase close to 5.25 km/sec ~200 m below Reflector B, consistent with the dominance of lower crustal doleritic-gabbroic rocks (Figure 3).

Seismic reflection data and the study of carbonate samples suggest that: (a) horizontal Reflector B represents a surface where the top of the basaltic oceanic crust was eroded and truncated at a former sea level. This implies that the summit of the Vema transverse ridge emerged at some stage in the past above sea level, i.e., formed an island; (b) the unit above reflector B represents a 400-500 m thick carbonate platform, that grew on the eroded surface during subsidence; (c) an horizontal reflector (Reflector A) observed within the carbonate platform roughly 100 m below the top (Figure 3a), suggests that the growth of the platform was interrupted by a second younger sea level erosional event, possibly caused by eustatic sealevel changes superimposed on lithospheric thermal subsidence. Reconstructions of sea level changes [*Haq et al.,* 1987; *Abreu and Anderson,* 1998] show a strong sealevel drop within the 12-10 Ma time interval, i.e., within the Sr isotopic age range for the Vema carbonate platform; (d) ray tracing forward modelling (Figure 3) suggests that the thickness of the upper basaltic crust below erosional surface B is reduced to ~200 m due probably to mostly subaerial erosion of the upper ~1 km of basaltic crust; consequently, lower crustal units (dyke complex and gabbros) are found close to the top of the igneous section; (e) a 10 km long stretch of horizontal reflector B was detected on the crest of the Vema transverse ridge roughly 2 km east of the eastern edge of the main portion of the reflector (Figure 3a). This short stretch of reflector B is not capped by a carbonate unit but lies close to the present day seafloor. It probably represents the erosional surface of a small fragment of upper oceanic crust, i.e., a former small island that emerged to the east of the longer Vema island.

5.3.1.1. Vema Carbonate Platform: Facies Analysis

Facies analysis and age determinations of samples obtained before 1983 are in *Bonatti et al.* [1983]. Following restudy of some of the old samples and of a study of new post-1983 cruise

samples, we recognized 6 main facies (Table 1). Facies V1 (Figure 2b) and V2 have been recovered from the western portion of the Vema platform; facies V1, V3 (Figure 2c), V4, V5 from the eastern portion of the platform; facies V1 and V6 from the central part of the platform. Samples from different sites along the Vema carbonate platform, although characterized by different textures, are dominated by the same biota assemblages, i.e.: perforate larger benthic foraminifera, red algae and rare corals. No real reef facies have been recognized. We suggest a ramp or a flat-topped shelf geometry for the platform.

Nannofossil calcareous biostratigraphy on three samples gives ages older than 9.4 Ma and 2 Ma (see online *Supporting Material*).

The occurrence in the western part of the platform of sedimentary dykes filled by shallow-water carbonates and the intense dissolution of calcitic Miogypsina tests provide evidence of fresh water diagenesis, suggesting subaerial exposure. The emergence of the platform was accompanied and/or followed by tensional cracking, fissuring and leaching of the early consolidated limestones. Subsequent shallow-water skeletal deposits (related to subsidence and/or sea-level rise) penetrated the tensional cracks and dykes. The horizontal seismic Reflector A, identified within the carbonate platform, probably records this emergence episode (Figure 3a).

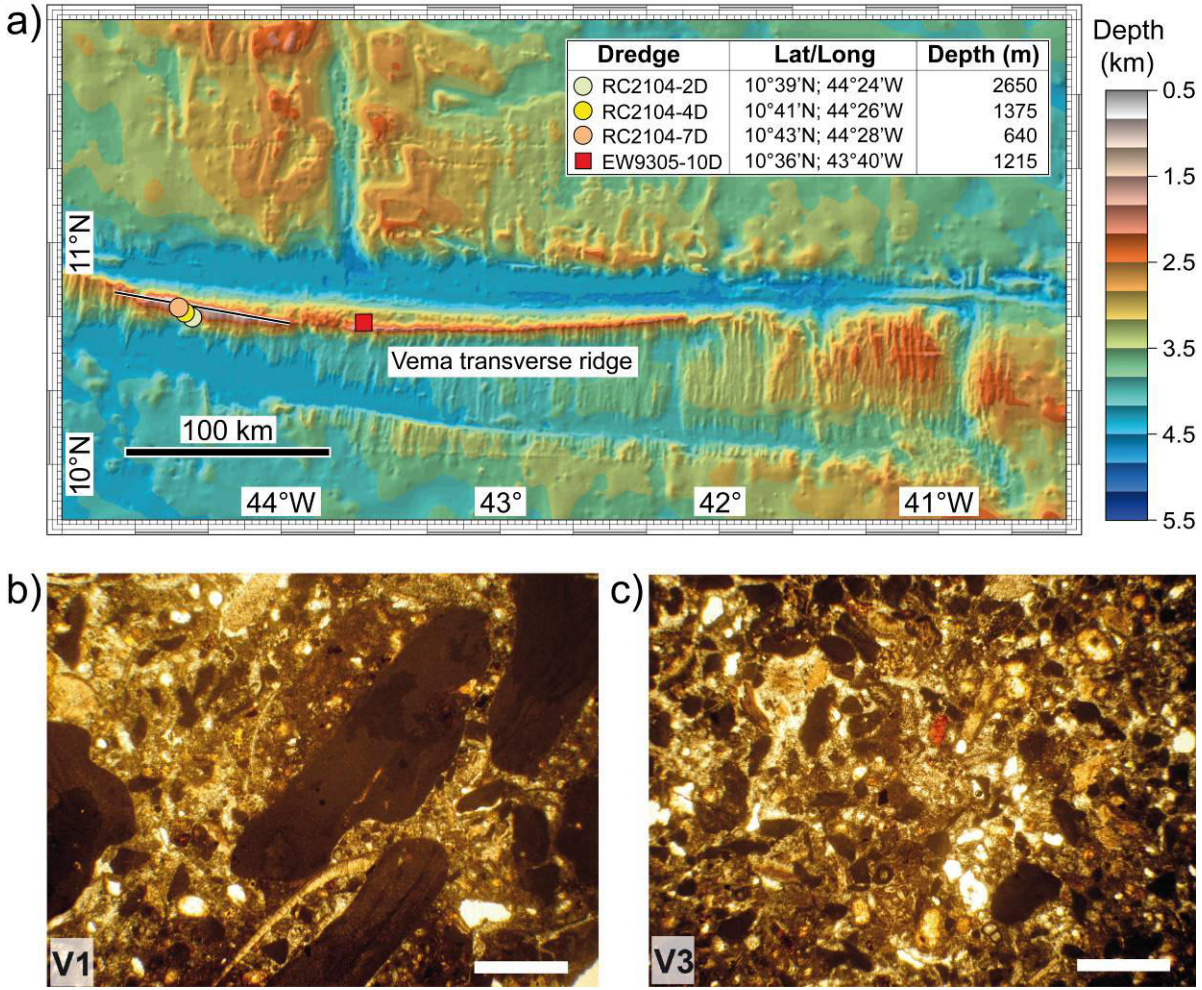

Figure 5.2 *The Vema transform fault and photomicrographs of limestone samples from the Vema transverse ridge.* **a)** *Bathymetry of the Vema region, data from Bonatti et al. [2003]. Red square and circles indicate locations of studied samples. Black solid line marks location of the multichannel seismic line VEMA-02, shown in Figure 3.* **b)** *Facies V1: red-algae floatstone with fine-grained bioclastic matrix. (c) Facies V3: moderately well-sorted bioclastic packstone, rich in red-algae fragments. Scale bar = 1 mm.*

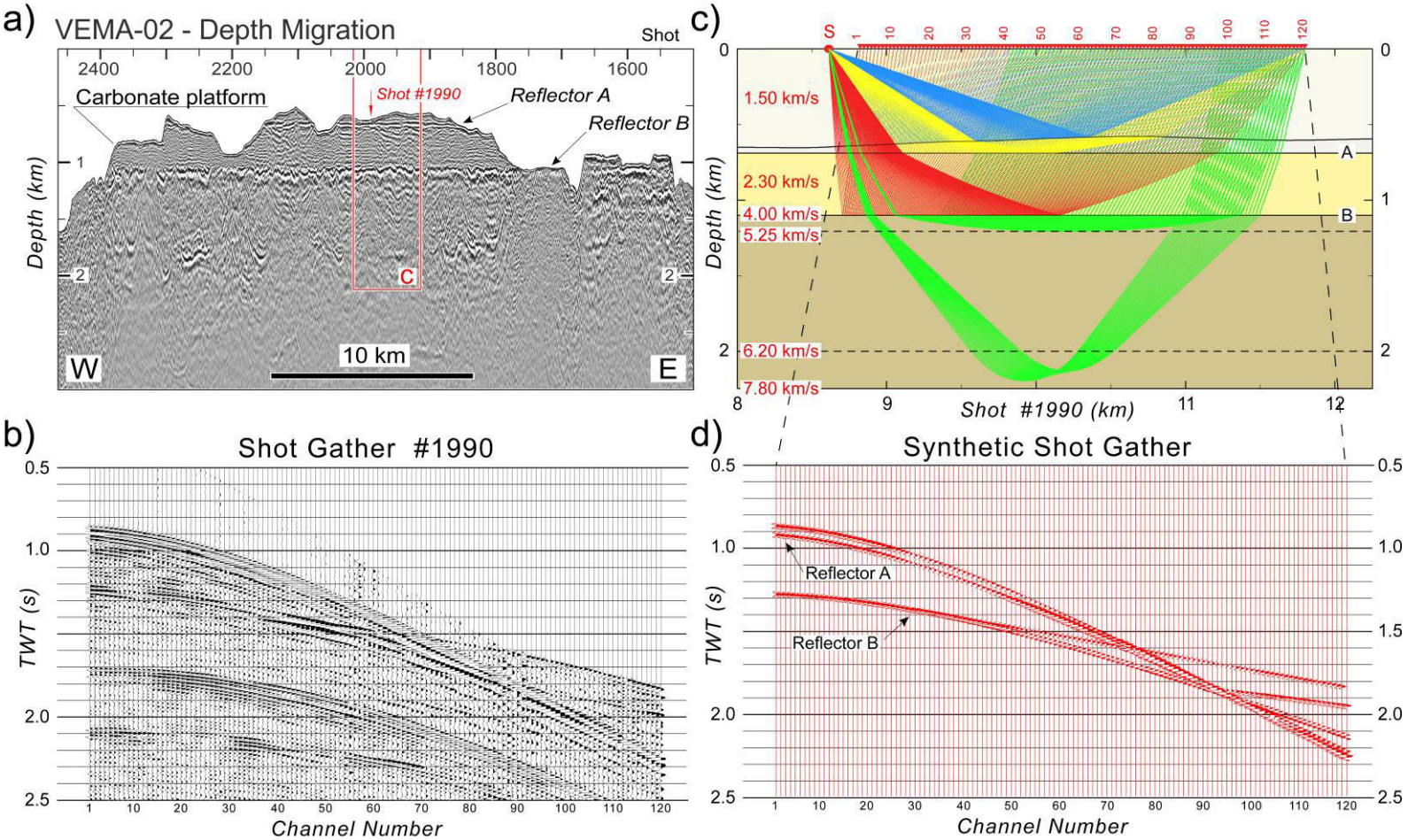

Figure 5.3 a) *Depth migrated seismic line VEMA-02 running along the crest of the Vema transverse ridge. The velocity model used in the post-stack depth migration has been obtained constraining P-wave velocities by forward modelling. Ray-tracing modelling suggests that most of the oceanic upper crust has been eroded with lower crustal gabbro/dolerite and mantle peridotites very close to the base of limestones (Reflector B). Labelled red box indicates location of geological model in Figure 3c.* **b)** *Recorded shot gather.* **c)** *Geological model, seismic velocities and ray paths. Two point ray tracing boundary problem was solved by using paraxial rays in Cartesian coordinates [Cerveny et al., 1988]. Thick solid lines mark seismic reflectors; dashed lines mark layer boundaries with vertical gradient of seismic velocities.* **d)** *Synthetic shot gather*

5.3.1.2 Sr Isotopic Ages of Vema's Limestones

We took advantage of the temporal variations of seawater $^{87}Sr/^{86}Sr$ ratio [*Edmond, 1992*] to estimate the age of the Vema carbonates. The ratio $^{87}Sr/^{86}Sr$ was determined in a number of carbonate samples, and the corresponding ages were derived from regression curves of *Mc Arthur et al.* [2001] and *Mc Arthur and Howarth* [2004]. Given possible post-depositional recrystallization of the carbonates, as well as possible admixture with carbonates younger than the original platform phases, we surmise that the oldest calculated ages are closest to the real age of the platform. The maximum ages fall around 11 Ma (Table 2). This age is close to the age estimated for the transtensional flexure and uplift event of a lithospheric slab at the southern side of the Vema transform [*Bonatti et al.,* 2005].

5.3.2 Sunken Islands at the Romanche Transform

The Mid Atlantic Ridge is offset near the equator by the ~950 km Romanche transform, the longest transform of the entire mid ocean ridge system (Figure 4a). Given its length and slip rate, the age contrast at the ridge/transform intersections is close to 50 Ma. The transform deformation zone is peculiar in so far as it is lens-shaped, with an up to 120 km width [*Ligi et al.*, 2002]. This wide and complex transform deformation zone, contrasting with the narrow (a few km) deformation zone observed in most oceanic transforms, has led to the concept of oceanic "megatransforms" [*Ligi et al.,* 2002]. A prominent "transverse ridge" runs E-W parallel to the transform in the African plate opposite to the eastern ridge/transform intersection; it extends outside the active transform on the northern side of the aseismic fracture zone (Figure 4a). The transverse ridge probably originated from flexure and uplift of slivers of oceanic lithosphere originally generated at the western segment of the Mid Atlantic Ridge. Given a half spreading rate of 16 mm/a [*Cande et al.,* 1988], the age of this portion of the transverse ridge basaltic crust is over 50 Ma, with some uncertainty due to

temporal variations of spreading rate and offset length, as well as to possible migrations of the transform boundary. Transpressive deformation may also have played a role in shaping the Romanche transverse ridge, as suggested by folding and thrusting observed in lower Cretaceous to Eocene deposits immediately E of the eastern ridge-transform intersection [*Bonatti et al.,*1996; *Gasperini et al.,* 2001].

The summit of this portion of the transverse ridge reaches ~875 m below sea level, a roughly 4 km topographic anomaly relative to the oceanic lithosphere thermal subsidence curve. Multichannel seismic reflection profiles taken along the crest of the transverse ridge revealed three elevated, roughly 50 km long segments, each underlain by a strong horizontal reflector, capped by units that, based on sampling, consist of carbonate platforms [*Bonatti et al.,* 1994; *Gasperini et al.,* 1997b]. They have been identified from W to E as Romanche sunken islands A, B and C (Figure 5). Sampling of the slopes below Reflectors R_1 (Paleoisland A), R_2 (Paleoisland B) and R_3 (Paleoisland C) released oceanic basalts and dolerites, suggesting that the three horizontal reflectors represent surfaces of erosion at a sea level of the upper basaltic oceanic crust, that had been uplifted above sea level, forming three islands. Assuming a P-wave acoustic velocity of 2 km/s for the limestones, a thickness ranging between 200 and 300 meters can be estimated for the carbonate platforms.

Paleoisland A (Figure 4b) is ~32 km long in an E-W direction, and ~6.5 km wide. It displays a ~300 m thick carbonate platform; stratified sediments prograde westward from the platform, into a ~5 km wide shallow basin bound to the west by a ~70 m high and ~450 m wide non transparent relief that, based on detailed morpho-bathymetry of *Gasperini et al.* [1997b] may represent a continuous bank within the main platform.

Paleoisland B (Figure 4c) is the smallest (about 5 km wide); it has an irregular morphology probably determined in part by crustal erosional collapse. This relief shows a strong horizontal reflector (R_2) below an about 250 m thick carbonate platform.

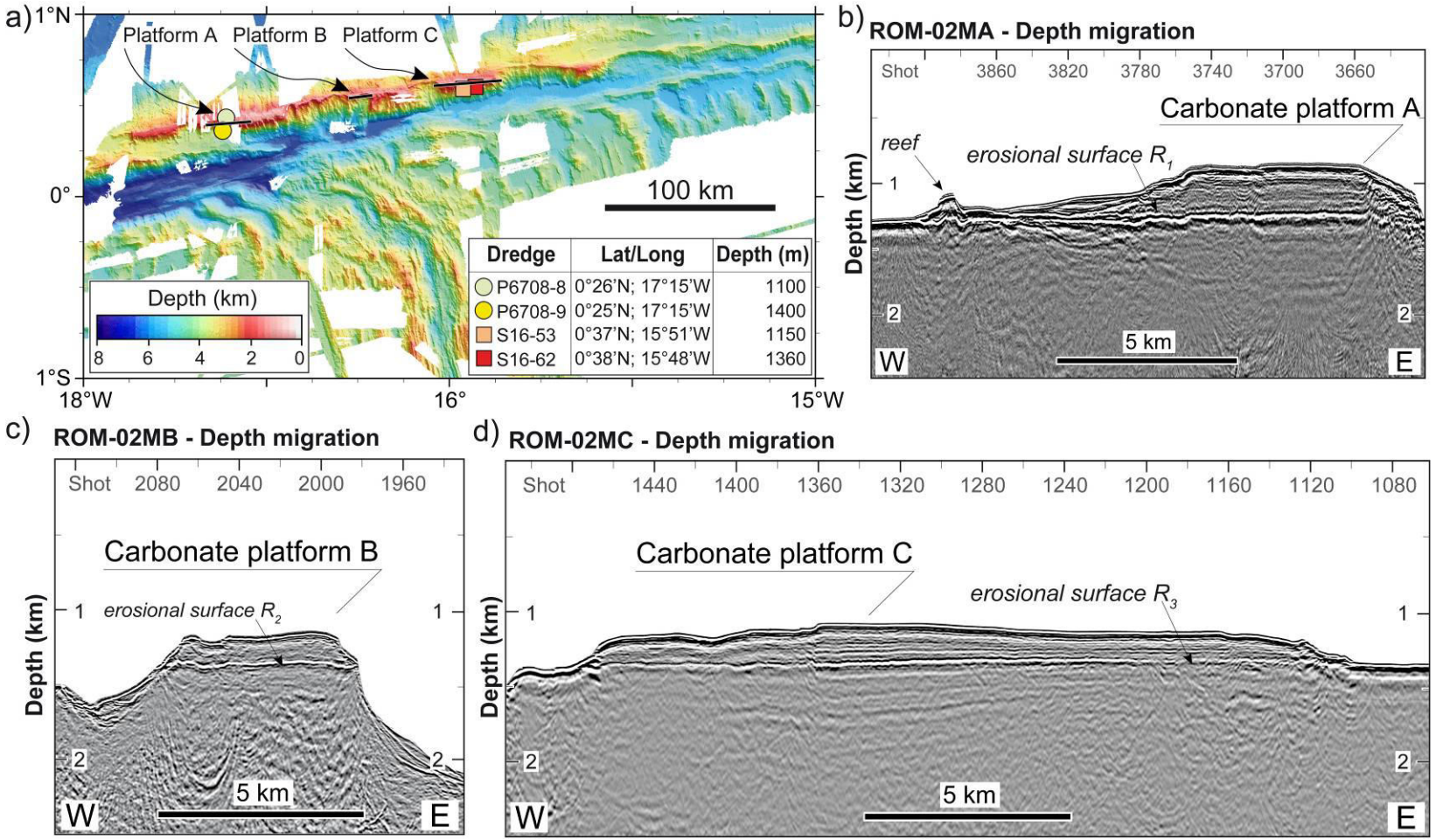

Figure 5.4 The Romanche Megatransform. **a)** Multibeam bathymetry of the Romanche eastern ridge-transform intersection and of the northern transverse ridge obtained by merging our data [*Gasperini et al.*, 1997a] with those of EQUAMARGE2, CONADAK and ROMANCHE1 cruises (IFREMER). Circles and squares indicate locations of studied samples from Platform A and Platform C, respectively. Multichannel seismic profiles (black lines) shown in Figures 4b, 4c and 4d are also indicated; **b)** seismic profile ROM-02MA (Paleoisland A); **c)** ROM-02MB (Paleoisland B); **d)** ROM-02MC (Paleoisland C).

Paleoisland C has a very regular morphology (Figure 4d); it is about 25 km long (E-W), 1.5 km wide (N-S) and it displays a ~300 m thick carbonate platform resting on horizontal reflector (R_3). Reflector R_3 lies close to the seafloor at the eastern edge of the relief indicating a portion of erosional surface without a significant carbonate cap.

5.3.2.1 Romanche Carbonate Platforms: Facies Analysis

Limestone samples recovered from Paleoislands A and C were studied already by *Bonatti et al*. [1977]. Based on a new study of these and other samples we recognized eight main facies (Table 1 and Figure 5).

The main biota components of the Romanche carbonate platforms are: perforate larger benthic foraminifera, red algae and corals (mostly *Porites).* Significant additional components are ooids, that show tangential aragonitic needles at the SEM. These components are similar to those observed at the Vema carbonate platform. Textures, structures and biota assemblages suggest a rimmed shelf with a variety of facies from subtidal to intertidal, and from the margin (both oolitic shoals and framestone fabric) up to the slope of the platform. No typical lagoon facies material was observed.

The Romanche carbonate platforms record a prolonged period of exposure (documented by fresh-water diagenesis), non-deposition and lithification. Subsequent extensional tectonics promoted fracturing and formation of neptunian dykes that were filled by new transgressive shallow-water sediments. Paleoisland A and C show contrasting facies distribution. Oolitic sands are dominant in the westernmost Paleoisland A. Coated grains as observed on Paleoisland A occur normally when salinity exceeds 35.8 $^{0}/_{00}$ [*Lees,* 1975]; thus, they are not common in carbonates from the equatorial region. The easternmost edge of Paleoisland C, on the contrary, is rich in coral reef materials. The intense phosphatization of the oolitic facies and the unusual presence of

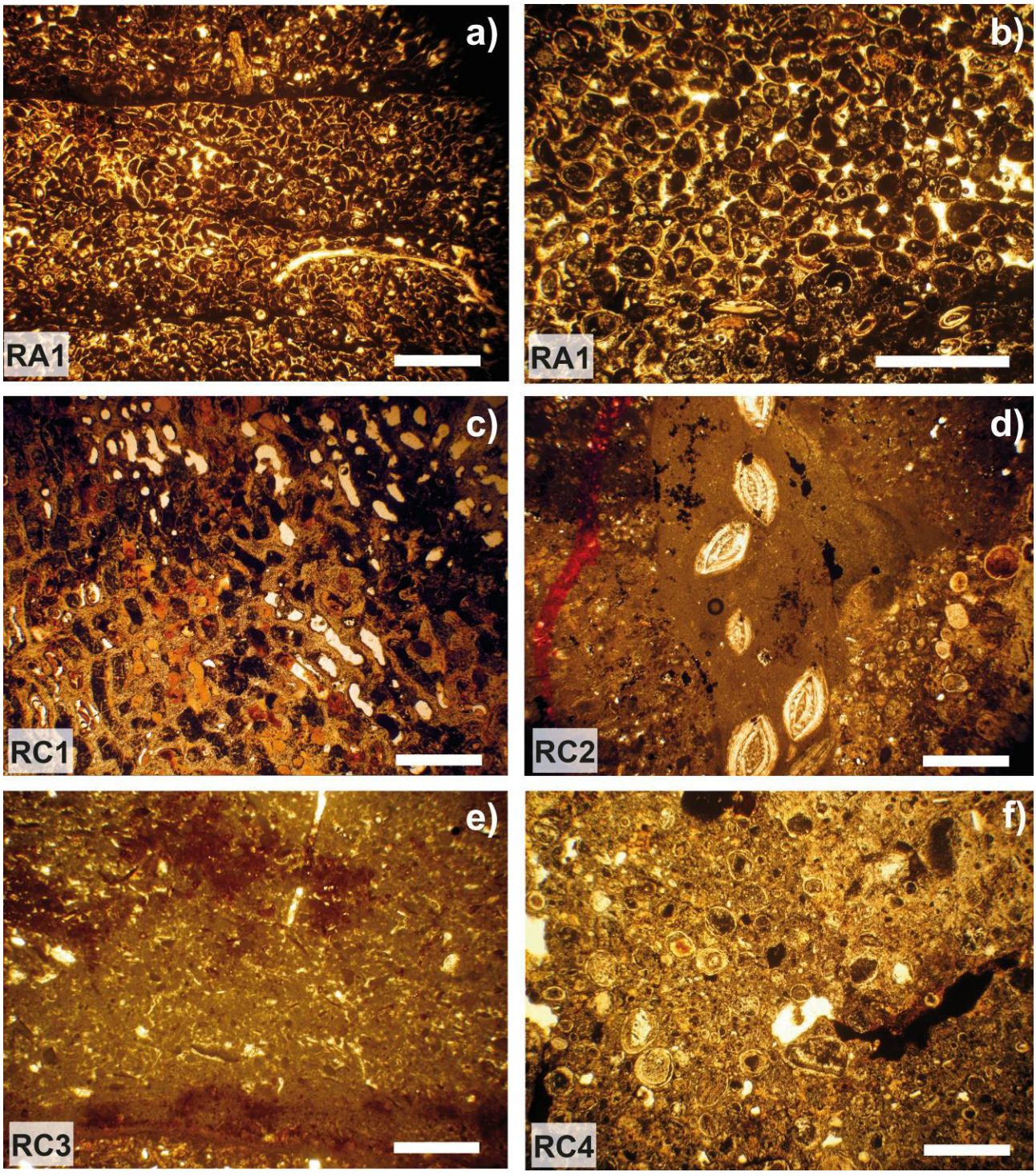

Figure 5.5 *Photomicrographs of some carbonate facies of Romanche platforms. Facies RA1:* **a)** *laminae of oolitic grainstone separated by microbial mats; and* **b)** *superficial ooids and coated grains with nuclei mostly made by planktonic foraminifera.* **c)** *Facies RC1: coral framestone (Porites).* **d)** *Facies RC2: neptunian dyke filled with Amphistegina rich wackestone.* **e)** *Facies RC3: peloidal wackestone with desiccation shrinkage.* **f)** *Facies RC4: oncoidal wackestone with leaching cavities. Scale bar = 1mm.*

planktonic foraminifera as nuclei of ooids suggest high water fertility, probably induced by upwelling currents [*Hallock and Schlager,* 1986]. Modern carbonate platforms show a significant influence of the prevailing wind directions on the type of carbonate production. Examples from the Atlantic Bahamian platforms [*Gebelein,* 1974] and from western Pacific platforms [*Wilson and Vecsei, 2005*] provide evidence that framework-built marginal reefs develop mostly on margins facing into the prevailing wind-related current direction. The Romanche sunken islands, lying in the belt of trade winds blowing persistently from the East, may be affected by strong upwelling of nutrient-rich deep waters on their western lee side, explaining the development of oolitic shoals on Paleoisland A. The oolitic sands, under the Trade Winds influence, underwent reworking and off-bank transport promoting deposition at the bank edge and its westward-prograding geometry. At the same time, persistent wind-generated wave action on the eastern side may have promoted mixing of the surface waters, helping the growth of patch reefs on Paleoisland C.

Calcareous nannofossil biostratigraphy on four samples from Paleoisland A gives ages older than 3.8 Ma and 0.46 Ma (see online *Supporting Material*).

5.3.2.2 Sr Isotopic ages of Romanche's Limestones

$^{87}Sr/^{86}Sr$ ratios measured in samples of Romanche carbonate Paleoisland A give an oldest age close to ~10 Ma (Table 2). Sr isotopic data are available for only one sample from Paleoisland C, with a calculated age of ~6 Ma (Table 2).

5.3.3 Sunken Island at the Atlantis II Transform

The Atlantis II transform offsets the ultraslow spreading Southwest Indian Ridge by about 200 km (Figure 6a). A deep transform valley is bordered by a 6-km high transverse ridge created by a 7.5 m.y. long transtension phase due to a spreading direction change at ~19.5 Ma [*Dick et al.,* 1999, *Baines et al.,* 2003]. Atlantis Bank lies on this ridge reaching a minimum depth of 700 m

close to the center of the transform offset. It is 100 km from the eastern ridge-transform intersection, and has a crustal age of ~11.3 Ma [*Dick et al.*, 2000]. The summit is a 25 km^2 wave-cut platform with a total relief of ~50 m with numerous low erosional haystacks clustered in its center surrounded by a smooth gently sloping terrace consisting of exposed gabbro-mylonite bedrock and carbonate beach sands [*Dick et al.*, 1999]. The Ocean Drilling Program drilled 1504 m into Atlantis Bank, recovering 1308 m of gabbro and a single 0.5 m diabase dike from Hole 735B [*Dick et al.,* 2000]. This confirmed that Atlantis Bank is an uplifted block of lower crust exposed in a large oceanic core complex [*Natland and Dick.,* 2001]. The bank, due to the remarkable preservation of ancient shorelines and beaches was named for the fabled island of Atlantis. Atlantis Bank, contrary to the other tectonic islands we have studied, has no carbonate platform due to its paleo and present position south of Darwin's carbonate line, where reef carbonates are not found [*Grigg*, 1982].

5.3.3.1 Atlantis Bank Carbonate Platform: Facies Analysis

A number of limestone samples were dredged from the summit of Atlantis Bank. Four main facies were identified based on sedimentary textures and biotic components (Table 1 and Figure 6). The most abundant biota components are bryozoans, mostly in the erect growth-forms [*sensu Nelson et al.,* 1988]. Mollusks are locally as abundant; benthonic foraminifera are ubiquitous (especially lagenids and miliolids; Figures 6b and 6c); planktonic foraminifera are also common and are dominant in muddy sediments (Figure 6d). Red algae are absent or present just as fine-grained fragments. Non-skeletal carbonate grains (e.g. ooids) as well as coral framestone are totally absent. This skeletal composition is commonly known as "foramol" and "molechfor" or, more generally, as a heterozoan association [*sensu James*, 1997], typical of temperate water carbonate deposits. It is consistent with Atlantis Bank being located within the southern warm temperate biogeographic province, roughly parallel to the equator, at approximately 30° S latitude. Sediments with bryozoan-dominated skeletal material are deposited in modern and Tertiary carbonates from subtropical to

temperate carbonate platforms in the Mediterranean realm [*Nebelsik*, 1989; *Fornos and Ahr,* 1997; *Mutti et al.* 1997; *Corda and Brandano* 2003] as well as in southwestern Australia and New Zealand [*Nelson et al.* 1988; *James et al.*, 1992] and in the US mid-Atlantic coastal plain [*Coffey and Read*, 2007].

The location of Atlantis Bank suggests similarity with the high-energy hydrodynamics off southern Australia rather than the relatively quiet waters of the Mediterranean Sea. In particular, the Lacepede shelf and the Rottnest shelf, along the southern and southwestern Australian continent [*James et al.,* 1992; *James et al.,* 1999], appear to be appropriate modern counterparts for the Atlantis Bank carbonates. These shelves are commonly swept by ocean swells that move sediments to depths of 140 m. Above this depth (between 80-140 m) bryozoan-rich sands dominate; below bryozoan-rich muddy facies are prevalent [*James et al.,* 1992].

Based on texture and biotic components, the limestones from Atlantis Bank were deposited on a 100-200 m deep platform, both in a high-energy zone affected by strong waves and currents (testified by grain-supported textures, microfacies AT1; Table 1 and Figure 6b) as well as in a low-energy environment, below the swell base, where skeletal fragments removed from shallower zones could accumulate together with muddy sediments (matrix-supported textures, microfacies AT2; Table 1 and Figure 6c). Strong currents affecting the Atlantis Bank carbonate platform may explain the large amount of gravel-sized skeletal debris swept from shallower areas into deeper zones and the slope. The swell base could have been the depth limit between high-energy and low-energy environments, explaining the high proportion of mud in a poorly sorted skeletal facies (AT3; Table 1 and Figure 6d). In analogy to observations by *James et al.* [1992], the shallow platform may have

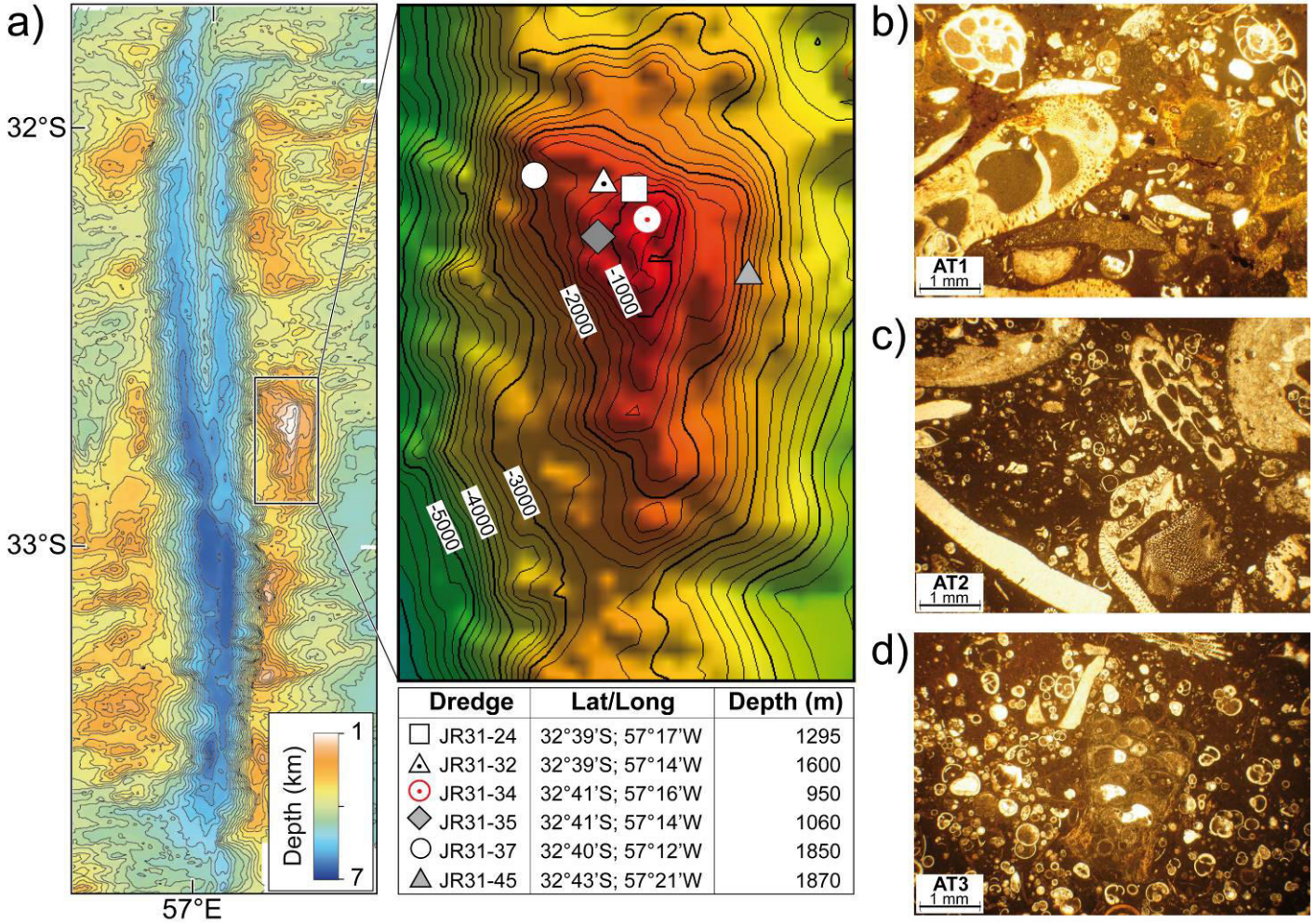

Dredge	Lat/Long	Depth (m)
JR31-24	32°39'S; 57°17'W	1295
JR31-32	32°39'S; 57°14'W	1600
JR31-34	32°41'S; 57°16'W	950
JR31-35	32°41'S; 57°14'W	1060
JR31-37	32°40'S; 57°12'W	1850
JR31-45	32°43'S; 57°21'W	1870

Figure 5.6 *Atlantis II transform fault.* **a)** *Bathymetry of the Atlantis II. Detailed bathymetry of the Atlantis Bank and dredge samples location are shown in the inset.* **b)** *Photomicrographs of facies AT1: Floatstone-rudstone with bryozoan fragments and benthic foraminifera (lenticulinids, lagenids);* **c)** *photomicrographs of facies AT2: skeletal floatstone with a wackestone matrix rich in planktonic foraminifera;* **d)** *Photomicrographs of facies AT3: planktonic packstone-wackestone with scattered coarse-grained bryozoan and echinoid fragments.*

been a zone of minor carbonate accumulation, whereas the deeper shelf and slope could have represented a zone of active sediment accumulation.

The scarcity-absence of important calcareous phototrophs such as red algae, common in many non-tropical carbonates, may indicate deposition under poorly lighted waters and under eutrophic conditions [*Mutti and Hallock,* 2003; *Halfar and Mutti,* 2005]. The Atlantis Bank carbonates may have been deposited within an open, deep platform characterized by poorly lighted waters with high nutrient levels caused by oceanic upwelling. A relatively deep and eutrophic environment is suggested also by: a) the presence of deep benthonic foraminifera (such as lagenids); b) the dominance of filter-feeding organisms such as bryozoans and echinoids; c) the abundance of planktonic foraminifera and the common occurrence of boring activity. Age determinations of some Atlantis Bank samples are constrained by planktonic assemblages [*L. Di Bella* pers. comm.]. *G. margaritae*, *G. tumida* and *Globorotalia* gr. *crassaformis* occur in samples JR31-24/1 and JR31-24/15 suggesting a Zanclean age (early Pliocene) [*Bolli and Saunders*, 1985; *Iaccarino et al.*, 2007], in agreement with Sr isotopic ages.

Nannofossil calcareous biostratigraphy of seven samples gives ages ranging between middle Miocene to Pleistocene (see online *Supporting Material*).

5.3.3.2 Sr Isotopic Ages of Atlantis Bank's Limestones

$^{87}Sr/^{86}Sr$ calculated ages measured in bulk and in isolated bioclastic fragments range between 4.5 and 2.3 Ma (Table 2). These ages, significantly younger than the Atlantis Bank crustal age, show that the carbonate samples were deposited far from the ridge-transform intersection after the Bank sank below sea level.

5.4 A Modern Example of Oceanic Tectonic Island: St Peter-Paul Rocks

The islets of St Peter and St Paul are located in the equatorial Atlantic (Figure 1) along the St Paul transform system, which offsets the Mid-Atlantic Ridge by 580 km. Darwin landed on the islets from the Beagle in 1832 and recognized that they are different from most oceanic islands in so far as they are not volcanic [*Darwin*, 1839]; in fact, they are made mostly of mylonitized mantle-derived lherzolite [*Melson et al.,* 1972; *Bonatti,* 1990] (*Auxiliary Figure A1*). There are 5 larger islets covering about 15,000 m^2 (Figure 7); the maximum height above sea level reached by the islets is about 18 m. The islets are at the summit of an East-West transverse ridge extending for ~90 km adjacent the active St Paul transform domain (St Peter and St Paul's Massif, according to *Hekinian et al.,* 2000; Figure 7). Transcurrent and transpressive seismic epicenters [*Wolfe et al.,* 1993] and high-resolution bathymetry indicate that the Massif is affected by a left-overstep along the right-lateral fault that causes transpressive uplift (Figure 7).

Two erosional terraces are present in the three largest islets, 4-5 m and 7-9 m above sea level [*Motoki et al.,* 2009], suggesting similar rates of uplift and absence of tilting in the islets. Based on ^{14}C age determinations on fossil sea level markers, the islets were subjected to uplift during the last 6,600 years at an average rate of ~1,5 mm/a [*Motoki et al*., 2009; *Campos et al.,* 2010]. St Peter and St Paul, then, are transform-related tectonic islands "in the making", with uplift that may possibly be followed by future subsidence, erosion and formation of a carbonate platform.

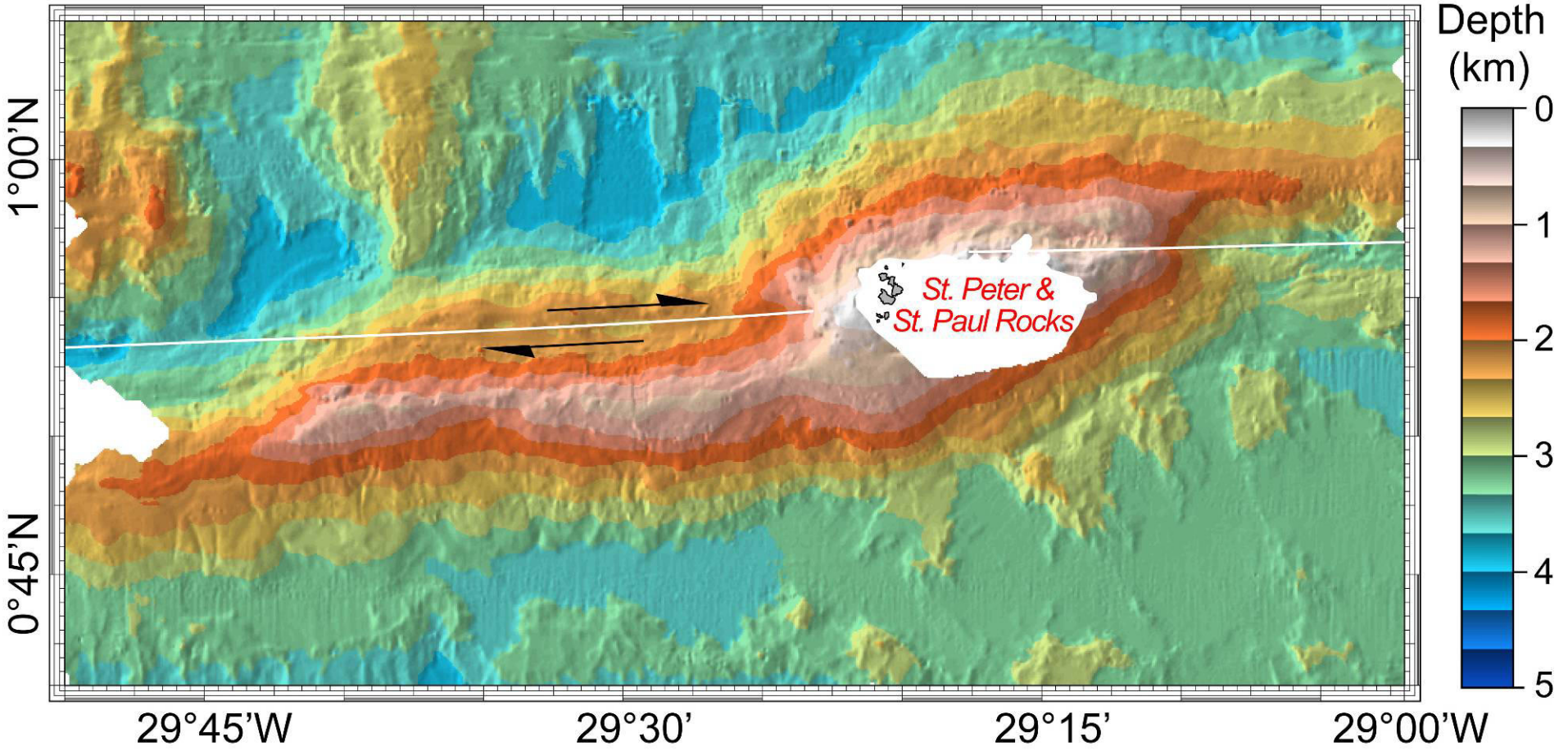

Figure 5.7 *Bathymetry of the St Peter and St Paul's Massif (data from Gasperini et al. [1997a] and Hekinian et al. [2000]). The left overstep of the right-lateral St Paul transform fault implies transpression at St Peter and St Paul Rocks area.*

5.5 Discussion

5.5.1 Environmental Significance of the Vema and Romanche Carbonate Facies

The Vema and Romanche platforms show carbonate facies typically consisting of "rhodalgal associations" dominated by red algae and perforate large benthic foraminifera. Although corals were abundant during the Miocene, coral communities are present only as locally minor patch reefs, in contrast with many well-known examples from warm-water carbonate systems [*Lees and Buller,* 1972]. Factors influencing the biota communities include temperature and water fertility [*Lees and Buller,* 1972; *Pomar,* 2001; *Brandano and Corda,* 2002; *Mutti and Hallock,* 2003; *Brandano et al.* 2010]. Optimal temperature range for coral reef development is between 23° and 25° C [*Veron*, 1995]. Concerning nutrients, *Larson et al.* [1995] as well as *Wilson et al.* [1998] report a latitudinal crisis belt coinciding with the high productivity - upwelling equatorial belt. Tropical "non-chlorozoan" deposits similar to our carbonate facies are reported by *Wilson and Vecsei* [2005] in modern and Cenozoic platforms from SE Asia and northern Australia, inferring preferential development of these facies in humid tropical or nutrient upwelling areas. Based on latitude of the Vema and Romanche carbonate platforms, high seawater fertility rather than temperature was probably a major controlling factor. Equatorial upwelling and humid conditions may have increased shallow water absorption of light, favoring plankton blooms (note the abundance of planktonic foraminifera as nuclei of ooids and/or planktonic foraminifera with incipient coatings). This created conditions suitable for carbonate platforms dominated by non-framework building biota, such as larger benthic foraminifera and coralline algae, with only minor patch reefs containing *Porites*.

The occurrence of *Amphistegina* in the limestones of Romanche Paleoisland C (Table 1) may suggest that these equatorial platforms could have served in the Miocene as stepping stones for the Caribbean-type Amphistegina assemblages that extend across the Atlantic to the Cabo Verde Islands [*Bernoulli et al.*, 2007].

The absence of reef facies on the Vema platform, in contrast to its presence, although minor, at the Romanche platforms, could be due to differences in water quality, related to run-off from adjacent land areas. Humid equatorial regions produce high terrestrial run-off and onshore organic productivity. As shown by Miocene equatorial carbonates from Indonesia [*Wilson*, 2002], some organisms are tolerant of high nutrient input, (i.e., larger benthic foraminifera, pectinids, coralline algae and echinoids), while corals (i.e., hermatypic corals) appear to be less tolerant. The latitude of the Vema transverse ridge (11° N) is close to that of Caribbean reefs off northern Venezuela. Reef building suffered in this region (Falcón Basin) a decline in Early Miocene time, attributed to changes in regional water quality [*Edinger and Risk*, 1994; *Von der Heydt and Dijkstra*, 2005]. *Johnson et al.* [1990] suggest that a switch in the outlet position of an ancestral Orinoco River might have caused the regional decline in reef building by altering surface-water characteristics, just as modern Orinoco and Amazon outflows exert strong control on shallow-water habitats off the coast of northeastern South America. Observations from space, [*Hu et al.*, 2004] demonstrated the influx of continent-derived materials on open ocean waters over distances exceeding 2000 km. Considering spreading rates, the Vema carbonate platform was closer to the continent during Mid Miocene, suggesting that the Orinoco River terrigenous input influenced the carbonate producing biota, inhibiting the growth of coral communities.

5.5.2 Origin of Oceanic Tectonic Islands

The non-volcanic islands described in this paper formed due to vertical motions of lithospheric blocks related to transform tectonics. Even slight changes in ridge/transform geometry, i.e., changes in orientation of mid-ocean ridge segments offset by transform boundaries, can cause either transtension or transpression along the transform, resulting in vertical motions of lithospheric slabs [*Bonatti,* 1978]. Modern tectonic islands St. Peter-Paul Rocks, are still in a phase of uplift,

representing the youthful stage in the 'uplift-emersion-erosion-subsidence-carbonate platform formation' cycle typical of tectonic islands.

Vertical motions are particularly well constrained at the Vema transform [*Bonatti et al.,* 2005]. Ridge-parallel seafloor fabric immediately south of the Vema transform changed orientation by ~5° in ~11-10 Ma crust, implying a slight change in ridge/transform geometry that caused transtension normal to the transform. Flexure of the lithospheric slab bordering the southern side of the transform followed, with uplift of the edge of the slab along the transform boundary. Modeling suggests that uplift was maximal where lithospheric thickness was highest [*Bonatti et al.*, 2005], that is, in the oldest western part of the slab that emerged above sea level. Uplift ceased after the ridge-transform system settled into the new geometry. Subsidence, sub-aerial erosion and truncation of the emerged slab at a sea level and growth of a shallow-water carbonate cap followed. The 11-10 Ma Sr isotopic ages of the carbonate platform are compatible with the timing of the flexure and uplift of the lithosphere slab estimated from magnetic anomalies. However, the presence in some of the platform samples of early Miocene fossils [*Bonatti et al.,* 1994a] may indicate a first stage of crustal uplift at the inside corner high, followed by the transtensional uplift at 11–10 Ma. The average subsidence rate of the Vema transverse ridge has been estimated assuming that it subsided as a single block starting soon after the end of the uplift phase at 10 Ma. The spreading half rate decreased from 17.2 mm/a between 26 and 19 Ma to ~16.9 mm/a between 19 and ~10 Ma, and then to ~13.6 mm/a from 10 Ma to present [*Bonatti et al.*, 2003], implying a 23 to 26 Ma crustal age below the carbonate cap. The wave-truncated horizontal surface of oceanic crust at the base of the carbonate platform lies presently 1100 m below sea level, suggesting an average subsidence rate slightly over 0.1 mm/a. This rate is higher than thermal subsidence (< 0.1 mm/a) of 23 to 26 Ma old crust predicted by the depth/square root of age law.

The three Romanche sunken islands also formed due to transform related transtension/transpression, although processes and timing are less precisely constrained than at

Vema. Given that erosional surfaces R_1, R_2 and R_3 lie at about the same depth below sea level, platforms A, B and C formed probably during the same time interval. Combining sea level changes, stratigraphic determination on key fossil species, and the growth potential of bioconstructors through a numerical model, an age range between 23 and 17 Ma was obtained for platform A [*Gasperini et al.*, 1997a]. This suggests a 0.06 mm/a subsidence rate of the Romanche sunken islands since middle Miocene, assuming a present day 1200-1300 m depth of the erosional surface at the base of the carbonate platform. Sr isotopic ages of Romanche platform A samples (up to 10 Ma) are significant lower than those estimated by Gasperini et al. [1997b]. The complex tectonic framework of the eastern Romanche may have resulted in multiple stages of transtension/transpression and in more than one event of uplift, emersion and subsidence.

Atlantis Bank originated as an oceanic core complex emplaced at the eastern ridge-transform intersection of the Atlantis II Fracture Zone on the Southwest Indian Ridge, that subsequently underwent additional uplift due to transtension across the transform due to a spreading direction change. Our data show that the carbonate rocks include a fauna deposited at around 100 – 200-m water depth around 2.4 to 4.5 Ma. It is presently ~700 m deep, giving a subsidence rate of 0.1 to 0.2 mm/a. Assuming a constant subsidence rate, the bank was at sea level at around 5-7 Ma, earlier if the subsidence was faster. The exposed gabbros on the wave-cut platform are deeply pitted where chemical erosion removed plagioclase. Thus, layering and other features defined by less easily weathered pyroxene and amphibole stand out in videos and still camera images (*Auxiliary Figure A2*). This form of weathering is generally associated with a sub-aerial environment. Pitted samples and outcrops were collected by the Shinkai 6500 submersible down to below 1700 m water depth. Thus, given the subsidence rate inferred from our dating, Atlantis Bank was probably uplifted to ~1000 m above sea level at or near the inside corner high. Similar modern uplifts are not known at ridge-transform intersections. However, Anna de Koningh Seamount is an ultramafic/gabbro

tectonic block [*Fisher et al.,* 1986] uplifted to ~-234 m at the western inside-corner high of the DuToit F.Z. on the Southwest Indian ridge, suggesting that large uplifts can occur in such settings.

5.5.3 Oceanic Islands: a Classification

Oceanic islands (excluding continental fragments) can be classified in two main groups: (a) "hot" volcanic islands and (b) "cold" tectonic islands. The "hot" volcanic islands include two subgroups: (a_1) islands formed by excess volcanism due to mantle melting anomalies either along mid ocean ridges or within oceanic plates; (a_2) islands formed by excess volcanism due to suprasubduction "wet" mantle melting, i.e., island arcs. "Cold" tectonic islands include those due to transform-related vertical tectonic movements of slivers of oceanic lithosphere, as described in this paper (Figure 8). Tectonic islands are preferentially found along transverse ridges and inside-corner highs flanking transform faults at slow and ultraslow spreading ridges, where large vertical motions are common (Figure 8).

"Hot" islands rise above sea level, evolve and sink within time intervals that depend mostly on the velocity of the oceanic plate relative to the source of the mantle-melting anomaly. The lifetimes of volcanic islands from fast-spreading oceans (i.e., the Hawaiian Chain) tend to be shorter than those from slow-spreading oceans (i.e., Canaries, Cabo Verde). Hot islands are generally constructed of erupted basaltic rocks, including low-density pyroclastics and hyaloclastites. Tectonic islands, however, are made of uplifted tectonic massifs of lower ocean crust and mantle gabbro and peridotite, unroofed along detachment faults at ridge/transform intersections and/or uplifted due to changes in ridge/transform geometry causing transtension and/or transpression.

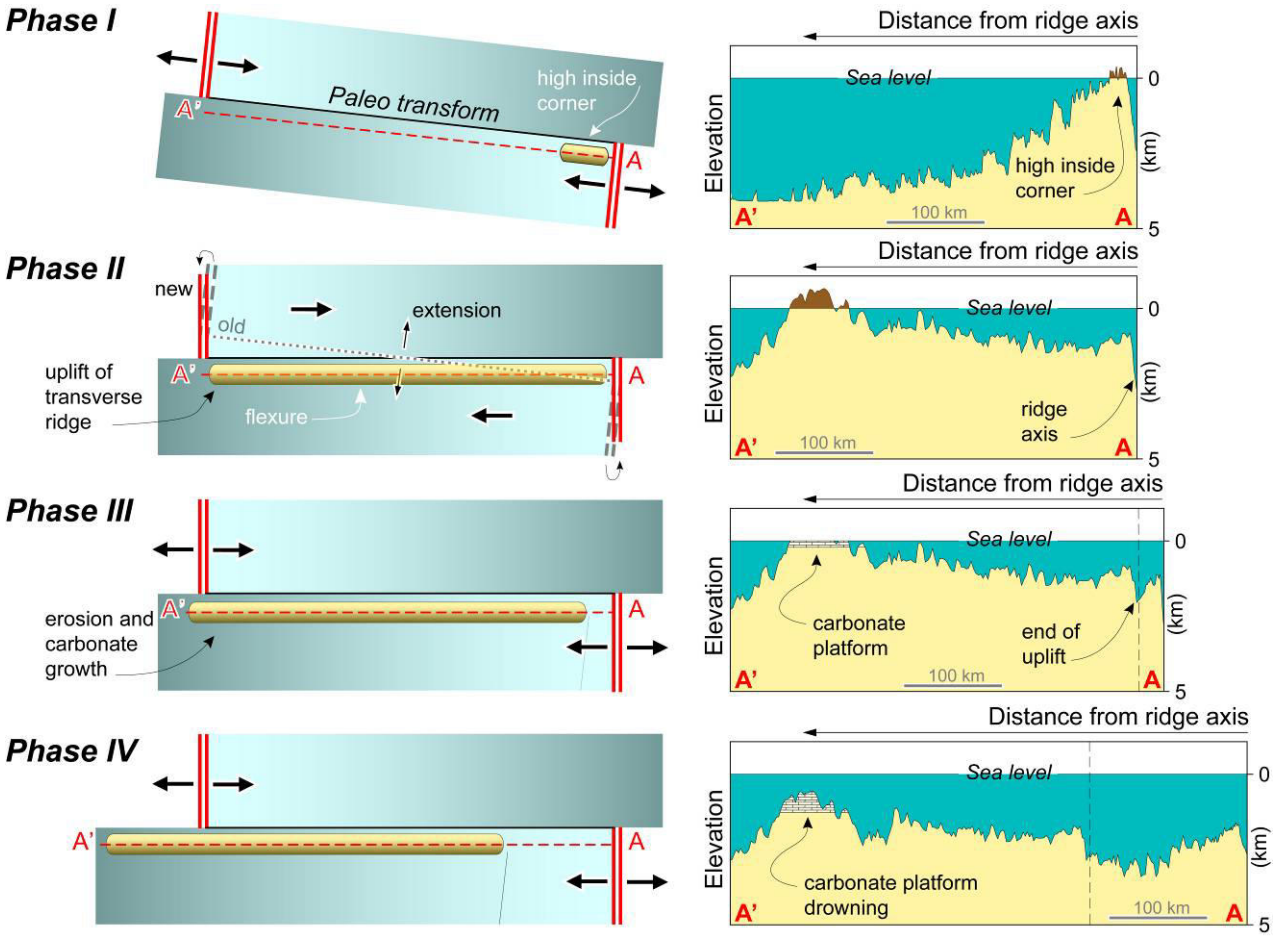

Figure 5.8 Cartoon showing the formation and evolution of tectonic islands. Red dashed line A-A' (left panels) marks the location of the topographic profiles showed in the right panels. **Phase I**: formation of a prominent inside corner high at a long-offset ridge-transform intersection. Inside corner high may reach sea level. **Phase II**: change in plate kinematics causing local transtensional/transpressional tectonics resulting in uplift of a sliver of oceanic lithosphere and formation of the transverse ridge [*Bonatti et al., 1994b*; *Pockalny et al.*, 1996; *Bonatti et al.*, 2005]. **Phase III**: end of uplift and erosion of the emerged portions of the transverse ridge at or close to sea level with formation of wave cut terraces. Thermal subsidence starts allowing space for carbonate platform growth. **Phase IV**: carbonate platform drowning due to environmental stress-induced deterioration in the potential for platform growth and/or tectonic-controlled rapid-sinking of the transverse ridge.

Although they generally have an anomalously high bulk density compared to the surrounding crust, they are often anomalously uplifted relative to the age-depth subsidence curve.

Carbonate platforms can develop on oceanic islands, given favorable biological, physical and chemical conditions. The geometry of carbonate platforms depends on: pre-existing topography (either a volcanic system or an uplifted lithospheric block), as well as on hydraulic energy and type of produced sediment that, in turn, is controlled by environmental conditions. The morphology of the platforms tends to be different in the two classes of islands. Volcanic islands tend to form circular or sub-circular platforms, that can enclose areas of low-energy (lagoons), in a scheme hinted at already by *Darwin* [1842]. In contrast, tectonic islands, generally associated with transform offsets, form long and narrow platforms, elongated parallel to the transform (Figure 8). An example is the ~50 km long, ~3 km wide Vema paleo-island (Figures 2a and 3a). Low-energy lagoons are rare in tectonic islands, due to their long-narrow basement morphology.

Rate of production and accumulation of carbonate sediments is affected by rate of vertical motion and eustatic sea level oscillations, that is, the rate at which accommodation space is created. During sea-level rise, platforms on volcanic islands can aggrade in all depositional systems (from the lagoon to the margin) enhancing carbonate production, and can aggrade and prograde during sea-level fall and stillstand (low- or high-stand). In contrast, carbonate platforms on tectonic island can aggrade during sea-level rise but their peculiar long and narrow morphology can affect the efficiency of the carbonate factory and thus the amount of carbonate production. During sea-level fall and still stand, being the escarpments generally very steep, little progradation can occur and significant volumes of produced material may be shed off the platform edge into the transform valley.

In conclusion, the evolution of tectonic sunken islands in the Atlantic and in the Indian Oceans has been reconstructed based on seismic reflection data, facies analysis, and carbonate Sr-isotopic dating. St Peter-Paul Rocks (equatorial Atlantic) are a modern example of a tectonic island “in the

making". "Cold' tectonic islands from different oceans and spreading rates display similar histories of uplift and subsidence, driven by the combined effects of vertical tectonics and lithospheric cooling, different from those of typical "hot" volcanic islands characterized by rapid growth and subsequent monotonic subsidence.

Acknowledgements

Thanks are due to G. Bortoluzzi (Ismar-CNR) for helping out with the open source software GMT ("General Mapping Tools"). We are grateful to L. Di Bella for Atlantis Bank planktonic foraminifera analysis, and to D. Bernoulli and an anonymous reviewer for constructive comments that helped us to improve the paper

References

Abreu, V. S., and J. B. Anderson (1998), Glacial eustasy during the Cenozoic: Sequence stratigraphic implications, *Bull. Am. Ass. Petrol. Geol., 82,* 1385–1400.

Baines, G., M. J. Cheadle, H. J. B. Dick, A. Hosford Scheirer, B. John, N. Kusznir, and T. Matsumoto (2003), Mechanism for generating the anomalous uplift of oceanic core complexes: Atlantis Bank, southwest Indian Ridge, *Geology, 31*, 1105–1108.

Bernoulli, D., L. Hottinger, S. Spezzaferri, and P. Stille (2007), Miocene shallow-water limestones from Sao Nicolau (Cabo Verde): Caribbean-type benthic fauna and time constraints for volcanism, *Swiss J. Geosci.*, *100*, 215–255.

Bolli, H. M., and J. B. Saunders (1989), Oligocene to Holocene low latitude planktic foraminifera, in *Plankton Stratigraphy*, *Cambridge Earth Science Series,* vol. 1, edited by H. M. Bolli, J. B. Saunders, and K. Perch-Nielsen, pp. 155–262, Cambridge University Press, Cambridge.

Bonatti, E. (1978), Vertical tectonism in oceanic fracture zones, *Earth Planet. Sci. Lett., 37*, 369–379.

Bonatti, E. (1990), Subcontinental mantle exposed in the Atlantic Ocean on St.Peter-Paul islets, *Nature, 345*, 800–802.

Bonatti, E., D. Brunelli, W. R. Buck, A. Cipriani, P. Fabretti, V. Ferrante, L. Gasperini, and M. Ligi (2005), Flexural uplift of a lithospheric slab near the Vema transform (central Atlantic): timing and mechanisms, *Earth Planet. Sci. Lett., 240*, 642–655.

Bonatti, E., M. Ligi, A.M. Borsetti, L. Gasperini, A. Negri and R. Sartori (1996), Lower Cretaceous deposits trapped near the Mid-Atlantic Ridge, *Nature*, *380*, 518–520.

Bonatti, E., M. Ligi, D. Brunelli, A. Cipriani, P. Fabretti, V. Ferrante, L. Gasperini, and L. Ottolini (2003), Mantle thermal pulses below the Mid-Atlantic Ridge and temporal variations in the formation of oceanic lithosphere, *Nature, 423*, 499–505.

Bonatti, E., M. Ligi, L. Gasperini, G. Carrara, and E. Vera (1994a), Imaging crustal uplift, emersion and subsidence at the Vema Fracture Zone, *Eos Trans., AGU, 75,* 371-372.

Bonatti, E., M. Ligi, L. Gasperini, A. Peyve, Y. Raznitsin, and Y. J. Chen (1994b), Transform migration and vertical tectonics at the Romanche fracture zone, equatorial Atlantic, *J. Geophys. Res., 99,* 21779–21802.

Bonatti, E., M. Sarnthein, A. Boersma, M. Gorini, and J. Honnorez (1977), Neogene crustal emersion and subsidence of the Romanche Fracture Zone, equatorial Atlantic, *Earth Planet. Sci. Lett., 35*, 369–383.

Bonatti, E., R. Sartori, and A. Boersma (1983), Vertical crustal movements at the Vema Fracture Zone in the Atlantic: evidence from dredged limestones, *Tectonophysics, 91*, 213–216.

Brandano M., M. Brilli, L. Corda, and M. Lustrino (2010), Miocene C-isotope signature from the central Apennine successions (Italy): Monterey versus regional controlling factors, *Terra Nova, 22*, 125–130.

Brandano, M., and L. Corda (2002), Nutrients, sea level and tectonics: constrains for the facies architecture of Miocene carbonate ramp in central Italy, *Terra Nova, 14*, 257–262.

Campos, T. F. C., F. H. R. Bezerra, N. K. Srivastava, M. M. Vieira, and C. Vita-Finzi (2010), Holocene tectonic uplift of the St Peter and St Paul Rocks (Equatorial Atlantic) consistent with emplacement by extrusion, *Mar. Geol., 271*, 177–186.

Cande, S. C., J. L. LaBraque, and W. F. Haxby (1988), Plate kinematics of the South Atlantic: isochron C34 to present, *J. Geophys. Res., 93,*13479–13492.

Cerveny, V., L. Klimes, and I Psencik (1988), Application of dynamic ray tracing, *Phys. Earth Planet. Interiors*, *51,*25–35.

Coffey, B. P., and J. F. Read (2007), Subtropical to temperate facies from a transition zone, mixed carbonate–siliciclastic system, Palaeogene, North Carolina, USA, *Sedimentology, 54*, 339–365.

Corda, L., and M. Brandano (2003), Aphotic zone carbonate production on a Miocene ramp, central Apennines, Italy, *Sediment. Geol., 161*, 55–70.

Darwin, C. R. (1839), Journal of researches into the geology and natural history of the various countries visited by H.M.S. Beagle under the command of Captain Fitzroy, R. N. from 1832 to 1836, Henry Colburn, London.

Darwin, C. R. (1842), *Coral Reefs*, Smith-Elder, London.

Darwin, C. R. (1844), Geological observations on the volcanic islands visited during the voyage of H.M.S. Beagle, together with some brief notices of the geology of Australia and the Cape of Good Hope. Being the second part of the geology of the voyage of the Beagle, under the command of Capt. Fitzroy, R.N. during the years 1832 to 1836. Smith Elder and Co., London.

Dick, H. J. B., C. J. MacLeod, P. T. Robinson, S. Allerton, and M. Tivey (1999), A high resolution bathymetric map of Atlantis Bank, in *Proceedings of Ocean Drilling Program*, *Initial Reports*, vol. 176, edited by H. J. B. Dick et al., College Station, TX 77845-9547, Ocean Drilling Program, Back Envelope Map.

Dick, H. J. B., J. H. Natland, J. C. Alt, W. Bach, D. Bideau, J. S. Gee, S. Haggas, J. G. H. Hertogen, G. Hirth, P. M. Holm, B. Ildefonse, G. J. Iturrino, B. E. John, D. S. Kelley, E. Kikawa, A. Kingdon, P. J. LeRoux, J. Maeda, P. S. Meyer, D. J. Miller, H. R. Naslund, Y. L. Niu, P. T. Robinson, J. Snow, R. A. Stephen, P. W. Trimby, H. U. Worm, and A. Yoshinobu (2000), A Long In-Situ Section of the Lower Ocean Crust: Results of ODP Leg

176 Drilling at the Southwest Indian Ridge, *Earth Planet. Sci. Lett., 179*, 31-51.

Edinger, E. N., and M. Risk (1994), Oligocene-Miocene extinction and geographic restriction of Caribbean Corals: roles of Turbidity, Temperature and Nutrients, *Palaios, 9,* 576–598.

Edmond, J. M. (1992), Himalayan Tectonic, Weathering Processes, and the Strontium Isotope Record in Marine Limestones, *Science, 258,* 1594–1597.

Fabretti, P., E. Bonatti, A. Peyve, D. Brunelli, A. Cipriani, X. Dobrolubova, V. Efimov, S. Erofeev, L. Gasperini, J. A. Hanley, M. Ligi, A. Perfiliev, V. Rastorguyen, Y. Raznitsin, G. Savelieva, V. Semjenov, S. Sokolov, S. Skolotnev, S. Susini, and I. Vikentyev (1998), First results of cruise S19 (PRIMAR Project); petrological and structural investigations of the Vema transverse ridge (Equatorial Atlantic), *G. Geol.*, *60,* 3–16.

Fisher, R. L., H. J. B. Dick, J. Natland, and P. S. Meyer (1986), Mafic/ultramafic suites of the slowly spreading Southwest Indian Ridge: PROTEA Exploration of the Antarctic Plate Boundary, 24°E - 47°E, *Ofioliti*, *11*, 147–178.

Fornos, J. J., and W. M. Ahr (1997), Temperate carbonates on a modern, low-energy, isolated ramp: the Balearic platforms, Spain, *J. Sediment. Res., 67,* 364–373.

Gasperini L., D. Bernoulli, E. Bonatti, M. Borsetti, M. Ligi, A. Negri, R. Sartori, and K. von Salis (2001), Lower Cretaceous to Eocene sedimentary transverse ridge at the Romanche Fracture Zone and the opening of the Equatorial Atlantic, *Mar. Geol., 176,* 101–119.

Gasperini L., E. Bonatti, D. Brunelli, G. Carrara, A. Cipriani, P. Fabretti, D. Gilod, M. Ligi, A. Peyve, S. Skolotnev, S. Susini, P. Tartarotti and N. Turko (1997a), New data on the geology of the Romanche F.Z., equatorial Atlantic: PRIMAR-96 cruise report, *G. Geol., 59,* 3–18.

Gasperini, L., E. Bonatti, M. Ligi, R. Sartori, A. Borsetti, A. Negri, A. Ferrari, and S. Sololov, (1997b), Stratigraphic numerical modeling of a carbonate platform on the Romanche transverse ridge, equatorial Atlantic, *Mar. Geol., 136,* 245–257.

Gebelein, C. D. (1974), Guidebook for Modern Bahamian Platform Environments, *Geol. Soc. American*, Annual meeting.

Grigg, R. W. (1982), Darwin point: a threshold for atoll formation, *Coral Reefs*, *1*, 29–34.

Halfar, J., and M. Mutti (2005), Global dominance of coralline red-algal facies: A response to Miocene oceanographic events, *Geology, 33*, 481– 484.

Hallock, P., and W. Schlager (1986), Nutrient excess and the demise of coral reefs and carbonate platforms, *Palaios, 1*, 389–298.

Haq, B. U., J. Hardenbol, and P. R. Vail (1987), Chronology of fluctuating sea-levels since the Triassic, *Science, 235*, 1156–1167.

Hekinian, R., T. Juteau, E. Gràcia, B. Sichler, S. Sichel, G. Udintsev, R. Apprioual, and M. Ligi (2000), Submersible observations of Equatorial Atlantic mantle: The St. Paul Fracture Zone region, *Mar. Geophys. Res., 21*, 529–560.

Hu C., E. T. Montgomery, R. W. Schmitt, and F. E. Muller-Karger (2004), The dispersal of the Amazon and Orinoco River water in the tropical Atlantic and Caribbean Sea: observation from space and S-PALACE floats, *Deep-Sea Res. PT II, 51*, 1151–1171.

Iaccarino, S. M., I. Premoli Silva, M. Biolzi, L. M. Foresi, F. Lirer, E. Turco, and M. R. Petrizzo (2007), Practical manual of Neogene planktonic foraminifera, International School on Planktonic Foraminifera. VI Course. Neogene, Perugia (Italy).

James, N. P. (1997), The cool-water carbonate depositional realm, in *Cool-Water Carbonates, SEPM Special Publication*, vol. 56, edited by N. P. James, and J. Clarke, pp. 1–20, Tulsa, Oklahoma.

James, N. P., Y. Bone, C. Von Der Borch, and V. A. Gostin (1992), Modern carbonate and terrigenous clastic sediments on a cool water high energy, mid-latitude shelf: Lapacede, southern Australia, *Sedimentology, 39,* 877–903.

James, N. P., L. S. Collins, Y. Bone, and P. Hallock (1999), Subtropical carbonates in a temperate realm: modern sediments on the southwest Australian Shelf, *J. Sediment. Res., 69,* 1297–321.

Johnson K. G., M. Sanchez-Villagra, and O. A. Aguilera (1990), The Oligocene-Miocene transition on the coral reefs in the Falcòn Basin (NW Venezuela), *Palaios, 24,* 59–69.

Larson, R. L., E. Erba, M. Nakanishi, D. D. Bergersen, and J. M. Lincoln (1995), Stratigraphic vertical subsidence and paleolatitudinal histories of Leg 144 Guyot,. *Proc. Ocean Drill. Program, Sci. Results, 144*, 915–933.

Lees, A. (1975), Possible influence of salinity and temperature on modern shelf carbonate sedimentation, *Mar. Geol., 19*, 159–198.

Lees, A., and A. T. Buller (1972), Modern temperate-water and warm-water shelf carbonate sediments contrasted, *Mar. Geol., 13*, M67–M73.

Li, D., G. A. Shields-Zhou, H. F. Ling, and M. Thirlwall (2011), Dissolution methods for strontium isotope stratigraphy: Guidelines for the use of bulk carbonate and phosphorite rocks, *Chem. Geol., 290*, 133–144.

Ligi, M., E. Bonatti, L. Gasperini, and A. N. B. Poliakov (2002), Oceanic broad multifault transform plate boundaries, *Geology, 30*, 11–14.

Ligi, M., and G. Bortoluzzi (1989), PLOTMAP: geophysical and geological applications of good standard quality cartographic software: *Comput. Geosci., 15*, 519–585.

McArthur, J. M., and R. J. Howarth (2004), *Sr-isotope stratigraphy*. In: Gradstein, F., Og, J. and Smith A.G., (Eds.), A geological timescale 2004. Cambridge University Press, Cambridge.

McArthur, J. M., R. J. Howarth, and T. R. Bailey (2001), Strontium isotope stratigraphy: LOWESS version 3. Best-fit line to the marine Sr-isotope curve for 0 to 509 Ma and accompanying look-up table for determining numerical ages, *J. Geol., 109*, 155–169.

Melson, W. J., S. R. Hart, and G. Thompson (1972), St.Paul's Rocks, Equatorial Atlantic: Petrogenesis, Radiometric Ages, and implications on Sea-Floor Spreading, *Geol. Soc. Am. Mem., 132*, 241–272.

Morgan, W. J. (1972), Deep mantle convection plumes and plate motions, *AAPG Bulletin, 56*, 203–213.

Motoki, A., S. E. Sichel, T. F. C. Campos, N. K. Srivatav, and R. Soares (2009), Taxa de soerguimento atual do arquipélago de Sao Pedro e Sao Paulo, Oceano Atlantico Equatorial, *REM, Ouro Preto, 62,* 331–342.

Mutti, M., and P. Hallock (2003), Carbonate systems along nutrients and temperature gradients: some sedimentological and geochemical constraints, *Int. J. Earth. Sci., 92*, 465–475.

Mutti, M., D. Bernoulli, and P. Stille (1997), Temperate carbonate platform drowning linked to Miocene oceanographic events: Maiella platforms margin, Italy, *Terra Nova, 9*, 122–125.

Natland, J. H., and H. J. B. Dick (2001), Formation of the lower ocean crust and the crystallization of gabbroic cumulates at a very slowly spreading ridge, *J. Volcanol Geoth. Res., 110*, 191–233.

Nebelsik, J. H. (1989), Temperate water carbonate facies of early Myocene Paratethys (Zogelsdorf Formation, lower Austria), *Facies, 21*, 11–40.

Nelson, C. S., S. L Keane, and P. S. Head (1988), Non-tropical carbonate deposits on the modern New Zealand shelf, *Sediment. Geol., 60*, 71–94.

Pockalny, R. A., P. Gente, and W. R. Buck (1996), Oceanic transverse ridges: A flexural response to fracture-zone-normal extension, *Geology*, *24*, 71–74.

Pomar, L. (2001), Types of carbonate platforms: a genetic approach*, Basin Res., 13,* 313–334.

Sclater, J. G., R. N. Anderson, and M. Lee Bell (1971), Elevation of ridges and evolution of the central eastern Pacific, *J. Geophys. Res., 76*, 7888–7915.

Terakado, Y., H. Shimizu, and A. Masuda (1988), Nd and Sr isotopic variations in acidic rocks formed under a peculiar tectonic environment in Miocene Southwest Japan, *Contrib. Mineral. Petr., 99,* 1–10.

Veron, J. E. N. (1995), *Corals in Space and Time. The Biogeography and Evolution of the Scleractinia*, Cornell Univ. Press, Ithaca.

Von der Heydt, A., and H. A. Dijkstra (2005), Flow reorganization in the Panama Seaway: A cause for the demise of Miocene corals? *Geophys. Res. Lett., 32,* L02609, doi:10.1029/2004GL020990.

Wessel, P., and W. H. F. Smith (1998), New improved version of the Generic Mapping Tools released: *EOS, Transaction of American Geophysical Union*, *79*, 579.

Wilson, J. T. (1963), A possible origin of the Hawaiian Islands, *Can. J. Phys., 41*, 863–870.

Wilson, M. E. J. (2002), Cenozoic carbonates in Southeast Asia: implication for equatorial carbonate development, *Sediment. Geol., 147*, 295–428.

Wilson, M. E. J., and A. Vecsei (2005), The apparent paradox of abundant foramol facies in low latitudes: their environmental significance and effect on platform development, *Earth Sci. Rev., 69,* 133–168.

Wilson, P. A., H. C. Jenkyns, H. Elderfield, and R. L. Larson (1998), The paradox of drowned carbonate platforms and the origin of Cretaceous Pacific guyots, *Nature, 30*, 889–894.

Wolfe, C. J., E. A. Bergman, and S. C. Solomon (1993), Oceanic transform earthquakes with unusual mechanisms or locations relation to fault geometry and state of stress in the adjacent lithosphere, *J. Geophis. Res., 98,* 16187–16211.

Platform	Sample	Facies	Texture and components	Environment
Vema	RC2104-4D/A RC2104-4D/B RC2104-4D/C RC2104-4D/A1 RC2104-4D/B1 RC2104-4D/C1 RC2104-4D/C2 EW9305-10D/1D	V1	Floatstone-rudstone dominated by red algae and larger (*Amphistegina)* and small benthic foraminifera. Corals are rare.Cracks and sedimentary dykes are present.	Moderate to deeper parts of the photic zone (inner-middle ramp).
	RC2104-2D/A RC2104-7D/A	V2	Pebbly mudstone with planktonic foraminifera, benthonic skeletal debris with carbonate clasts (often bioeroded) and volcanic clasts.	Platform slope
	EW9305-10D/3 Sedimentary-dike in: EW9305-10D/1D	V3	Well-sorted bioclastic packstone, mostly represented by red-algae fragments, with occasional floating rhodoliths and fragments of *Porites.*	Inner ramp
	EW9305-10D/3 EW9305-10D/1C	V4	Oncoidal wackestone with planktonic foraminifera exhibiting frequent incipient coatings. Isopacous and meniscus cement. Intense micritization.	Subtidal-intertidal
	EW9305-10D/11 EW9305-10D/5 EW9305-10D/1A EW9305-10D/1B	V5	Wackestone-packstone with planktonic foraminifera. Not completely lithified.	Pelagic environment
	RC2104-7D/coral RC2104-7D/bivalve EW9305-10D/3 coral	V6	Cold-water coral assemblage formed by the ahermatypic scleractinian coral *Madrepora oculata* in association with the symbiotic polychaete *Eunice* sp., and gorgonian deep-water corals (unidentified species).	Re-colonization of the platform in the bathyal zone during the last deglaciation
Romanche A	P6707-8/1A P6707-8/1B P6707-8/1C P6707-8/2 P6707-8/3 P6707-8/4 P6707-8/5A P6707-8/5B P6707-8/6A P6707-8/6B P6707-8/10 P6707-8/11 P6707-8/12 P6707-8/12B P6707-8/13A P6707-8/XA	RA1	Oolitic grainstone with subordinate echinoids. Good sorting and cross laminations. Alternating laminae separated by microbial mats. Ooids are mostly superficial, their nuclei are frequently planktonic foraminifera tests. Under SEM they show aragonite needles with long axes mostly tangentially oriented.	Mobile shoal
	P6707-9/SL1 P6707-8/1 P6707-8/2 P6707-8/9 P6707-8/13 P6707-8/A P6707-8/B P6707-8/C P6707-8/XB	RA2	Wakestone-packstone with ooids, coated grains and larger foraminifera. Irregular vugs related to chemical leaching.	Inter-subtidal with episodic exposure fringe

Paleoisland	Sample	Facies	Texture and components	Environment
Romanche A	P6707-8/7	RA3	Packstone with planktonic foraminifera and with carbonate and volcanic lithoclasts.	Platform slope
	P6707-8/S9	RA4	Poorly lithified planktonic-rich limestones.	Pelagic environment
Romanche C	S16-62/3 S16-62/5 S16-62/6 S16-53/13 S16-53/14A	RC1	Floatstone-rudstone-framestone with corals (*Porites)* and with red algae and larger foraminifera. Fringes of isopachous cement with residual porosity.	Platform margin
	S16-53/2 S16-62/13a S16-62/13b S16-62/13b1	RC2	Packstone-floatstone to wackestone with larger foraminifera *(Miogypsina,, Amphistegina*) and coral fragments. Intense leaching of calcitic *Miogypsina* tests, reddish micrite intraparticle-porosity infilling.	Inner ramp (temporary exposure) ?
	S16-53/2	RC3	Peloidal wackestone-packstone with rare benthonic foraminifera. Diffuse desiccation shrinkage and stromatolite-like laminae. Neptunian dykes are present.	Inter-tidal
	S16-62/2 S16-62/8 S16-62/11 S16-62/12	RC4	Oncoidal wackestone-packstone with bio-lithoclasts. Micritization and irregular leaching derived cavities, are common features.	Inter-subtidal (temporary exposure)
	S16-53/4	RC5	Rudstone-floatstone rich in planktonic foraminifera and with bioclasts and carbonate lithoclasts.	Platform slope
Atlantis Bank	JR31-34/4 a JR31-34/4 b JR31-34/4 c	AT1	Floatstone-rudstone with coarse-grained bryozoan-echinoid fragment and with benthic foraminifera (mostly lagenids).	Deep platform within the current action
	JR31-34/a JR31-34/b JR31-34/c JR31-34/d	AT2	Skeletal wackestone-packstone with abundant planktonic foraminifera, benthonic foraminifera (lagenids, miliolids, anomalinids), and bryozoan-echinoid fragments.	Deep platform below the current action
	JR31-24/1 JR31-24/15 JR31-32/8 JR31-32/10 JR31-32/17 JR31-32/18 JR31-35/5 JR31-35/6	AT3	Planktonic-rich packstone with gravel-sized skeletal fragments of bryozoans, mollusks and larger foraminifera.	Platform-edge slope
	JR31-45/2 JR31-37/1 JR31-37/3 JR31-37/4 JR31-32/9	AT4	Poorly lithified packstone-wackestone with planktonic foraminifera and fine-grained benthic skeletal debris.	Deep slope

Table 5.1 *Carbonate facies of the Vema, Romanche and Atlantis Bank carbonate platforms.*

Platform	Sample	Method	$^{87}Sr/^{86}Sr$	Minimum age*	Mean age**	Maximum age***
Vema	RC2104-4D/A	TIMS	0.708873 (18)	9.65	10.41	11.27
	RC2104-4D/A[§]	TIMS	0.708851 (18)	10.30	11.18	12.45
	RC2104-4D/B	TIMS	0.708847 (17)	10.48	11.34	12.59
	RC2104-4D/B[§]	TIMS	0.708844 (17)	10.59	11.52	12.71
	RC2104-4D/C2	MC-ICP-MS	0.708897 (15)	8.91	9.7	10.37
	RC2104-4D/A1	MC-ICP-MS	0.708964 (15)	6.21	6.66	7.4
	RC2104-4D/B1	MC-ICP-MS	0.708861 (15)	10.1	10.8	11.85
	RC2104-4D/C1	MC-ICP-MS	0.708884 (15)	9.42	10.06	10.74
	RC2104-2D/A	TIMS	0.708993 (17)	5.68	6.01	6.39
	RC2104-7D/coral	TIMS	0.709151 (17)	0.22	0.62	1.12
	RC2104-7D/bivalve	TIMS	0.709177 (17)	0.00	0.00	0.00
	EW9305-10D/3-coral	TIMS	0.709182 (17)	0.00	0.00	0.00
	EW9305-10D/3	TIMS	0.708844 (17)	10.62	11.80	12.71
	EW9305-10D/1C	TIMS	0.709095 (17)	1.35	1.70	2.30
	EW9305-10D/1C[§]	TIMS	0.709090 (17)	1.42	1.82	2.45
	EW9305-10D/11	TIMS	0.709174 (17)	0.00	0.00	0.00
	EW9305-10D/1A	TIMS	0.708952 (18)	6.43	7.10	8.45
	EW9305-10D/1B	TIMS	0.708971 (18)	6.03	6.45	7.20
Romanche A	P6707-8/1°	TIMS	0.708938 (17)	6.90	7.64	9.12
	P6707-8/1B	TIMS	0.708886 (17)	9.28	10.00	10.74
	P6707-8/1C	TIMS	0.708985 (15)	5.85	6.13	6.56
	P6707-8/1C[§]	TIMS	0.708959 (17)	6.27	6.84	7.69
	P6707-8/5A	TIMS	0.708964 (17)	6.17	6.66	7.54
	P6707-8/5B	TIMS	0.708969 (16)	6.08	6.51	7.24
	P6707-8/6A	TIMS	0.708941 (17)	6.79	7.52	8.97
	P6707-8/12B	TIMS	0.708951 (18)	6.43	7.14	8.51
	P6707-8/13A	TIMS	0.708937 (17)	6.86	7.68	9.17
	P6707-8/A	TIMS	0.708910 (18)	7.85	9.29	10.02
	P6707-8/B	TIMS	0.708906 (17)	8.30	9.43	10.14
	P6707-8/C	TIMS	0.708953 (17)	6.40	7.07	8.35
	P6707-9/SL1[¤]	TIMS	0.709004 (19)	5.33	5.82	6.18
	P6707-9/SL1[¤]	TIMS	0.708997 (20)	5.50	5.94	6.37
	P6707-9/SL1[¤]	TIMS	0.708989 (18)	5.71	6.07	6.53
	P6707-8/7	TIMS	0.708949 (17)	6.53	7.22	8.56
	P6707-8/S9	TIMS	0.709177 (17)	0.00	0.00	0.00
Romanche C	S16-53/13	TIMS	0.708988 (17)	5.75	6.09	6.50
Atlantis Bank	JR31-34/4	MC-ICP-MS	0.709066 (16)	2.02	2.67	4.53
	JR31-34/4c	MC-ICP-MS	0.709081 (12)	1.653	2.15	2.64
	JR31-34/8	MC-ICP-MS	0.709067 (15)	2.02	2.63	4.39
	JR31-34/8c	MC-ICP-MS	0.709076 (13)	1.77	2.30	2.99
	JR31-34/8a	MC-ICP-MS	0.709085 (13)	1.555	2.01	2.52
	JR31-34/8b	MC-ICP-MS	0.709077 (13)	1.77	2.27	2.87
	JR31-24/1	MC-ICP-MS	0.709019 (15)	4.95	5.52	5.87
	JR31-24/15	MC-ICP-MS	0.709043 (13)	3.31	4.74	5.27
	JR31-32/8	MC-ICP-MS	0.709059 (13)	2.37	3.28	4.73
	JR31-32/10	MC-ICP-MS	0.709053 (15)	2.48	4.01	5.01
	JR31-32/10[¤]	MC-ICP-MS	0.709045 (13)	3.07	4.65	5.17
	JR31-35/5	MC-ICP-MS	0.709155 (12)	0.231	0.629	0.953
	JR31-35/5[¤]	MC-ICP-MS	0.709159 (15)	0.000	0.550	0.930
	JR31-37/3	MC-ICP-MS	0.709129 (13)	0.888	1.146	1.363
	JR31-45/2	MC-ICP-MS	0.708870 (13)	9.90	10.50	11.14

Table 5.2 *Strontium isotope determinations of the Vema, Romanche and Atlantis Bank limestones. Data in parentheses represent the cumulative error, calculated by adding in quadrature 1□ of each single run (internal error) and 2□ of repeated measurements of the standard SMR 987 (external error).*
**Maximum age (Ma) obtained from the mean isotopic value -2□ (standard deviation) on the upper limit age curve.*
***Mean age (Ma) obtained from the mean isotopic value on the mean age curve. ***Minimum age (Ma) obtained from the mean isotopic value +2□ on the lower limit age curve.*
[§]*The filament was re-analyzed.*
[¤]*A micro-portion of the same sample was processed and analyzed separately.*

Auxiliary Material

5.6 Calcareous nannofossil biostratigraphy

We analyzed the calcareous nannofossil assemblages in our samples in order to estimate ages of limestones. Sample ages have been estimated using the zonal scheme of *Okada and Bukry* [1980], *Young* [1998], *Marino and Flores* [2002], and *Raffi et al*. [2006]. Slides have been prepared by smearing a few drops of wet sediment onto a coverslip. The smear slides were then analyzed with a ZEISS polarizing microscope at ×1250 magnification.

Most of the samples contain few to none calcareous nannofossils because of poor preservation of the flora due to dissolution. The following terminology has been applied: LO: Last occurrence; FO: first occurrence.

5.6.1 Vema Sunken Island

EW9305-10D/1A

The assemblage is characterized by the presence of *Sphenolithus moriformis* (FO CP10- LO CN7), *Coccolithus pelagicus*, *Helicosphaera euphratis* and *Discoaster challengeri*. This sample is not younger than 9.4 Ma.

EW9305-10D/1B

This sample characterized by the co-occurrence of *Discoaster loeblichii*, *Discoaster brouweri* (FO CN6- LO CN12d), *Sphenolithus abies* (LO CN12aA-CN12aB) and *Sphenolithus moriformis*, is not younger than 2 Ma.

EW9305-10D/1

This sample contains *Sphenolithus moriformis* (FO CP10- LO CN7) and *Sphenolithus heteromorphus* (FO CN3- LO CN4). It is not younger than 9.4 Ma.

5.6.2 Romanche Paleoisland A

P6707- 8/A

Presence of *Catinaster coalithus*, *Reticulofenestrae pseudoumbilicus* >7 µm (LO CN11b), *Discoaster calcaris*, *Discoaster quinqueramus*. Due to the presence of the *Ret. Pseudoumbilicus* >7 µm the is not younger than 3.8Ma

P6707- 8/B

Presence of *Sphenolithus capricornutus*, *Sphenolithus moriformis*, *Reticulofenestrae pseudoumbilicus* >7 µm (LO CN11b), *Discoaster deflandrei*. Due to the presence of *Ret. pseudoumbilicus* >7 µm, the sample is not younger than 3.8Ma

P6707-8/C

Very rare presence of *Discoaster challengeri*, *Sphenolithus moriformis*, *Reticulofenestra pseudoumbilicus* >7 µm (LO CN11b). Due to the presence of the *Ret. pseudoumbilicus* >7 µm the sample is not younger than 3.8Ma

P6707-8/1A

This sample contains *Reticulofenestra* spp. and *Pseudoemiliana lacunosa* (LO CN14a-CN14b); it is not younger than 0.460 Ma.

5.6.3 Atlantis Bank

JR31-34/4

The assemblage contains *Reticulofenestra minutola*, *Reticulofenestra haqii*, *Watznaueria* spp., *Reticulofenestra pseudoumbilicus* >7 µm (LO CN11b) and *Syracosphaera histrica*. Due to the presence of the *Ret. pseudoumbilicus* >7 µm the sample is not younger than 3.8 Ma.

JR31-24/1

Few species were detected in this sample, *Gephyrocapsa caribbeanica, Calcidiscus leptoporus* and *Sphenolithus abies* (LO CN12aA–CN12aB). The presence of *Sphenolithus abies* makes this sample not younger than 3.65 Ma.

JR31-24/15

The assemblages contain *Umbilicosphaera sibogae, Syracosphaera* spp., *Gephyrocapsa oceanica, Gephyrocapsa* small *Helicosphaera carteri, Watznaueria* spp., *Calcidiscus leptoporus* and *Pseudoemiliania lacunosa* (LO CN14a-CN14b). The rare presence of *Pseudoemiliania lacunosa* makes this sample not younger than 0.460 Ma.

JR31-32/8

Reticulofenestra perplexa, Reticulofenestra producta, Reticulofenestra stavensis, Reticulofenestra bisecta, Calcidiscus leptoporus and *Calcidiscus macintyrei* (LO CN13bA–CN13bB) were found in this sample. The rare presence of *Calcidiscus macintyrei* makes this sample not younger than 1.6 Ma.

JR31-32/10

This sample contains *Reticulofenestra perplexa, Reticulofenestra producta, Reticulofenestra stavensis, Reticulofenestra bisecta* and *Calcidiscus macintyrei* (LO CN13bA–CN13bB). The rare presence of *Calcidiscus macintyrei* makes this sample not younger than 1.6 Ma.

JR31-37/3

Reticulofenestra spp., *Reticulofenestra pseudoumbilicus* >7 µm, large *Gephyrocapsa* (>5.5 µm) (FO CN13bB- LO CN13bD), and *Gephyrocapsa muellerae* characterize this assemblage. The presence of the large *Gephyrocapsa* (>5.5 µm) gives an age between 1.56<x<1.2 Ma.

JR31-45/2

This sample contains *Reticulofenestra bisecta, Coccolithus miopelagicus,* and *Biscutum* spp. The rare presence of *Coccolithus miopelagicus* (LO CN7) gives an age not younger than ~11 Ma.

References

1. Marino, M., and J. A. Flores (2002), Miocene to Pliocene calcareous nannofossil biostratigraphy at ODP Leg 177 Sites 1088 and 1090, *Mar. Micropaleont., 45*, 291–307.

2. Okada, H., and D. Bukry (1980), Supplementary modification and introduction of code numbers to the low-latitude coccolith biostratigraphic zonation (Bukry, 1973; 1975), *Mar. Micropaleont., 5*, 321–325.

3. Raffi, I., J. Backman, E. Fornaciari, H. Pälike, D. Rio, L. Lourens, and F. Hilgen (2006), A review of calcareous nannofossil astrobiochronology encompassing the past 25 million years, *Quat. Sci. Rev.,* 25, 3113–3137.

4. Young J. R. (1998), Neogene, in: *Calcareous nannofossil biostratigraphy, British Micropalaeontological Society Series,* edited by P. R. Bown , pp. 225–265, Kluwer Academic Publishers, Dordrecht, Nederland.

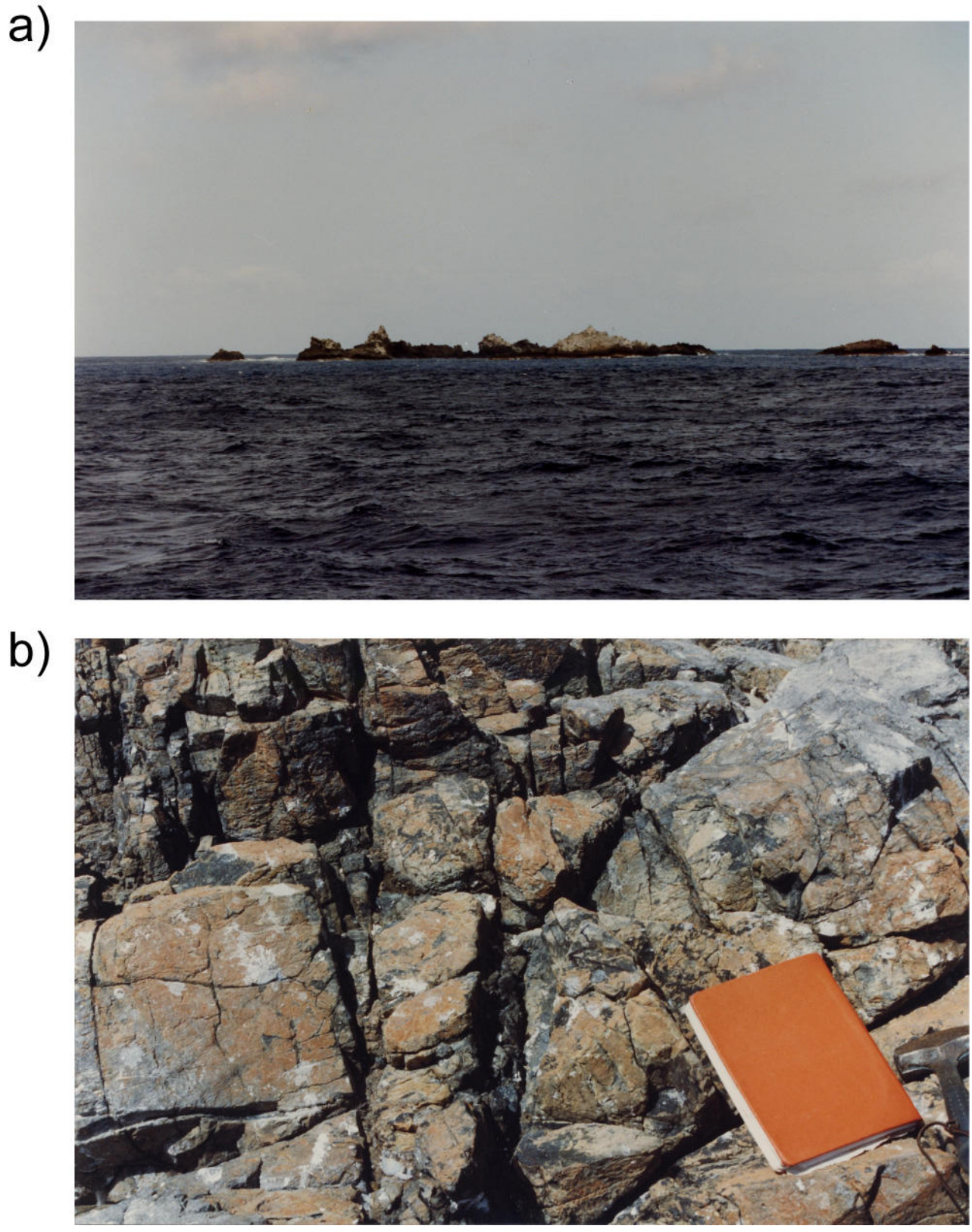

Figure 5.9 *St Peter and St Paul Rocks. (a) View of the islands from the R/V Strakhov; (b) outcrop of peridotite rocks.*

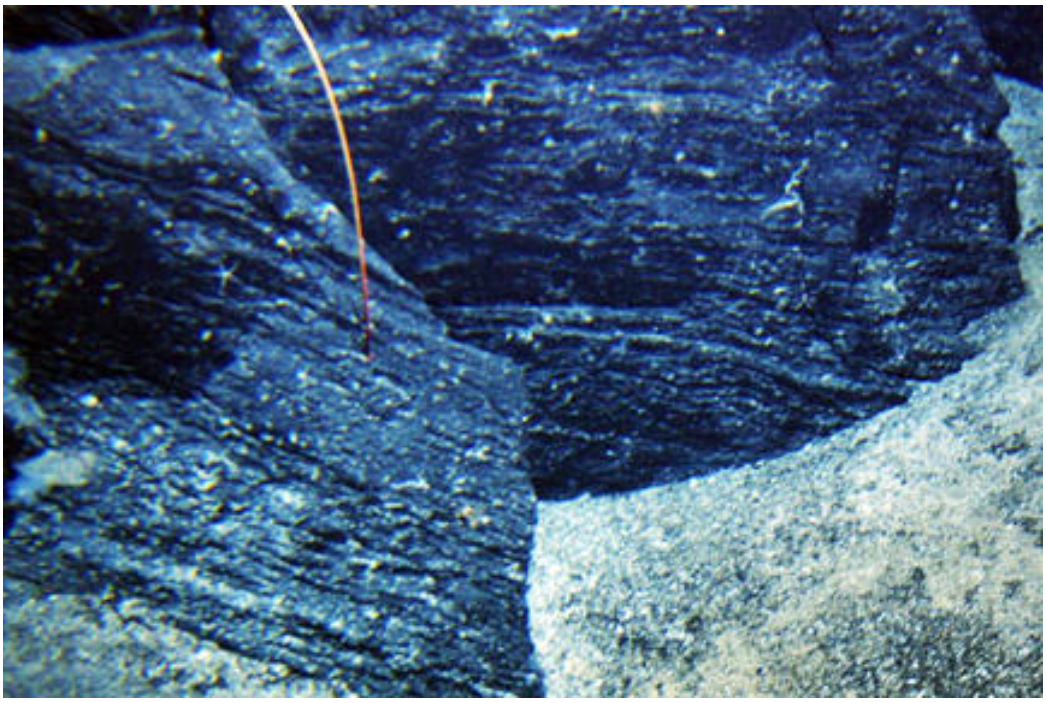

Figure 5.10. *JAMSTEC Shinkai 6500 submersible still photo of a weathered and pitted outcrop of foliated gabbro at 1500-m depth taken on Dive 647 at 32°50.05'S, 57°15.70'E on an outward facing fault at the southern end of the Atlantis Bank.*

Chapter 6

Rhodalgal-Foramol facies in equatorial carbonates: insights from Miocene oceanic tectonic sunken islands (central Atlantic)

Corda L. and C. Palmiotto
In preparation for *"Palaeogeography, Palaeoclimatology, Palaeoecology"*

Abstract

Shallow-water carbonates ranging in thickness from 250 to 500 m have been deposited during the Miocene on the summit of transverse ridges flanking the Romanche and Vema transforms that offset the equatorial Mid-Atlantic Ridge. These carbonate platforms are dominated by the same biota assemblages consisting of perforate larger benthic foraminifera and red algae. Corals are present occasionally as minor components.

We propose that equatorial upwelling and humid conditions may have created the conditions suitable for the predominance of calcitic organisms over aragonitic corals. We discuss also additional factors (i.e. elevated CO_2 levels, hydrothermal brine fluxes, rivers-related nutrient input, biological-induced precipitation processes, substratum stability or instability and platform geometry) that could have played a significant role in favouring specific features that characterize our Atlantic carbonates relative to other known examples from the equatorial realm.

6.1 Introduction

Differences between warm-water and temperate carbonate systems have been widely discussed [*Lees and Buller*, 1972; *Nelson et al.,* 1988; *James,* 1997; *James and Lukasik*, 2010]; however, differences and variations within warm-water carbonates are not yet well-known. Despite a growing number of studies on modern and ancient shallow-water carbonate and mixed depositional environments, some aspects are not yet sufficiently clarified, i.e., the number of potential factors affecting the carbonate production in equatorial realm, their specific role, relative effects and mutual relationships.

The aim of this study is to provide new insights into equatorial carbonate systems. We will evaluate whether the abundance of larger benthic foraminifera and red algae associations together with the occurrence of ooids within the equatorial Atlantic during Late Miocene, was controlled predominantly by nutrient availability, or by other factors including salinity, water transparency and mid-ocean ridges hydrothermal brines.

6.2 Geological background

We analysed shallow-water carbonates dredged from tectonic sunken islands Vema, Romanche A and Romanche C in the equatorial Atlantic (Figure 6.1) [*Bonatti et al.,* 1983; *Bonatti et al.,* 1994a; *Bonatti et al.,* 1994b; *Bonatti et al,* 2005; *Gasperini et al.,* 1997]. These sunken islands were at sea level during the Miocene [*Palmiotto et al.,* 2013] and they represent the summit of the transverse ridges adjacent to the Vema and Romanche transform faults that offset the equatorial Mid-Atlantic Ridge respectively by 320 and 900 km.

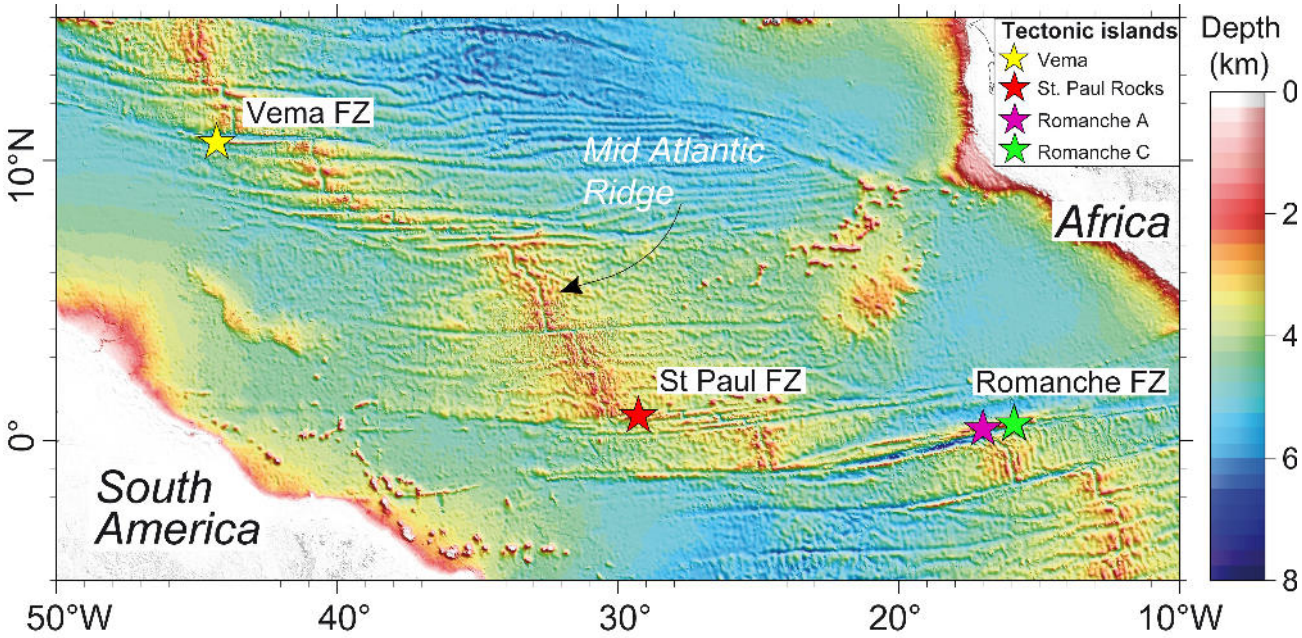

Figure 6.1. *Location of tectonic islands in equatorial Atlantic Ocean. FZ= Fracture Zone. Bathymetry data are from General Bathymetric Chart of the Oceans (GEBCO_08 grid). This map was performed using the GMT [Wessel and Smith, 1995].*

Multichannel seismic reflection profiles acquired along the Vema and Romanche transverse ridges have detected strong seismic horizontal reflectors separating an upper seismic-stratified sequences, formed by sedimentary rocks, from a lower seisemic-non-stratified sequences, formed by oceanic crust and upper mantle rocks [*Bonatti et al.,* 1983; 1993; 1994; 2005]. The horizontal Reflector R is an erosive surface; this implies that the summit of the transverse ridges emerged above sea level forming narrow islands that subsequently underwent subsidence and erosion at sea level. These sunken islands were subsequently capped by a thick unit of shallow-water carbonates during the Miocene; vertical tectonic motions have been suggested to explain the uplift and sink of the Vema and Romanche tectonic islands [*Gasperini et al.,* 1997; *Bonatti et al.,* 1983; 1994a; 1994b; *Bonatti et al.,* 2005; *Palmiotto et al.,* 2013].

The southern transverse ridge of the Vema transform at 11° N reaches over 3 km above the predicted lithosphere thermal contraction level, forming a large topographic positive anomaly (Figure

6.2). It consists of a sliver of oceanic lithosphere [*Bonatti et al.,* 2005] truncated by an erosive surface (Reflector R) and capped by 400-500 m of platform carbonates. The growth of the platform has been interrupted by a fast sinking in the Late Miocene and today its summit is ~500 m below sea level.

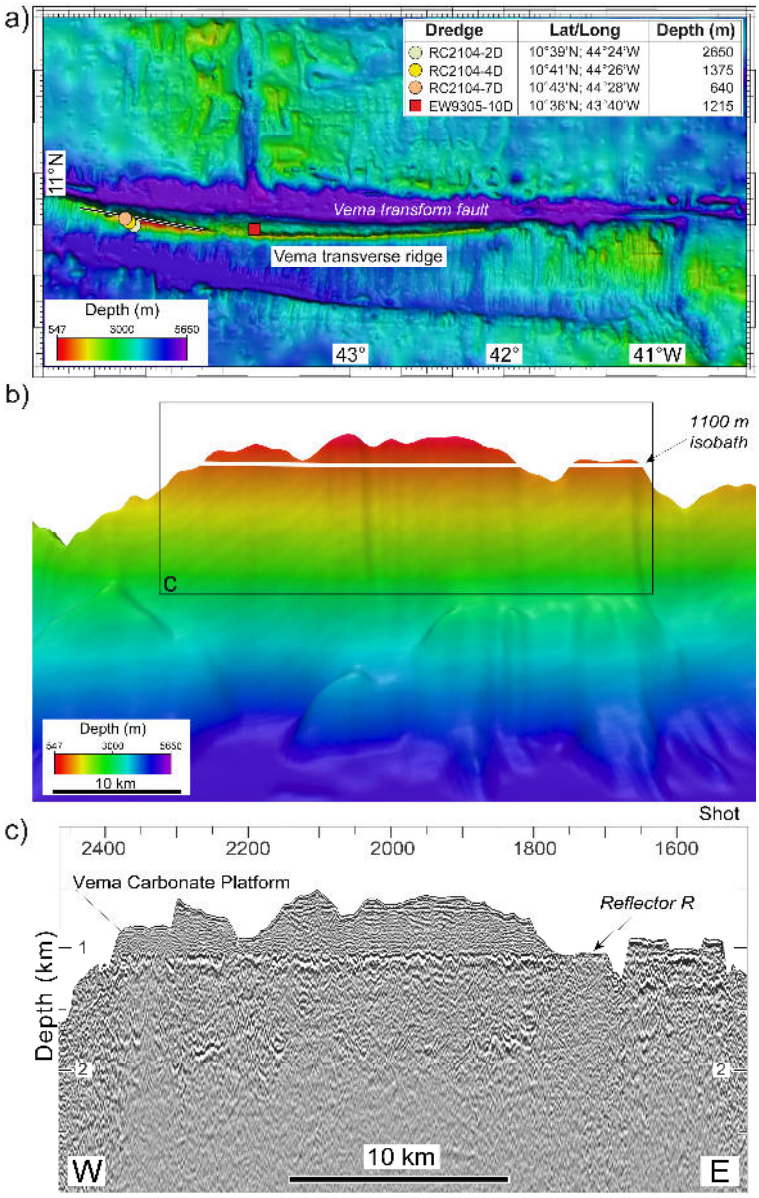

Figure 6.2. *Vema transform fault. a) Bathymetric 2D map (data from Bonatti et al., 2003). Location of dredges along the Vema southern transverse ridge and of the seismic profile VEMA-02; b) Bathymetric 3D map of a portion of the Vema transverse ridge. Box c shows the seismic profile VEMA-02; c) Multichannel seismic reflection profile VEMA-02 (Bonatti et al., 2005; Palmiotto et al., 2013) shows that the summit of the Vema transverse ridge was at sea level, forming Vema Paleoisland. Reflector R indicates the non-conformity between the basement and the sedimentary unit. Spatial analysis and mapping were performed using the GMT [Wessel and Smith, 1995] and PLOTMAP [Ligi and Bortoluzzi, 1989] packages.*

Very close to the Equator, the northern transverse ridge of the Romanche transform-reaches ~ 4 km above the level predicted by thermal subsidence (Figure 6.3). It is constituted by a block of oceanic lithosphere uplifted above sea level, eroded and capped by about 250-300 m of shallow-water carbonates. Subsequently, the platform underwent a rapid drowning up to its present depth, ~ 900-1100 m below sea level.

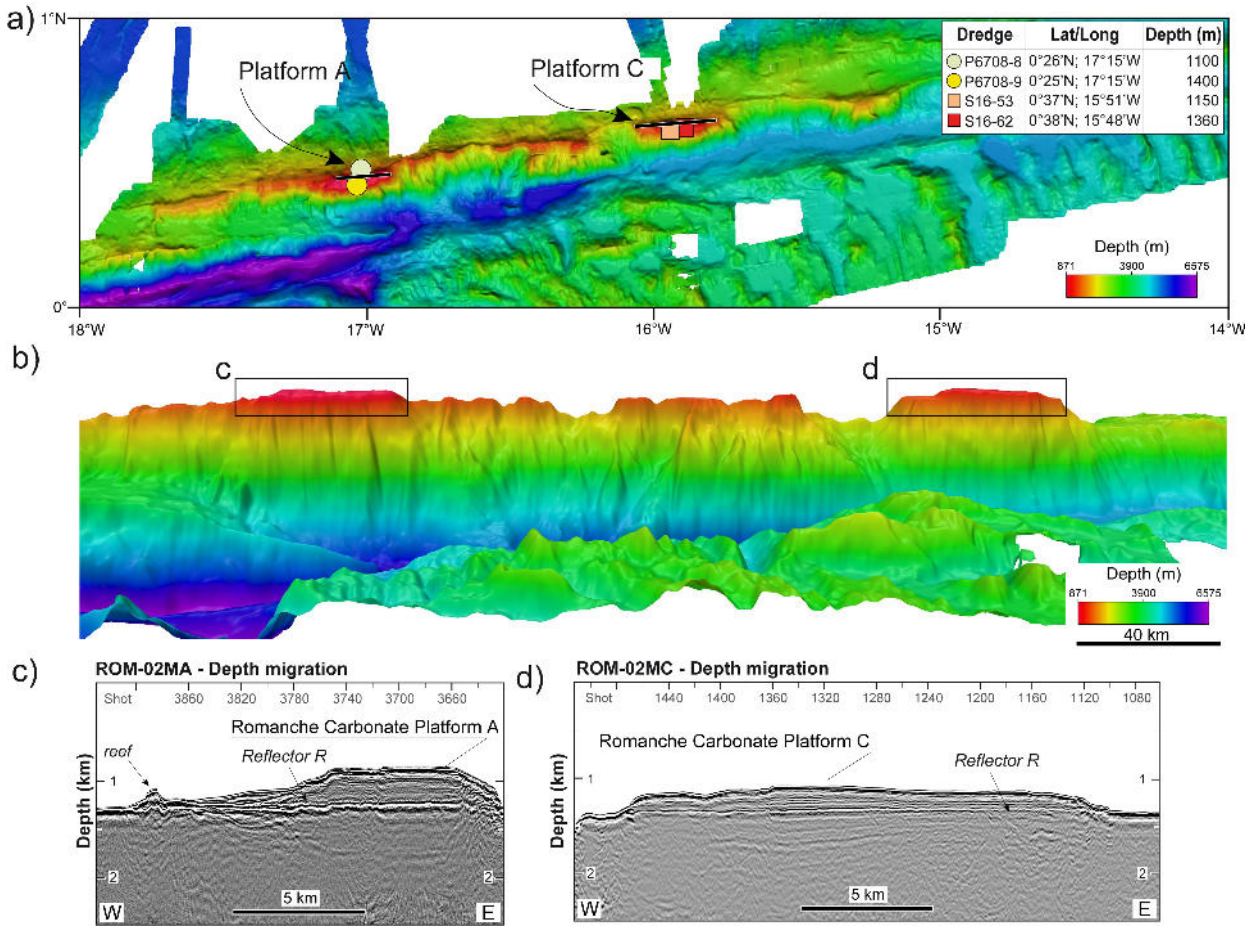

Figure 6.3. *Romanche eastern ridge – transform intersection.* **a)** *Bathymetric 2D map obtained by merging our data (Gasperini et al., 1997) with those of EQUAMARGE2, CONADAK and ROMANCHE1 cruises (IFREMER). Location of dredges along the Romanche northern transverse ridge and of the seismic profiles ROM-02MA and ROM-02MC.* **b)** *Bathymetric 3D map of a portion of the Romanche transverse ridge. Boxes c and d show seismic profiles ROM-02MA and MC.* **c)** *Multichannel seismic profile ROM-02MA (Gasperini et al., 1997; Palmiotto et al., 2013) shows that the summit of the Romanche transverse ridge was at sea level, forming Romanche Paleoisland A;* **d)** *Multichannel seismic profile ROM-02MC [Gasperini et al., 1997; Palmiotto et al., 2013] shows that the summit of the Romanche transverse ridge was at sea level, forming Romanche Paleoisland C. Spatial analysis and mapping were performed using the GMT [Wessel and Smith, 1995] and PLOTMAP [Ligi and Bortoluzzi, 1989] packages.*

Biostratigraphical analyses on thin section from the basal part of the Romanche platform (occurrence of *Miogypsina)* suggest Early Miocene for the base of the carbonate deposition. Strontium-isotope ages carried out on samples from the Romanche platform extends from 10 to 6 Ma [*Palmiotto et al.,* 2013]. No ages are available for drowning facies. The strontium ages obtained on Vema platform carbonates fall around 11 Ma; the age of the drowning facies is at 7 Ma [*Palmiotto et al.,* 2013].

6.3 Facies analyses

Carbonate samples were dredged from the top and the flanks of the sunken islands Vema, Romanche A and Romanche C (Figures 6.2 and 6.3) [*Bonatti et al.* 1977; *Bonatti et al.,* 1983; *Gasperini et al.,* 1997]. In this work, we will present results of facies analyses from new post-1983 cruises samples and from a restudy of old samples.

Based on texture, structure and biotic assemblages a variety of shallow-water microfacies have been recognized representing different depositional environments. A thin crust rich in ferromanganese oxides and phosphates separating the neritic carbonates from the overlying planktonic mudstones-wackestone has been frequently observed in many dredged samples (Figure 6.4). These mineralized surfaces testify the rapid sinking and drowning of the Atlantic platforms.

6.3.1 Vema platform

The recognized microfacies have been grouped into 5 main facies (V1-V5) reflecting different environments from middle and inner ramp to inter-tidal environment (more details in Table 6.1). Facies V1 (Figure 6.5) has been recovered from all the sectors of the Vema Platform (western, central and eastern portion), facies V2 from the western portion of the platform, facies V3 (Fiure 6.5), V4, V5 from the eastern part. Although there is a considerable variability in the Vema shallow-water deposits, they

are typically dominated by *rhodalgal-foramol* sediment associations having red algae, larger foraminifera and small benthic foraminifera as main components, whereas no real reef facies have been recognized. Even if the facies analysis has been carried out only on dredging points, based on texture and components, we assume a ramp or a flat-topped shelf geometry for the Vema platform.

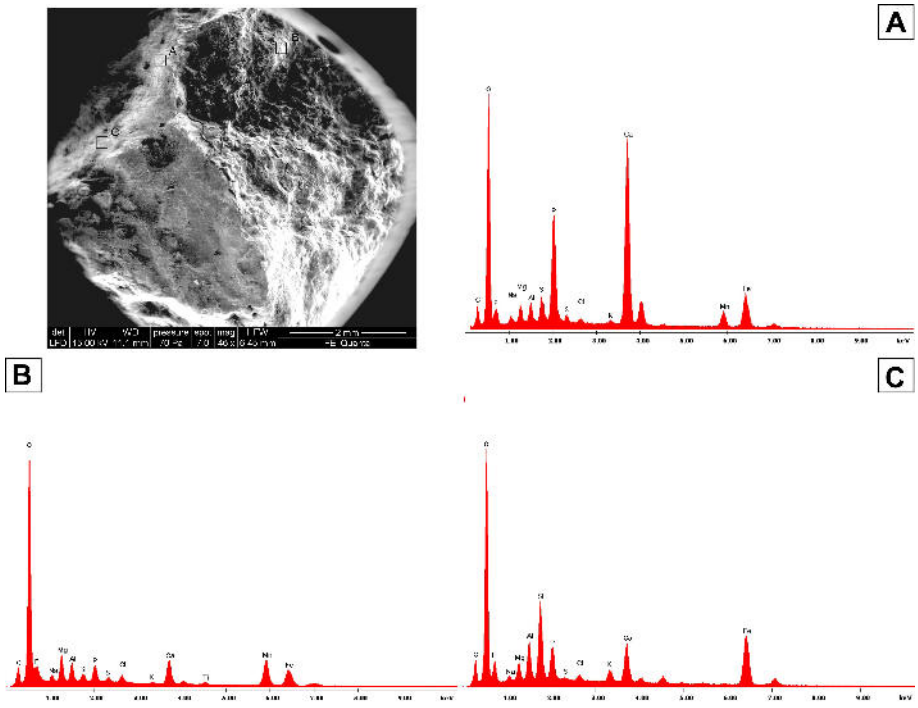

Figure 6.4 *Scanning Electron image (SEM) of the mineralized crust separating the shallow-water carbonates from the overlying planktonic-rich deposits. SEM-EDS elemental spectra of the crust. [A]: predominant phosphates (high P and Ca contents), [B]: predominant Mn-Iron-oxides, [C]: predominant Iron-oxides.*

6.3.2 Romanche platforms

Romanche carbonate samples were dredged from two different sunken islands along the Romanche northern transverse ridge. The recognized microfacies have been grouped into 8 main facies (Figure 6.5); RA1-3 from Romanche A and RC1-5 from Romanche C. Biota assemblages include red algae, larger benthic foraminifera and subordinate corals; ooids are also significant components. The observed microfacies associations probably reflect production and accumulation on a rimmed shelf consisting of a variety of environments from intertidal to subtidal with localised reefs or shoals (more details in Table 6.2).

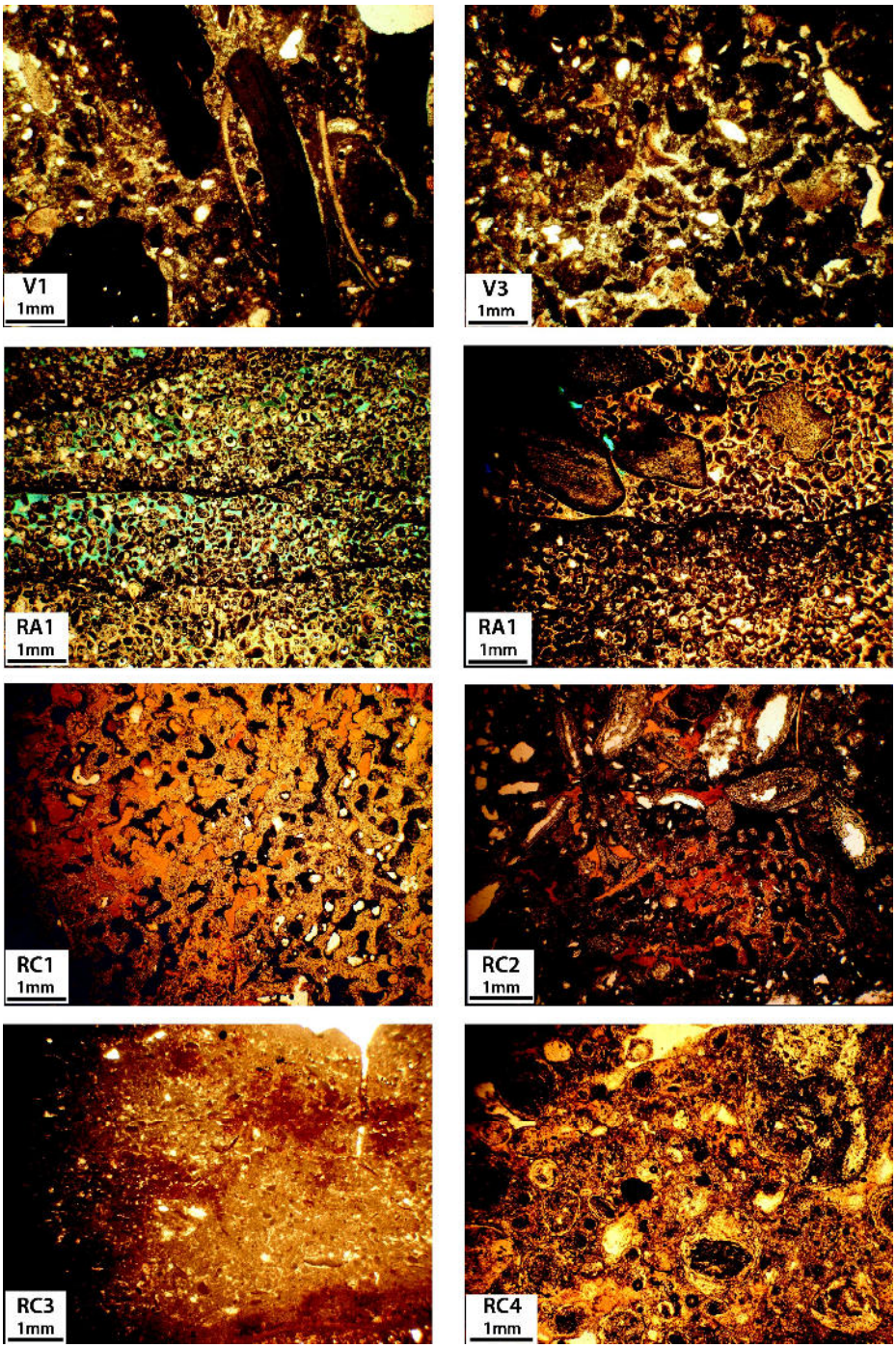

Figure 6.5 *Photomicrographs of some carbonate facies of Vema and Romanche platforms. Facies V1: red-algae floatstone with a fine-grained bioclastic matrix; facies V3: moderately well-sorted bioclastic packstone rich in red-algae fragments; facies RA1 (left): laminae of oolitic grainstone separated by microbial mats; facies RA1 (right) superposition of laminae of oolitic grainstone with different grain size, the upper one appear as a "shelly lag" rich in echinoids fragments; facies RC1: coral framestone (Porites); facies RC2: packstone-floatstone with larger foraminifera (Migypsina), the intense leaching of Miogypsina tests document fresh-water diagenesis; facies RC3: peloidal wackestone with desiccation shrinkage; facies RC4: oncoidal wackestone with leaching derived cavities. Scale bar = I mm.*

6.4 Palaeoenvironmental interpretation of Vema and Romanche shallow-water carbonates

6.4.1 Controlling factors

Although the Vema and Romanche Miocene low-latitude platforms fall into the warm water realm, some of the recognized features are in agreement whereas some others are at odds with models derived from their warm water counterparts. The identified carbonate biofacies, with dominance of perforate larger benthic foraminifera and red algae and the paucity-or-absence of coral communities, consist typically of rhodalgal associations, and do not conform completely to the perceived views on warm-water carbonates as reported from literature [i.e. *Lees and Buller,* 1972; *Nelson*, 1988]. On the contrary, the occurrence of oolitic-rich facies is consistent with examples from arid-tropical platforms [*Lees,* 1975; *Opdyyke and Wilkinson,* 1990].

We will try to evaluate how Atlantic equatorial carbonate systems may have responded to possible controlling factors (as temperature, nutrients, climate, oceanographic setting, ocean chemistry and platform morphology), and which of them are dominant:

a) *Temperature.* The role of temperature changes over carbonate biogenic associations has long been recognized [*Lees and Buller,* 1972, *Lees,* 1975; *James,* 1997; *Mutti and Hallock,* 2007]. Modern tropical and subtropical ocean basins, within 20° to 30° of the Equator, are dominated by coral-rich facies associations [*Sclanger and Konishi,* 1975], because the temperature constrains for coral reef development is between 23°C and 25°C [Veron, 1995];

b) *Water fertility.* Nutrient concentration in ocean waters may influence profoundly shallow-water communities and particularly reef development [*Hallock and Schlager,* 1986; *Carannante et al.,* 1988; *Hallock*, 2001; *Pomar,* 2001; *Brandano and Corda,* 2002; *Mutti and Hallock,* 2003; *Halfar and*

Mutti, 2005; *Wilson and Vecsei*, 2005; *Brandano et al.,* 2010a]. High seawaters fertility favors calcite-dominated biota assemblages and it is responsible for non coral-dominated communities even in the tropics;

c) *Rainfall*. Rainfall rates may also have a significant impact on the "carbonate factory" (particularly on reef growth) resulting in considerable clastic input and related water turbidity, lowered aragonite saturation, paucity of marine cement precipitation due to rainfall dilution, intensive leaching and meteoric diagenesis [*Wilson,* 2002];

d) *CO_2 levels*. It is inferred that increased CO_2 levels both in atmosphere and in seawater (by accelerating weathering and increasing surface-water productivity and by reducing carbonate saturation) may control skeletal assemblages favoring calcite-dominated organisms [*Pomar and Hallock,* 2007; *Brandano et al.,* 2010b];

e) *Substratum stability*. Corals are apparently non able to tolerate substrates covered by coarse clastics [*Maniwavie et al.,* 2001] and may be inhibited to grow as reef communities capable of forming real reefs, whereas both larger benthic foraminifera and coralline algal rhodoliths, are often associated with unstable substrates [*Testa and Bosence,* 1999]. In addition, substratum instability due to the continuous seismic activity along the oceanic transform faults [*Sykes,* 1967] may control the carbonate factory of the tectonic islands;

f) *Platform geometry.* Carbonate platforms characterized by long and very narrow shape, with very steep slopes such as the tectonic islands *sensu Palmiotto et al.* [2013], could influence the type of carbonate production/accumulation because of the reduced space for coral communities to grow and prograde.

6.4.2 Discussion

The low-latitude platform carbonates from Vema and Romanche transforms developed during the Miocene time and are typically dominated by rhodalgal association with absence of corals or with corals forming only local rims and patch reefs (Figure 6.5, facies RC1).

Lower and Middle Miocene carbonates display a wide worldwide distribution of reefs [*Fransen et al.,* 1996]; extensive occurrence of coral reefs are reported also during the Late Miocene on a number of Pacific atolls [*Bourrouilh-Le Jan and Hottinger,* 1988] as well as in the Caribbean [*Collins et al.,* 1996] and Mediterranean regions [*Esteban,* 1996]. Similarly, *Wilson* [2008] reports that the coral-dominated facies continue to be important in SE Asia from Early Miocene to the present. In summary, although the Miocene is a time climatically favorable to coral reefs, our Atlantic platforms show a clear dominance of coralline red-algal facies. As a consequence, we discard temperature as the dominant control on Atlantic biota community.

Rhodalgal lithofacies are known to develop extensively in nutrient-rich waters and to predominate under mesotrophic and slightly eutrophic conditions [*Carannante et al.,* 1988, *Hallock,* 2001; *Pomar,* 2001; *Brandano and Corda,* 2002; *Mutti and Hallock,* 2003; *Halfar and Mutti,* 2005; *Wilson and Vecsei,* 2005; *Brandano et al.,* 2010a]. A number of features characterizing our Atlantic carbonates suggest a significant role exerted by an excess in nutrient levels that are: the abundance of micritization and bioerosion processes; the ubiquitous presence of planktonic foraminifera (frequently displaying incipient coatings and also occurring as nuclei of ooids in the oolitic grainstone facies); a strongly bioeroded and mineralized crust with phosphates and ferromanganese oxides separating the shallow-water carbonates from the overlying planktonic-rich deposits. *Mutti and Bernoulli* [2003] have provided evidence of the role of the trophic resource control on microbial micrite formation and phosphate mineralization.

In addition, the equatorial realm coincides with a high productivity upwelling belt [*Larson et al.,* 1995; *Wilson,* 2002; *Wilson,* 2008] where high rainfall, with related terrestrial run-off, and strong upwelling may account for the high fertility of seawaters. As shown by some Miocene equatorial carbonates from Indonesia [*Wilson,* 2002; *Wilson & Evans,* 2002; *Wilson,* 2008], organisms found to be tolerant to higher nutrient input, include some larger benthic foraminifera, pectinids, coralline algae and echinoids; many corals (i.e. hermatypic corals) appear to be less tolerant. Accordingly, the latitude of the Atlantic platforms, suggests water fertility as a significant controlling factor.

Additional features displayed by the Atlantic carbonates provide evidences also for high levels of humidity, such as: dissolution at a grain-scale and leaching-related signatures affecting the carbonates during temporary subaerial exposures; absence of evaporites; general paucity of isopachous and radiaxial cements or their occasional occurrence exclusively within the facies representing high-energy environments, particularly in the windward sides facing the open ocean (i.e. V1, RC1). All these features suggest similarities with examples from equatorial realm rather then with other well-studied arid tropical environments such the Persian Gulf.

Beyond nutrients and humidity, another factor which must be considered is the geodynamic context of the platforms and its influence on seawater chemistry. The two major contributors to ocean chemistry are river water and hydrothermal brines at mid-ocean ridges [*Spencer and Hardie*, 1990]. The Atlantic carbonate platforms developed on uplifted slivers of oceanic crust-flanking the Romanche and Vema transforms that offset the equatorial Mid-Atlantic Ridge. We suggest that CO_2 pulses associated with magmatic activity along the Mid-Atlantic Ridge could have favored the calcite-dominated rhodalgal-foramol associations by lowering the carbonate ion concentration in ocean waters. It is known that aragonite secretion is energetically expensive to maintain under conditions of reduced saturation [*Hallock,* 2001]. Furthermore it is known that mid-oceanic ridges act as a huge rock-fluid ion exchange system for Ca^{2+} and Mg^{2+}. Hydrothermal circulation of seawater in the basaltic oceanic crust

modulates the Mg/Ca ratio of seawater, Ca^{2+} being released to the fluid and Mg^{2+} being extracted from seawater [*Stanley and Hardie,* 1998]. It is known that high Mg/Ca ratios favor the formation of aragonite whereas low Mg/Ca ratios favour calcite [*Morse et al.,* 1997]. As a consequence, hydrothermal fluxes from the Mid-Atlantic Ridge, may have lowered the Mg/Ca mole ratio in seawater favouring calcitic skeleton carbonate producers (rhodalgal-foramol associations) and hindering reef building organisms. In contrast, *Snow and Dick* [1995] and *Ligi et al.* [2013] report that when sea water reacts with mantle-derived peridotites, significant amounts of Mg can be released from the rock into the ocean, rising the Mg/Ca ratio. Nevertheless the evaluation on the quantitative ratio of ion exchanges between seawater and basalts *vs.* seawater and peridotites is still a matter of debate. If we assume that the Mid-Atlantic shallow waters, where the Romanche and Vema carbonates developed, suffered the hydrothermal alteration predominantly of the immediately underlying basaltic substratum, it seems likely to interpret the low-Mg/Ca ratio as a significant factor limiting the growth of framework fabrics in that justifying the poor occurrence of chlorozoan facies in Romanche platform respect other platforms reported in the equatorial realm (e.g. framework fabrics have been detected only in facies RC1 at Romanche C).

Ultimately, we surmise that equatorial upwelling and humid conditions could have increased surface-water productivity, plankton blooms and absorption of light in shallow waters. The combination of the two cited conditions together with CO_2 input in seawater (and related reduced saturation state) and hydrothermal brine fluxes in the basaltic substratum (and related lowered Mg/Ca mole ratio) provided the potential for the "rhodalgal-foramol" associations and thus created conditions suitable for development of carbonate platforms with limited or no framework reef development.

It cannot be excluded, however, that the stability of the substrate may have further influenced the first colonizing carbonate communities. It is worth remembering that the seismic horizontal reflectors separating the carbonate rocks from the underlying crustal basalts (Figures 6.2c and 6.3c-d)

represent surfaces of erosion of the uplifted crustal blocks at a sea level; during subsequent phases of subsidence this surface was colonized by carbonate communities [*Palmiotto et al.,* 2013]. Accordingly, it is likely that the first shallow-water carbonates of the Atlantic platforms developed predominantly as shifting carbonate sands on a mobile clastic volcanic substrate and consequently the low stability of the eroded substrate could have further contributed to limit the growth of reefal communities.

A possible confirmation of our hypothesis about the prominence of the above cited factors may come from St. Peter and Paul's Rocks, the only modern example of oceanic tectonic island. These uninhabited islets are located in the active zone of the St. Paul transform fault, in the equatorial Atlantic. The Rocks are the summit of a sigmoidal feature called St. Peter and St. Paul Massif, costituited of an seismically active 8-9 Ma old lithosphere. This small archipelago is characterized by the absence of reef-builders and the dominance of coralline algae in associations with bryozoans, polychaete worm tubes and gastropods [*Campos et al.,* 2010]. We assume that the typical "rhodalgal" assemblage of St. Peter and Paul's Rocks should be related to the interaction between multiple factors such as: elevated rainfall rate (and related lowered water salinity), sea water nutrient enrichment due to the interaction between oceanic currents and the submarine relief [*Feitoza et al.,* 2003], substratum instability related to the strong seismic activity [*Wolfe et al.,* 1993]. Transcurrent and transpressive seismic epicenters [*Wolfe et al.,* 1993] and high-resolution bathymetry indicate that the St. Peter and St. Paul Massif is affected by a left-overstep along the right-lateral fault that causes transpressive uplift [*Palmiotto et al.,* 2013]. It is however to be considered that the continuous uplifting of the oceanic island (present uplifting has been calculated by *Campos et al.* [2010] at 1.5 mm/a) may have strongly inhibited the development of a well productive carbonate platform.

6.5 Vema equatorial carbonates vs Romanche equatorial carbonates: what caused the differences?

The Romanche and Vema platforms developed in the equatorial Atlantic respectively very close to the equator and at 11°N. Specific features of equatorial carbonate systems [*Wilson and Vecsei,* 2005; *Wilson,* 2012], commonly include: extensive foramol-rhodalgal deposits and, sometimes contemporaneous shallower water chlorozoan facies; lack of coated grains; poor preservation of peloids; lack of associations with evaporites; extensive vadose dissolution.

Overall the biota associations of the Vema and Romanche platforms (Tables 6.1 and 6.2), and St. Paul's Rocks as well, are consistent with the equatorial realm where they developed; nevertheless, some specific features do not conform completely and need to be further assessed, i.e.:

1) absence of coral reef frameworks at Vema platform

2) occurrence of ooid-rich facies in Romanche platform.

The absence of coral buildups at the Vema platform, in contrast with their occurrence, even if limited, at the Romanche platform, needs a further explanation. It is known that the upper trophic limit for coral reef development and particularly of the chlorophyll concentration, that is considered a proxy for nutrients, approximate average values of 0.3 mg/m^3 [*Hallock,* 2001]. If environmental conditions remain under intermediate mesotrophic to eutrophic conditions, photozoan association such as corals, may be locally present even if in low abundance and diversity [*Halfar et al.,* 2004]. *Wilson and Vecsei* [2005] report the occurrence, even if non extensive, of coral reefs at shallow-water depths in all warm-water regions. The latitudinal location of the Vema transform ridge (11° N) is comparable to the Caribbean reef of northern Venezuela. The extensive reef building of this region (Falcón Basin) suffered, by the Early Miocene, a general decline that was attributed to changes in regional water quality [*Edinger and Risk,* 1994, *Von der Heydt and Dijkstra,* 2005]. In particular *Johnson et al.* [2009]

suggest that the assumed switch in the outlet position of an ancestral Orinoco River might have caused the regional decline in reef building by altering surface-water characteristics, just as modern Orinoco and Amazon outflows exert strong control on shallow-water habitats off the coast of northeastern South America. Based on observation from space, *Hu et al.* [2004] demonstrate the influx on open ocean waters of materials deriving from adjacent continents over distances exceeding 2000 km. These authors report patches of low-salinity surface waters dominated mostly by colored dissolved organic material and secondary by chlorophyll, away from the mouth of the Orinoco river between 60°W and 40°W. The present position of the drowned Vema carbonate platform is approximately between 45° W and 44° W. Considering the spreading rate of the crust south of the Vema transform calculated from 10 Ma to present (approximately at 13.6 mm/a after *Bonatti et al.*, 2005) it is likely to presume a further proximity of the Miocene Vema carbonate platform to the Orinoco discharge that could have strongly influenced the carbonate producing biota by inhibiting the coral communities to grow.

Concerning the occurrence of coral buildups at the Romanche paleoislands, it is worth to note that the coral reef communities grew exclusively along the eastern Platform C. We interpret the growth of coral reefs, albeit of limited extension, along the eastern Romanche platform as a consequence of its greater distance (relative to the Vema platform) from the South-American river influence, being the modern high productivity zone related to African rivers not significant off the coastal environments [*Jansen and Van Iperen,* 1991; *Binet et al.,* 1995]. Therefore, a possible nutrient input from the East is here discarded.

In addition, many modern analogues for ancient carbonate platforms, show the influence of the prevailing wind directions on the type of carbonate production. The occurrence of reefal facies exclusively at the windward side of the Romanche platform is consistent with many examples from the Atlantic Ocean, Bahamian platform [*Gebelein,* 1974], from the western Pacific Ocean and from SE Asia platforms [*Wilson and Vecsei,* 2005] where framework-built marginal reefs mostly developed on

margins facing into the prevailing wind-related current directions. We suggest that the persistence of wind-generated waves on the eastern side of the Romanche platform, lying within the Trade Wind Belt, could have promoted mixing of the surface waters, thus helping the growth of patch reefs.

The extensive occurrence of oolitic facies at the leeward side of the Romanche platform appears to be at odd with modern and ancient counterparts from the equatorial realm and not sufficiently justified by the significant upwelling of nutrient-rich deeper waters on the western side induced by the predominant Trade Winds. Marine ooids are particularly well developed around the tropics at approximately 25° north and south when salinity exceeds 35.8 ‰; they are commonly lacking in equatorial carbonates [*Lees,* 1975; *Opdyyke and Wilkinson,* 1990; *Wilson,* 2002; *Wilson*, 2012]. No modern ooid shoals are reported on mid-ocean atolls [*Scoffin,* 1987] with very few exceptions from the Pacific Ocean [*Rankey and Reeder,* 2009]. Overall, coated grains and evaporite formation are commonly interpreted as features indicating arid tropical regions. At equatorial latitudes surface waters exhibit decreased saturation values that primarily reflect reduced CO_3^{2-} concentration due to the higher CO_2 of upwelling water [*Broeker and Peng*, 1982] but in part reflecting higher rainfall and lower evaporation [*Opdyke and Wilkinson,* 1990]. Salinities for the modern equatorial platforms vary between 31‰ and 32‰. These values, that may not represent factor limiting coral development (salinity tolerance for reef corals is given as 25‰ and 42‰, *Coles and Jokiel,* 1992), may exert a major control on ooid formation.

Traditional theories stress that ooids are almost wholly physico-chemical precipitates; nevertheless there is considerable evidence that biological processes (mostly cyanobacteria) may play a significant role in ooid formation in otherwise unfavourable conditions [*Mitterer,* 1971; *Suess and Futterer,* 1972]. Some oolitic laminae have been related to the formation of micrite envelops coupled with cement precipitation favoured by algal photosynthesis [*Bathurst,* 1966; *Davies et al.*, 1978; *Arenas and Pomar,* 2010]. *Pedley* [1992] and *Ford and Pedley* [1996] highlighted a close genetic link

between marine stromatolites and biomediated tufas; these authors also inferred that in many cases, i.e. for the travertines formation, much of the precipitation is biomediated by means of procaryote-microphyte biofilms (microbial communities mostly dominated by diatoms, cyanobacteria and heterotrophic bacteria).

The extensive micrite formation (intense micritization, micrite envelops, biofilms) and bioerosion displayed by our Atlantic equatorial carbonates, the intense phosphatization of the oolitic facies and the unusual presence of planktonic foraminifera as nuclei of ooids, are all features consistent with high levels of nutrients. Increased nutrient availability may stimulate the growth of microbes algae and infaunal suspension feeders [*Halloch and Schlager,* 1986; *Perrin et al.,* 1995], and in general the growth of algal-bacterial mats.

Our carbonates show diffuse and intense occurrence of iron-oxides crusts (Figure 4). It is demonstrated by experiments in the equatorial Pacific Ocean [*Coale et al.,* 1996] that the addition of iron ions in sea waters may induce a significant physiological response resulting in a massive phytoplancton bloom, mostly diatoms. Also *Larson and Erba* [1999] report that some excess hydrothermal metals, such as iron, may "fertilize" areas of normal biological productivity causing increasing in microbiota communities. We propose that hydrothermal brine fluxes related to the Mid-Atlantic Ridge, may have injected iron ions into shallow waters promoting diatoms blooms, and consequently may have favored precipitation of oolitic laminae biomediated by microbial communities also under unfavorable conditions of water saturation.

Based on the above, we surmise that possible factors promoting ooid-facies formation at the Romanche platform were: a) phytoplancton bloom and related biomediated precipitation induced by iron-rich hydrothermal brines; b) increased ions Ca^{+2} from hydrothermal alteration of the underlying basaltic crust.

The absence of oolitic deposits at the Vema platform, developed under geodynamic conditions similar to those of the Romanche platforms, may be due to the major influence of the freshwater plumes of the Amazon and Orinoco rivers. The modern freshwater plume from the Amazon covers a wide area of the Atlantic from 0°-15° N and 50°-60°W [*Chérubin and Richardson,* 2007]. However, other factors may influence the growth of oolitic sediments (i.e: influence of tides vs. waves and geomorfics patterns) [*Rankey et al.,* 2011]. According with these authors, given comparable physicochemical ocean conditions both for Vema and Romanche platforms, we propose that other variables such as paleomorphology of the substratum or hydrodinamism could have played an inhibiting factor for oolitic-sands development at the Vema platform.

6.6 Summary and conclusions

The overall predominance of calcitic larger benthic foraminifera and coralline algae over aragonitic corals in the equatorial Atlantic platforms has been related to:

a) high nutrient concentrations and reduced water clarity;

b) humid conditions and related reduced salinities and increased water fertility;

c) elevated CO_2 levels (associated to magmatic activity along the Mid-Atlantic Ridge);

d) decreased values in Mg/Ca ratio (from hydrotermal alteration of oceanic basaltic substratum);

e) geometry of substratum and instability of the carbonate platforms.

At the Vema platform these main controlling factors were associated with a significant water plume from the Orinoco river and its related nutrient input and plankton blooms. This additional mechanism may be responsible for hindering the potential for framework development at Vema, in contrast with the presence, even if limited, of coral reef facies at Romanche.

The interesting development of oolitic shoals at Romanche platform developed within a clear equatorial realm has been related to biological-induced precipitation favoured by excess hydrothermal metals such as iron.

Acknowledgements

Thanks are due to E. Bonatti (LDEO-Columbia University; Ismar-CNR) for his advise. We are grateful to M. Ligi (Ismar-CNR) and G. Bortoluzzi (Ismar-CNR) for helping out with the open source software GMT ("General Mapping Tools") and with the software "PLOTMAP".

References

Arenas, C., and L. Pomar (2010), Microbial deposits in upper Miocene carbonates, Mallorca, Spain, Palaeogeography, Palaeoclimatology, Palaeoecology, 297, 465 – 485.

Binet et al (1995), The influence of runoff and fluvial outflow on the eosystems and living resources of west African coastal waters, *FAO Fischeries Technical Paper, 349*.

Bonatti, E., D. Brunelli, W. R. Buck, A. Cipriani, P. Fabretti, V. Ferrante, L. Gasperini, and M. Ligi (2005), Flexural uplift of a lithospheric slab near the Vema transform (central Atlantic): timing and mechanisms, *Earth Planet. Sci. Lett., 240*, 642–655.

Bonatti, E., Ligi, M., Gasperini, L., Peyve, A., Raznitsin, Y. & Chen, Y.J. (1994). Transform migration and vertical tectonics at the Romanche fracture zone, equatorial Atlantic. *Jour. Geophys. Res.* , *99,* 21779-21802.

Bonatti, E., M. Ligi, L. Gasperini, G. Carrara, and E. Vera (1994a), Imaging crustal uplift, emersion and subsidence at the Vema Fracture Zone, *Eos Trans., AGU, 75,* 371-372.

Bonatti, E., M. Ligi, L. Gasperini, A. Peyve, Y. Raznitsin, and Y. J. Chen (1994b), Transform migration and vertical tectonics at the Romanche fracture zone, equatorial Atlantic, *J. Geophys. Res., 99,* 21779–21802.

Bonatti, E., Sartori, R. & Boersma, A. (1983). Vertical crustal movements at the Vema Fracture Zone in the Atlantic: evidence from dredged limestones. *Tectonophysics*, 91, 213-216.

Bonatti, E., Sarnthein, M., Boersma, A., Gorini, M. & Honnorez, J. (1977). Neogene crustal emersion and subsidence of the Romanche Fracture Zone, equatorial Atlantic. *Earth Planet Sci. Lett.*, 35, 369-383.

Brandano M., M. Brilli, L. Corda, and M. Lustrino (2010), Miocene C-isotope signature from the central Apennine successions (Italy): Monterey versus regional controlling factors, *Terra Nova, 22*, 125–130.

Brandano, M., and L. Corda (2002), Nutrients, sea level and tectonics: constrains for the facies architecture of Miocene carbonate ramp in central Italy, *Terra Nova, 14*, 257–262.

Broecker, W. S., and T. H. Peng (1984), The role of $CaCO_3$compensation in the glacial to interglacial atmospheric CO2 change, *Global Biogeochemical Cycles, 1*, 15 – 29.

Campos, T. F. C., F. H. R. Bezerra, N. K. Srivastava, M. M. Vieira, and C. Vita-Finzi (2010), Holocene tectonic uplift of the St Peter and St Paul Rocks (Equatorial Atlantic) consistent with emplacement by extrusion, *Mar. Geol., 271*, 177–186.

Carannante G., M. Esteban, J. D. Milliam, and L. Simone (1988), Carbonate lithofacies as paleolatitude indicators: problems and limitations, *Sedimentary Geology, 60,* 333–346.

Coale, K. H., S. E. Fitzwater, R. M. Gordon, K. S. Johnson, and R. T. Barber, Control of community growth and export production by upwelled iron in the equatorial Pacific Ocean, Nature, 379, 621 – 624.

Coles, S. L., and P. L. Jokiel (1992), Effect of salinity of Coral Reefs. In: Connell, D. H., and D. H. Hawiser (eds), Pollutiun in tropical acquatic systems, CRC Press Inc, London, 147 – 166.

Collins, L.S., A. F., Budd, and A. G. Coates (1996), Earliest evolution associated with closure of the tropical American Seaway, *Proc. Natl. Acad. Sci. USA, 93,* 6069–6072.

Davies, P. J., B. Bubela, and J. Ferguson (1978), The formation of ooids, Sedimentology, 25, 703–730.

Edinger, E. N., and M. Risk (1994), Oligocene-Miocene extinction and geographic restriction of Caribbean Corals: roles of Turbidity, Temperature and Nutrients, *Palaios, 9,* 576–598.

Esteban, M. (1996), An overview of Miocene reefs from Mediterranean areas: general trends and facies models. In: Franseen, E., Esteban, M., Ward, W.C., Rouchy, J.M. (Eds.), Models for Carbonate

Stratigraphy from Miocene Reef Complexes of the Mediterranean Regions: Society of Economic Paleontologists and Mineralogists, Concepts in Sedimentology and Paleontology Series, 5, 3–53.

Feitoza, B. M., L. A. Rocha, O. J. Luiz-Junior, S. R. Floeter and J. L. Gasparini (2003), Reef fishes of St. Paul's Rocks: new records and notes on biology and zoogeography, *Aqua, Journal of Ichthyology and Aquatic Biology, 7,* 61 – 82.

Ford, T. D., and H. M. Pedley (1996), A review of tufa and travertine deposits of the world, *Earth Science Reviews, 41,* 117-175.

Fransen et al., (SEPM)

Gasperini, L., E. Bonatti, M. Ligi, R. Sartori, A. Borsetti, A. Negri, A. Ferrari, and S. Sololov, (1997), Stratigraphic numerical modeling of a carbonate platform on the Romanche transverse ridge, equatorial Atlantic, *Mar. Geol., 136,* 245–257.

Gebelein, C. D. (1974), Guidebook for Modern Bahamian Platform Environments, *Geol. Soc. American*, Annual meeting.

Halfar, J., and M. Mutti (2005), Global dominance of coralline red-algal facies: A response to Miocene oceanographic events, *Geology, 33*, 481– 484.

Halfar, J., L. Godinez-Orta, M. Mutti, J. E. Valdez-Holguín, and J. M. Borges (2004), Nutrient and temperature controls on modern carbonate production: an example from the Gulf of California, Mexico, *Geology, 32,* 213–216.

Hallock, P., 2001. Coral reefs, carbonate sediments, nutrients, and global change. In: Stanley, G.D. (Ed.), The History and Sedimentology of Ancient Reef Systems. Kluwer Academic and Plenum Publishers, New York, pp. 387–427.

Hallock, P., and W. Schlager (1986), Nutrient excess and the demise of coral reefs and carbonate platforms, *Palaios, 1*, 389–298.

Hottinger, L. (1988), Conditions for generating carbonate platforms, Memorie Società Geologica Italiana, 40, 265 – 271.

Hu C., E. T. Montgomery, R. W. Schmitt, and F. E. Muller-Karger (2004), The dispersal of the Amazon and Orinoco River water in the tropical Atlantic and Caribbean Sea: observation from space and S-PALACE floats, *Deep-Sea Res. PT II, 51*, 1151–1171.

James, N. P. (1997), The cool-water carbonate depositional realm, in *Cool-Water Carbonates, SEPM Special Publication*, vol. 56, edited by N. P. James, and J. Clarke, pp. 1–20, Tulsa, Oklahoma.

James, N. P., and J. J. Lukasik (2010), Cool and cold water carbonates. In James, N. P., and Dalrymple, R. W. (eds), Facies models 4, Geological Association of Canada, St. John's, Newfoundland, 369 – 398.

Jansen, J. H. F. and, J. M.Van Iperen (1991), A 220,000-year climatic record for the east equatorial Atlantic Ocean and equatorial Africa: Evidence from diatoms and opal phytoliths in the Zaire (Congo) deep-sea fan, *Paleoceanography, 6,* doi: 10.1029/91PA01631.

Johnson et al. (2009)

Larson, R. L., and E. Erba (1999), Onset of the mid-Cretaceous greenhouse in the Barremian–Aptian: igneous events and the biological, sedimentary, and geochemical responses, *Paleoceanography, 14,* 663–678.

Larson, R. L., E. Erba, M. Nakanishi, D. D. Bergersen, and J. M. Lincoln (1995), Stratigraphic vertical subsidence and paleolatitudinal histories of Leg 144 Guyot,. *Proc. Ocean Drill. Program, Sci. Results, 144*, 915–933.

Lees, A. (1975), Possible influence of salinity and temperature on modern shelf carbonate sedimentation, *Mar. Geol., 19*, 159–198.

Lees A., and Buller A.T. (1972), Modern temperate-water and warm-water shelf carbonate sediments contrasted, *Marine Geology, 13*, 67–73.

Ligi, M., E. Bonatti, M. Cuffaro, and D. Brunelli (2013), Post-Mesozoic Rapid Increase of Seawater Mg/Ca due to Enhanced Mantle-Seawater Interaction, Scientific reports, 3 1-8.

Maniwavie, T., J. Rewald, J. Atisi, T. P. Wagner, and P. L. Munday (2001), Recovery of corals after volcanic eruptions in Papua New Guinea, *Coral Reefs, 20,* 24.

Mitterer, R. M. (1971), Influence of natural organic matter on CaCO3 precipitation: in Mitterer, R. M. and O.P. Bricker (Ed.), Carbonate Cements, Johns Hopkins Univ. Press .

Morse, J. W., Q. W. Wang, and M.Y Tsio (1997), Influences of temperature and Mg/Ca ratio on $CaCO_3$ precipitates from seawater, *Geology, 25,* 85–87.

Mutti, M., and P. Hallock (2003), Carbonate systems along nutrients and temperature gradients: some sedimentological and geochemical constraints, *Int. J. Earth. Sci., 92*, 465–475.

Nelson, C. S., S. L Keane, and P. S. Head (1988), Non-tropical carbonate deposits on the modern New Zealand shelf, *Sediment. Geol., 60*, 71–94.

Opdyke, B. N., and B. H. Wilkinson (1990), Paleolatitude distribution of Phanerozoic marine ooids and cements, *Palaeogeography, Palaeoclimatology, Palaeoecology, 78,* 135 – 148.

Palmiotto, C., L. Corda, M. Ligi, A. Cipriani, H. J. B. Dick, E. Douville, L. Gasperini,, P. Montagna, F. Thil, A. Borsetti, B. Balestra, and E. Bonatti (2013), Non-volcanic tectonic islands in ancient and modern oceans, *Geochemistry Geophysics Geosysyems,* doi: 10.1002/ggge.20279.

Pedley, H. M. (1992), Freshwater (Phytoherm) reefs: the role of biofilms and their bearing on marine reef cementation, *Proc. Yorks Geol. Soc., 46,* 141 – 152.

Perrin, C., D. Bosence, and B. Rosen (1995), Quantitative approaches to palaeozonation and palaeobathymetry of corals and coralline algae in Cenozoic reefs. In: Marine Palaeoenvironmental Analysis from Fossils (Eds D. W. J. Bosence and P. A. Allison), *Geol. Soc. London Spec. Publ., 83,* 181–229.

Pomar, L ., (2001) Ecological control of sedimentary accommodation: evolution from a carbonate ramp to rimmed shelf, Upper Miocene, Balearic Islands. *Palaeogeography, Palaeoclimatology, Palaeoecology,* 175, 249-272.

Pomar, L., and P. Hallock (2007), Changes in coral-reef structure through the Miocene in the Mediterranean province: adaptive versus environmental influence, *Geology, 35*, 899–902.

Rankey, E. C, and S. L. Reeder (2011), Holocene oolitic marine sand complexes of the Bahamas: *Journal of Sedimentary Research*, *81*, 97–117.

Rankey, E. C., Reeder, S. L.., and Garza-Perez, R. (2011), controls on links between geomorphical and surface sedimentological variability: aitutaki and maupiti atolls, south pacific ocean, *Journal of Sedimentary Research, 81,* 885-900.

Rankey, E. C., and S. L. Reeder (2009), Holocene ooids of Aiutaki Atoll, Cook Islands, South Pacific, *Geology, 37,* 971-974.

Schlanger, S. O., and K. Konishi (1975), The geographic boundary between the Coral-Algal and Bryozoan-Algal limestone facies: a paleolatitude indicator, IX Internal. Congr. Sedimentol., Nice.

Scoffin, T. P. (1987), An introduction to carbonate sediments and rocks, Blackie and Son, Bishopbriggs, Glasgow.

Snow, J.E., and H. J. B. Dick (1995), Pervasive magnesium loss by marine weathering of peridotites, *Glochim Cosmoch Acta, 59,* 4219–4235.

Spencer, R. J., and L. A Hardie (1990), Control of seawater composition by mixing of river waters and mid-ocean ridge hydrothermal brines, in Spencer, R.J., and Chou, I.-M., eds., Fluid-mineral interactions: A tribute to H.P. Eugster: Geochemical Society Special Publication, 19, 409–419.

Stanley, S. M., and L. A Hardie (1998), Secular oscillations in the carbonate mineralogy of reef-building and sediment-producing organisms driven by tectonically forced shifts in seawater

Suess, E., and D. Futterer (1972), aragonitic ooids: experimental precipitation from seawater in the presence of humic acid, *Sedimentology, 19*, 129 – 139.

Testa, V., and D. W. J. Bosence (1999), Physical and biological controls on the formation of carbonate and siliciclastic bedforms on the north-east Brazilian shelf, *Sedimentology,46,* 279–301.

Tucker, M. E., and V. P. Wright (1991), Carbonate Sedimentology: Oxford, Wiley Blackwell, p.496.

Veron, J. E. N. (1995), *Corals in Space and Time. The Biogeography and Evolution of the Scleractinia*, Cornell Univ. Press, Ithaca.

Von der Heyd, A., and A. Dijkstra (2005), Flow reorganizations in the Panama Seaway: A cause for the demise of Miocene corals?, Geophys., Res., Lett., 32, doi:10.1029/2004GL020990.

Wilson, M. E. J. (2002), Cenozoic carbonates in Southeast Asia: implication for equatorial carbonate development, *Sediment. Geol., 147*, 295–428.

Wilson M.E.J. (2008), Global and regional influences on equatorial shallow-marine carbonates during the Cenozoic, *Palaegeography Palaeclimatology Palaeoecology, 265,* 262-274.

MEJ Wilson, MJ Evans, Sedimentology and diagenesis of Tertiary carbonates on the Mangkalihat Peninsula, Borneo: implications for subsurface reservoir quality, Marine and petroleum geology,19, 873-900.

Wilson, M. E. J., and A. Vecsei (2005), The apparent paradox of abundant foramol facies in low latitudes: their environmental significance and effect on platform development, *Earth Sci. Rev., 69,* 133–168.

Table 6.1 Carbonate samples and microfacies of Vema platform.

Sample	Facies	Texture and components	Environment
RC2104-4D/A RC2104-4D/B RC2104-4D/C RC2104-4D/A1 RC2104-4D/B1 RC2104-4D/C1 RC2104-4D/C2 EW9305-10D/1D	V1	Medium-to coarse-grained floatstone-rudstone with larger with red algae, often in the form of rhodoliths, and larger foraminifera (*Amphistegina).* Subordinately fragments of echinoids, bryozoans and small benthic foraminifera, pelecypods and planktonic foraminifera are also present. Corals are rare. Cracks and sedimentary dykes may affect this facies.	Moderate to deeper parts of the photic zone (inner-middle ramp)
RC2104-2D/A RC2104-7D/A	V2	Pebbly mudstone with planktonic foraminifera, benthonic skeletal debris with carbonate clasts (often bioeroded) and volcanic clasts.	Platform slope
EW9305-10D/3 Sedimentary-dike in: EW9305-10D/1D	V3	Well-sorted, medium-grained bioclastic packstone, mostly represented by red-algae fragments, with occasional floating rhodoliths and fragments of *Porites.* This facies has been recognized also as sedimentary-dykes fillings within the microfacies V1.	Inner ramp
EW9305-10D/3 EW9305-10D/1C	V4	Oncoidal wackestone containing planktonic foraminifera with frequent incipient coatings. Intergranular space and voids with isopacous and meniscus cement. Intense micritization.	Subtidal-intertidal
EW9305-10D/11 EW9305-10D/5 EW9305-10D/1A EW9305-10D/1B	V5	Wackestone-packstone with planktonic foraminifera. Not completely lithified.	Pelagic environment

Table 6.2 Carbonate samples and microfacies of Romanche platforms

Island	Sample	Facies	Texture and components	Environment
Romanche A	P6707B-8/1A (LC11) P6707B-8/1B (LC18) P6707B-8/1C (LC17) P6707B-8/2 P6707B-8/3 P6707B-8/4 P6707B-8/5A (LC 7) P6707B-8/5B (LC 8) P6707B-8/6A (LC9) P6707B-8/6B (LC10) P6707B-8/10 (Pill10) P6707B-8/11 (Pill11) P6707B-8/12 (Pill12) P6707B-8/12B (LC14) P6707B-8/13A (LC16) P6707B-8/XA	RA1	Oolitic grainstone with subordinate coarse-grained fragments of echinoids. Mostly superficial ooid whose nuclei are frequently planktonic foraminifera tests. Good sorting and cross laminations. Alternating beds with different grain-size separated by microbial mats.	Mobile shoal
	P6707B-9/SL1 P6707B-8/1 (Pill1) P6707B-8/2 (Pill2) P6707B-8/9 (Pill9) P6707B-8/13 (Pill13) P6707B-8/A (LC1) P6707B-8/B (LC2) P6707B-8/C (LC3) P6707B-8/XB	RA2	Wakestone-packstone with coated grains and rare larger foraminifera. Skeletal fragments and planktonic foraminifera with incipient coatings. Irregular vugs without planar orientation have been related to chemical leaching.	Inter-subtidal with episodic exposure episodes
	P6707B-8/7 (LC6)	RA3	Packstone with planktonic foraminifera and with carbonate and volcanic lithoclasts.	Platform slope

Table 6.2 continued Carbonate samples and microfacies of Romanche platforms

Island	Sample	Facies	Texture and components	Environment
Romanche C	S16-62/3 S16-62/5 S16-62/6 S16-53/13 S16-53/14A	RC1	Floatstone-rudstone with coral fragments occurring in a packstone matrix with larger foraminifera. Framestone fabric with *Porites* colonies and encrusting red algae is also present. Isopachous cement fringes within porosities.	Platform margin and/or patch reef
	S16-53/2 S16-62/13a S16-62/13b S16-62/13b1	RC2	Packstone-floatstone to wackestone with larger foraminifera (*Miogypsina, Amphistegina*) and subordinate coral fragments in a fine-grained bioclastic matrix. Intense leaching and reddish micrite intraparticle-porosity infilling.	Inner-middle ramp (temporary exposure)
	S16-53/2	RC3	Peloidal wackestone-packstone with rare small benthonic foraminifera. Diffuse desiccation shrinkage and stromatolite-like laminae. Neptunian dykes filled by facies RC2 are present.	Inter-tidal
	S16-62/2 S16-62/8 S16-62/11 S16-62/12	RC4	Oncoidal wackestone-packstone with bio-lithoclasts. Micritization, leaching derived cavities, laminar calcrete crusts are common features.	Inter-supratidal
	S16-53/4	RC5	Rudstone-floatstone rich in planktonic foraminifera with floating coarse-grained skeletal fragments (corals, mollusks) and with bioclasts and carbonate lithoclasts.	Platform slope

Chapter 7

St. Paul Rocks (Penedos de São Pedro)

St. Paul Rocks is the only modern example of oceanic tectonic islands. These uninhabited islets are located in Atlantic Ocean (Figure 7.1), 100 north of the equator line, 990 km north-east Fernando de Noronha (Brazil) and 1890 km south-west of Senegal (West Africa).

Figure 7.1 *Location and aerial view of St. Paul Rocks (equatorial Atlantic Ocean).*

7.1 Historical Aspects

St. Paul Rocks was discovered by accident in 1511, when one of a convoy of six ships led by Don Garcia de Noronha, sailing from Brazil to the island of Sao Tome, struck the Rocks during the night [*Edward,* 1985]. The ship "Sao Pedro" was lost and the Rocks were name after her. The Rocks first appared on a chart of Jorge Reinel in 1519: he abbreviated the name of Sao Pedro in "S^{am} P^{o}". Later, all the other cartographers (including Mercator in his 1538 chart) thought that the abbreviation was "Sao Paolo". So, from the middle of nineteenth century, the complete name became "St. Paul Rocks, or Penedo de Sao Pedro" (Figure 7.2A). However, according to another theory, the double name is explained because the ship "Sao Pedro" was rescued by another vessel of the same group called "Sao Paolo" [*Campos et al.,* 2008].

According to *Edwards* [1985], from the sixteenth century on several oceanographic expeditions went to the Rocks (Figure 7.2B). In the 1799 the Captain of the ship *Perseverance*, A. Delano, visited the islets. Here marked on the absence of vegetation and the abundance of sharks and described the Rocks as "*the most dreary spot I ever saw, the sea roaring and surging on all sides*" [*Delano*, 1817]. The most famous expedition to the Rocks was that of the Captain FitzRoy and Charles Darwin aboard of H.M.S. *Beagle*, in the February 1832. Darwin was the first geologist to understand that the origin of the islets was not volcanic. In his Journal of researches into the natural history and geology of the countries visited during the voyage of H.M.S. Beagle round the world, under the command of Capt. Fitz Roy, he writes: "*It is not of volcanic origin; and this circumstance, which is the most remarkable point in its history… properly ought to exclude it from present volume. It is composed of rocks, unlike any which I have met with, and which I cannot characterize by any name, and must therefore describe…*" [*Darwin,* 1844].

In the 1942 St Paul Rocks are included in the Pernambuco State (Brazil). On June 25, 1998, the Brazilian Navy inaugurated the Saint Peter and Saint Paul Archipelago Scientific Station.

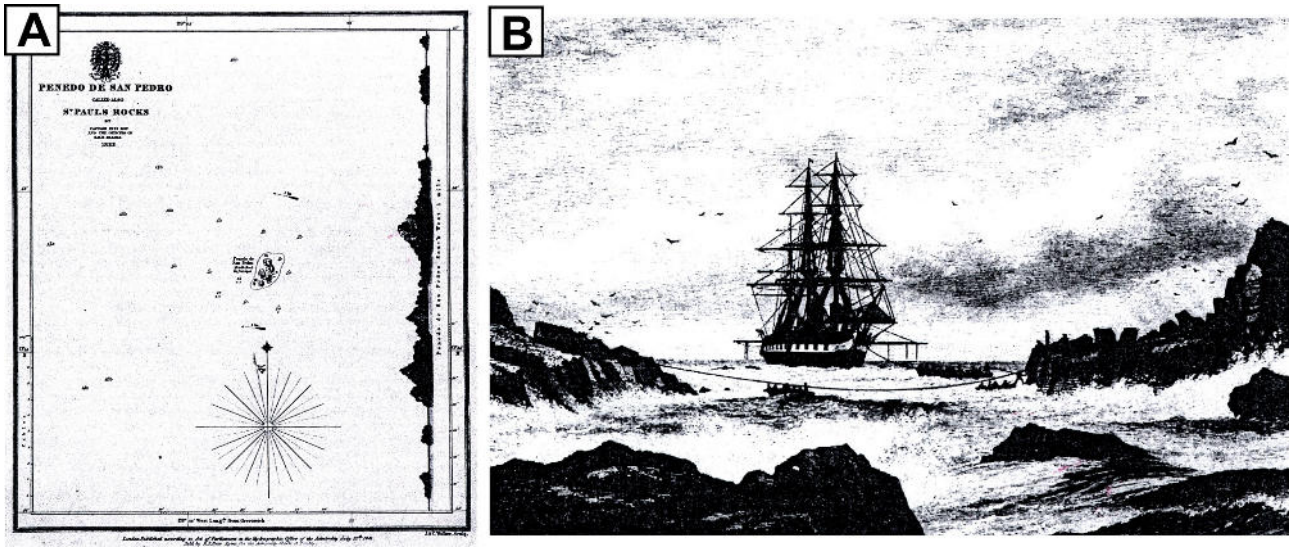

Figure 7.2 A. *Chart of St. Paul's prepared by Capt. FitzRoy and his officers during the visit of H. M. S. Beagle in 1832 when Charles Darwin scrambled ashore.* **B.** *H. M. S. Challenger at St. Paul's in August 1873* [*Tizard et al.,* 1884].

7.2 Geological and geomorphological setting

St. Paul Rocks is located in the active zone of the St. Paul transform that offsets the equatorial Mid-Atlantic Ridge by 580 km (Figure 7.3A). The Rocks are the summit of a sigmoidal feature called St. Peter and St. Paul Massif, that is part of the transverse ridge of the St. Paul transform. This massif is costituited of an seismically active 8-9 Ma old lithosphere. It is about 90 km in length and 21 km wide at the 3000 m contour line (Figure 7.3A - box) The Saint Peter and Saint Paul Massif (SPPR) can be divided in two different features (Figure 7.3B): the Southern Ridge and the Northern Ridge [*Hekinian et al.,* 2000] with a graben (~ -2500 m) thtough which runs the active transform fault. Earthquake locations and mechanisms along the western portion of the St. Paul F.Z. in the area of SPPR massif indicate that the main seismic events extend E–W direction within a band of less than 2 km wide [*Wolfe et al.,* 1993]. Transcurrent and transpressive seismic epicenters [*Wolfe et al.,* 1993] and high-resolution bathymetry indicate that the Massif is affected by a left-overstep along the right-lateral fault that causes transpressive uplift (Figure 7.3A and C).

The North Ridge is composed by fractured and mylonitized peridotites and gabbros. Ultramafics rocks can be intruded by basaltic dyke at various depths, shallower than 2700 m below sea level. The North Ridge includes the islets of St. Paul Rocks, which are now 18 m above sea level.

The South Ridge is characterized by non-mylonitized peridotite topped with a graben-like structure with basaltic outcrops. Indurated carbonate partially coated with a thin film of manganese oxides was found at 2030–1999 m depth on top of serpentinized peridotite. It consists of a rugged surface with spiny and irregular features covering a surface of more than 100 m in diameter and having a thickness of more than 15 m. This carbonate-rich material is colonized by living sponges.

The rocks of the islets are ultramafic mylonitized plutonic rocks (Figure7.4): there are no volcanic rocks on the emerged part of the archipelago [*Bonatti,* 1990; *Melson et al.,* 1972].

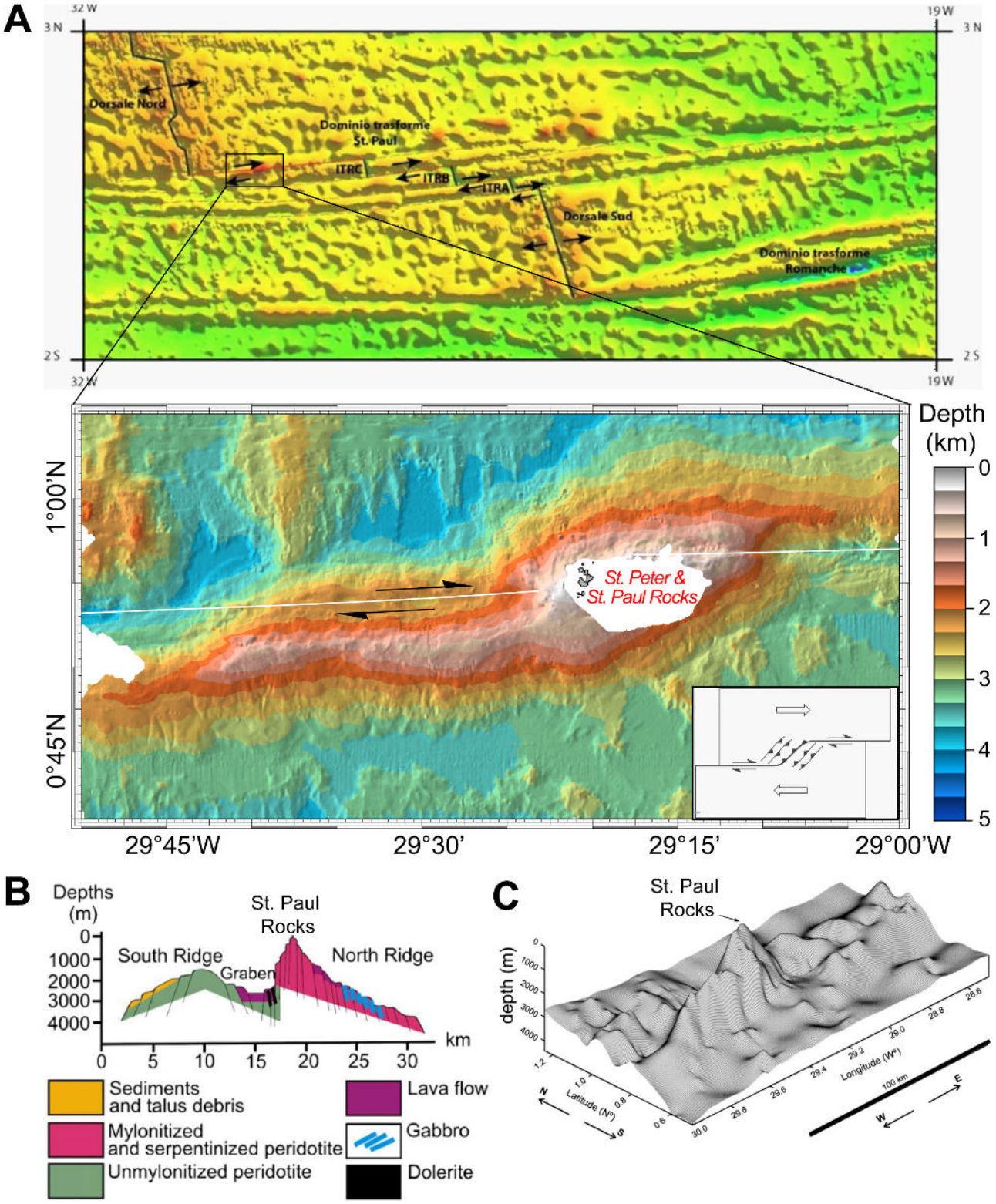

Figure 7.3 A. *Geological setting of St. Paul transform fault (equatorial Atlantic Ocean). The black box evidences the St. Peter and St. Paul Massif, and the location of St. Paul Rocks in the overstep region;* **B.** *N–S-trending interpretative cross-section of the north and south massifs in the St Paul transform decoupled by an E–W active fault* [modified from *Hekinian et al.,* 2000]; **C.** *Detailed topography of St. Peter and St. Paul Massif* [modified from *Motoki et al.,* 2009].

St. Paul Rocks is formed by 10 small islands and many rockheads (Figure 7.4); Belmonte, Sudeste, Nordeste and Cabral are the four biggest islands. The total emerged area reaches about 15,000 m^2, the distance between the extreme points reaches just 420 m, and the highest point (18 m above sea level) is located on the Nordeste Island. These islets present irregular and curvilinear, winding countours, and steep slopes (> 80° - Figure 7.4). They form a horseshoe-shape cove (Figure 7.4), with average dimension of 100 m of length, 50 m of width and just 8 m of depth. The largest islands are separated by narrow and deep channels. The morphology of St. Paul Rocks may limit accommodation space and may influence the growth of a coral communities in a zone with biological, chemical and physical favourable conditions.

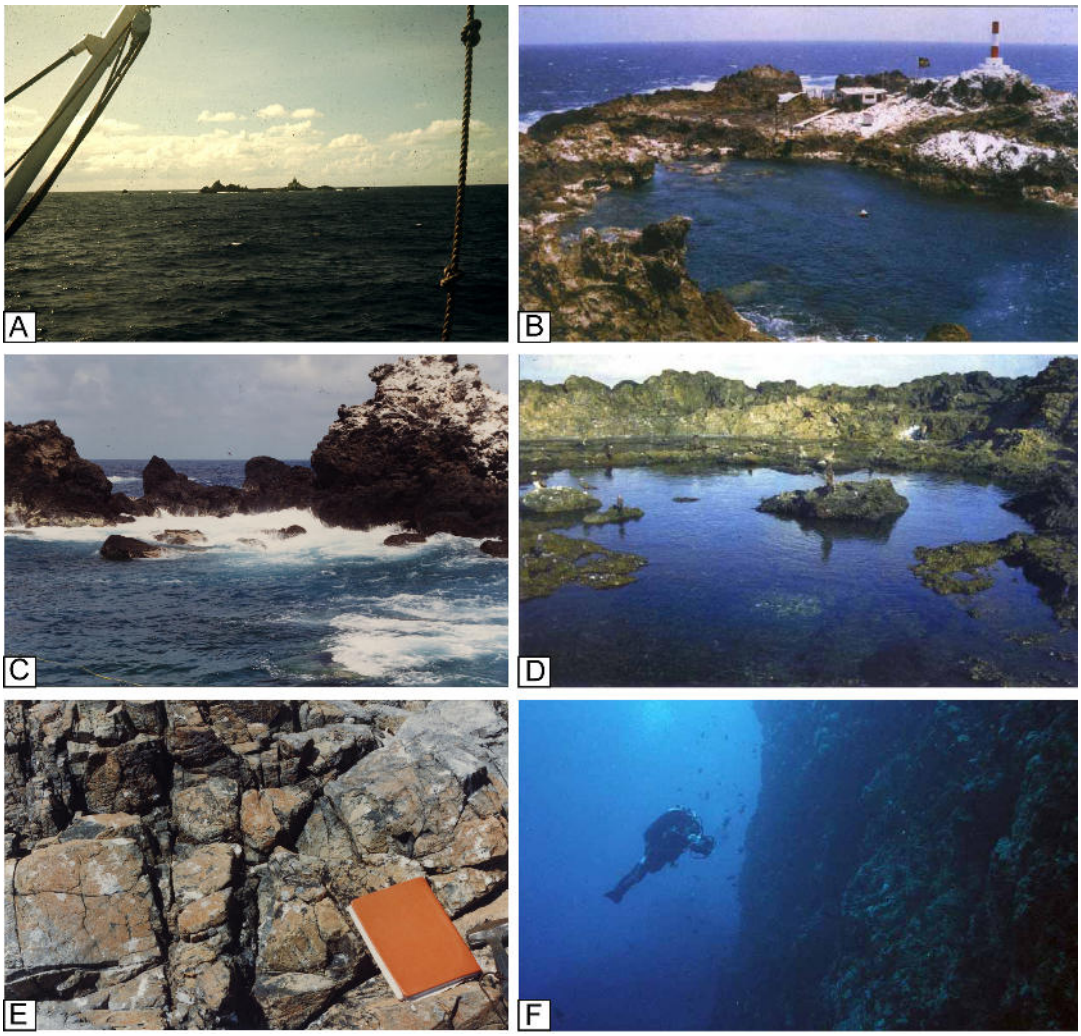

Figura 7.4 A. *View of St. Paul Rocks form the R/V Strackov;* **B.** *Bay situated between the Belmont, Challenger and Cabral Islets*; **C.** *Wave erosion of peridote rocks;* ***D****. Tide pool at Belmonte islet, it is flushed with fresh seawater at high tide*; **E.** *Outcrop of peridotite rocks of St Paul;* **F.** *Vertical clef, the typical reef habitat of St. Paul Rocks* [*Feitoza et al.,* 2003].

Two erosional terraces are present in the three largest islets (Figure 7.5), 4-5 m and 7-9 m above sea level [*Motoki et al.,* 2009], suggesting similar rates of uplift and absence of tilting in the islets. Based on ^{14}C age determinations on fossil sea level markers, the islets were subjected to uplift during the last 6,600 years at an average rate of ~1,5 mm/a [*Motoki et al*., 2009; *Campos et al.,* 2010].

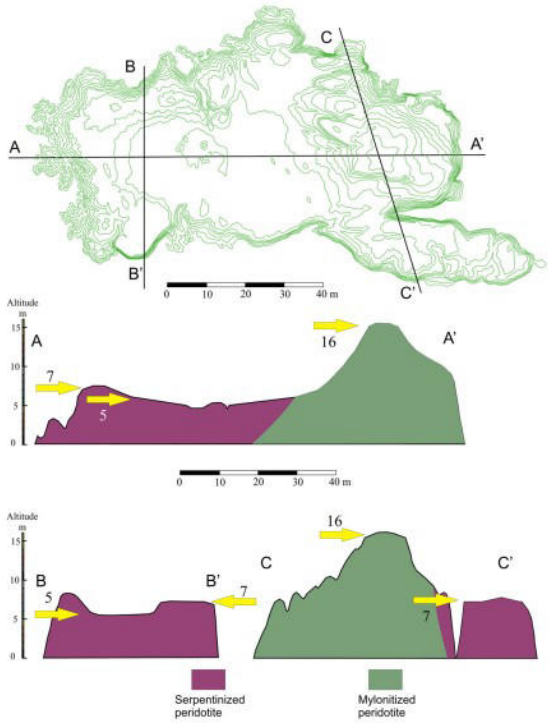

Figura 7.5 *Topographic and geological cross sections across Belmonte Islet. Yellow arrows indicate terraces and numbers indicate terrace height [Campos et al., 2010].*

7.3 Climatic and Hydrological Aspects

St. Paul Rocks is located in the equatorial system of marine currents, and it is under the direct influence of the South-equatorial current that superficially flows E-W and the submerged equatorial current flowing in the opposite direction (W-E) at depths between 60 to 100 m. This submerged current is the fastest of all equatorial currents, reaching speeds greater than about 3.6 km/h. These two currents acting together generate a sea water nutrient enrichment, due to the resurgence from the interaction with the submarine relief. The water temperature ranges from 23 to 26.5° C; the range of visibility in the seawater ranges from 12 to 30 m [*Feitoza et al.,* 2003].

Concerning the meteorological conditions, St Paul Rocks is under the direct influence of the Intertropical Convergence Zone, whose dynamics affects the rain systems of the Brazilian northeast coast. For this reason, the Rocks have among the largest pluviometric indices in the all Atlantic Ocean, and consequently, reduced superficial salinity.

7.4 Biological aspects

St Paul Rocks has a strategic geographical location, positioned at the Equator Line and in the middle of the Atlantic Ocean, between South America and Africa. For this reason, these islets influence the life cycle of many migratory species that utilize them as a shelter, feeding, and reproductive zone [*Feitoza et al.,* 2003]. The low species richness in the archipelago can be associated with its small area and consequent local microhabitat scarcity. The rocky substrate is covered by various algal species. In small marine-sandy areas of the coves species of mollusks, crustaceans, and other typical organisms were observed. St. Paul Rocks is under the influence of two important marine currents; therefore, the ichthyofauna of this archipelago is similar to that of Brazilian, Caribbean and African areas, as a result of dispersion and establishment of larvae. About 14 species of algae were observed [*Feitoza et al.,* 2003]. At the tides oscillation zone there are incrusted red algae; in the sublitoraneous region the zoanthid *Pallythoa caribeorum* (at depths from 3 to 8 m) was observed as well as numerous green algae species *Caulerpa sp*. (at depths from 3 to 30 m; Figure 7.6 A). The coral species *Madracis decactis* and *Scolymia wellsi* are concentrated at depths between 30 and 45 m. Two species of black coral (*Anthipates sp*.) were identified in the archipelago, at depths above 45 m [*Feitoza et al.,* 2003]. About 58 species of reef fishes live in the Archipelago; in contrast, there are 17 species of pelagic fishes that utilize the small region mainly as a feeding zone and as an area for reproduction [*Feitoza et al.,* 2003]. St. Paul Rocks presents a considerable degree of endemism: four species of damselfishes (*Stegastes Sanctipauli* – Figure 7.6 B*, Enneanectes smith, Chaetodon obliquus, Anthias salmonpuctatus*).

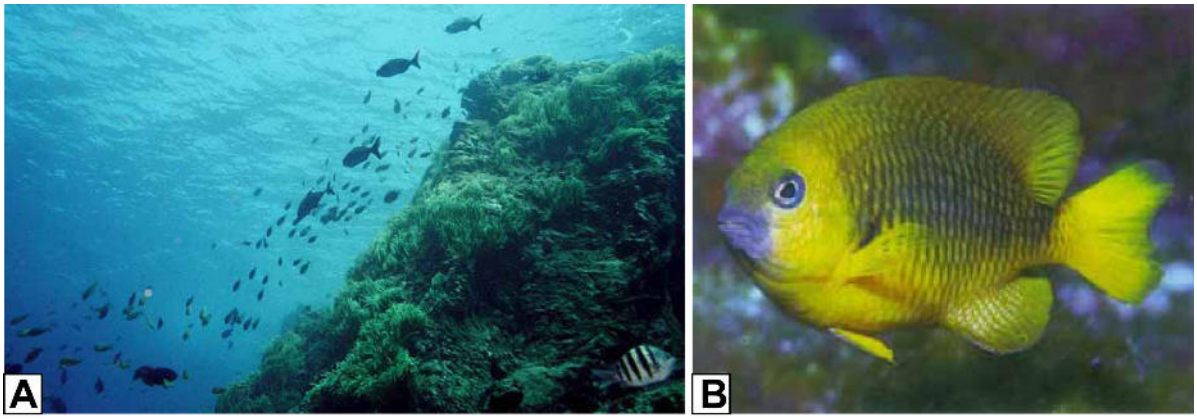

Figura 7.6 A. *Underwater view at St. Paul Rocks, with the green algae Caulerpa sp. dominating most of the sublitoral zone;* **B.** *Endemic fish of St. Paul Rocks "Stegastes Sanctipauli adult"* [*Feitoza et al.,* 2003].

Finally, the Brazilian archipelago is also a landing territory for local populations of marine birds (Figure 7.7), like the brown boobies (*Sula leucogaster*) and the brown noddies (*Anous stolidus*).

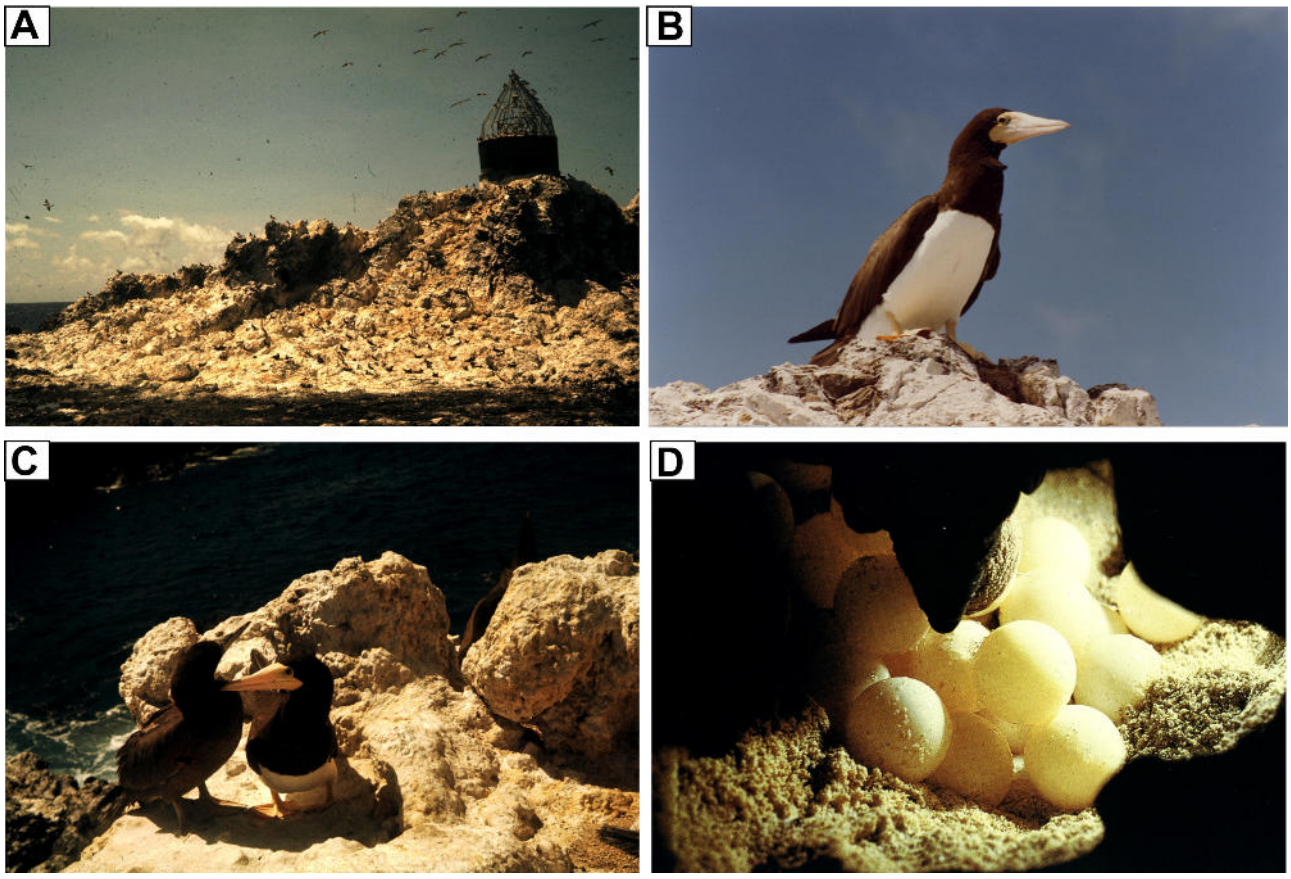

Figura 7.7 A. *The old metereological station on St. Paul Rocks;* **B.** *Male of Sula leucogaster;* **C.** *Couple of Sula leucogaster,* **D.** *Eggs of Sula leucogaster on the peridotite rocks of St. Paul Rocks.*

References

Bonatti, E. (1990), Subcontinental mantle exposed in the Atlantic Ocean on St.Peter-Paul islets, *Nature, 345*, 800 – 802.

Campos, T. F. C., F. H. R. Bezerra, N. K. Srivastava, M. M. Vieira, and C. Vita-Finzi (2010), Holocene tectonic uplift of the St Peter and St Paul Rocks (Equatorial Atlantic) consistent with emplacement by extrusion, *Mar. Geol., 271*, 177–186.

Campos, T. F. C., J. Das V. Neto, N. K. Srivastava, R. A. Petta, L. A. Hartmann, J. F. Silveira de Moraes, L. Mendes, S. R. M. Silveira (2008), Saint Peter and Saint Paul's Archipelago, Tectonic uplift of infra-crustal rocks in the Atlantic Ocean, SIGEP 002, Geological and Palaeontological Sites of Brazil.

Darwin, C. R. (1844), Geological observations on the volcanic islands visited during the voyage of H.M.S. Beagle, together with some brief notices of the geology of Australia and the Cape of Good Hope. Being the second part of the geology of the voyage of the Beagle, under the command of Capt. Fitzroy, R.N. during the years 1832 to 1836. Smith Elder and Co., London.

Delano, A. (1817), Narrative of voyages and travels in the northern and southern hemispheres; comprising three voyages around the world; together with a voyage of survey and discovery in the Pacific Ocean and oriental islands, *Boston,* 598.

Edward, A. J. (1985), Saint Paul's Rocks: a bibliographical review of the natural history of a MidAtlantic Island, *Archives of Natural History, 12,* 31 – 49.

Hekinian ,R., T. Juteau, E. Gràcia, B. Sichler, S. Sichel, G. Udintsev, R. Apprioual, and M. Ligi (2000), Submersible observations of equatorial atlantic mantle: the st. paul fracture zone region, *Marine Geophysical Researches, 21,* 529 – 560.

Feitoza, B. M., L. A. Rocha, O. J. Luiz-Junior, S. R. Floeter and J. L. Gasparini (2003), Reef fishes of St. Paul's Rocks: new records and notes on biology and zoogeography, *Aqua, Journal of Ichthyology and Aquatic Biology, 7,* 61 – 82.

Melson, W.J., Hart, S.R., Thompson, G. (1972), St. Paul's Rocks, Equatorial Atlantic: Petrogenesis, Radiometric Ages, and Implications on Sea-Floor Spreading, *The Geological Society of America ,Inc. Memory, 132.*

Motoki, A., S. E. Sichel, T. F. C. Campos, N. K. Srivatav, and R. Soares (2009), Taxa de soerguimento atual do arquipélago de Sao Pedro e Sao Paulo, Oceano Atlantico Equatorial, *REM, Ouro Preto, 62,* 331–342.

Tizard, T. H., H. N. Moseley, J. Y. Buchanan, and J. Murray (1884), Narrative of the cruise of H. M. S. Challenger. Report of the Scientific Results of the Exporing Vojage of H. M. S. Challenger 1873-76, *Narrative, 1,* 1 – 509.

Wolfe, C. J., E. A. Bergman, and S. C. Solomon (1993), Oceanic transform earthquakes with unusual mechanisms or locations relation to fault geometry and state of stress in the adjacent lithosphere, *J. Geophis. Res., 98,* 16187–16211.

Conclusions

In my PhD thesis I focused my research on the origin and the evolution of non-volcanic tectonic islands related to vertical tectonics along transform and megatransform faults offsetting slow and ultra-slow mid-ocean ridges.

Oceanic islands can be divided, according to their origin, in volcanic and non-volcanic or tectonic. Volcanic islands are due to excess volcanism caused by thermal and/or compositional mantle melting anomalies, either along mid-ocean ridges, (Iceand in the Atlantic Ocean), or within oceanic plates (Society Islands in the Pacific Ocean). They can also be formed by volcanism caused by suprasubduction "wet" mantle melting (Tonga islands in the Pacific Ocean). In contrast, oceanic tectonic islands are due not to volcanism but to vertical motions of blocks of oceanic lithosphere. They are located along: (a) slow and ultra-slow mid-ocean ridges, where the intense tectonic activity is due to periods where no magma supply is available; (b) slow and ultra-slow slip transform faults, where vertical tectonics create transverse ridges, among the major positive topographic anomalies of the ocean bottom; (c) long-lived detachment faults forming oceanic core complexes.

Previous work on sunken islands established that they originated as a result of vertical motion of lithospheric blocks due to transform-related transtension and/or transpression tectonics. In order to further understand the origin and the evolution of tectonic islands, I used in my PhD thesis various geophysical and geological marine data.

The distribution of earthquakes along mid-ocean ridges and transform faults has been used to identify the current geometry of plate boundaries and tectonically active structures. Earthquakes distribution can be obtained either using data deriving from teleseismic earthquakes, or studying continuous records of data acquired through hydrophone arrays. The temporal and spatial distribution of seismicity can be used to answer questions regarding also the development of detachment faults during plate accretion. These low-angle faults are responsible for roughly the 50% of the extension of the oceanic crust along slow spreading centers exuming lower crust and

upper mantle and creating oceanic core complexes, massifs that in some cases can reach close to sea level, forming oceanic tectonic islands. Strong seismicity is also located along “megatransforms” faults. These are a new class of transform faults presenting a complex deformation zone similar to that of continental transform systems, ~ 100-km wide and hundreds-km long. Examples are the Romanche transform, where the Mid-Atlantic Ridge is offset by a lens-shaped, about 900-km-long, 100-km-wide sliver of deformed lithosphere bound by two major transform valleys, and the 750-km-long, 120-km-wide Andrew Bain transform on the Southwest Indian Ridge. Numerical modeling predicts the development of wide multiple transform boundaries when the age offset is above a threshold value of ~ 30 Ma, i.e., in extra-long (> 500 km) slow-slip transforms.

Bathymetric and seismic reflection data have been used to investigate the morphology and the structure of most of tectonic sunken islands. A large number of dredges along paleoislands allowed to know the composition of their rocks, their $^{87}Sr/^{86}Sr$ isotopic age and carry out facies analysis to understand their paeloenvironment. Five sunken tectonic islands have been identified by bathymetric images and multichannel seismic reflection profiles along mid-ocean ridges. Four of them are located in equatorial Atlantic Ocean. The “Vema” paleoisland is the summit of the transverse ridge at the Vema transform fault (~11°); it is now about 450 m below sea level and it is capped by a ~ 500 m thick shallow-water carbonate platform dated by $^{87}Sr/^{86}Sr$ at ~11-10 Ma. Three other paleoislands have been detected on the summit of the eastern transverse ridge of the Romanche transform fault (equatorial Atlantic); we identified them, from W to E, as “Romanche A”, “Romanche B” and “Romanche C”. These paleoislands are now at 900-1000 m below sea level and they are capped by about 250-300 m thick shallow-water carbonate platforms with 10 to 6 Ma Sr isotopic ages.

Both Vema and Romanche islands formed due to vertical tectonics related to transtension/transpression along long-offset slow-slip transforms. Even slight changes in ridge/transform geometry, i.e., changes in orientation of mid-ocean ridge segments offset by transform boundaries, can cause either transtension or transpression along the transform, resulting

in vertical motions of lithospheric slabs. The ridge-parallel seafloor fabric immediately south of the Vema transform changed orientation by ~5° in ~11-10 Ma crust, implying a slight change in ridge/transform geometry that caused transtension along the transform. Flexure of the lithospheric slab bordering the southern side of the transform followed, with uplift of the edge of the slab along the transform boundary. Uplift ceased after the ridge-transform system settled into the new geometry. Subsidence, sub-aerial erosion and truncation of the emerged slab at a sea level and growth of a shallow-water carbonate cap followed. The 11-10 Ma Sr isotopic ages of the carbonate platform are compatible with the timing of the flexure and uplift of the lithosphere slab estimated from magnetic anomalies. The three Romanche sunken islands also formed due to transform related transtension/transpression, although processes and timing are less precisely constrained than at Vema. Given that erosional surfaces of the three islands lie at about the same depth below sea level, the platforms "Romanche A, B and C" formed probably during the same time interval. The complex tectonic framework of the eastern Romanche may have resulted in multiple stages of transtension/transpression and in more than one event of uplift, emersion and subsidence.

Vema and Romanche carbonate platforms are dominated by *rhodalgal-foramol* sediment associations consisting of perforate larger benthic foraminifera and red algae. Corals are present occasionally as minor components. In particular, subordinate corals and ooids are also significant components in Romanche biota, whereas no reef facies have been recognized in the Vema Platform. One question is, what caused the differences between Vema and Romanche equatorial carbonates? We propose that equatorial upwelling and humid climate may have set conditions suitable for the predominance of calcitic organisms over aragonitic corals. Additional may have been elevated CO_2 levels, hydrothermal brine fluxes, rivers-related nutrient input, biological-induced precipitation processes, substratum stability or instability and platform geometry.

Another paleoisland is "Atlantis Bank", located along the Atlantis II transform fault, that offsets the Southwest Indian Ridge. Atlantis Bank was an island when it was located at the ridge – transform intersection, while at present it is about 700 m below sea level. The most abundant biota

components of Atlantic carbonate samples are bryozoans; mollusks are locally as abundant, benthonic foraminifera are ubiquitous, planktonic foraminifera are also common. Based on texture and biotic components, the limestones from Atlantis Bank were deposited on a 100-200 m deep platform, in a high-energy zone affected by strong waves and currents. $^{87}Sr/^{86}Sr$ calculated ages of Atlantis bioclastic fragments range between 4.5 and 2.3 Ma. Atlantis Bank originated as an oceanic core complex emplaced at the eastern ridge-transform intersection of the Atlantis II Fracture Zone on the Southwest Indian Ridge, that subsequently underwent additional uplift due to transtension across the transform due to a spreading direction change.

The only modern example of tectonic island is St. Paul Rocks, located in the active zone of the St. Paul transform that offsets the equatorial Mid-Atlantic Ridge by 580 km. The Rocks are the summit of a sigmoidal topographic feature called St. Peter and St. Paul Massif, part of the transverse ridge of the St. Paul transform. This massif is made of seismically active 8-9 Ma old lithosphere. The archipelago has been rising about 1.5 mm/a in the last 6000 years and it is the result of transpressive tectonics in the active zone of St. Paul Transform Fault.

The results of my PhD study added more knowledge on the origin and the evolution of oceanic tectonic islands: a) Their evolution is not monotone, as in volcanic islands; they can reach sea level multiple times. “Cold’ tectonic islands from different oceans and spreading rates display similar histories of uplift and subsidence, driven by the combined effects of vertical tectonics and lithospheric cooling. Their evolution is different from those of typical “hot” volcanic islands characterized by rapid growth and subsequent monotonic subsidence. b) The narrow elongated shape of tectonic islands differs from the volcanic circular form, influencing the geometry and the development of carbonate platforms and fauna associations. Carbonate platforms can develop on oceanic islands, given favorable biological, physical and chemical conditions. The morphology of the platforms tends to be different in the two classes of islands. Volcanic islands tend to form circular or sub-circular platforms, that can enclose areas of low-energy (lagoons); in contrast,

tectonic islands, generally associated with transform offsets, form long and narrow platforms, elongated parallel to the transform. Low-energy lagoons are rare in tectonic islands, due to their long-narrow basement morphology. Rate of production and accumulation of carbonate sediments is affected by rate of vertical motion and eustatic sea level oscillations, that is, the rate at which accommodation space is created. During sea-level rise, platforms on volcanic islands can aggrade in all depositional systems (from the lagoon to the margin) enhancing carbonate production, and can aggrade and prograde during sea-level fall and stillstand (low- or high-stand). In contrast, carbonate platforms on tectonic island can aggrade during sea-level rise but their peculiar long and narrow morphology can affect the efficiency of the carbonate factory and thus the amount of carbonate production. During sea-level fall and still stand, being the escarpments generally very steep, little progradation can occur and significant volumes of produced material may be shed off the platform edge into the transform valley. c) Tectonic sunken islands could function as stepping stones in the paleobiogeography of the Miocene. The occurrence of *Amphistegina* in the limestones of Romanche Paleoisland C may suggest that these equatorial platforms could have served in the Miocene as stepping stones for Caribbean-type Amphistegina assemblages that extend across the Atlantic to the Cabo Verde Islands. Additional research could investigate slow and ultraslow mid-ocean ridges and transform faults in order to identify new oceanic tectonic sunken and or sunken islands (as the Anna De Koningh Seamount along the Dutoit transform fault, in the South West Indian Ocean), in order to update the insular paleobiogeography of the Neozoic era.